UNIVERSITY OF OKLAHOMA

GRADUATE COLLEGE

SCANNING TUNNELING MICROSCOPY STUDIES OF

GROWTH MEDIUM & TEMPERATURE DEPENDENT STRUCTURAL PHASES

OF ALKANETHIOL SELF-ASSEMBLED MONOLAYERS,

REACTIVE SELF-ASSEMBLED MONOLAYERS, &

FLAT GOLD NANOPARTICLE/INDIUM TIN OXIDE SUBSTRATES

AND

A SCANNING SURFACE PHOTOVOLTAGE MICROSCOPY STUDY

FOR LOCAL MECHANICAL STRESS CHARACTERIZATION

IN COMPLEMENTARY METAL OXIDE SEMICONDUCTOR DEVICES

A DISSERTATION

SUBMITTED TO THE GRADUATE FACULTY

in partial fulfillment of the requirements for the

Degree of

DOCTOR OF PHILOSOPHY

By

DAHANAYAKA LIYANAGE DAMINDA HEMAL DAHANAYAKA
Norman, Oklahoma
2010

SCANNING TUNNELING MICROSCOPY STUDIES OF
GROWTH MEDIUM & TEMPERATURE DEPENDENT STRUCTURAL PHASES
OF ALKANETHIOL SELF-ASSEMBLED MONOLAYERS,
REACTIVE SELF-ASSEMBLED MONOLAYERS, &
FLAT GOLD NANOPARTICLE/INDIUM TIN OXIDE SUBSTRATES
AND
A SCANNING SURFACE PHOTOVOLTAGE MICROSCOPY STUDY
FOR LOCAL MECHANICAL STRESS CHARACTERIZATION
IN COMPLEMENTARY METAL OXIDE SEMICONDUCTOR DEVICES


A DISSERTATION APPROVED FOR THE
HOMER L. DODGE DEPARTMENT OF PHYSICS & ASTRONOMY




BY


_____
Dr. Lloyd A. Bumm, Chair


_____
Dr. Ronald L. Halterman


_____
Dr. Matthew B. Johnson


_____
Dr. Michael B. Santos


_____
Dr.  Wai Tak Yip

TO

MY PARENTS, WIFE, SON

AND

IN LOVING MEMORY OF MY GRANDMOTHER AND UNCLE

## Acknowledgments

This arduous achievement wouldn't have accomplished without tremendous help and support I generously received from many individuals whom I highlight below.

My thesis advisor Professor Lloyd A. Bumm deserves special thanks. He meticulously turned me from just an enthusiastic student to an enthusiastic and successful researcher. He never failed to provide me with encouragement and new directions. I would like to express my sincere gratitude to him for all the support and guidance he offered me throughout my studies. Thank you very much for everything you did for me!

I also thank all the committee members Dr. R. L. Halterman, Dr. M. B. Johnson, Dr. M. B. Santos, Dr. W. T. Yip and former committee member Dr. J. P. Shaffer for their excellent comments and input for the successful completion of this thesis. I specially thank Dr. Halterman for the constant supply of molecules for this research. The useful discussions I had with him helped me gain a better understanding of chemistry. I also thank Dr. Johnson for allowing me to use his lab resources, Dr. Joel Keay for helping me to use the AFM and XPS, Dr. Syed Ali Beer Mohamed and Kevin Hobbs for helping me with the XPS measurements and the analysis.

Dr. James A. Slinkman, Mr. Phill V. Kaszuba and Mr. Leon Moszkowicz at IBM/Burlington were excellent mentors and wonderful friends as well. Their persuasive and reassuring support motivated me to establish the SSPVM method for stress detection. Their kind hospitality made my stay at Burlington an unforgettable and pleasant experience. I also want to thank Dr. Charles P. Daghlian,

iv

# Table of Contents

vii

# List of Tables

## List of Figures

xiv

## Abstract

Self-assembled monolayers (SAMs) of alkanethiolates on Au(111) represent promising platforms to study the molecular surfaces and interfaces for applications ranging from molecular electronics, nanophotonics to biology. Understanding the effect of growth conditions on SAMs particularly on their structural features is important from both fundamental and applied points of view. Knowledge of SAM structural features and structural phase transitions provides important insights into molecular packing for the control of the molecular self-assembly.

We compared SAMs grown from different media, from 1 mM C10 solution in decalin, hexadecane and triethylene glycol and from C10 vapor. We present a molecularly-resolved scanning tunneling microscopy study showing the dependence of the SAM structure on the growth conditions. We have established conditions for making samples almost vacancy islands (VI) free with very large SAM domains of $(2\sqrt{3} \times 3)$rect. superstructure and $(\sqrt{3} \times 4\sqrt{3})R30°$ striped-phase and investigated the orientation of low-index step edges of Au(111) for normal and striped-phase SAMs. We showed that the striped phase is stable to converting to $(2\sqrt{3} \times 3)$rect. below 40 °C.

We demonstrate that flat gold nanoparticles (FGNPs) supported on indium tin oxide glass (ITO) are excellent substrates for molecularly-resolved STM imaging of alkanethiol SAMs. Nanoparticles were characterized using STM, TEM, and SEM techniques. Surface treatment techniques, $Ar/O_2$ and $H_2$ plasma treatments, dry thermal annealing and exposures to $UV/O_3$, were used to prepare the surfaces of

FGNPs supported on ITO and Au/mica substrates for high-resolution STM imaging of alkanethiol SAMs.

We developed a convergent approach to functionalize SAM surfaces. Ordered mixed monolayers comprised of alkanethiols and azidoalkanethiols islands are formed and subsequent IMesCu$^I$Br catalyzed [3+2] "click" cycloaddition reaction with substituted alkyne introduced dilute substituent onto the ordered surface.

Mechanical stress is one of the major factors in current design and manufacture of very large scale integrated (VLSI) devices. Mechanical stress in deep sub-micron silicon technologies can drastically alter carrier mobility (e.g., approximately 25% dependent on device geometry). This affects the device performance. Current in-line production stress metrology is conducted only at a wafer monitor level. The available stress measurement techniques such as micro-Raman spectroscopy, nano beam diffraction (NBD), converging electron beam diffraction (CEBD) either do not have required resolution or they require complex data interpretation. We present a method for measuring mechanical stress in deep sub-micron silicon devices with high spatial resolution using scanning Kelvin probe force microscopy and scanning surface photovoltage (SSPVM) techniques.

# Chapter 1

## Introduction

### 1.1    Self Assembled Monolayers

Self-assembled monolayers (SAMs) provide a convenient, flexible, and simple system with which to tailor the interfacial properties of various types of materials (e.g. metals, metal oxides, and semiconductors) and provide promising platforms for the study of molecular surfaces and interfaces. SAMs are organic assemblies formed by the adsorption of molecular constituents from solution or from the gas phase onto the surface of solids. The adsorbates organize spontaneously into crystalline structures. The molecules or ligands that form SAMs have a chemical functionality, or "headgroup", with a specific affinity for a substrate. In many cases, because of the high affinity of the headgroups for the surface they displace adsorbed adventitious organic materials from the surface.

SAMs of alkanethiolates and their derivatives on Au{111} have drawn considerable attention as a model system for fundamental studies in nanoscale surface science.[1-6] The alkanethiol-Au {111} system forms a well ordered SAM due to the chemisorptions of the sulfur head groups on the Au surface and the van der Waals interactions between alkyl chains. Structure of SAM greatly depends on growth conditions. Knowledge of SAM structural features and structural phase transitions provide important insights into molecular packing for the control of the molecular self-assembly. Therefore understanding the effect of different growth conditions on the structural features of SAMs is important.

Extensive investigations have been carried out to understand fundamental features of alkanethiolate SAMs such as the molecular structure, growth process, stability, and interface properties using surface sensitive spectroscopy and microscopy.[3,7-19] Among those, scanning tunneling microscopy (STM) has allowed study of the structure of SAMs with molecular resolution.[7-8,10-11,13-15,20]

The results of experiments presents in chapter one describe the effect of growth medium on the structure of the monolayer and characteristics and kinetic stability of structures of monolayers deposited at elevated temperatures.

## 1.2 Flat Gold Nanoparticles

Nanophotonics and molecular plasmonics are developing nanoscale optical sciences and technologies where light is confined and controlled on dimensions much smaller than its wavelength.[21-22] At the molecular scale, it takes the form of excited state energy flow between molecules such as in nature's photosynthetic systems and in artificially engineered molecules.[23-24] On slightly larger length scales, optically resonant structures such as metal nanoparticles can be used as nanophotonic antenna. Incident light (far-field) excites the plasmon resonance modes in the nanoparticle which have highly localized near-field modes that concentrate the incident optical energy near their surfaces. When molecules are located in the near-field region, this effect is responsible for surface enhanced fluorescence[24-28] and surface enhanced Raman scattering (SERS),[29-32] which are applications of the general concept of molecular plasmonics.[33] At even longer length scales, the coupled plasmon modes of nanoparticle arrays have been used to confine and to guide photonic energy to build plasmon optics.[34-37] The plasmon resonances of

subwavelength metal apertures impart them with anomalous transmission characteristics,[38] and have been applied to create plasmonic lenses.[39] Recently, shaped nanoparticles have attracted attention because of their application as photonic antennae.[40-42]

Adjusting the shape of the nanoparticle tunes the plasmon resonance frequency and controls the spatial structure of the near-field.[43] The very large SERS enhancements of $10^{14}$ observed in single molecule SERS experiments are thought to be due at least in part, to near-field hot spots around the particles.[44] Utilizing the local hot spots of shaped nanoparticles for molecular plasmonics/nanophotonics will require precise placement of the molecular components at these positions as well as verification of their location.

Typical nanoparticles have high curvature, therefore not flat enough for the STM to achieve molecular resolution where atomically flat terraces are required. Hence, the production and characterization of optically resonant atomically flat metallic nanoparticles that can be used as platforms for ordered self-assembled monolayers are important. The flat substrates will also be used for STM-based imaging of molecules and can be used for spatially precise excitation of molecules. These substrates offer the unique advantage that simultaneous structural and optical measurements can be made due to the FGNP's behavior as a photonic antenna.

In chapter two we establish methodology for growing atomically flat gold nanoparticles (FGNPs), depositing them onto indium tin oxide (ITO) coated glass supporting substrates, and coating the FGNPs with self-assembled monolayers.

## 1.3    Surface Pre-treatment of Flat Gold Nnaoparticles

Au has been widely used as a substrate for studies of self-assembled monolayes of alkanethiol molecules.[3,13,45-48] Au substrates which are used in STM studies are typically Au{111} oriented thin films on mica or Au{111} surfaces of bulk single crystals.[8,19,49-53] The surface of Au should be atomically flat, or compose of atomically flat terraces large for high resolution STM of SAMs.

Au surfaces stored under ambient conditions or solution prepared colloidal nanoparticles have ubiquitous carbonaceous and ionic contaminants adsorbed on their surfaces.[54] Surface treatment or conditioning of FGNP/ITO substrates is required if the solution grown surface with adsorbents interfere with the subsequent experiments. For instance, solution grown FGNPs synthesized by the reduction of Au from $HAuCl_4$ with citric acid usually result in adsorbed citrate ions and/or surfactants to the particle surface.[55] The knowledge of FGNP surface morphology or shape upon pretreatments is not available. Therefore a detailed investigation is required to understand the surface morphology, the terrace size and structure of these nanoparticles after pretreatments, and how they influence the formation of alkanethiol SAMs.

Common procedures for treating Au surfaces include electrochemical oxidation,[56] immersion into a strongly oxidizing solutions such as piranha solution,[57] exposure to $UV/O_3$,[58] or plasma ($O_2$, $H_2$, Ar),[59] $H_2$ flame annealing, and thermal annealing.[60] Sputtering also is typically employed to treat single crystal Au surfaces in UHV. Dry techniques are more suitable for treatment of FGNP/ITO substrates compared to wet chemical processes. Because the later bear the potential danger of contamination as well as possible degradation of ITO substrate induced by the reagents used.

Chapter three describes the systematic investigation of dry surface treatments of FGNP/ITO substrates using thermal annealing, Ar/O$_2$ plasma, H$_2$ plasma, and UV/O$_3$ exposure, and study of the surface morphology/terrace structure along and subsequent alkanethiol SAM growth.

## 1.4 Reactive Self Assembled Monolayers

Properties of SAM surfaces can be tuned by controlling the spatial arrangement (physical structure) of the SAM and the chemical properties of the exposed functional group. SAMs are used as a support matrix to immobilize other molecules (redox-molecules, oligonucleotides or any other molecule with a functional group of interest) or nanomaterials on surfaces such as gold, silver, silicon, and silica.[2,4,61] Typically functional molecules are tethered to a thiol pendent group in one end and co-deposited with alkanethiol or backfilled into the already formed alkanethiol monolayer.[62-63] This process does not always produce good results. Some molecules do not form well ordered monolayers on their own while others reduce the crystalline order of the existing alkanethiol monolayer. Thus it may not be practical to grow a well-ordered SAM using a thiol with any arbitrary terminal functional group.[62]

A possible methodology that circumvents this problem is to first grow a monolayer of thiol with a reactive end group. Then in a subsequent step, a second molecule which has the desired chemical functional group couples to the functional SAM surface. This in-situ coupling reduces a significant amount of time involved in process development and synthesizing individual functional molecules and enables use of large number of functional groups. Click chemistry has been widely used to couple between

two groups and has been demonstrated as versatile and highly selective.[64] Although all Click reactions may not be suitable for every situation, Sharpless "click" chemistry, specifically which uses $Cu^I$-catalyzed 1,3-dipolar cycloaddition of azide and alkyne has been proved to be very effective way to make connections between broad variety of functional groups.[65-66] Not only does this produce a high yield but the chemistry is relatively simple. The functional groups used in click chemistry are highly specific, do not react with each other or with solvents. Incorporation of azide and alkyne groups into other molecules is relatively easy. The reaction occurs under very mild conditions and the coupling occurs only between the two reactants.

We demonstrate molecularly resolved STM images of reactive SAMs of azide before and after reacting with *p*-tolylacetylene in chapter four.

## 1.5    Process Induced Mechanical Stress in Integrated Devices

Process-induced mechanical stress is an important parameter in engineering the performance of sub-micron size microelectronic devices such as complementary metal oxide field effect transistors (CMOS FETs) and bipolar junction transistors (BJTs). Uncontrolled stress can be parasitic and can degrade device performance.  But controlled stress can be used to enhance performance of some devices. For example, stress is currently used to enhance the performance of devices in strained Si/SiGe technologies.[67-72] Thus it is vital to accurately monitor and control stress in these structures. The available methods for measuring stress are not suitable for current in-line production stress metrology. Because they do not have required resolution, need complex data interpretation, or destructive. Therefore the demand for a method of measuring and

manipulating mechanical stress quantitatively with high spatial resolution exists in the

semiconductor industry.

**1.6 References for chapter 1**

(1)     Schonenberger, C.; Jorritsma, J.; Sondag-Huethorst, J. A. M.; Fokkink, L. G. J. Domain Structure of Self-Assembled Alkanethiol Monolayers on Gold. *J. Phys. Chem.* **1995**, *99,* 3259.


(2)     Love, J. C.; Estroff, L. A.; Kriebel, J. K.; Nuzzo, R. G.; Whitesides, G. M. Self-Assembled Monolayers of Thiolates on Metals as a Form of Nanotechnology. *Chem. Rev.* **2005**, *105,* 1103.


(3)     Vericat, C.; Vela, M. E.; Benitez, G. A.; Martin Gago, J. A.; Torrelles, X.; Salvarezza, R. C. Surface Characterization of Sulfur and Alkanethiol Self-Assembled Monolayers on Au(111). *J. Phys.: Condens. Matter* **2006**, *18,* R867.


(4)     Schreiber, F. Structure and Growth of Self-Assembling Monolayers. *Prog. Surf. Sci.* **2000**, *65,* 151.


(5)     Bumm, L. A.; Arnold, J. J.; Cygan, M. T.; Dunbar, T. D.; Burgin, T. P.; Jones, L., II; Allara, D. L.; Tour, J. M.; Weiss, P. S. Are Single Molecular Wires Conducting? *Science* **1996**, *271,* 1705.


(6)     Tour, J. M. Molecular Electronics. Synthesis and Testing of Components. *Acc. Chem. Res.* **2000**, *33,* 791.


(7)     Poirier, G. E.; Fitts, W. P.; White, J. M. Two-Dimensional Phase Diagram of Decanethiol on Au(111). *Langmuir* **2001**, *17,* 1176.


(8)     Camillone III, N.; Eisenberger, P.; Leung, T. Y. B.; Schwartz, P.; Scoles, G.; Poirier, G. E.; Tarlov, M. J. New Monolayer Phases of *n*-Alkane Thiols Self-Assembled on Au(111): Preparation, Surface Characterization, and Imaging. *J. Chem. Phys.* **1994**, *101,* 11031.


(9)     Camillone, N.; Leung, T. Y. B.; Schwartz, P.; Eisenberger, P.; Scoles, G. Chain Length Dependence of the Striped Phases of Alkanethiol Monolayers Self-Assembled on Au(111): An Atomic Beam Diffraction Study. *Langmuir* **1996**, *12,* 2737.

(10)    Fitts, W. P.; White, J. M.; Poirier, G. E. Low-Coverage Decanethiolate Structure on Au(111): Substrate Effects. *Langmuir* **2002**, *18*, 1561.

(11)    Fitts, W. P.; White, J. M.; Poirier, G. E. Thermodynamics of Decanethiol Adsorption on Au(111): Extension to 0 °C. *Langmuir* **2002**, *18*, 2096.

(12)    Poirier, G. E. Mechanism of Formation of Au Vacancy Islands in Alkanethiol Monolayers on Au(111). *Langmuir* **1997**, *13*, 2019.

(13)    Poirier, G. E. Characterization of Organosulfur Molecular Monolayers on Au(111) using Scanning Tunneling Microscopy. *Chem. Rev.* **1997**, *97*, 1117.

(14)    Poirier, G. E.; Pylant, E. D. The Self-Assembly Mechanism of Alkanethiols on Au(111). *Science* **1996**, *272*, 1145.

(15)    Poirier, G. E.; Tarlov, M. J. The c(4 × 2) Superlattice of *n*-Alkanethiol Monolayers Self-Assembled on Au(111). *Langmuir* **1994**, *10*, 2853.

(16)    Poirier, G. E.; Tarlov, M. J. Molecular Ordering and Gold Migration Observed in Butanethiol Self-Assembled Monolayers Using Scanning-Tunneling-Microscopy. *J. Phys. Chem.* **1995**, *99*, 10966.

(17)    Poirier, G. E.; Tarlov, M. J.; Rushmeier, H. E. 2-Dimensional Liquid-Phase and The p × √3 Phase of Alkanethiol Self-Assembled Monolayers On Au(111). *Langmuir* **1994**, *10*, 3383.

(18)    Qian, Y. L.; Yang, G. H.; Yu, J. J.; Jung, T. A.; Liu, G. Y. Structures of Annealed Decanethiol Self-Assembled Monolayers on Au(111): an Ultrahigh Vacuum Scanning Tunneling Microscopy Study. *Langmuir* **2003**, *19*, 6056.

(19)    Woodward, J. T.; Walker, M. L.; Meuse, C. W.; Vanderah, D. J.; Poirier, G. E.; Plant, A. L. Effect of an Oxidized Gold Substrate on Alkanethiol Self-Assembly. *Langmuir* **2000**, *16*, 5347.

(20)    Yang, G.; Liu, G.-y. New Insights for Self-Assembled Monolayers of Organothiols on Au(111) Revealed by Scanning Tunneling Microscopy. *J. Phys. Chem. B* **2003**, *107*, 8746.

(21)     Hutter, E.; Fendler, J. H. Exploitation of Localized Surface Plasmon Resonance. *Adv. Mater.* **2004**, *16*, 1685.

(22)     Lieber, C. M. Nanoscale Science and Technology: Building a Big Furture from Small Things. *MRS Bull.* **2003**, *28*, 486.

(23)     Swallen, S. F.; Kopelman, R.; Moore, J. S.; Devadoss, C. Dendrimer Photoantenna Supermolecules: Energetic Funnels, Exciton Hopping and Correlated Excimer Formation. *J. Mol. Struct.* **1999**, *486*, 585.

(24)     Lakowicz, J. R.; Shen, Y.; D'Aurita, S.; Malicka, J.; Fang, J.; Gryczynski, Z.; Gryczynski, I. Radiative Decay Engineering 2. Effects of Silver Island Films on Fluorescence Intensity, Lifetimes, and Resonance Energy Transfer. *Anal. Biochem.* **2002**, *301*, 261.

(25)     Lakowicz, J. R. Radiative Decay Engineering 3: Surface Plasmon-Coupled Directional Emission. *Anal. Biochem.* **2004**, *324*, 153.

(26)     Lakowicz, J. R. Radiative Decay Engineering 5: Metal-Enhanced Fluorescence and Plasmon Emission. *Anal. Biochem.* **2005**, *337*, 171.

(27)     Lakowicz, J. R. Radiative Decay Engineering: Biophysical and Biomedical Applications. *Anal. Biochem.* **2001**, *298*, 1.

(28)     Gryczynski, I.; Malicka, J.; Gryczynski, Z.; Lakowicz, J. R. Radiative Decay Engineering 4: Experimental Studies of Surface Plasmon-Coupled Directional Emission. *Anal. Biochem.* **2004**, *324*, 170.

(29)     Kelly, K. L.; Coronado, E.; Zhao, L. L.; Schatz, G. C. The Optical Properties of Metal Nanoparticles: The Influence of Size, Shape, and Dielectric Environment. *J. Phys. Chem. B* **2003**, *107*, 668.

(30)     Mock, J. J.; Barbic, M.; Smith, D. R.; Schultz, D. A.; Schultz, S. Shape Effects in Plasmon Resonance of Individual Colloidal Silver Nanoparticles. *J. Chem. Phys.* **2002**, *116*, 6755.

(31)     Kneipp, K.; Kneipp, H.; Itzkan, I.; Dasari, R. R.; Feld, M. S. Ultra Sensitive Chemical Analysis by Raman Spectroscopy. *Chem. Rev.* **1999**, *99*, 2957.

(32)     Campion, A.; Kambhampati, P. Surface-Enhanced Raman Scattering. *Chem. Soc. Rev.* **1998**, *27*, 241.


(33)     Van Duyne, R. P. Molecular Plasmonics. *Science* **2004**, *306*, 985.


(34)     Maier, S. A.; Kik, P. G.; Atwater, H. A.; Meltzer, S.; Harel, E.; Koel, B. E.; Requicha, A. A. G. Local Detection of Electromagnetic Energy Transport Below the Diffraction Limit in Metal Nanoparticle Plasmon Waveguides. *Nat. Mater.* **2003**, *2*, 229.


(35)     Yin, L.; Vlasko-Vlasov, V. K.; Pearson, J.; Hiller, J. M.; Hua, J.; Welp, U.; Brown, D. E.; Kimball, C. W. Subwavelength Focusing and Guiding of Surface Plasmons. *Nano Lett.* **2005**, *5*, 1399.


(36)     Liu, Z.; Steele, J. M.; Srituravanich, W.; Pikus, Y.; Sun, C.; Zhang, X. Focusing Surface Plasmons with a Plasmonic Lens. *Nano Lett.* **2005**, *5*, 1726.


(37)     Ditlbacher, H.; Krenn, J. R.; Schider, G.; Leitner, A.; Aussenegg, F. R. Two-Dimensional Optics with Surface Plasmon Polaritons. *Appl. Phys. Lett.* **2002**, *81*, 1762.


(38)     Ebbesen, T. W.; Lezec, H. J.; Ghaemi, H. F.; Thio, T.; Wolff, P. A. Extraordinary Optical Transmission Through Sub-Wavelength Hole Arrays. *Nature* **1998**, *391*, 667.


(39)     Lezec, H. J.; Degiron, A.; Devaux, E.; Linke, R. A.; Martin-Moreno, L.; Garcia-Vidal, F. J.; Ebbesen, T. W. Beaming Light from a Subwavelength Aperture. *Science* **2002**, *297*, 820.


(40)     Fromm, D. P.; Sundaramurthy, A.; Schuck, P. J.; Kino, G.; Moerner, W. E. Gap-Dependent Optical Coupling of Single "Bowtie" Nanoantennas Resonant in the Visible. *Nano Lett.* **2004**, *4*, 957.


(41)     Grober, R. D.; Schoelkopf, R. J.; Prober, D. E. Optical Antenna: Towards a Unity Efficiency Near-Field Optical Probe. *Appl. Phys. Lett.* **1997**, *70*, 1354.


(42)     Xia, Y.; Halas, N. J. Shape-Controlled Synthesis and Surface Plasmonic Properties of Metallic Nanostructures. *MRS Bull.* **2005**, *30*, 338.


(43)     Hao, E.; Schatz, G. C. Electromagnetic Fields Around Silver Nanoparticles and Dimers. *J. Chem. Phys.* **2004**, *120*, 357.

(44)    Nie, S.; Emory, S. R. Probing Single Molecules and Single Nanoparticles by Surface-Enhanced Raman Scattering. *Science* **1997**, *275*, 1102.


(45)    Dunbar, T. D.; Cygan, M. T.; Bumm, L. A.; McCarty, G. S.; Burgin, T. P.; Reinerth, W. A.; Jones, L.; Jackiw, J. J.; Tour, J. M.; Weiss, P. S.; Allara, D. L. Combined Scanning Tunneling Microscopy and Infrared Spectroscopic Characterization of Mixed Surface Assemblies of Linear Conjugated Guest Molecules in Host Alkanethiolate Monolayers on Gold. *J. Phys. Chem. B* **2000**, *104*, 4880.


(46)    Vericat, C.; Vela, M. E.; Salvarezza, R. C. Self-Assembled Monolayers of Alkanethiols on Au(111): Surface Structures, Defects and Dynamics. *Phys. Chem. Chem. Phys.* **2005**, *7*, 3258.


(47)    Love, J. C.; Estroff, L. A.; Kriebel, J. K.; Nuzzo, R. G.; Whitesides, G. M. Self-Assembled Monolayers of Thiolates on Metals as a Form of Nanotechnology. *Chem. Rev.* **2005**, *105*, 1103.


(48)    Schreiber, F.; Eberhardt, A.; Leung, T. Y. B.; Schwartz, P.; Wetterer, S. M.; Lavrich, D. J.; Berman, L.; Fenter, P.; Eisenberger, P.; Scoles, G. Adsorption Mechanisms, Structures, and Growth Regimes of an Archetypal Self-Assembling System: Decanethiol on Au(111). *Phys. Rev. B* **1998**, *57*, 12476.


(49)    Barrena, E.; Palacios-Lidon, E.; Munuera, C.; Torrelles, X.; Ferrer, S.; Jonas, U.; Salmeron, M.; Ocal, C. The Role of Intermolecular and Molecule-Substrate Interactions in the Stability of Alkanethiol Nonsaturated Phases on Au(111). *J. Am. Chem. Soc.* **2004**, *126*, 385.


(50)    Kautz, N. A.; Kandel, S. A. Alkanethiol/Au(111) Self-Assembled Monolayers Contain Gold Adatoms: Scanning Tunneling Microscopy before and after Reaction with Atomic Hydrogen. *J. Am. Chem. Soc.* **2008**, *130*, 6908.


(51)    Monnell, J. D.; Stapleton, J. J.; Jackiw, J. J.; Dunbar, T.; Reinerth, W. A.; Dirk, S. M.; Tour, J. M.; Allara, D. L.; Weiss, P. S. Ordered Local Domain Structures of Decaneselenolate and Dodecaneselenolate Monolayers on Au{111}. *J. Phys. Chem. B* **2004**, *108*, 9834.


(52)    Ron, H.; Rubinstein, I. Alkanethiol Monolayers on Preoxidized Gold. Encapsulation of Gold Oxide under an Organic Monolayer. *Langmuir* **1994**, *10*, 4566.

(53)    Subramanian, S.; Sampath, S. Enhanced Thermal Stability and Structural Ordering in Short Chain *n*-Alkanethiol Monolayers on Gold Probed by Vibrational Spectroscopy and EQCM *Anal. Bioanal. Chem.* **2007**, *388*, 135.

(54)    Ron, H.; Matlis, S.; Rubinstein, I. Self-Assembled Monolayers on Oxidized Metals. 2. Gold Surface Oxidative Pretreatment, Monolayer Properties, and Depression Formation. *Langmuir* **1998**, *14*, 1116.

(55)    Turkevich, J.; Stevenson, P. C.; Hillier, J. Study of the Nucleation and Growth Processes in the Synthesis of Colloidal Gold. *Discuss. Faraday Soc.* **1951**, *11*, 55.

(56)    Feng, C. L.; Li, Y.; Tong, Y. C. Cleaning and Elecrochemical Characterization of Gold Surface. *Liaoning Shifan Dax.Xue.Zir.Kex.* **2004**, *27*, 440.

(57)    Evans, S. D.; Sharma, R.; Ulman, A. Contact Angle Stability: Reorganization of Monolayer Surfaces? *Langmuir* **1991**, *7*, 156.

(58)    Sondaghuethorst, J. A. M.; Fokkink, L. G. J. Potential-Dependent Wetting Of Octadecanethiol-Modified Polycrystalline Gold Electrodes. *Langmuir* **1992**, *8*, 2560.

(59)    Sabatani, E.; Rubinstein, I.; Maoz, R.; Sagiv, J. Organized Self-Assembling Monolayers on Electrodes : Part I. Octadecyl Derivatives on Gold. *J. Electroanal. Chem.* **1987**, *219*, 365.

(60)    Sakata Tomomi; Okabe Yuichi; Kuwabara Kei; Sato Norio; Ono Kazuyoshi; Shimoyama Nobuhiro; Machida1 Katsuyuki; Hiromu, I. Surface Cleaning of Gold Structure by Annealing during Fabrication of Microelectromechanical System Devices. *Japanese Journal of Applied Physics* **2009**, *48*, 26501.

(61)    Schreiber, F. Self-Assembled Monolayers: from 'Simple' Model Systems to Biofunctionalized Interfaces. *J. Phys.-Condes. Matter* **2004**, *16*, R881.

(62)    Chidsey, C. E. D.; Bertozzi, C. R.; Putvinski, T. M.; Mujsce, A. M. Coadsorption of Ferrocene-Terminated and Unsubstituted Alkanethiols on Gold: Electroactive Self-Assembled Monolayers. *J. Am. Chem. Soc.* **1990**, *112*, 4301.

(63)    Collman, J. P.; Devaraj, N. K.; Eberspacher, T. P. A.; Chidsey, C. E. D. Mixed Azide-Terminated Monolayers: A Platform for Modifying Electrode Surfaces. *Langmuir* **2006**, *22*, 2457.

(64)    Rodionov, V. O.; Fokin, V. V.; Finn, M. G. Mechanism of the Ligand-Free Cu$^I$-Catalyzed Azide-Alkyne Cycloaddition Reaction. *Angew. Chem. Int. Ed.* **2005**, *44*, 2210.

(65)    Rostovtsev, V. V.; Green, L. G.; Fokin, V. V.; Sharpless, K. B. A Stepwise Huisgen Cycloaddition Process: Copper(I)-Catalyzed Regioselective "Ligation" of Azides and Terminal Alkynes. *Angew. Chem. Int. Ed.* **2002**, *41*, 2596.

(66)    Kolb, H. C.; Finn, M. G.; Sharpless, K. B. Click Chemistry: Diverse Chemical Function from a Few Good Reactions. *Angew. Chem. Int. Ed.* **2001**, *40*, 2004.

(67)    Haugerud, B. M.; Bosworth, L. A.; Belford, R. E. Mechanically Induced Strain Enhancement of Metal-Oxide-Semiconductor Field Effect Transistors. *J. Appl. Phys.* **2003**, *94*, 4102.

(68)    Andrieu, F.; Ernst, T.; Ravit, C.; Jurczak, M.; Ghibaudo, G.; Deleonibus, S. In-Depth Characterization of the Hole Mobility in 50-nm Process-Induced Strained MOSFETs. *IEEE Electron Device Lett.* **2005**, *26*, 755.

(69)    Roldan, J. B.; Gamiz, F.; Cartujo-Cassinello, R.; Cartujo, P.; Carceller, J. E.; Roldan, A. Strained-Si on Si$_{1-x}$Ge$_x$ MOSFET Mobility Model. *IEEE Trans. Electron Devices* **2003**, *50*, 1408.

(70)    Maikap, S.; Yu, C. Y.; Jan, S. R.; Lee, M. H.; Liu, C. W. Mechanically Strained Strained-Si NMOSFETs. *IEEE Electron Device Lett.* **2004**, *25*, 40.

(71)    Keyes, R. W. High-Mobility FET in Strained Silicon. *IEEE Trans. Electron Devices* **1986**, *33*, 863.

(72)    Zhang, Y.; Fischetti, M. V.; Soree, B.; Magnus, W.; Heyns, M.; Meuris, M. Physical Modeling of Strain-Dependent Hole Mobility in Ge *p*-Channel Inversion Layers. *J. Appl. Phys.* **2009**, *106*, 083704.

# Chapter 2

## Characteristics of Alkanethiol/Au(111) Self-Assembled Monolayers (SAMs): A Scanning Tunneling Microscopy Study of Temperature and Growth Medium Dependent Structures

### 2.1 Abstract

Self-assembled monolayers (SAMs) of alkanethiolates on Au(111) represent promising platforms for the study of molecular surfaces and interfaces. Understanding the effect of growth conditions on the structural features of SAMs is particularly important from both fundamental and applied points of view. Knowledge of SAM structural features and structural phase transitions provide important insights into molecular packing for the control of the molecular self-assembly. This chapter presents a systematic STM study of the structure of alkanethiol/Au(111) SAMs grown at different temperatures and in different media. The typical structural features of SAMs include (i) the $(\sqrt{3} \times \sqrt{3})R30°$ overlayer lattice and related superstructures, (ii) the structural domain boundaries between crystalline domains with different orientational and translational registration, (iii) molecular defects where the alkanethiolate molecules are absent or disordered and (iv) substrate vacancy islands (VIs) that are one atomic layer deep holes in the Au{111} surface characteristic of some growth conditions. We have compared SAMs grown from different media, from 1 mM C10 solution in decalin, hexadecane and triethylene glycol and from C10 vapor. We present a molecularly-resolved scanning tunneling microscopy study showing the dependence of the SAM structure on the growth conditions. The sizes of VIs are observed to increase with increasing growth temperature due to Ostwald

ripening. This trend is the same for both solution and vapor grown SAMs, although the structure of the C10 monolayers can vary significantly with the growth medium. In solution at 100 °C (decalin and triethylene glycol), growth gives a monolayer dominated by a striped-phase, while vapor growth gives $(2\sqrt{3} \times 3)$rect. with large domains and few, if any, VIs. For vapor grown SAMs, we have established conditions for making samples almost VI free with very large SAM domains. When the $(2\sqrt{3} \times 3)$rect. SAM is present, the Au step edges annealed to the Au<110> direction.

Further increase of the deposition temperature leads to formation of the striped-phase $(\sqrt{3} \times 4\sqrt{3})$R30°. To grow this phase, the partial pressure of C10 must be slightly below the saturation vapor pressure. Excess or less amount of alkanethiol leads to the normal $(2\sqrt{3} \times 3)$rect. structure or disordered (incomplete) stripe structure. Stripes orient in the C10 nearest neighbor direction (Au<211>) and the low index step edges align in the same direction as stripes (Au<211>) in contrast to the $(2\sqrt{3} \times 3)$rect. SAM. Vapor-grown striped-phase SAM samples which were quenched in cryobath (isopropanol bath, −52 °C) and in a liquid nitrogen bath (−196 °C) have confirmed that the observed structures are representative of high-temperature phase. On the other hand, solution-grown SAMs have been observed to transition to the striped-phase between 60 °C and 80 °C followed by gradual disordering of the structure above 100 °C. Also we showed that the striped phase is stable to converting to $(2\sqrt{3} \times 3)$rect. below 40 °C.

## 2.2 Introduction

Self assembled monolayers (SAMs) of alkanethiolates and their derivatives on Au{111} have drawn considerable attention as a model system for fundamental studies in nanoscale surface science.[1-6] The alkanethiol-Au{111} system forms a well ordered SAM

due to the chemisorption of the sulfur head groups on the Au surface and the van der Waals interactions between alkyl chains. Extensive investigations have been carried out to understand fundamental features of alkanethiolate SAMs such as the molecular structure, growth process, stability, and interface properties using surface sensitive spectroscopy and microscopy.[3,7-19] Among those, scanning tunneling microscopy (STM) has allowed study of the structure of SAMs with molecular resolution.[7-8,10-11,13-15,20]

The experiments describe in this chapter study the effect of growth medium on the structure of the monolayer and the characteristics and kinetic stability of structures of monolayers deposited at elevated temperatures. The alkanethiols used throughout this study are 1-octanethiol, 1-decanethiol and 1-dodecanethiol. The solvents (Figure 2.1) used are ethanol, *n*-butanol, decalin, *n*-hexadecane, and triethylene glycol. Ethanol, *n*-butanol, and triethylene glycol are alcohols with increasingly higher boiling points.

1-octanethiol

1-decanethiol

1-dodecanethiol

ethanol

*n*-butanol

decalin

*n*-hexadecane

triethylene glycol

C   H   S   O
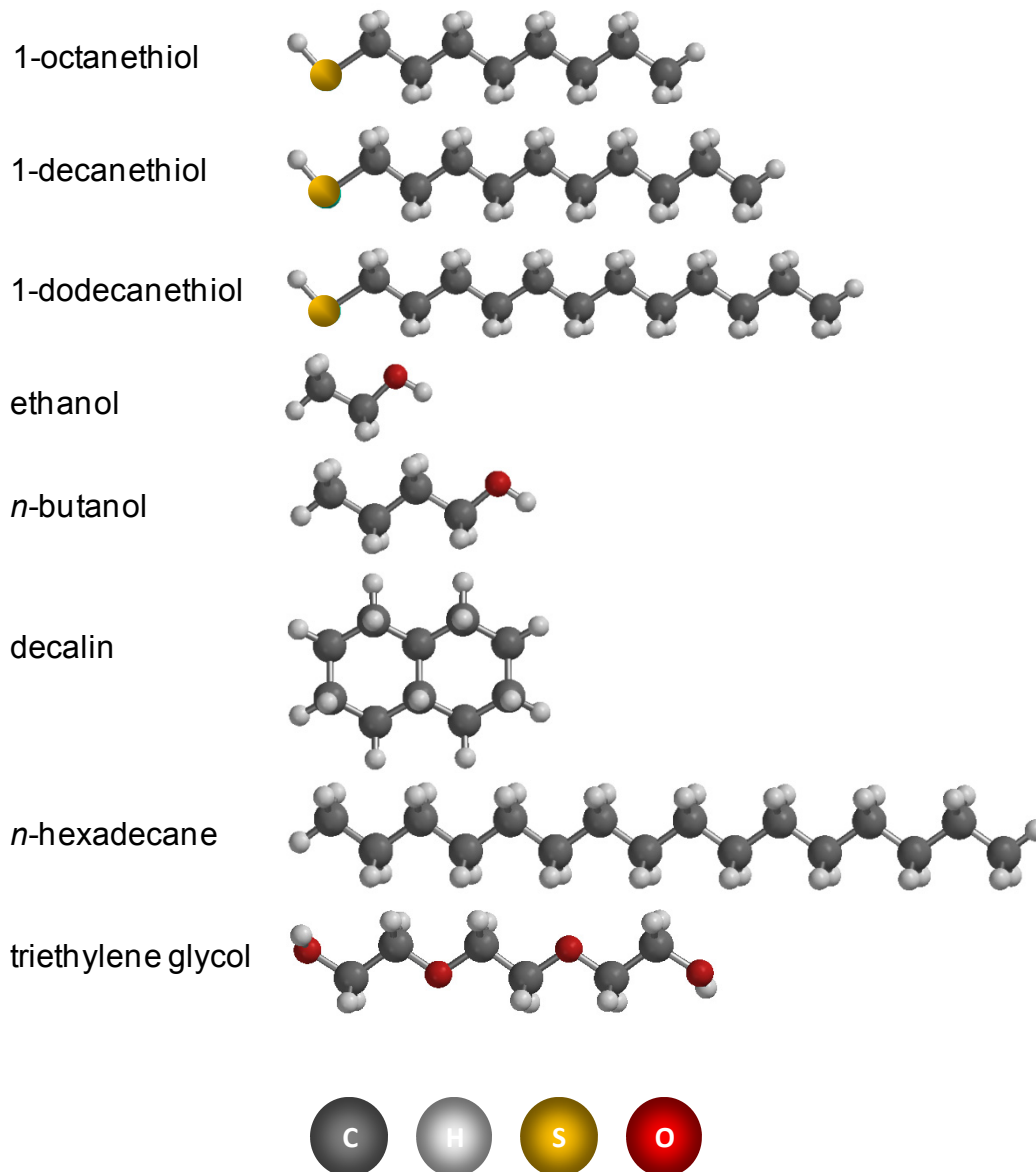
**Figure 2.1 Alkanethiols and solvents used in the study**

## 2.2.1   Structure of Alkanethiol/Au(111) SAM

Due to their ease of preparation, alkanethiol SAMs on Au(111) are the most extensively studied  model system. They have been characterized by variety of techniques such as ellipsometry,[21-22] infrared reflectance absorption spectroscopy (IRRAS),[22-23] X-ray photoelectron spectroscopy (XPS),[24-26] and scanning probe microscopy.[7-8,10-11,13-15,20]

Diffraction and spectroscopic methods have established the basic structure of alkanethiol SAMs.[4,13,27-28] Many other structures other than the basic structure also have been observed at different deposition conditions.[3,13,15,17,29-31]

Alkanethiolate molecules adopt a trigonal close packed lattice ($\sqrt{3} \times \sqrt{3}$)R30° on Au(111) at saturation coverage with nearest neighbor spacing of 0.499 nm (=$\sqrt{3}$a, where a=0.288 nm is the Au(111) nearest neighbor spacing, Figure 2.2), a structure commensurate with respect to the underlying gold lattice.[8,15,17,30,32-38] Porter et al. reported the first STM images of ($\sqrt{3} \times \sqrt{3}$)R30° lattice of ethanethiol and octanethiol on Au{111}.[39] The ($\sqrt{3} \times \sqrt{3}$)R30° unit cell consist of one atom and has an area of 0.2165 nm$^2$, surface coverage θ is 0.33 (relative to the Au(111) surface) and the alkyl chain tilt angle $\alpha$ is 30º from the surface normal. This corresponds to one thiol molecule for every three Au surface atoms. Superstructures of the ($\sqrt{3} \times \sqrt{3}$)R30° are frequently observed. Typically these are based on the ($2\sqrt{3} \times 4\sqrt{3}$)R30° unit cell with four molecules. These can have two to four distinct molecules, typically thought to exist with different alkyl chain twist ($\beta$) angles (Figure 2.3a).[4,13,27-28,40] The factors which determine the structure of SAMs include; the interactions between thiol head groups with the gold lattice, the site where the sulfur atom binds to the gold surface, Van der Waals interactions among alkyl chains, interactions among alkanethiol end groups, and the surface coverage of alkanethiol molecules.[3,29]
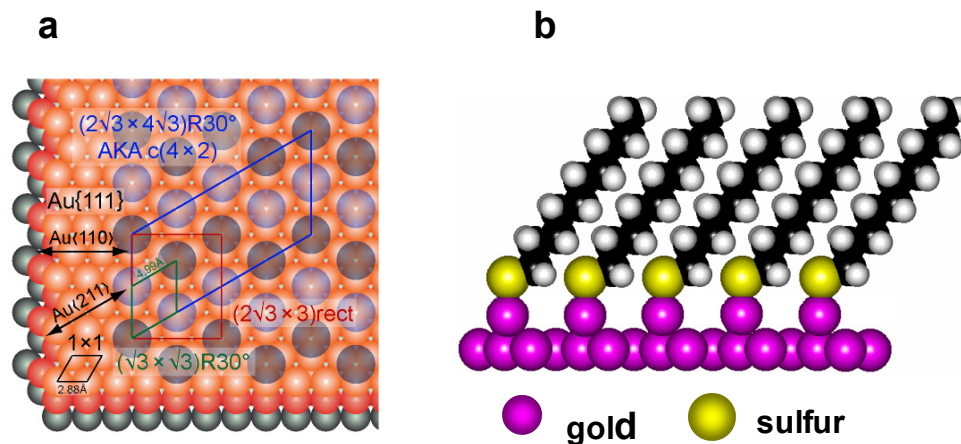
**Figure 2.2 Structure of the alkanethiol overlayer on Au(111):** a) the 2D overlayer lattice showing only the sulfur head groups at the fcc three-fold hollow site; b) cross section of alkanethiol SAM on Au(111) with sulfur head group adsorbed to the Au adatom proposed by Mazzarello et al.[41]
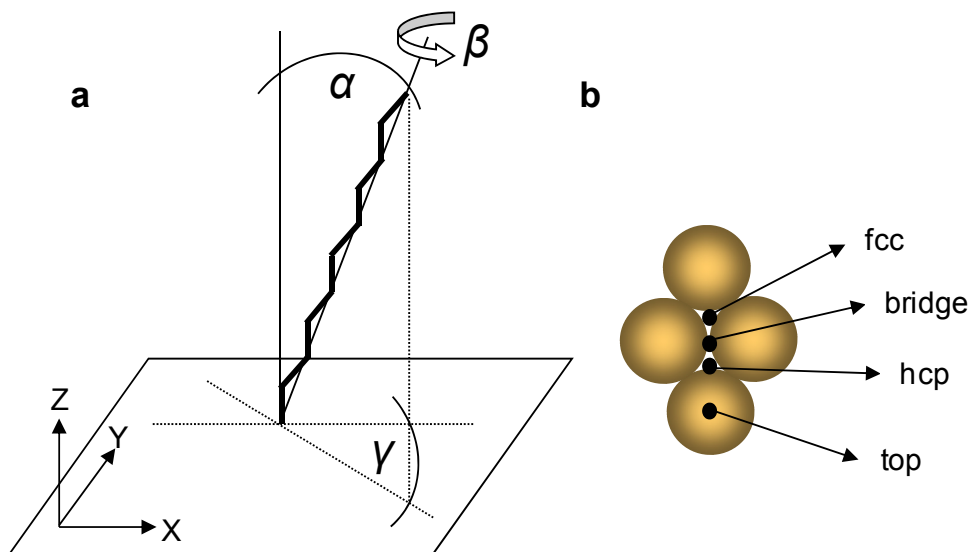


**Figure 2.3 Orientation and possible adsorption sites of the alkanethiol molecule on Au(111):** a) Schematic representation of an alkanethiol molecule on Au(111) defining the three angles describing its orientation. α is the polar angle of the chain axis from the surface normal, $\beta$ is the twist of the plane of the all-trans alkane back bone and $\gamma$ is the azimuthal angle defines the direction of the tilt; b) adsorption site nomenclature for an fcc (111) surface.
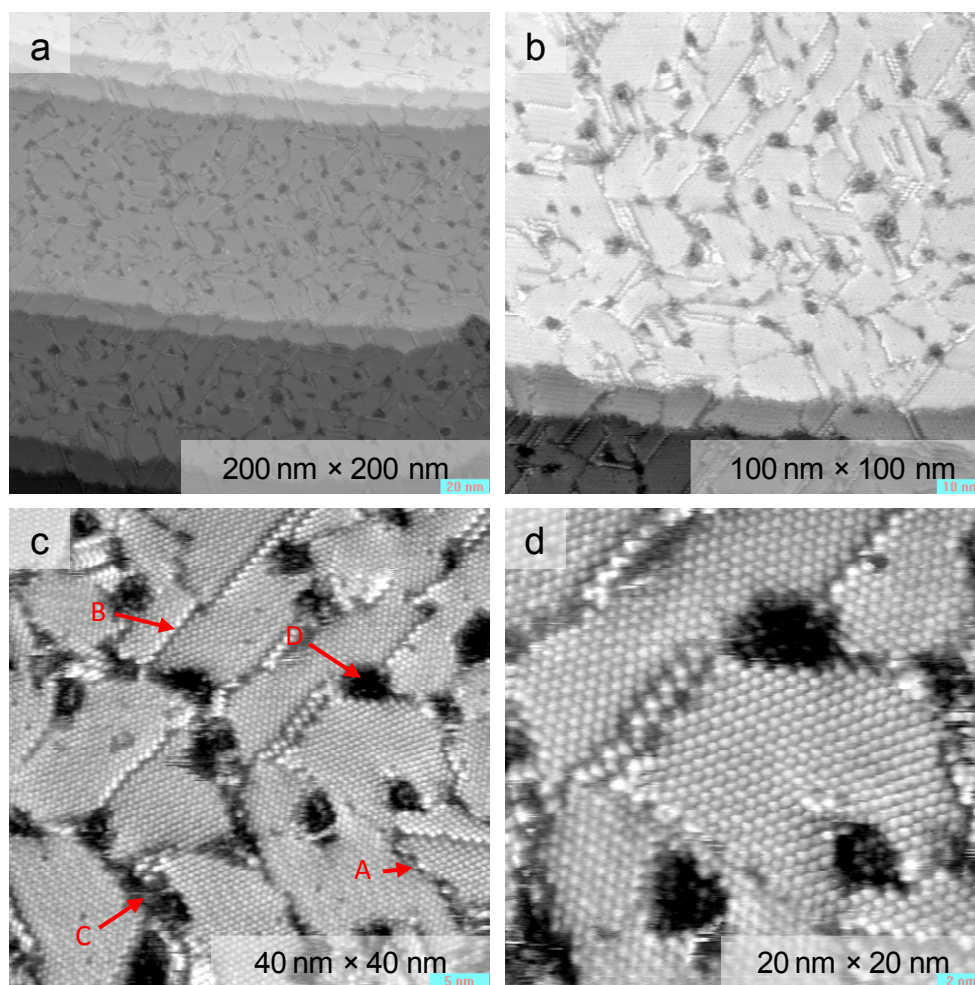
**Figure 2.4 Normal 1-decanethiol SAM on Au(111) surface:** a) 200 nm scan area which shows large area of the SAM as well as gold terraces, b) 100 nm image, c) 40 nm image, which shows domain boundaries (A), missing rows of molecules (B), disordered molecules (C), and vacancy islands (D), d) 20 nm image.
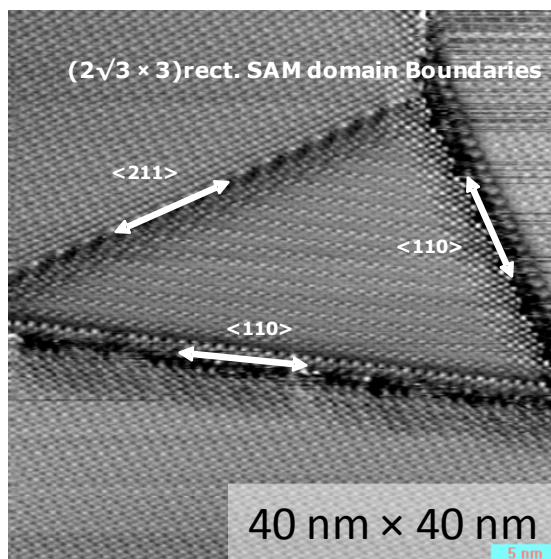
**Figure 2.5 High resolution STM image of a 1-decanethiol SAM exhibiting the (2√3 × 3)rect. superstructure of (√3 × √3)R30°** of vapor-phase grown SAMs at 100 °C; The image shows two types of low index structural domain boundaries. Missing zig-zag row structural domain boundaries are oriented along Au<110> while missing straight row structural domain boundaries oriented along Au <211>.

## 2.2.1.1 The (2√3 × 3)rect. Super Lattice

The (√3 × √3)R30° alkanethiolate SAMs has a superstructure denoted as (2√3 × 3)rect. with four molecules per unit cell (Figure 2.2a).[15,33,38,42-44] In most of the literature cited in this thesis, the superstructure of alkanethiol is referred as the c(4 × 2) which is relative to the (√3 × √3)R30° and is not relative to the Au (1 × 1) mesh. This is inconsistent with the standard practice of crystallography. Therefore we adopt (2√3 × 3)rect. for the superlattice as in Woodruff et al.[45] This super lattice unit cell consists of four alkanethiols with two like pairs. The modulation in intensity is due to the existence of two confirmations (twist angles, $\beta$) of 1-decanethiol molecules.[38,40,46] The existence of (2√3 × 3)rect. super lattice has been confirmed with He diffraction methods [38,43-44], grazing incidence X-ray diffraction (GIXD) [47] and STM studies.[15,17,33,48] Fenter et al. proposed

21

that neighboring sulfur atoms form surface disulfide. Although Fenter's model is not widely accepted, it has been further supported with resonant sum-frequency generation.[49]
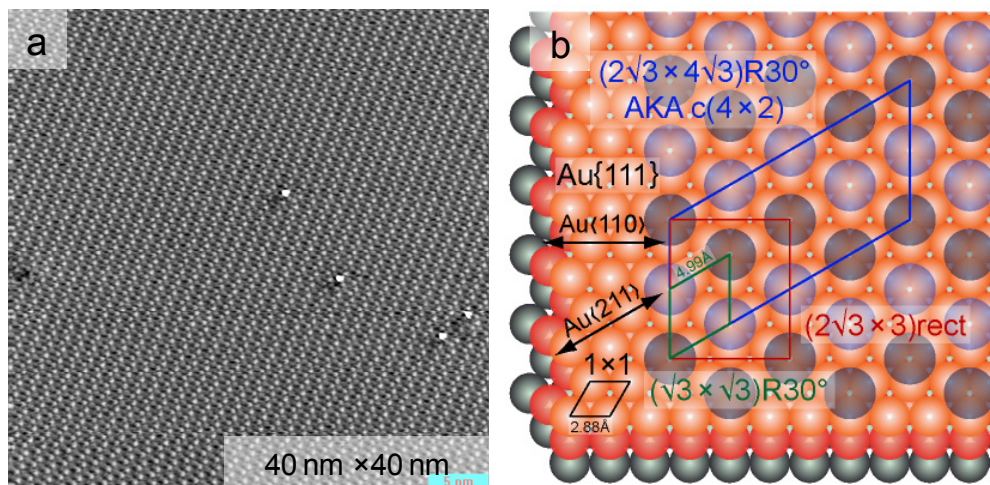


**Figure 2.6 The $(2\sqrt{3} \times 3)$rect. super lattice of the $(\sqrt{3} \times \sqrt{3})$R30° structure of 1-decanethiol on Au(111) surface**: a) STM image, b) schematic diagram of the alkanethiol overlayer showing the sulfur atoms in the fcc three-fold hollow sites.

### 2.2.2 Characteristics of Self Assembled Monolayers

Alkanethiol SAMs on Au{111} have common structural characteristics:

(i) Structural domain boundaries, that are attributed to a boundary between two regions with orientational and translational differences of molecules (marked as "A" in Figure 2.4c) or missing rows of molecules that may be straight or zig-zag (marked as "B" in Figure 2.4c). The missing straight rows are in Au <211> directions while missing zig-zag rows are in Au<110> directions (Figure 2.5).[1]

(ii) Molecular defects where alkanethiol molecules are absent or disordered (marked as "C" in Figure 2.4c).

22

(iii)    Substrate vacancy islands (VIs) (marked as "D" in Figure 2.4c) that are one atomic layer deep pits in the Au(111) surface which are a result from the restructuring of the Au(111) surface during SAM growth.[29]

In early studies it has been reported that the VI density increases with increasing alkanethiol concentration, and decreases with increasing length of the hydrocarbon chain These were first observed by Haussling et al.[50] Later Edinger et al.[51] observed that the depth of the VIs was the same as a lower terrace so concluded that they were one Au(111) atomic layer deep and are not a feature of the monolayer. Many subsequent studies have confirmed their conclusion.[16-17,32,52-56] In Figure 2.4d, highly ordered SAM structures can be seen inside the VI. There have been several mechanisms proposed for the formation of vacancy islands. The first model attributed the VIs to etching of Au in the alkanethiol solution during growth, because they observed that the amount of Au present in the solution after growth corresponded approximately to one monolayers worth.[51] However VIs also form during SAM grown from gas phase thiol, where etching cannot occur.[14,21] Poirier proposed a mechanism by which excess Au atoms are ejected from the surface as the ($\sqrt{3} \times 23$) reconstruction is lifted during SAM growth. The presence of Au ad-atoms during the assembly process supports their hypothesis that restructuring of the Au(111) surface occurs.[12] The vacancy islands can also undergo a process of coarsening due to surface diffusion of Au atoms to form larger vacancy islands (Ostwald ripening). The driving force in this process is minimization of the step-edge energy wherein small vacancy islands combine to form larger ones and eventually diffuse to the step edges where the VIs disappear.[16-17,52] The Au surface diffusion can be accelerated by having the monolayer in a liquid like disorder,[16] with invasive tunneling

conditions,[32,53,57] and with increasing temperature.[8,32,53-54,58] Further, in addition to VIs, Au substrates have other structural features such as steps and inter-grain boundaries (polycrystalline Au films) also contribute to SAM features.[29]

In some practical applications of SAMs, it is desired to minimize the number of domain boundaries, missing rows, VIs, and disordered areas. A number of procedures to achieve this have been investigated. These include choice of solvents, formation of SAMs at controlled potential, repeated immersions followed by voltammetric cycles, and thermal treatment.[29] Among all these procedures, thermal treatment of SAMs is considered to be a better approach. Thermal treatment has been applied to alkanethiol SAMs during their growth in solution as well as after the growth. Adsorption from solution at temperatures from $-20\,°C$ to $78\,°C$,[54,59-62] or annealing of the SAMs (50–100 $°C$)[1,13,32] in air or UHV conditions have been shown to reduce the number of VIs, and to obtain large ordered domains. However, post-growth annealing of SAM may not be a good choice due to competing degradation processes (desorption and/or oxidation of the thiol). It is known that SAMs grown at higher temperatures exhibit lower number of domain boundaries, missing rows, VIs and disordered areas. [61] Although defects can never be completely eliminated, their density can be significantly reduced.

### 2.2.3 Striped-Phases of Alkanethiol SAMs

Other than the normal $(\sqrt{3} \times \sqrt{3})R30°$ structure and its $(2\sqrt{3} \times 3)$rect. super structure, there are also a variety of structures referred to as striped-phase because their salient feature are linear rows of adsorbate molecules, typically running along Au<211>. These striped-phases of alkanethiol can be divided into two categories namely lying down and standing up phases depending on the orientation of the molecular backbone with respect

to the surface normal. For the lying down phases, the chains are parallel to the surface ($\alpha$ = 90°). Stripe spacing depends on the chain length and azimuthal angle ($\beta$). The standing up striped-phases have $\alpha$ < 90° and different azimuthal angles. Therefore in general the entire range of phases observed in alkanethiol SAMs span from completely lying down phase to the normal ($\sqrt{3} \times \sqrt{3}$)R30° structure. These two types of stripes will be discussed in detail in the following sections.

## 2.2.3.1  Lying-Down Striped-Phases Far Below Saturation Coverage

The first ordered structures to nucleate on the Au(111) surface in the very initial stages of SAM growth are the lying down striped-phase. In these structures the sulfur head groups form rows and the alkyl chains lay flat on the surface also packing to optimize the inter-chain Van der Waals interactions.[8,13-14,16,27-28,30,34-36,63-64] They have been called striped-phases[8-9,14,16-17,31] and are generally denoted as ($p \times \sqrt{3}$) structures,[34] where $p$ is 7.5 < $p$ < 19 and a multiple of the Au{111} lattice constant (0.288 nm).[17,29,33-35] The value of $p$ mainly depends on the deposition conditions, thermal history, and the age of the sample initially but have a dependence on the packing density and the chain length after the structure reaches equilibrium.[8-9] These stripe structures have been observed by various experimental techniques such as STM,[8,30,34-35] low-energy electron diffraction,[65-66] and helium diffraction.[8-9] Most commonly observed stripe structures (Figure 2.7) have $p$ values of 7.5 ($\delta$ phase), 11.5 ($\beta$-phase) and 19 ($\chi$-phase).[30] The type of structure mainly depends on deposition conditions. The low density stripe structures can be prepared by gas-phase deposition,[9,30] brief immersion in dilute solutions[34] and thermal annealing of the sample.[26,35-36] In most cases two or more types of striped-phases exit in a single sample, depending on the deposition conditions and surface coverage.[31] The stripes are

aligned in the Au <211> direction of the Au substrate with a nearest neighbor distance of 0.499 nm. The $\delta$-phase has the same structural arrangement as the $\varphi$-phase (($\sqrt{3}$ × $\sqrt{3}$)R30°) except some molecular rows are missing periodically. All the other types of striped-phases have at least one molecule lying down parallel to the surface.[31]
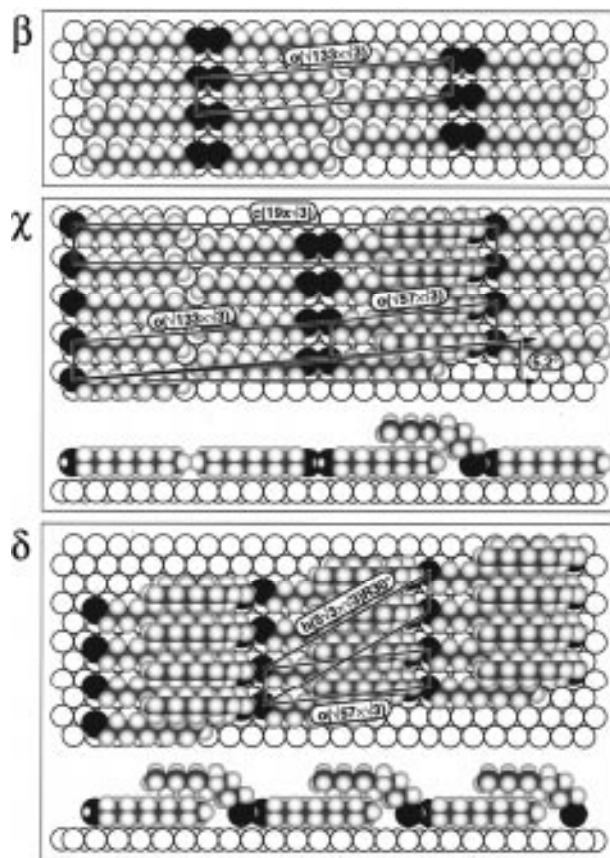


**Figure 2.7 Schematics of the lying-down stripe phases:** The $\alpha$, $\beta$, and $\gamma$-phases of decanethiol on Au(111) (Reprinted from Poirier et al.).[30]

### 2.2.3.2 Standing Up Striped-Phases

The entire range of stripe structures discussed in the previous section has at least one molecule lying down parallel to the surface. In our investigation we discuss a striped-phase which can be grown from both solution and vapor phase deposition at

26

elevated temperatures. The coverage is high enough (3/4 of the ($\sqrt{3} \times \sqrt{3}$)R30°) that incorporation of additional thiols is very slow at room temperature, distinguishing it from lying down striped-phases. This striped-phase is a ($\sqrt{3} \times \sqrt{3}$)R30°. It is a ($\sqrt{3} \times \sqrt{3}$)R30° missing every 4th nearest neighbor row. The structures produced with vapor were cleaner compared to those produced in solution. We demonstrate that this striped-phase grows when the vapor pressure of thiol is just below the saturation vapor pressure. The presence of sufficient thiol in the growth vial to maintain saturation vapor pressure leads growth of the normal ($\sqrt{3} \times \sqrt{3}$)R30° structure. This stripe structure is similar to the one described by Xiao et al. in post-deposition dry air annealed samples.[26] Our growth procedure produces the stripes reproducibly and has been verified by STM imaging to be uniform across the surface. A more detailed description of this striped structure will be presented in the following sections.

### 2.2.4 The Sulfur Atom Adsorption Site and Au Adatoms

The adsorption site of the S atom (bridge, three-fold hollow and, a-top sites) on the Au(111) surface is a matter of controversy with different experimental and theoretical results reported from different research groups.[67-72] Recently evidence has emerged that gold adatoms are present on the Au(111) surface. These include the experimental techniques such as X-ray standing wave experiments,[73] X-ray diffraction,[41] scanning tunneling microscopy[72] and theoretical calculations[41,74] (density functional theory and molecular dynamics).[41,71-73,75-78] Kautz et al. used an STM based method to measure the coverage of Au adatoms in a ($2\sqrt{3} \times 3$)rect. SAM. In this method, they compare an initial image of the SAM to an image after the SAM had been completely removed by reaction with atomic hydrogen. When the SAM is removed, the Au adatoms form islands on the

27

terraces or diffuse to the step edges. The increase in area of the Au coverage is the Au adatom coverage. They measure a 1:2 gold adatom : alkanethiol ratio, i.e. one gold adatom for every two alkanethiol molecules. Maksymovych et al.,[72] earlier reported the first STM images which support the adatom mediated bonding of alkanethiol species to Au(111) for low coverage methanethiol. They proposed that pairs of RS species bond via an Au adatom (RS-Au-RS). Mazzarello et al.,[41] also reported that two $CH_3S$ radicals are bound to a Au adatom that has been lifted from the gold substrate as found by simulations as well as by extensive photoelectron and grazing incidence X-ray diffraction measurements. Nagoya et al.[77] arrived at the same conclusion using density functional theory showing that the most stable structure of methanethiol on Au(111) is RS-Au-RS.

**2.2.5 Comparison of Deposition Methods of SAMs on Au/mica Substrates**

SAMs can be grown on Au/mica surfaces either from solution or from alkanethiol vapor. In both methods, the assembly mechanism is the same. First, molecules physisorb on the surface and then sulfur head group chemisorbs to the gold surface. As more and more molecules attach to the surface, they begin to adopt upright positions due to van der Waals interactions among the molecules. This process will continue until the entire surface is covered with the monolayer (Figure 2.8a). SAMs, highly dilute in a second "guest" component, can be prepared by "insertion" of a second molecule into an existing "matrix" SAM. This process takes advantage of molecular exchange that occurs at the SAM-solution interface. Insertion typically places the guest molecules at domain boundaries and other defects where exchange is most rapid (Figure 2.8b). A second, typically higher vapor pressure component can be added to an existing SAM. This process although similar to "insertion" is typically used to improve the crystalline order

in a poorly ordered SAM. For this application the added component is typically a matrix used to "back fill" the SAM, filling in the empty sites on the surface. This same result can be achieved with co-adsorption where both types of molecules are allowed to adsorb on the surface at the same time. If the interaction energies of both types of molecular components are the same, they adsorb at random positions and form a mixed SAM (Figure 2.8c). If the interaction energy is different, they can phase separate, forming distinct regions of each component molecule (Figure 2.8d).
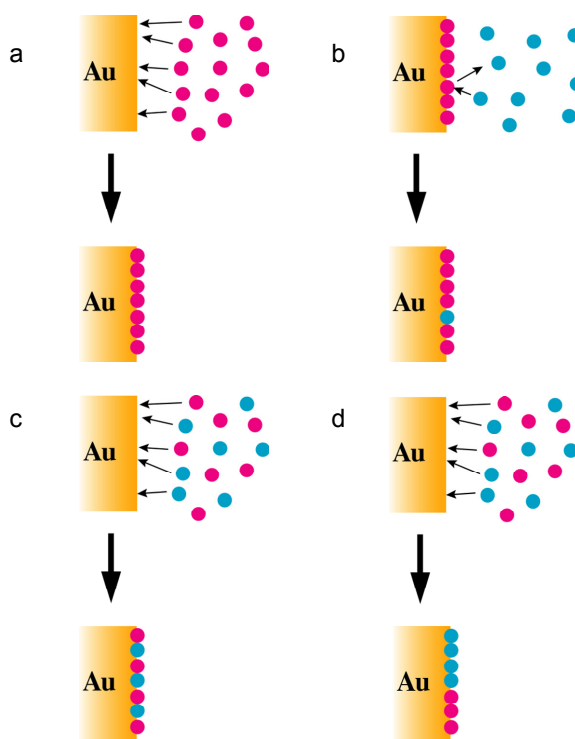


**Figure 2.8 Common deposition methods of SAMs:** Methods of making single or multi component SAMs either in solution or vapor; a) assembly of single component; b) insertion of guest molecule, c) co-adsoption of two components with same interaction energy, d) co-adsoption of two components with different interaction energy.

## 2.3 Materials and Methods

### 2.3.1 Au/mica Substrate

High resolution STM imaging requires an atomically flat surface. The substrate also plays an important role of defining the properties of the SAMs. Thiols have a very high affinity for gold.[27] Gold is inert and does not oxidize in air. Therefore it does not require special precautions and can be handled easily at ambient conditions. Gold films grown on mica sheets have (111) oriented crystal grains with large atomically flat terraces which are ideal for STM studies.[79] Au/mica substrates (1.0 × 1.1 cm Au film on 1.4 × 1.1 cm mica sheet cut into for equal pieces) used in the present study were obtained from Agilent Technologies (formerly Molecular Imaging). All substrates were $H_2$ flame annealed immediately before use and reuse.[80]

### 2.3.2 SAM Preparation

### 2.3.2.1 SAMs Grown from 1 mM C10 Solutions in Solvents

In this study, 1 mM solutions of 1-decanethiol in different solvents were used throughout. The solvents used were absolute ethanol, *n*-butanol, decalin, *n*-hexadecane, and triethylene glycol. Decalin (decahydronapthalene) is a compact saturated hydrocarbon. It is a bulky molecule and very unlikely to incorporate into the alkanethiol SAM because of its size. In contrast, *n*-hexadecane is similar in structure to alkanethiol and may incorporate into the growing SAM. triethylene glycol ((2-[2-(2-hydroxyethoxy)ethoxy]ethanol, a polar hydrogen bonding solvent), was selected as a high boiling point analog to ethanol. A summary of properties of these solvents are listed in the Table 2.1. SAMs of 1-decanethiols were formed on Au/mica surfaces by immersing

the substrate in 1mM 1-decanethiol solution in PFA vials at different temperatures. For

high temperature experiments, the samples were kept in a temperature controlled oven.

**Table 2.1 Alkanethiols and solvents used in these studies**

| Solvent | CAS Number (Supplier) | Melting point | Boiling point |
|---|---|---|---|
| 1-octanethiol | 111-88-6 (Sigma Aldrich) | −49 °C | 197-200 °C |
| 1-decanethiol | 544-76-3 (Sigma Aldrich) | −26 °C | 241 °C |
| 1-dodecanethiol | 112-55-0 (Sigma Aldrich) | −7 - −9 °C | 266 - 283 °C |
| ethanol (absolute) | 64-17-5 (Pharmco Products Inc) | −114 °C | 78.4 °C |
| *n*-butanol | 71-36-3 | −89.5 °C | 117.2 °C |
| decalin (decahydronapthalene) mixture of isomers | 91-17-8 (Sigma Aldrich) | −4 °C | 187–196 °C |
| *n*-hexadecane | 544-76-3 (Sigma Aldrich) | 18 °C | 287 °C |
| triethylene glycol (2-[2-(2-hydroxyethoxy)ethoxy]ethanol | 112-27-6 (Sigma Aldrich) | −7 °C | 285 °C |

## 2.3.2.2 SAMs Grown from C10 Vapor

SAMs were also grown by adsorption from vapor phase (no solvent). The deposition time

was standardized at 16 hours. The amount of C10 used varied depending on the

experiment. The C10 for experiments requiring smaller volume (0.1 & 0.3 μL) was

dispensed as a solution in $CH_2Cl_2$. Volumes greater than 1 μL were directly measured

using a micro pipette. PFA (5 mL) as well as glass (1 mL) vials were used at different

temperatures depending on the experiment.

The vapor pressure of C10 increases exponentially with temperature (Figure 2.9)

and can be calculated using the empirical equation

$$\log P = \left( A - \frac{B}{(C+T)} \right),$$ (2.1)

where $T$ is temperature in Celsius, and $A$, $B$, and, $C$ are empirical constants for each

component (Table 2.2).[81]
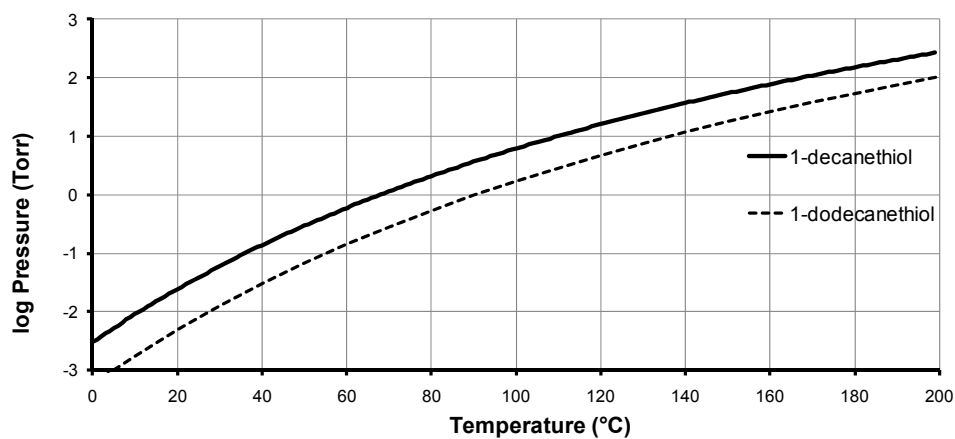


**Figure 2.9 Vapor pressure of 1-decanethiol and 1-dodecanethiol versus temperature.**[81]

**Table 2.2 Values of *A*, *B*, and *C* in Equation 2.1 for C10 and C12.**[81]

|   | C10 | C12 |
|---|---|---|
| *A* | 7.3529 | 7.62037 |
| *B* | 1955.2892 | 2309.1 |
| *C* | 198.052 | 212.597 |

### 2.3.2.3 Quenching of High Temperature Growth

Samples which were taken out from the oven were subjected to fast or slow quenching. Slow quenching was done at room temperature for 10 minutes, while fast quenching requires immersion of the sample and the vial in a cryobath (isopropanol bath, -52 °C) or in a liquid nitrogen bath (-196 °C) for about 10 minutes immediately after taking from the oven.

### 2.3.2.4 Cleaning of Vials and Au/mica

PFA vials (purchased from Jenson Inert Products) were used to prepare SAMs. The vials were cleaned by heating in $H_2SO_4$ at 60 °C then boiled in DI water (3 times) followed by drying them in an oven at 180 °C for three hours. The samples were rinsed with absolute ethanol and blown dried with nitrogen.

### 2.3.3 Scanning Tunneling Microscope

The STM used is a homebuilt beetle-style STM with an RHK Technology SPM100 controller and XPMPro software. The tunneling current was measured using an Axon CV4 current amplifier. STM imaging was performed in dry $N_2$ at room temperature. The Probe tips were clipped Pt-Ir (80 : 20) wire. STM images are typically recorded at −1.0V sample bias and a 1.0 pA tunneling current. The STM scan head assembly rests on a steel platform (600 lbs) (see Figure 2.10a) supported by pneumatic isolators. Because of the

large mass of the STM platform, the system has a very low resonant frequency. Therefore transmission of noise from the floor to the STM platform is strongly attenuated. Without the pneumatic isolators, we find that the building vibrations contribute noise on the order of the SAM corrugation (0.1–0.2 Å). The whole system is inside an acoustic isolation box which is constructed of three layers of alternating reflectors (MDF and Pb) and absorbers (foam). The dense lead/MDF barriers reflect sound, while the intervening layers of foam absorb it. The layers of lead are electrically connected and grounded so that they create a Faraday cage isolating the system from electromagnetic interference.
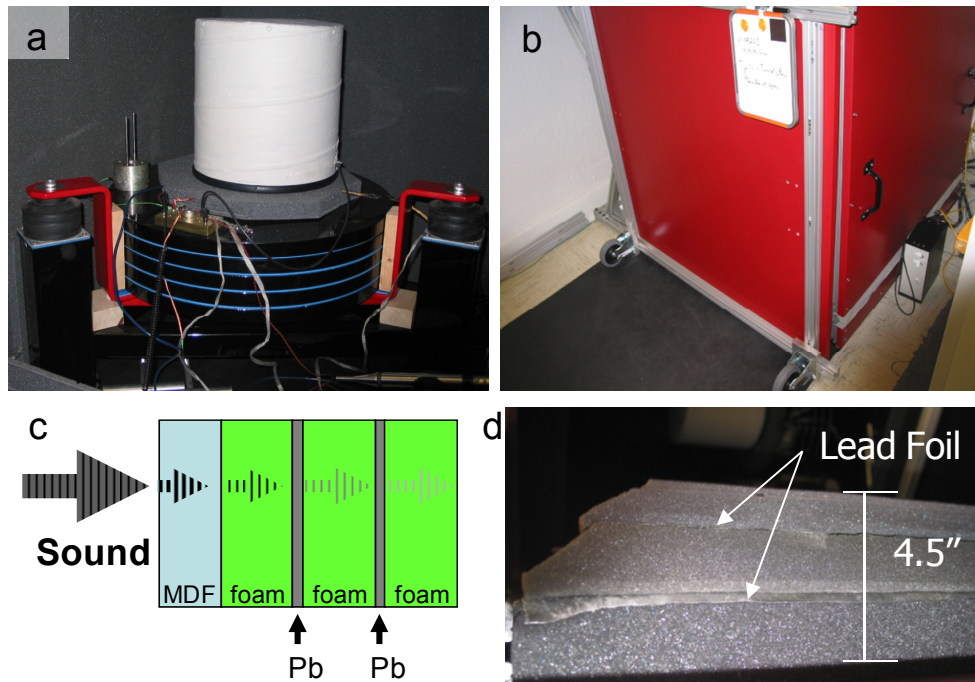


**Figure 2.10 Vibration isolation system of the STM:** a) 600 lb pneumatic platform for isolation from floor vibrations, b) STM enclosure for acoustic and electromagnetic isolation, c) schematic diagram showing a cross-section of the wall construction of the STM enclosure, d) photograph of the foam and lead layers.

34

**2.3.4 Oven and the Temperature Controller**
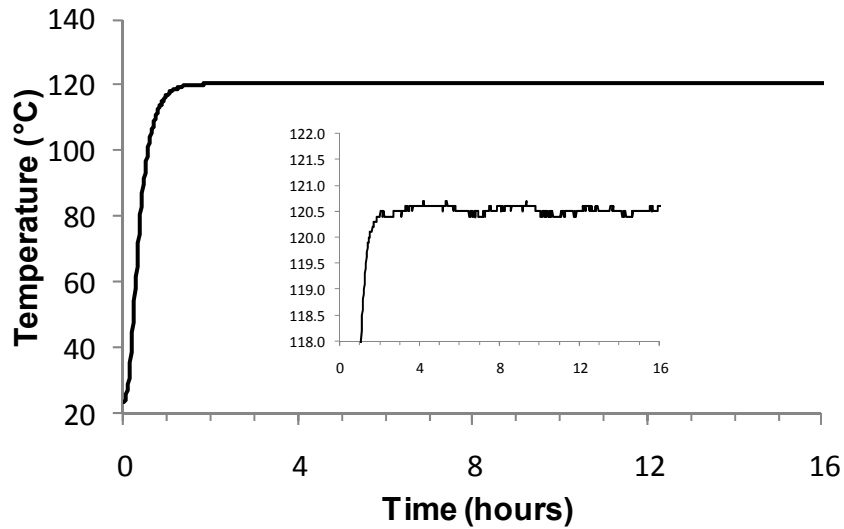


**Figure 2.11 Temperature-time graph of the oven** showing the typical thermal history of a 16 hour vapor grown C10 SAM, The inset is the same graph with a y scale range of 2 °C which shows the stability of the temperature during the deposition.

High temperature sample depositions were carried out inside an oven which is fitted with an Omega CN 9000 microprocessor temperature controller (0.1 °C resolution) with a Pt RTD temperature sensor. The omega data logger using Type-K thermocouples provides the thermal history of each growth. The thermal fluctuations naturally present due to the thermal regulation of the oven were significantly reduced by placing the sample vial inside a metal container. The time to heat the sample from room temperature to 120 °C is 1.5 hours. The graph shown in Figure 2.11 has a stable temperature of 120.5 ± 0.2 °C at the sample vial.

## 2.4    Results & Discussion

The main goals of experiments described in this section:

1.  Survey the solvent effect of the structure of SAMs at different temperatures.

2.  Investigate suitable conditions for making SAMs with fewer structural domain boundaries, missing rows, disordered areas and VIs.

3.  Investigate suitable conditions for making striped-phase SAMs.

4.  Investigate the striped-phase with respect to reverting to the low temperature ($2\sqrt{3} \times 3$)rect. phase and to adsorption of C10 from solution and vapor.

### 2.4.1    Growth Temperature and Medium Dependent Study of the Structure of Decanethiol SAMs on Au(111)

We investigate the dependence of the alkanethiol SAM structure on the growth medium (includes solution and vapor) and growth temperature in this section. C10 SAMs grown in different media at temperatures 20–140 °C (with increments of 20 °C) were studied with the STM. The choice of different media was discussed in section 0. Figure 2.12 is STM images of growth temperature dependent structures of C10 SAMs grown from different media (solutions and vapor). Our STM results indicate that the alkanethiol SAM structure is dependent on growth temperature. We observe formation of the typical ($\sqrt{3} \times \sqrt{3}$)R30° SAM structures at low temperatures which transition into a ($\sqrt{3} \times 4\sqrt{3}$)R30° striped-phase at higher temperatures for both solution-grown and vapor-grown SAMs. The observed phase transition temperature appears to be different for solution and vapor-grown SAMs. While solution-grown SAMs at 100 °C gives a monolayer dominated by a striped-phase, vapor grown SAMs gives a nearly VI free ($\sqrt{3} \times \sqrt{3}$)R30° phase at the same temperature. The striped-phase was observed at 120 °C

for vapor-grown SAMs. It was found that the growth of stripes from vapor strongly depends on both the growth temperature and the amount of C10 in the container.

The main observations are as follows: (i) faceted VIs; (ii) larger VIs at elevated temperatures; (iii) decrease of VI surface coverage at elevated temperature and the formation of nearly VI free structure at 100 °C for vapor-grown SAM; (iv) low-index step edges orient along Au<110> when the $(2\sqrt{3} \times 3)$rect. phase is present; (v) low-index step edge orient along Au<211> when $(\sqrt{3} \times 4\sqrt{3})$R30 striped-phase is present; (vi) transition to $(\sqrt{3} \times 4\sqrt{3})$R30 striped-phase for solution-grown SAMs occurs at lower temperature (~80 °C) than for vapor-grown SAMs (110–120 °C); (vii) gradually increasing disordered structures of solution-grown SAM at high temperatures (>100 °C). We discuss these observations in detail in the following sections.

For decalin-grown SAMs, we observed the onset of the $(\sqrt{3} \times 4\sqrt{3})$R30 striped-phase at 60 °C with long range order at 100 °C. On the other hand, we observed a $(2\sqrt{3} \times 3)$rect. SAM structure at 60 °C in the case of polar triethylene glycol solvent. The transition to $(\sqrt{3} \times 4\sqrt{3})$R30 striped-phase for SAMs grown in triethylene glycol occurs at 80 °C (Figure 2.12). At 120 °C and above no molecular order was observed for decalin and triethylene glycol-grown SAMs. The C10/hexadecane grown SAMs did not convert to $(\sqrt{3} \times 4\sqrt{3})$R30 striped-phase at all, instead showed signs of decomposition at 80 °C.
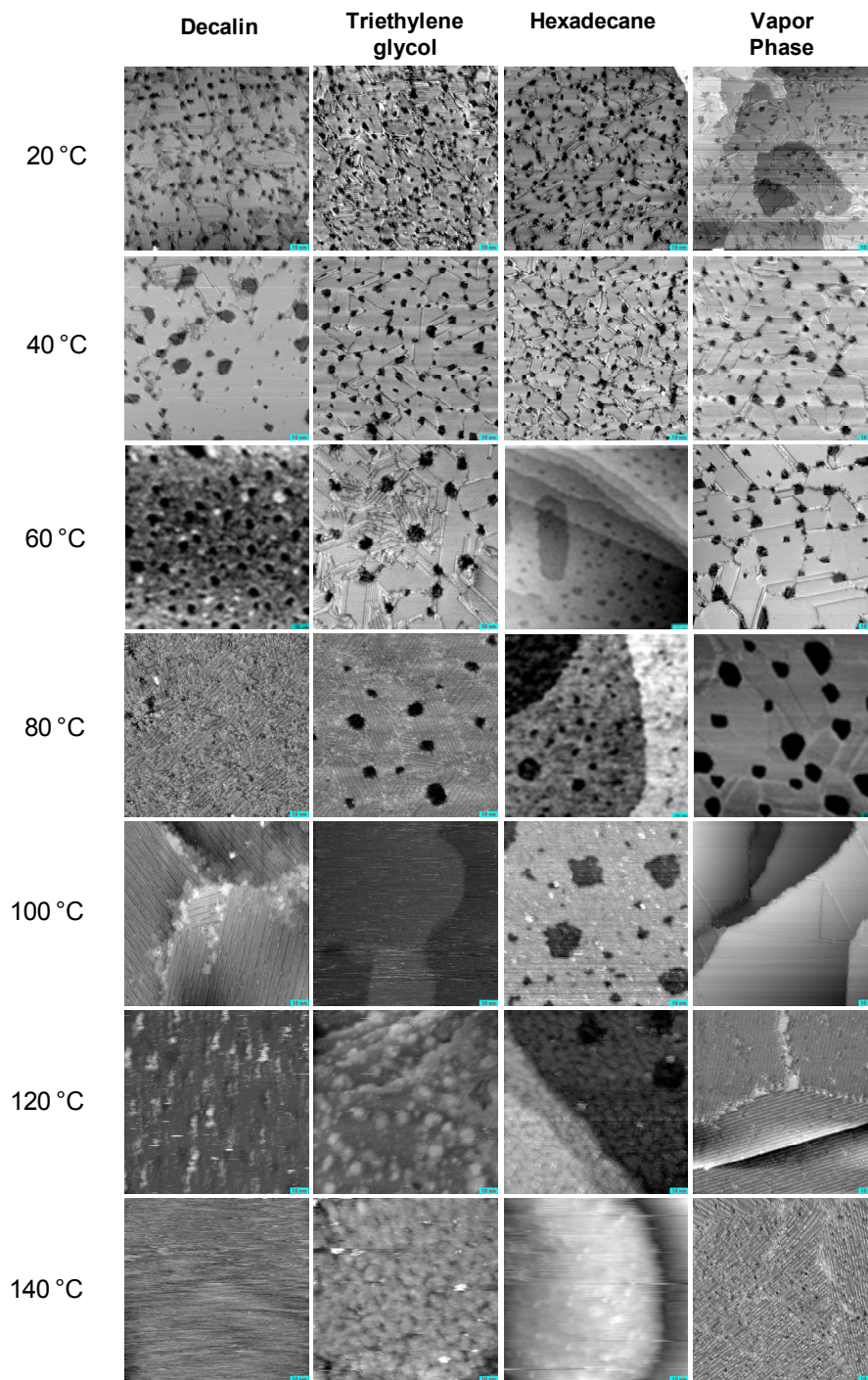
**Figure 2.12 STM micrographs of growth temperature effects on the 1-decanethiol SAM structures grown with C10 in different solvents and C10 vapor:** Scanning area for each image is 100 nm × 100 nm. The images are arranged in rows and columns by growth temperature and growth medium respectively. The temperature is indicated at the left and increases from top to bottom. The growth medium name is indicated at the top.

SAMs grown in hexadecane solvent showed increasing disorder in structures above 60 °C. The long chain structure of hexadecane might impede the structural growth of SAM at higher temperatures. We note that high resolution STM imaging of C10/hexadecane SAM grown at higher temperatures was difficult to perform. SAM growth is a dynamic process where both adsorption onto the surface as well as desorption from the surface is always occurring. We hypothesize that the solution grown samples produced stripe structures at lower temperatures than that of vapor grown samples because the barrier to desorption is lower in solution than in vapor. Following the same line of reasoning for the different solvent, would lead us to conclude that C10 was more soluble in triethylene glycol than decalin. This hypothesis could be checked by measuring the relative solubility of C10 in these solvents. However from our experiment we would expect the solubility at 80–100 °C to rank in the order of hexadecane > triethylene glycol > decalin.

The upper limit to the temperatures used in this study was determined by the onset of decomposition of the C10. For the purpose of this study, the onset of decomposition was the lowest temperature where the solution or neat C10 change to yellow/brown color (Table 2.3).

**Table 2.3 Decomposition onset temperatures observed for neat C10 and 1 mM C10 in different media**

| Medium | Temperature (°C) |
|---|---|
| neat C10 | 180 |
| C10/decalin | 120 |
| C10/triethylene glycol | 140 |
| C10/hexadecane | 140 |

### 2.4.1.1 Growth Temperature Dependent Annealing of Vacancy Islands During SAMs Growth

Both solution and vapor grown samples show the formation of the ($\sqrt{3} \times \sqrt{3}$)R30° phase. The effect of growth temperature on the structure of solution-grown SAM has previously been studied by Yamada et. al.[61] As in their work, we observed an increase in SAM structural domain size with temperature in all media studied.  This trend is nicely illustrated by the temperature series of vapor-phase grown SAMs (Figure 2.12). At 100 °C, nearly-VI free domains grow from vapor compared to 40 nm at 80 °C.

The growth of larger VIs at the expense of smaller VIs at higher growth temperature may be attributed to the Ostwald ripening process.[82] Ostwald ripening is characterized by the growth of large features at the expense of small ones. Our observation is consistent with those of other groups.[20,82] This phenomenon is driven by the tendency to reduce the overall boundary tension or step edge energy. In this case it is energetically favorable for Au atoms to diffuse from step edges and the edges of large VIs, filling in the small VIs.
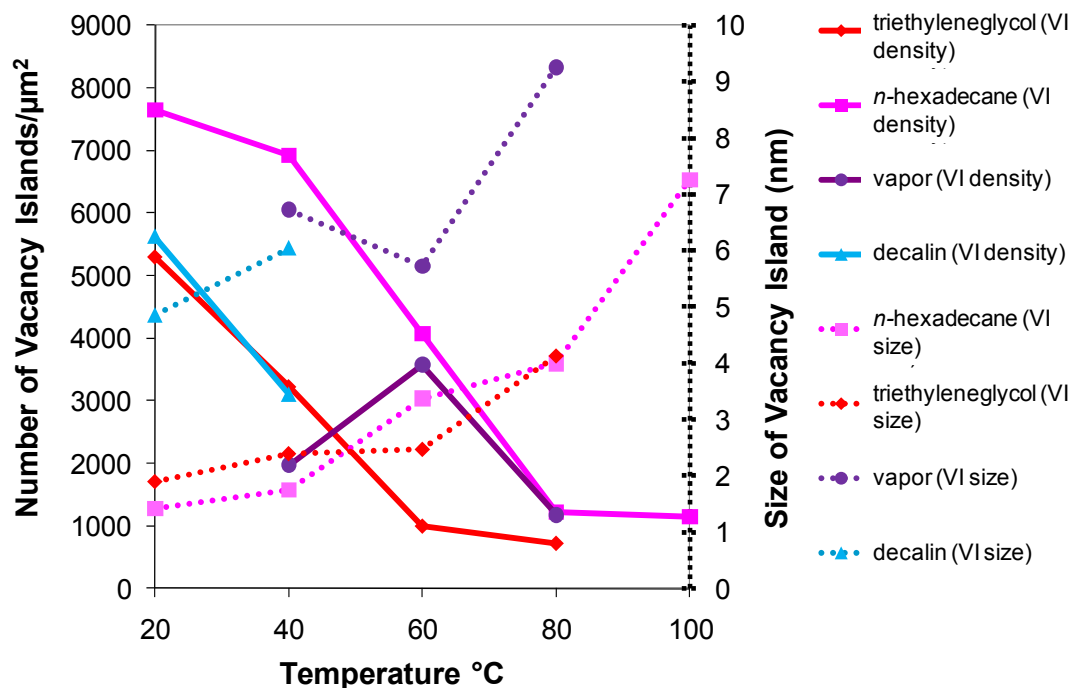
**Figure 2.13 Variation of size and number of vacancy islands as a function of growth temperature** for SAMs grown in three different solvents and SAMs grown from the 1-decanethiol vapor.

Figure 2.13 presents a quantitative analysis of growth temperature effects on the VIs. For vacancy island calculations, length and the width of all the VIs in a 200 nm × 200 nm image were measured. The VIs first grow larger with increasing temperature, then essentially disappear (anneal away) around 100 °C. Solution grown SAMs show monotonic trends with temperature increasing VI size and decreasing number. STM image in Figure 2.14 is VI free SAM grown from C10 vapor at 100 °C. The SAM exhibits very few domain boundaries and virtually no vacancy islands.
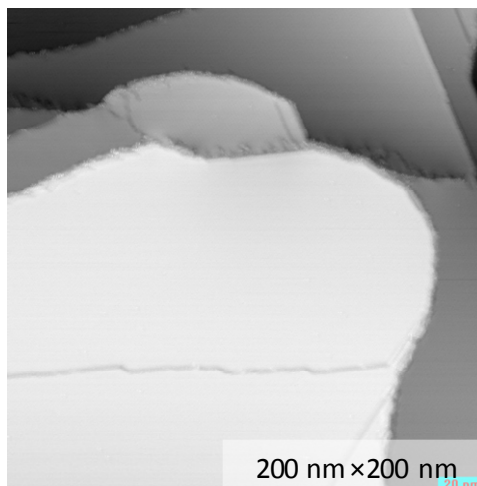
**Figure 2.14 STM micrograph of high temperature vapor-grown SAM:** $(2\sqrt{3} \times 3)$rect. phase with large Au(111) terraces and no VIs.
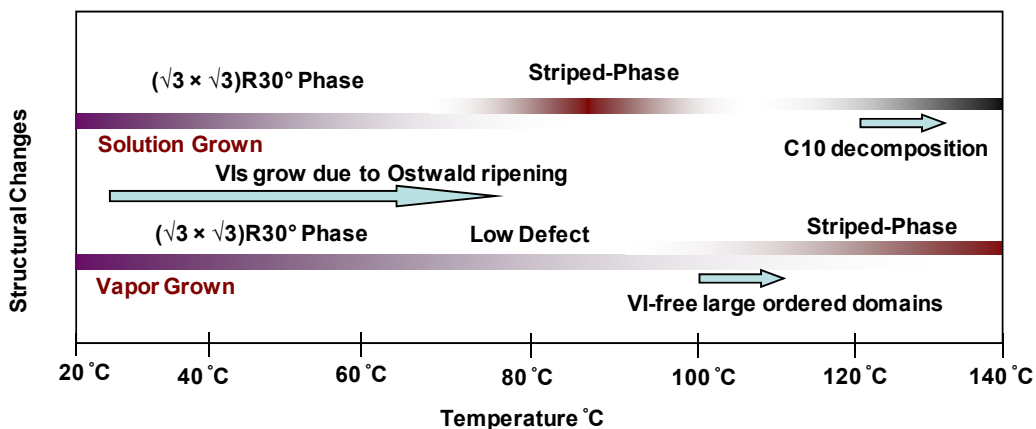


**Figure 2.15 An overview of the structural evolution of SAMs with growth temperature** under the conditions discussed in the text.

## 2.4.1.2   The $(\sqrt{3} \times 4\sqrt{3})$R30° Striped-Phase Structure

STM images of the $(\sqrt{3} \times 4\sqrt{3})$R30° striped-phase SAM are shown in Figure 2.16 a, b,

and c. The SAMs exhibits very few domain boundaries with virtually no vacancy islands.

42
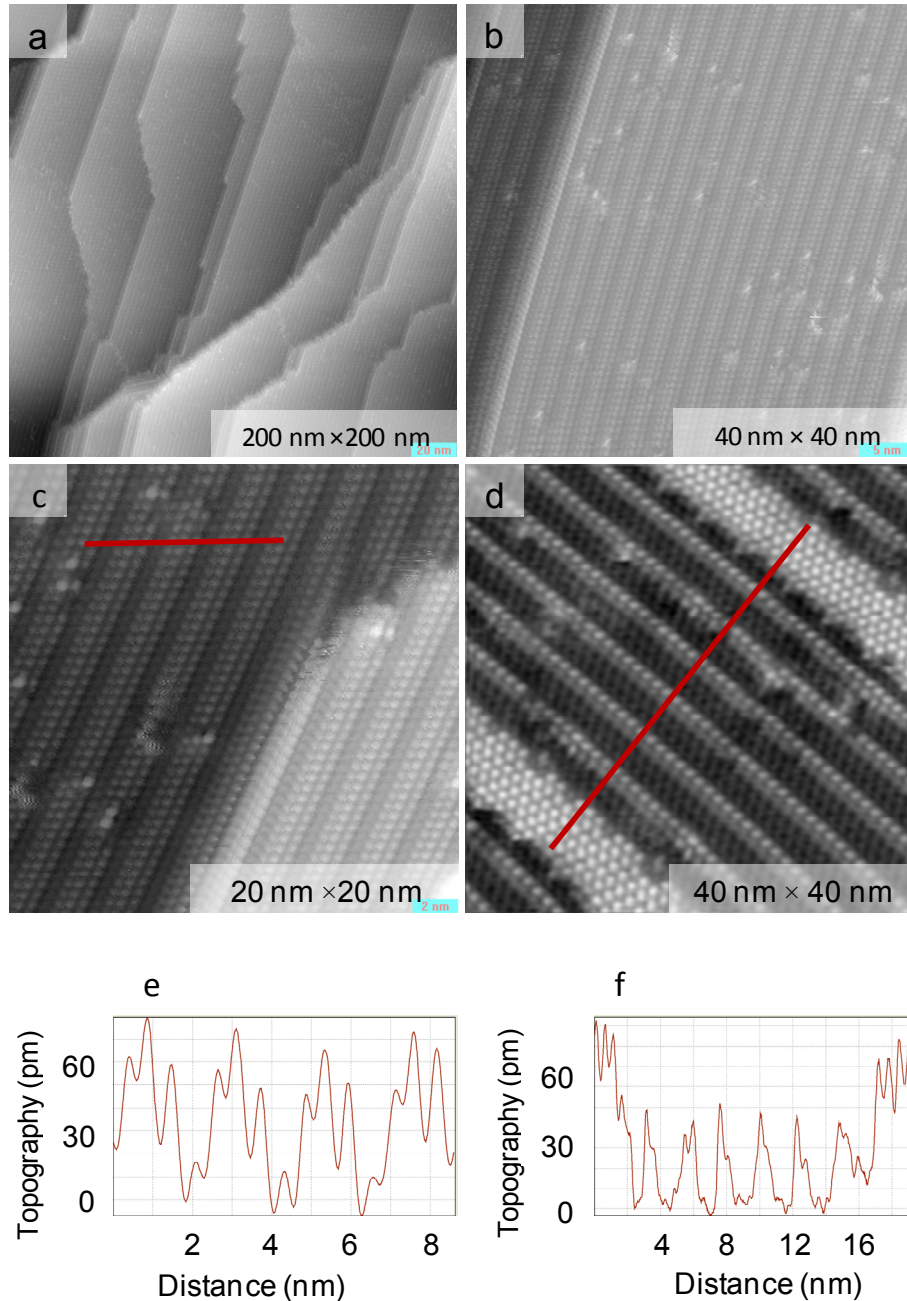
**Figure 2.16 STM micrographs of high temperature vapor-grown SAMs:** a, b, and c) The striped-phase at 120 °C, d) sample which is being converted to striped-phase, both $(\sqrt{3} \times \sqrt{3})R30°$ structure and $(\sqrt{3} \times 4\sqrt{3})R30°$ stripes are present, e and f) cross sections over "c" and "d", respectively.

Further investigation into the stripe structure shows that stripes run in the C10 nearest

neighbor direction, i.e. Au<211>. The width of the stripes is found to be 1.7 nm which

corresponds to four nearest neighbor rows. It is also possible to produce samples which

have both stripes and regular ($\sqrt{3} \times \sqrt{3}$)R30° structure either by reducing the deposition time or back filling an already prepared SAM.

One of the interesting features of the stripes is that all the molecular rows in a single stripe have different elevations (Figure 2.16 c) and especially the fourth row is significantly lower, sometimes even not visible. The difference in contrast of the first three molecules within a single stripe (Figure 2.16c) may be assigned to molecules placed in different adsorption sites or having different $\alpha$, $\beta$, or $\gamma$ angles and the fourth row is simply a missing molecular row. Considering the fact that the underlying Au surface is never exposed, the contrast difference along the missing row (Figure 2.16c) is assigned to a $CH_2$ group in the adjacent chain. Such a lattice structure differs from the striped-phases consisting of lying down molecules.[29] Figure 2.17d is a model for the striped-phase assuming the sulfur adsorbs at the three four hollow site of the fcc lattice of Au. We note, however, that STM images recorded at ambient temperature showed a stripe with four different elevations within the stripe, fast scan directions parallel or perpendicular to the rows also produced different contrast level. Therefore, it is difficult to provide conclusive evidence on the orientation of striped-phase molecular back bone.
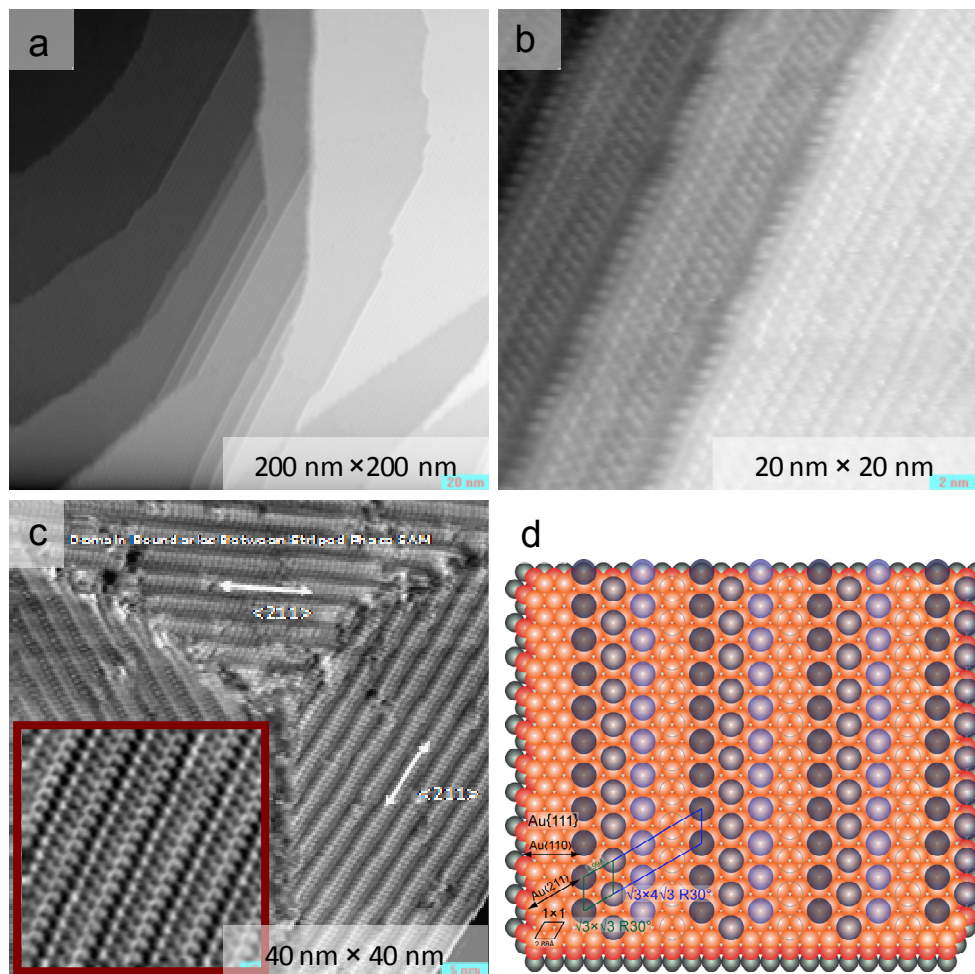
**Figure 2.17 A high-resolution STM micrographs showing vapor-phase grown stripe phases:** a) and b) striped-phase and Au<211> oriented step edges at 120 °C, c) stripes along the three <211> directions, inset figure (scanning area 20 nm × 20 nm) shows molecularly resolved stripes. d) a model which shows the possible arrangement of the molecular head groups on Au(111) surface. A stripe consists of three nearest neighbor rows plus a missing row.

### 2.4.1.3   Low Index Step Edge Orientation of Gold

The Au surfaces of both the high temperature VI free $(2\sqrt{3} \times 3)$rect. SAMs and the

$(\sqrt{3} \times 4\sqrt{3})$R30° striped-phase SAMs have low index step edges although their directions

are different. The low index steps of Au in the $(2\sqrt{3} \times 3)$rect. SAMs run along Au<110>

nearest neighbor direction (Figure 2.18a, and b)  while those of $(\sqrt{3} \times 4\sqrt{3})$R30° striped-

phase SAMs run along Au<211> next nearest neighbor directions (Figure 2.16a, b, c, and Figure 2.17a, and b). Therefore we hypothesize that the Au surface restructuring at high temperature is influenced by the structure of the alkanethiol monolayer on the surface.
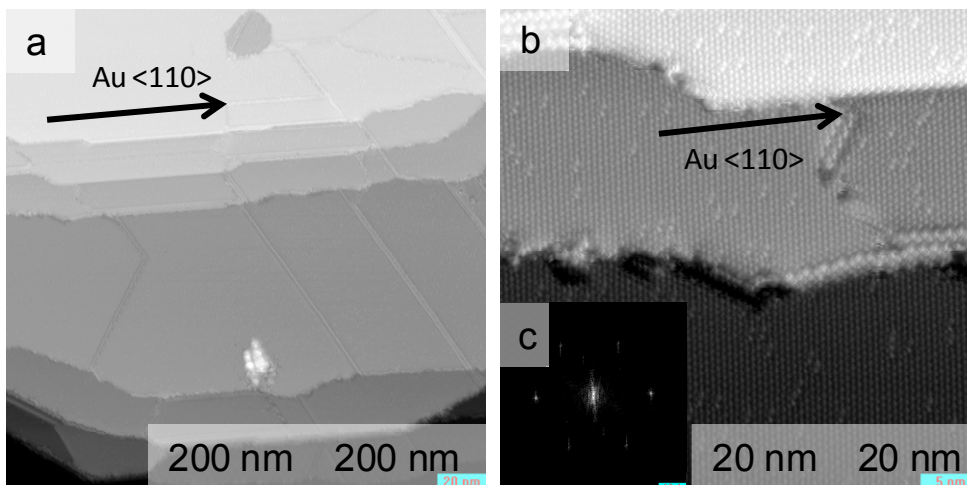


**Figure 2.18 Low index step edge directions of nearly VI free (2√3 × 3)rect. SAMs**: a and b) STM images, c) fft image of image b.

### 2.4.1.4   Surface Coverage of the Striped-Phase

The elevation of the stripes area is 0.28 nm lower than the (√3 × √3)R30° area which is an indication that the striped-phase has lower molecular coverage compared to the (√3 × √3)R30°. The surface coverage of (√3 × 4√3)R30° relative to (√3 × √3)R30° was calculated assuming that the molecular volume is constant and molecular area, i.e. the molecular foot print, depends on the surface coverage using the equation 2.2. Detail procedure of calculation of the surface coverage is given in Appendix 1. It was found that the relative surface coverage of the stripe SAMs is 0.83 compared to regular (√3 × √3)R30° SAM. Therefore it is confirmed that although packing density of molecules in stripe configuration is lower than the (√3 × √3)R30° structure but still they are in a standing up configuration.

$$\frac{A}{A'} = 1 - \frac{\Delta h}{h} \qquad\qquad 2.2$$

Where    $A$    –    area of $(2\sqrt{3} \times 3)$rect. SAM
           $A'$   –    area of $(\sqrt{3} \times 4\sqrt{3})$R30° SAM
           $h$    –    height of the $(2\sqrt{3} \times 3)$rect. SAM from the Au surface
           $\Delta h$  –    actual height difference of the two types of structures

### 2.4.1.5   Further Investigation of Conditions for Striped-Phase Formation

The growth temperature studies show a clear temperature dependence of the SAM structure, particularly the onset of the striped-phase. Our initial hypothesis was that the phase transition was temperature driven with the transition temperature near 115 °C. However this proved to be incorrect when we observed that $(2\sqrt{3} \times 3)$rect. would sometimes grow at 120 °C and $(\sqrt{3} \times 4\sqrt{3})$R30° stripes at 110 °C. Given that the set point of the temperature was stable to ±0.20 °C this was not likely due to a temperature error. The controlling factors for the phase transition proved to be both temperature and the amount of C10 in the vial compared with the amount of C10 required to achieve the saturation vapor pressure in the growth vial.

The vapor grown SAM samples discussed in previous sections were made by charging the 5 mL PFA vial with 1–2 μL of neat C10 liquid. Although our SAMs were usually reproducible, occasionally unexpected results were obtained, particularly when working at temperatures 110–120 °C. We noticed that increasing the initial charge of C10 liquid resulted in reproducible growth of $(2\sqrt{3} \times 3)$rect. at 120 °C. In the design of the original experiments we had incorrectly assumed that the amount of the C10 that would evaporate at the growth temperature to produce the saturation vapor pressure was only a small fraction of this charge. Thus we assumed that C10 was always in excess. However

if C10 was truly in excess, additional C10 liquid should have no effect. Therefore it was compelling to further investigate how the structure of SAMs varies with different charges of C10 at different temperatures. We also compared the results with three different volume vials (1 mL glass, 5 mL PFA, and 85 mL glass) to further test this hypothesis. To allow the results of different vials to be compared, we define a saturation parameter, S, which is the ratio of the charge of thiol to the amount required to achieve the saturation vapor pressure at the particular growth temperature (Equation 2.3). If $S$ is less than unity, all the C10 will be in the vapor phase at the growth temperature and the partial pressure of C10 will be less than its saturation vapor pressure. If $S$ is greater than unity, the partial pressure of C10 will equal its saturation vapor pressure and some C10 will be present as liquid. If $S$ is unity, the charge of C10 equals the amount required to saturate the vapor in the vial, so all the C10 charge will be in the vapor phase.

$$S = \frac{n_{charge}}{n_{sat.vap.}} = \frac{v\rho/M}{P_{sat.vap.}V/RT} \qquad 2.3$$

Where

| | | |
|---|---|---|
| $S$ | – | saturation parameter |
| $n_{charge}$ | – | moles of C10 charge |
| $n_{sat.\,vap.}$ | – | moles of C10 in the saturated vapor |
| $P_{sat.\,vap.}$ | – | equilibrium pressure (Torr) |
| $R$ | – | ideal gas constant (L Torr K$^{-1}$ mol$^{-1}$) |
| $T$ | – | temperature (K) |
| $V$ | – | volume of the vial (L) |
| $v$ | – | volume of thiol (L) |
| $\rho$ | – | density of thiol (g L$^{-3}$) |
| $M$ | – | molecular weight of thiol (g mol$^{-1}$) |

All the samples in this particular study were treated for 16 hours at temperatures ranging from 100 – 138 °C and C10 from 0.1 – 10 μL. Figure 2.19 consists of

representative STM images of such surfaces. Similar behavior was observed regardless of the size (volume) of the vial used for deposition. We observed that there is a clear relationship between the SAM structure and the saturation parameter, *S*. The apparent dependence on temperature is less strong. It was observed that for the formation of good clean stripes, the partial pressure of C10 inside the vial should be just below the saturation vapor pressure. Less than or more than the amount required for saturation produced incomplete stripes with defects or nearly VIs free ($\sqrt{3} \times \sqrt{3}$)R30° SAM respectively. In the Figure 2.20, we plot the saturation parameter, *S,* versus the deposition temperature for two different sizes of vials. The different colors represent the different type of structures and the shape of the symbol represents the size of vial. The line connecting the green symbols is the charge of C10 liquid required in the deposition vial to produce stripes. A large charge produced the ($2\sqrt{3} \times 3$)rect. structure, while a smaller charge produced incomplete stripes with defects. The samples which are immediately above saturation vapor pressure produced broken ($2\sqrt{3} \times 3$)rect. structure which we hypothesize the amount of C10 is not enough to retain the full ($2\sqrt{3} \times 3$)rect. structure but more than the amount for striped structure.
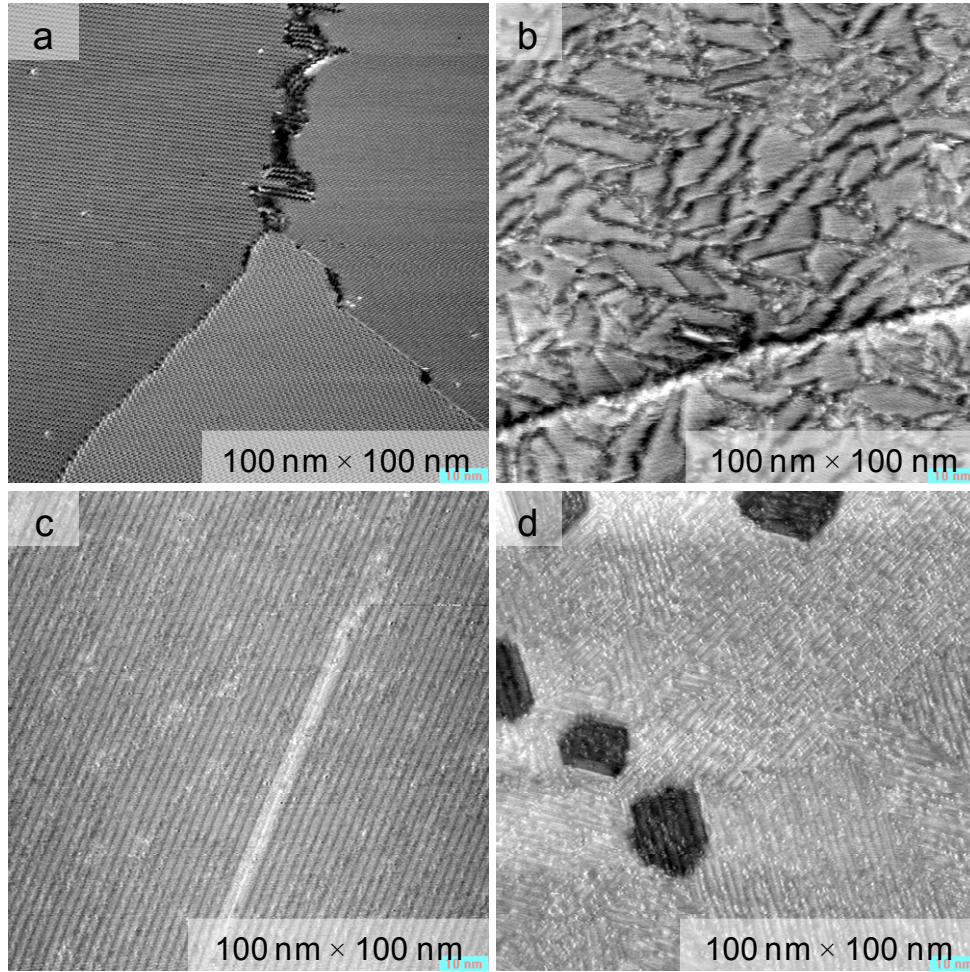
**Figure 2.19 Example of four different types of SAM structures observed and their classification for the C10 volume-temperature study**: a) full $(2\sqrt{3} \times 3)$rect. SAM, b) breaking up of the $(2\sqrt{3} \times 3)$rect., c) full stripe structure, d) incomplete stripes.
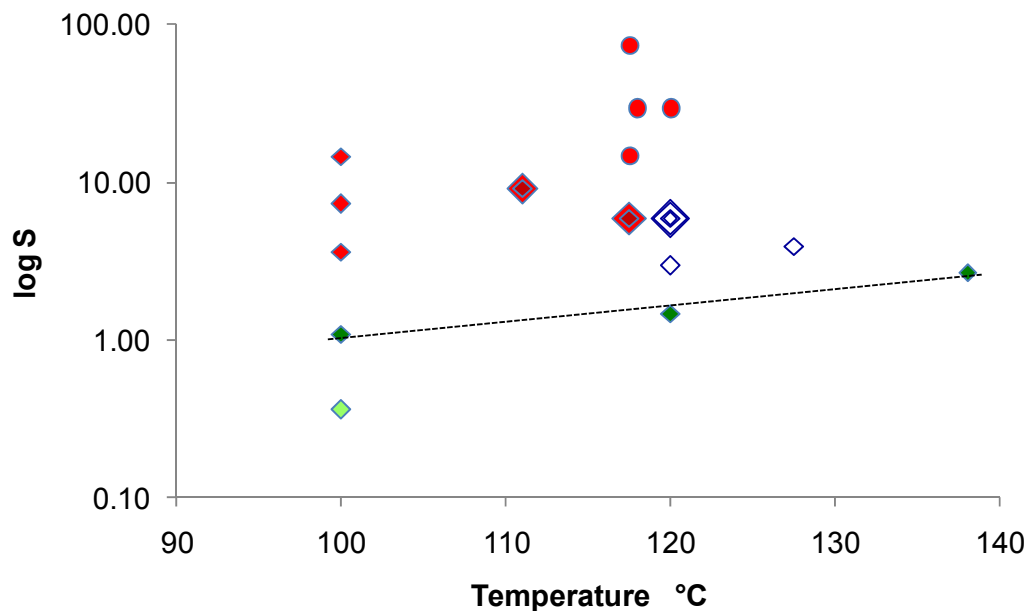
**Figure 2.20 The 1-decanethiol SAM structures grow with different charges of C10 as a function of temperature:** The line along the dark green data points marks the necessary conditions for making good stripes (data for the 85 mL vial is not shown).

### 2.4.1.6 Progression of Normal ($\sqrt{3} \times \sqrt{3}$)R30° Structure into Stripes

Most of our samples were made with 16 hour deposition time for both the convenience of overnight deposition and to ensure the SAM reaches its final structure for the particular depositing conditions. Therefore to answer the question of whether the formation of stripes is an abrupt change or whether it is a gradual change with time, it is necessary to study samples made with different deposition times. Figure 2.21 a–f is such a study with conditions 0.5 µL of liquid C10 in 5 mL PFA vial at 120 °C. Images a–f are from samples of 30 minutes, 1, 1.5, 2, 4, 6 hours. The 30 minutes sample consists of the

normal low temperature ($\sqrt{3} \times \sqrt{3}$)R30° thiol structure. It should be noted here that the time the oven takes to raise the temperature to 120 °C is 1.5 hours. Thus the first two samples (Figure 2.21a, and b) did not reach 120 °C. After one hour, the surface has converted to nearly defect free ($\sqrt{3} \times \sqrt{3}$)R30° structure. At 1.5 hours, the sample still has the defect free structure but shows some indication that some areas of SAM are beginning to change. At 2 hours a significant portion of the monolayer has been converted to strips but still some of ($\sqrt{3} \times \sqrt{3}$)R30° structure can be seen. This conversion is complete in 4 & 6 hours. The same trend of progression into stripes was seen in the samples made using 1 μL of C10. In this case the same trend was observed, but the appearance of the striped-phase was delayed requiring ten hours. One significant difference of 0.5 μL versus 1 μL made stripe SAMs is that samples with 0.5 μL still have faceted vacancy islands while the 1 μL one does not have any although both have well developed stripe structures. This can be explained by considering the times the samples take to achieve the stripes. The samples exposed to high temperature for a longer period of time have more time for Ostwald ripening to proceed. Therefore we can conclude that the structure of SAM is ($\sqrt{3} \times \sqrt{3}$)R30° at first and it gradually changes to ($\sqrt{3} \times 4\sqrt{3}$)R30° stripes by desorption of molecules with oxidation or leaking out of some of the alkanethiol in the vial.
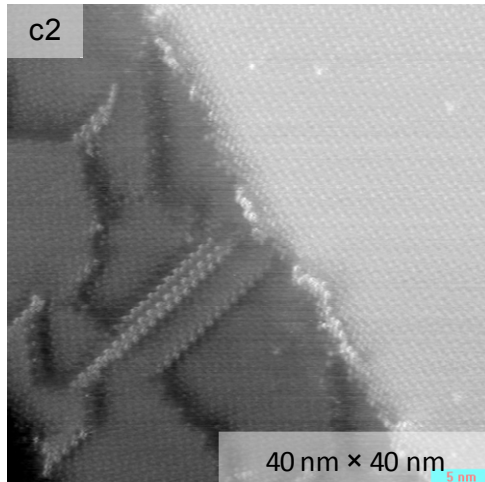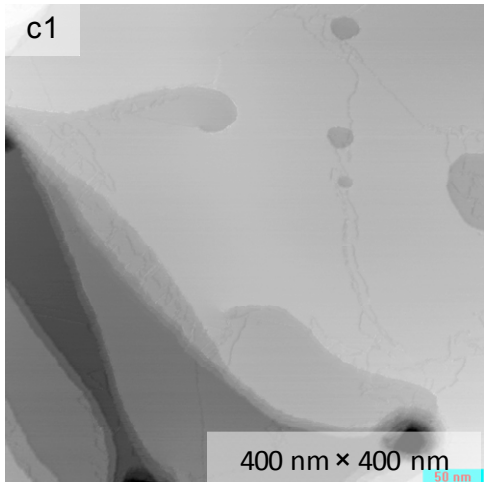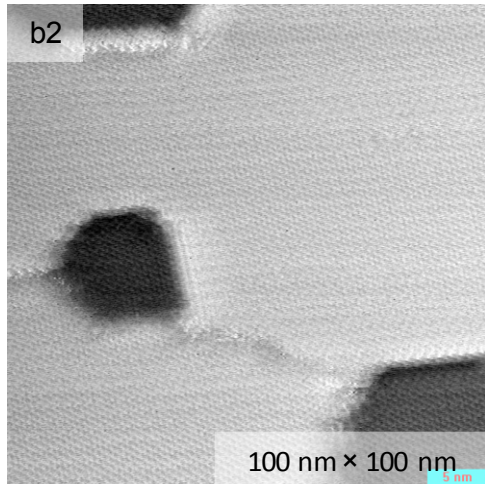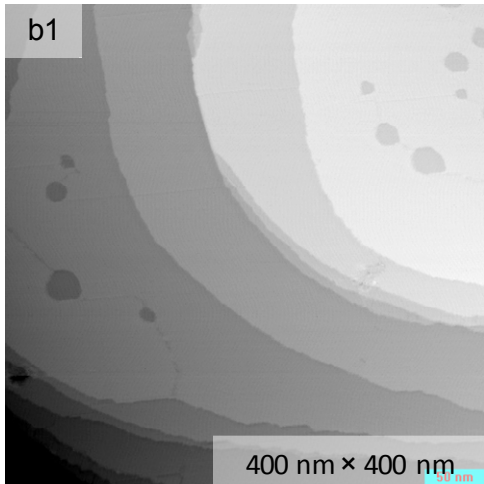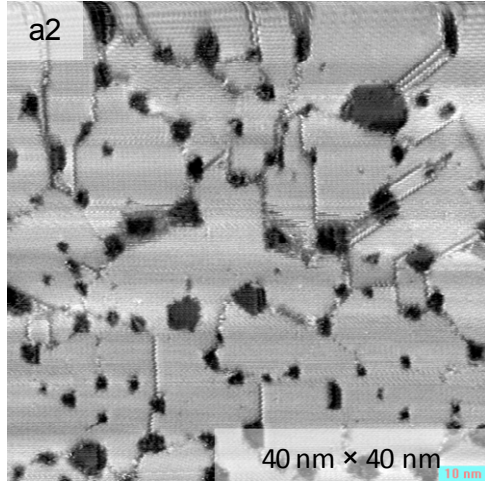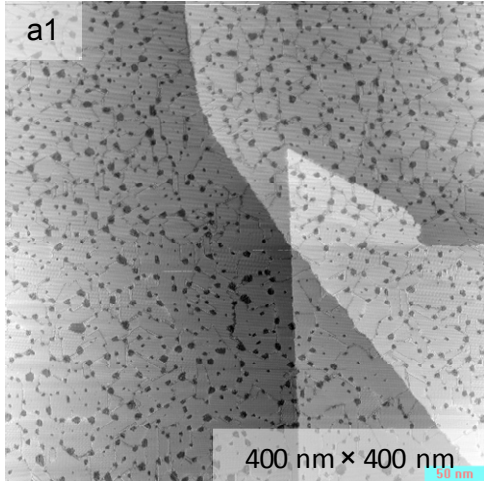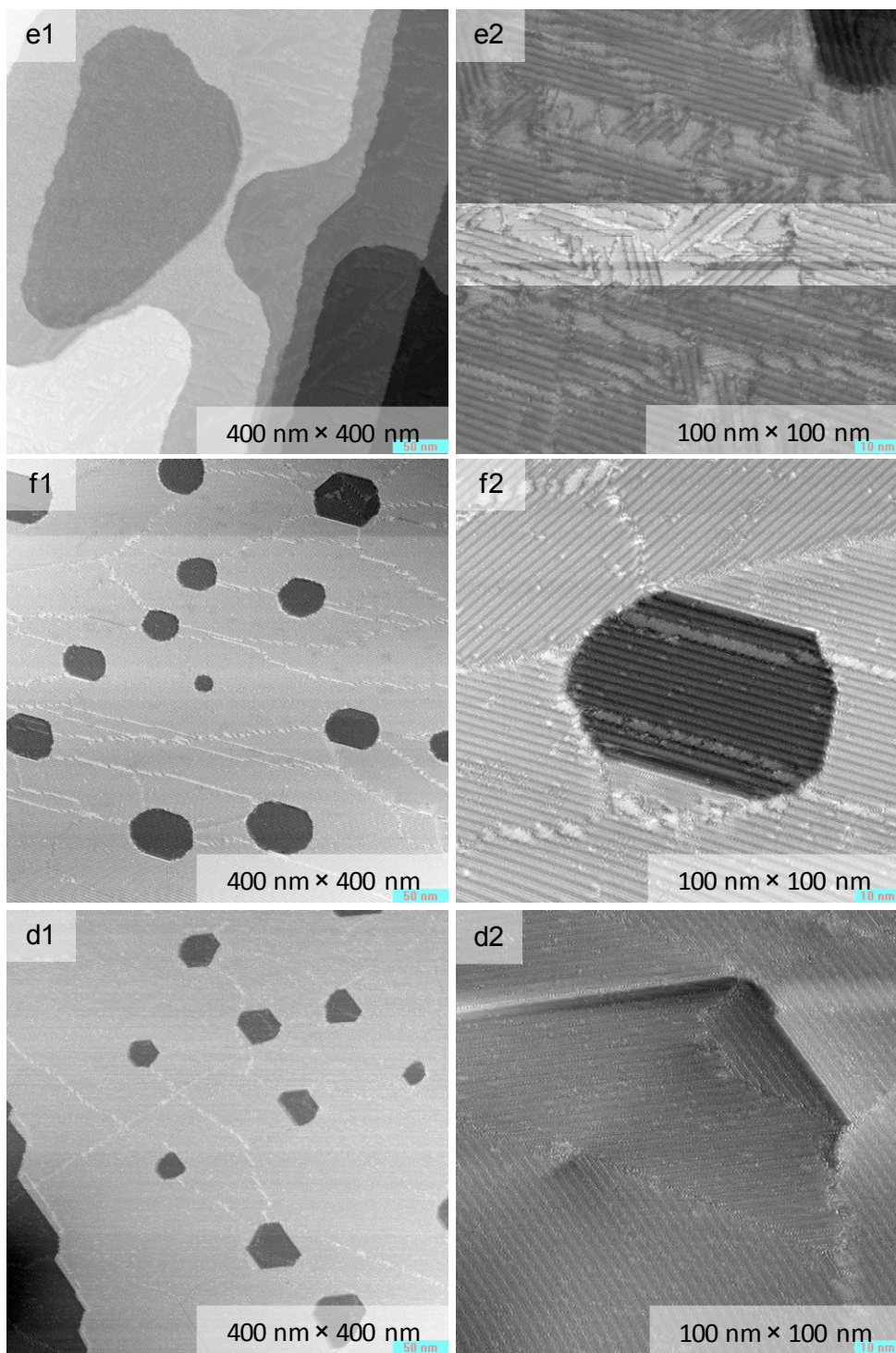
**Figure 2.21 Time evolution of a regular 1-decanethiol SAM into striped SAM** (deposition conditions: 0.5 µL of liquid C10 in 5 mL PFA vial at 120 °C); after a) 30 min, b) 1 hr, c) 1.5 hrs, d) 2 hrs, e) 4 hrs, and f) 6 hrs.

### 2.4.1.7 Quenching Rate Dependence of Striped-Phase SAMs from Their Growth Temperature

Although our samples are grown at high temperature, all STM imaging was performed at room temperature. We cannot say that the structure we observe in the high-temperature grown SAM structures exists at high temperature without performing STM imaging during SAM growth. We can test whether the high temperature structures form during the cooling phases. To explore this question we compared the SAM structures when samples were cooled slowly (from 120 °C to room temperature in about 10 minutes) to rapidly cooled samples (−196 °C liquid $N_2$ and −52 °C isopropanol bath). Figure 2.22 shows STM micrographs of the striped-phase samples allowed to (a) cool slowly inside the oven (b) subjected to quenching in a cryobath at −52 °C, (c) and in a liquid nitrogen bath. Our results indicate that no significant changes occur in SAM striped structure between fast and slow cool down. This confirms that the stripe structure is representative of high temperature formation.
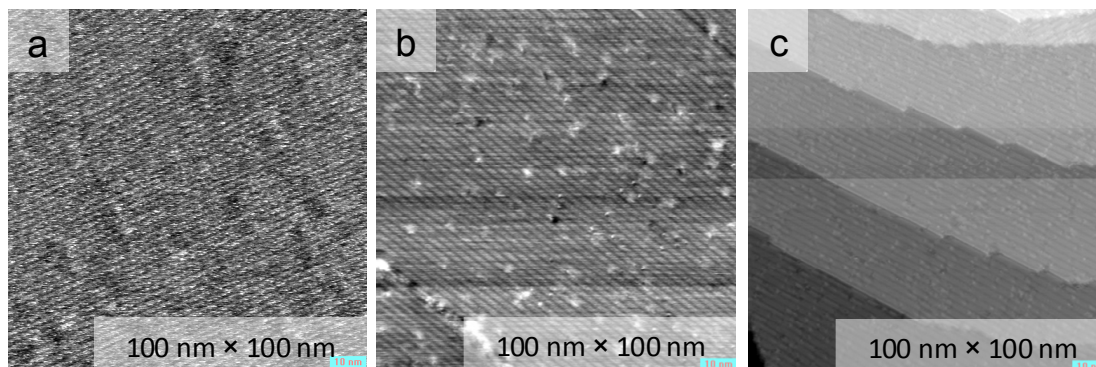


**Figure 2.22 The effect of quenching rate on the structure of striped-phase SAMs from their growth temperature (120 °C)** after 16hrs.: a) slow cool down (120 °C to room temperature in 10 mns), b) in a cryobath (isopropanol −52 °C), and c) in liquid nitrogen(−196 °C). The image area is 100 nm × 100 nm in each image.

## 2.4.2 C10 and C12 Mixed SAMs Grown from Vapor

Co-deposition of C10 and C12 from a mixture of 85% C10 and 15% C12 (17:1 in vapor) produced mixed SAMs which mostly consists of C12 molecules. Phase separation was not observed. As expected the surface consists of mostly of C12 molecules. It is reported in the literature that longer chain molecules prefer to attach to the surface than the shorter chain ones. Because the inter-chain Van der Waals energy favors the larger alkyl chain (C12 over C10). Therefore we expect the SAM to be enriched in the longer chain thiol compared to the vapor phase composition. Figure 2.23 shows that the C12 is clearly the majority component in the SAM although it is less than 6% of the vapor.
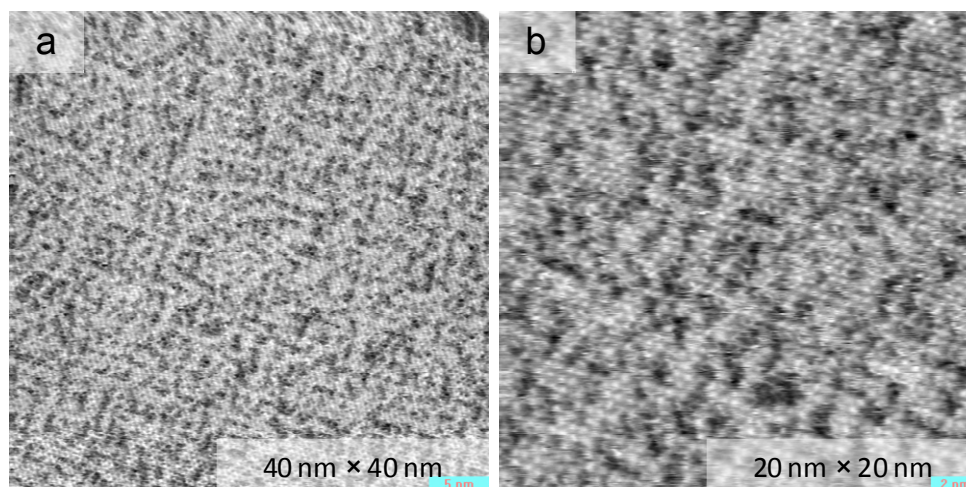


**Figure 2.23 C10 and C12 vapor co-deposited on Au(111)** at 110 °C for 16 hours (C10 : C12 liquid 85:15, vapor 17:1)

## 2.4.3 Kinetic Stability of the Striped-Phase Structure with Respect to Insertion of C10 and Reversion to (2√3 × 3)rect.

We carried out a systematic study of backfilling of striped SAMs at different temperatures from room temperature to 100 °C. A striped-phase SAM, grown at 120 °C was subsequently exposed to C10 vapor at different temperatures for 16 hours. If the

striped-phase SAM was an open structure, we would expect it to rapidly take up C10 molecules, convert to $(\sqrt{3} \times \sqrt{3})R30°$. However we find that the striped-phase is remarkably stable to converting to $(\sqrt{3} \times \sqrt{3})R30°$ at temperatures 40 °C and below (Figure 2.24 b, and c). Only at 60 °C (Figure 2.24d) does the SAM began to take up C10. The process is more rapid at 80 °C (Figure 2.24e). After 16 hours at 100 °C the conversion is complete (Figure 2.24f). Even at 60 and 80 °C the stripes-phase is not simply taking up C10 molecules in the interior of its domains again indicating that the structure is not open. Rather conversion to $(\sqrt{3} \times \sqrt{3})R30°$ nucleates at domain boundaries and spreads across the surface. Note that the growing $(\sqrt{3} \times \sqrt{3})R30°$ domains advance along the stripes. As the $(\sqrt{3} \times \sqrt{3})R30°$ reaches the Au step edges they reorient to the Au <110> typically associated with that SAM phase.

a1 — 200 nm × 200 nm

a2 — 40 nm × 40 nm

b1 — 200 nm × 200 nm

b2 — back filled at room temperature — 40 nm × 40 nm

c1 — 200 nm × 200 nm

c2 — back filled at 40 °C — 40 nm × 40 nm

58
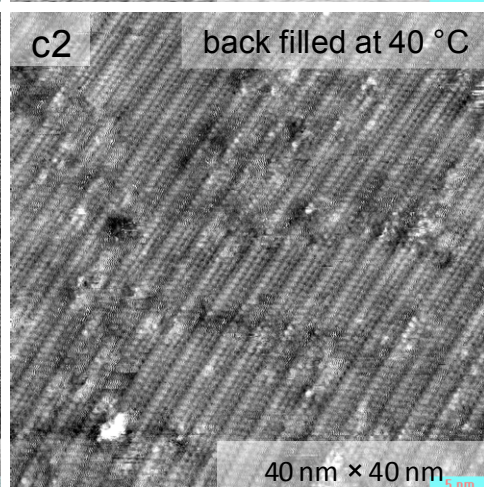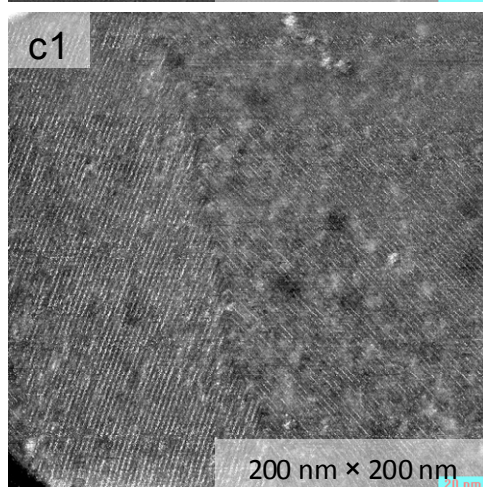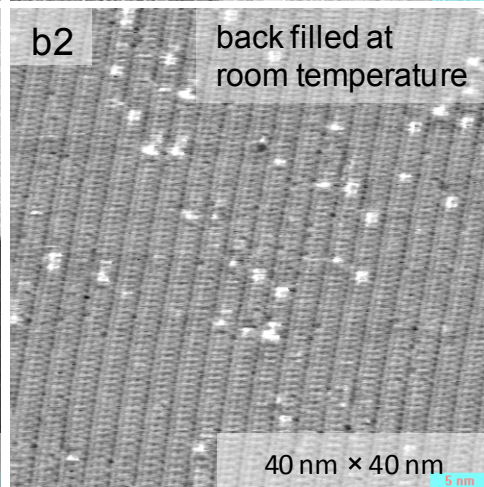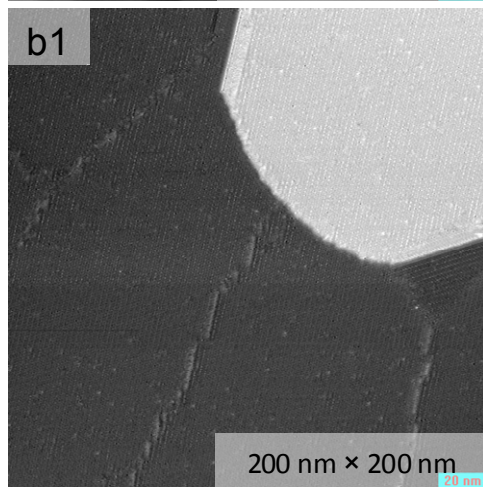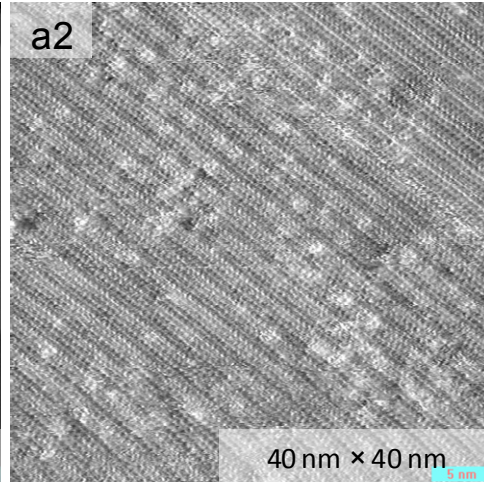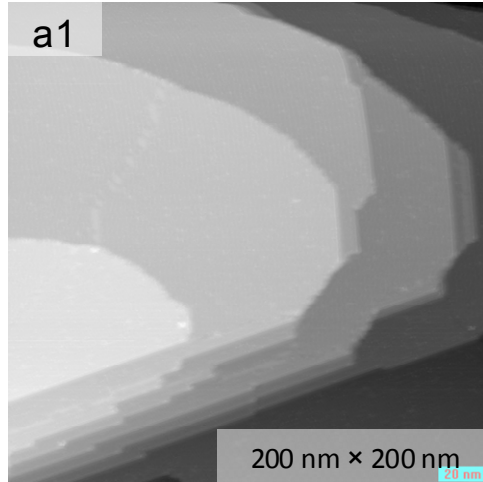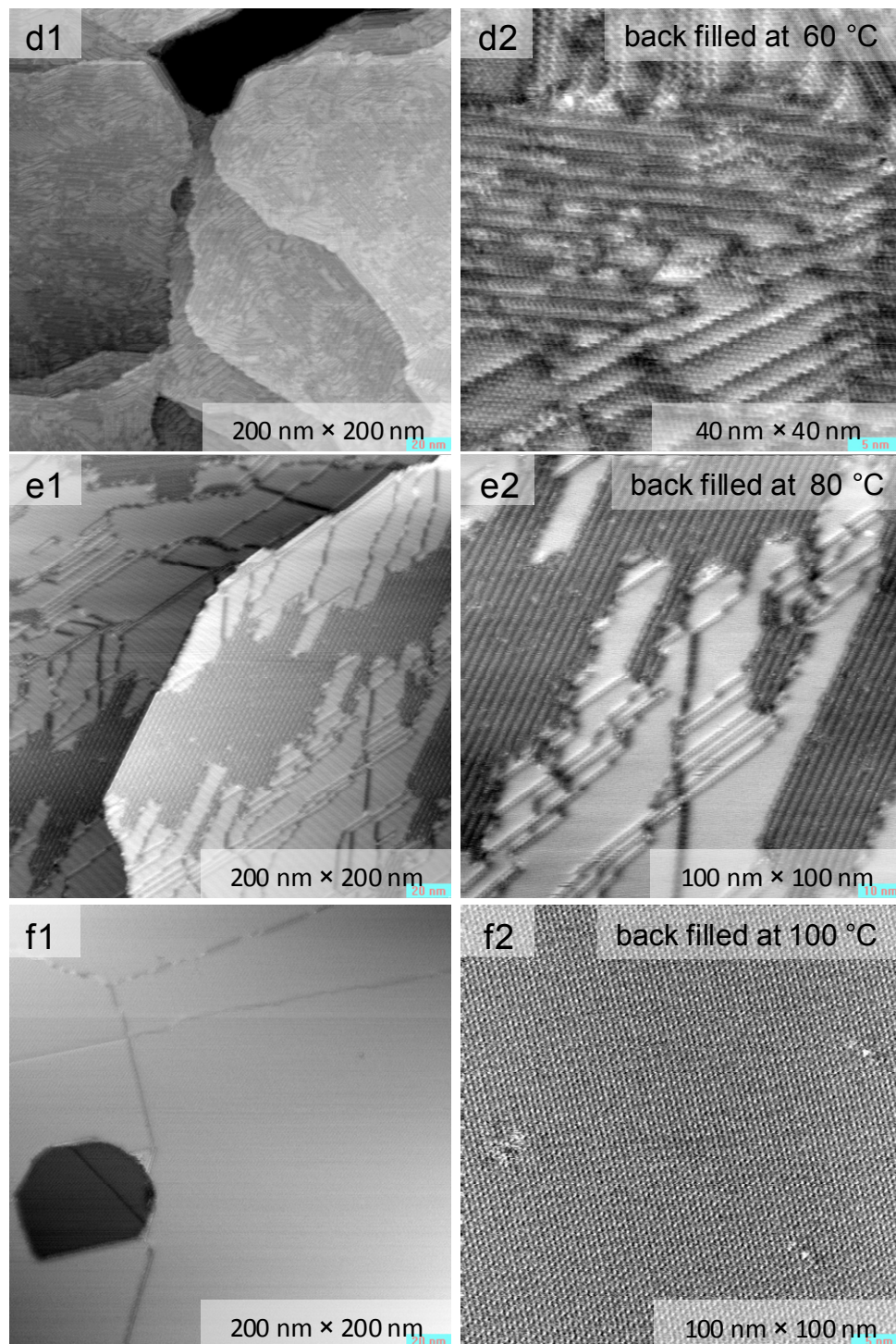
**Figure 2.24 Kinetic stability of the striped-phase with respect to back filling by C10** and reversion to (2√3 × 3)rect. at different temperatures for 16 hrs. Two different scan sizes are shown for each temperature. a) STM image of the initial striped SAM, stripes backfilled with C10 at b) room temperature, c) 40 °C, d) 60 °C, e) 80 °C, and f) 100 °C.

## 2.5 Conclusions

This chapter has presented a systematic study based on scanning tunneling microscopy (STM) to investigate growth temperature and solvent effects on the 1-decanethiol (C10) SAM features on Au{111} substrates. We have prepared SAMs of C10 grown from different solvents (ethanol, *n*-butanol, decalin, hexadecane and triethylene glycol) and vapor of C10 with growth temperatures ranging from 20 °C to 140 °C. Our STM study shows that the VIs undergo Ostwald ripening of which increases with increasing temperature for both solution and vapor grown SAMs. The structure of the C10 SAMs is observed to depend with temperature and solvent. For vapor grown SAMs, we have established conditions for making samples almost VIs free with very large SAM domains. When the $(2\sqrt{3} \times 3)$rect. SAM is present, the Au step edges annealed to the Au<110> direction.

Further increase of the deposition temperature leads to formation of the striped phase $(\sqrt{3} \times 4\sqrt{3})$R30°. To grow this phase, the partial pressure of C10 must be slightly below the saturation vapor pressure. Excess or less amount of alkanethiol leads to a incomplete (not clean) stripe structure or $(2\sqrt{3} \times 3)$rect. structure. The time associated with the formation of good stripes depends on the amount of alkanethiol. Stripes of C10 have been observed to be oriented in the C10 nearest neighbor direction (Au<211>) and the low index step edges aligned in the same direction as stripes (Au<211>) in contrast to the defect free $(\sqrt{3} \times \sqrt{3})$R30° SAM. Low temperature analysis of the vapor-grown striped-phase SAM has confirmed that the observed structures are representative of high-temperature phase. On the other hand, solution-grown SAMs have been observed to transition to the striped-phase between 60 °C and 80 °C followed by gradual disordering

of the structure above 100 °C. Also we showed that the striped-phase is stable to converting to (2√3 × 3)rect. below 40 °C.

## 2.6 References for Chapter 2

(1)      Schonenberger, C.; Jorritsma, J.; Sondag-Huethorst, J. A. M.; Fokkink, L. G. J. Domain Structure of Self-Assembled Alkanethiol Monolayers on Gold. *J. Phys. Chem.* **1995**, *99*, 3259.

(2)      Love, J. C.; Estroff, L. A.; Kriebel, J. K.; Nuzzo, R. G.; Whitesides, G. M. Self-Assembled Monolayers of Thiolates on Metals as a Form of Nanotechnology. *Chem. Rev.* **2005**, *105*, 1103.

(3)      Vericat, C.; Vela, M. E.; Benitez, G. A.; Martin Gago, J. A.; Torrelles, X.; Salvarezza, R. C. Surface Characterization of Sulfur and Alkanethiol Self-Assembled Monolayers on Au(111). *J. Phys.: Condens. Matter* **2006**, *18*, R867.

(4)      Schreiber, F. Structure and Growth of Self-Assembling Monolayers. *Prog. Surf. Sci.* **2000**, *65*, 151.

(5)      Bumm, L. A.; Arnold, J. J.; Cygan, M. T.; Dunbar, T. D.; Burgin, T. P.; Jones, L., II; Allara, D. L.; Tour, J. M.; Weiss, P. S. Are Single Molecular Wires Conducting? *Science* **1996**, *271*, 1705.

(6)      Tour, J. M. Molecular Electronics. Synthesis and Testing of Components. *Acc. Chem. Res.* **2000**, *33*, 791.

(7)      Poirier, G. E.; Fitts, W. P.; White, J. M. Two-Dimensional Phase Diagram of Decanethiol on Au(111). *Langmuir* **2001**, *17*, 1176.

(8)      Camillone III, N.; Eisenberger, P.; Leung, T. Y. B.; Schwartz, P.; Scoles, G.; Poirier, G. E.; Tarlov, M. J. New Monolayer Phases of *n*-Alkane Thiols Self-Assembled on Au(111): Preparation, Surface Characterization, and Imaging. *J. Chem. Phys.* **1994**, *101*, 11031.

(9)      Camillone, N.; Leung, T. Y. B.; Schwartz, P.; Eisenberger, P.; Scoles, G. Chain Length Dependence of the Striped Phases of Alkanethiol Monolayers Self-Assembled on Au(111): An Atomic Beam Diffraction Study. *Langmuir* **1996**, *12*, 2737.

(10)    Fitts, W. P.; White, J. M.; Poirier, G. E. Low-Coverage Decanethiolate Structure on Au(111): Substrate Effects. *Langmuir* **2002**, *18*, 1561.

(11)    Fitts, W. P.; White, J. M.; Poirier, G. E. Thermodynamics of Decanethiol Adsorption on Au(111): Extension to 0 °C. *Langmuir* **2002**, *18*, 2096.

(12)    Poirier, G. E. Mechanism of Formation of Au Vacancy Islands in Alkanethiol Monolayers on Au(111). *Langmuir* **1997**, *13*, 2019.

(13)    Poirier, G. E. Characterization of Organosulfur Molecular Monolayers on Au(111) using Scanning Tunneling Microscopy. *Chem. Rev.* **1997**, *97*, 1117.

(14)    Poirier, G. E.; Pylant, E. D. The Self-Assembly Mechanism of Alkanethiols on Au(111). *Science* **1996**, *272*, 1145.

(15)    Poirier, G. E.; Tarlov, M. J. The c(4 × 2) Superlattice of *n*-Alkanethiol Monolayers Self-Assembled on Au(111). *Langmuir* **1994**, *10*, 2853.

(16)    Poirier, G. E.; Tarlov, M. J. Molecular Ordering and Gold Migration Observed in Butanethiol Self-Assembled Monolayers Using Scanning-Tunneling-Microscopy. *J. Phys. Chem.* **1995**, *99*, 10966.

(17)    Poirier, G. E.; Tarlov, M. J.; Rushmeier, H. E. 2-Dimensional Liquid-Phase and The p × √3 Phase of Alkanethiol Self-Assembled Monolayers On Au(111). *Langmuir* **1994**, *10*, 3383.

(18)    Qian, Y. L.; Yang, G. H.; Yu, J. J.; Jung, T. A.; Liu, G. Y. Structures of Annealed Decanethiol Self-Assembled Monolayers on Au(111): an Ultrahigh Vacuum Scanning Tunneling Microscopy Study. *Langmuir* **2003**, *19*, 6056.

(19)    Woodward, J. T.; Walker, M. L.; Meuse, C. W.; Vanderah, D. J.; Poirier, G. E.; Plant, A. L. Effect of an Oxidized Gold Substrate on Alkanethiol Self-Assembly. *Langmuir* **2000**, *16*, 5347.

(20)    Yang, G.; Liu, G.-y. New Insights for Self-Assembled Monolayers of Organothiols on Au(111) Revealed by Scanning Tunneling Microscopy. *J. Phys. Chem. B* **2003**, *107*, 8746.

(21)    Chailapakul, O.; Sun, L.; Xu, C.; Crooks, R. M. Interactions Between Organized, Surface-Confined Monolayers and Vapor-Phase Probe Molecules. 7. Comparison of Self-Assembling *n*-alkanethiol Monolayers Deposited on Gold from Liquid and Vapor Phases. *J. Am. Chem. Soc.* **1993**, *115*, 12459.


(22)    Porter, M. D.; Bright, T. B.; Allara, D. L.; Chidsey, C. E. D. Spontaneously Organized Molecular Assemblies .4. Structural Characterization of *n*-Alkyl Thiol Monolayers on Gold by Optical Ellipsometry, Infrared-Spectroscopy, and Electrochemistry. *J. Am. Chem. Soc.* **1987**, *109*, 3559.


(23)    Nuzzo, R. G.; Dubois, L. H.; Allara, D. L. Fundamental-Studies Of Microscopic Wetting On Organic-Surfaces .1. Formation And Structural Characterization Of A Self-Consistent Series Of Polyfunctional Organic Monolayers. *J. Am. Chem. Soc.* **1990**, *112*, 558.


(24)    Laibinis, P. E.; Whitesides, G. M.; Allara, D. L.; Tao, Y. T.; Parikh, A. N.; Nuzzo, R. G. Comparison of the Structures and Wetting Properties of Self-Assembled Monolayers of *n*-Alkanethiols on the Coinage Metal-Surfaces, Cu, Ag, Au. *J. Am. Chem. Soc.* **1991**, *113*, 7152.


(25)    Badin, Mihaela G.; Bashir, A.; Krakert, S.; Strunskus, T.; Terfort, A.; Wöll, C. Kinetically Stable, Flat-Lying Thiolate Monolayers. *Angew. Chem. Int. Ed.* **2007**, *46*, 3762.


(26)    Xiao, X. D.; Wang, B.; Zhang, C.; Yang, Z.; Loy, M. M. T. Thermal Annealing Effect of Alkanethiol Monolayers on Au(111) in Air. *Surf. Sci.* **2001**, *472*, 41.


(27)    Ulman, A. Formation and Structure of Self-Assembled Monolayers. *Chem. Rev.* **1996**, *96*, 1533.


(28)    Delamarche, E.; Michel, B.; Biebuyck, H. A.; Gerber, C. Golden Interfaces: The Surface of Self-Assembled Monolayers. *Adv. Mater.* **1996**, *8*, 719.


(29)    Vericat, C.; Vela, M. E.; Salvarezza, R. C. Self-Assembled Monolayers of Alkanethiols on Au(111): Surface Structures, Defects and Dynamics. *Phys. Chem. Chem. Phys.* **2005**, *7*, 3258.


(30)    Poirier, G. E. Coverage-Dependent Phases and Phase Stability of Decanethiol on Au(111). *Langmuir* **1999**, *15*, 1167.

(31)    Qian, Y.; Yang, G.; Yu, J.; Jung, T. A.; Liu, G. Y. Structures of Annealed Decanethiol Self-Assembled Monolayers on Au(111): an Ultrahigh Vacuum Scanning Tunneling Microscopy Study. *Langmuir* **2003**, *19*, 6056.

(32)    Bucher, J.-P.; Santesson, L.; Kern, K. Thermal Healing of Self-Assembled Organic Monolayers: Hexane- and Octadecanethiol on Au(111) and Ag(111). *Langmuir* **1994**, *10*, 979.

(33)    Delamarche, E.; Michel, B.; Gerber, C.; Anselmetti, D.; Guentherodt, H. J.; Wolf, H.; Ringsdorf, H. Real-Space Observation of Nanoscale Molecular Domains in Self-Assembled Monolayers. *Langmuir* **1994**, *10*, 2869.

(34)    Yamada, R.; Uosaki, K. In Situ Scanning Tunneling Microscopy Observation of the Self-Assembly Process of Alkanethiols on Gold(111) in Solution. *Langmuir* **1998**, *14*, 855.

(35)    Staub, R.; Toerker, M.; Fritz, T.; Schmitz-Hubsch, T.; Sellam, F.; Leo, K. Flat Lying Pin-Stripe Phase of Decanethiol Self-Assembled Monolayers on Au(111). *Langmuir* **1998**, *14*, 6693.

(36)    Toerker, M.; Staub, R.; Fritz, T.; Schmitz-Hubsch, T.; Sellam, F.; Leo, K. Annealed Decanethiol Monolayers on Au(111) - Intermediate Phases Between Structures with High and Low Molecular Surface Density. *Surf. Sci.* **2000**, *445*, 100.

(37)    Pflaum, J.; Bracco, G.; Schreiber, F.; Colorado, R.; Shmakova, O. E.; Lee, T. R.; Scoles, G.; Kahn, A. Structure and Electronic Properties of $CH_3$- and $CF_3$- Terminated Alkanethiol Monolayers on Au(111): A Scanning Tunneling Microscopy, Surface X-ray and Helium Scattering Study. *Surf. Sci.* **2002**, *498*, 89.

(38)    Camillone III, N.; Chidsey, C. E. D.; Liu, G. Y.; Scoles, G. Substrate Dependence of the Surface Structure and Chain Packing of Docosyl Mercaptan Self-Assembled on the (111), (110), and (100) Faces of Single Crystal Gold. *J. Chem. Phys.* **1993**, *98*, 4234.

(39)    Widrig, C. A.; Alves, C. A.; Porter, M. D. Scanning Tunneling Microscopy Of Ethanethiolate And Normal-Octadecanethiolate Monolayers Spontaneously Adsorbed At Gold Surfaces. *J. Am. Chem. Soc.* **1991**, *113*, 2805.

(40)    Nuzzo, R. G.; Korenic, E. M.; Dubois, L. H. Studies Of The Temperature-Dependent Phase-Behavior Of Long-Chain Normal-Alkyl Thiol Monolayers On Gold. *J. Chem. Phys.* **1990**, *93*, 767.

(41)    Mazzarello, R.; Cossaro, A.; Verdini, A.; Rousseau, R.; Casalis, L.; Danisman, M. F.; Floreano, L.; Scandolo, S.; Morgante, A.; Scoles, G. Structure of a $CH_3S$ Monolayer on Au(111) Solved by the Interplay Between Molecular Dynamics Calculations and Diffraction Measurements. *Phys. Rev. Lett.* **2007**, *98*.

(42)    Noh, J.; Kato, H. S.; Kawai, M.; Hara, M. Surface Structure and Interface Dynamics of Alkanethiol Self-Assembled Monolayers on Au(111). *J. Phys. Chem. B* **2006**, *110*, 2793.

(43)    Fenter, P.; Eberhardt, A.; Eisenberger, P. Self-Assembly of *n*-Alkyl Thiols as Disulfides on Au(111). *Science* **1994**, *266*, 1216.

(44)    Fenter, P.; Schreiber, F.; Berman, L.; Scoles, G.; Eisenberger, P.; Bedzyk, M. J. On the Structure and Evolution of the Buried S/Au Interface in Self-Assembled Monolayers: X-ray Standing Wave Results. *Surf. Sci.* **1999**, *425*, 138.

(45)    Woodruff, D. P. The Interface Structure of *n*-Alkylthiolate Self-Assembled Monolayers on Coinage Metal Surfaces. *Phys. Chem. Chem. Phys.* **2008**, *10*, 7211.

(46)    Mar, W.; Klein, M. L. Molecular-Dynamics Study of the Self-Assembled Monolayer Composed of $S(CH_2)_{14}CH_3$ Molecules Using an all-Atoms Model. *Langmuir* **1994**, *10*, 188.

(47)    Fenter, P.; Eisenberger, P.; Liang, K. S. Chain-Length Dependence of the Structures and Phases of $CH_3(CH_2)_{N-1}SH$ Self-Assembled on Au(111). *Phys. Rev. Lett.* **1993**, *70*, 2447.

(48)    Bucher, J. P.; Santesson, L.; Kern, K. Selective Imaging Of Self-Assembled Monolayers By Tunneling Microscopy. *Appl. Phys. A* **1994**, *59*, 135.

(49)    Yeganeh, M. S.; Dougal, S. M.; Polizzotti, R. S.; Rabinowitz, P. Interfacial Atomic-Structure Of A Self-Assembled Alkyl Thiol Monolayer Au(111) - A Sum-Frequency Generation Study. *Phys. Rev. Lett.* **1995**, *74*, 1811.

(50)    Haussling, L.; Michel, B.; Ringsdorf, H.; Rohrer, H. Direct Observation of Streptavidin Specifically Adsorbed on Biotin-Functionalized Self-Assembled Monolayers with the Scanning Tunneling Microscope. *Angew. Chem., Int. Ed. Engl.* **1991**, *30*, 569.

(51)     Edinger, K.; Golzhauser, A.; Demota, K.; Woll, C.; Grunze, M. Formation of Self-Assembled Monolayers of N-Alkanethiols on Gold - A Scanning Tunneling Microscopy Study on The Modification of Substrate Morphology. *Langmuir* **1993**, *9*, 4.


(52)     Cavalleri, O.; Hirstein, A.; Kern, K. Ostwald Ripening of Vacancy Islands at Thiol Covered Au(111). *Surf. Sci.* **1995**, *340,* L960.


(53)     McCarley, R. L.; Dunaway, D. J.; Willicut, R. J. Mobility of the Alkanethiol-Gold (111) Interface Studied by Scanning Probe Microscopy. *Langmuir* **1993**, *9*, 2775.


(54)     Delamarche, E.; Michel, B.; Kang, H.; Gerber, C. Thermal Stability of Self-Assembled Monolayers. *Langmuir* **1994**, *10*, 4103.


(55)     Sondaghuethorst, J. A. M.; Schonenberger, C.; Fokkink, L. G. J. Formation Of Holes In Alkanethiol Monolayers On Gold. *J. Phys. Chem.* **1994**, *98*, 6826.


(56)     Schonenberger, C.; Sondaghuethorst, J. A. M.; Jorritsma, J.; Fokkink, L. G. J. What Are The Holes In Self-Assembled Monolayers Of Alkanethiols On Gold. *Langmuir* **1994**, *10,* 611.


(57)     Kim, Y. T.; Bard, A. J. Imaging And Etching Of Self-Assembled *n*-Octadecanethiol Layers On Gold With The Scanning Tunneling Microscope *Langmuir* **1992**, *8*, 1096.


(58)     Delamarche, E.; Michel, B. Structure and Stability of Self-Assembled Monolayers. *Thin Solid Films* **1996**, *273*, 54.


(59)     Bumm, L. A.; Arnold, J. J.; Charles, L. F.; Dunbar, T. D.; Allara, D. L.; Weiss, P. S. Directed Self-Assembly to Create Molecular Terraces with Molecularly Sharp Boundaries in Organic Monolayers. *J. Am. Chem. Soc.* **1999**, *121*, 8017.


(60)     Lewis, P. A.; Donhauser, Z. J.; Mantooth, B. A.; Smith, R. K.; Bumm, L. A.; Kelly, K. F.; Weiss, P. S. Control and Placement of Molecules via Self-Assembly. *Nanotechnology* **2001**, *12*, 231.


(61)     Yamada, R.; Wano, H.; Uosaki, K. Effect of Temperature on Structure of the Self-Assembled Monolayer of Decanethiol on Au(111) Surface. *Langmuir* **2000**, *16*, 5523.

(62)    Brett, C. M. A.; Kresak, S.; Hianik, T.; Brett, A. M. O. Studies on Self-Assembled Alkanethiol Monolayers Formed at Applied Potential on Polycrystalline Gold Electrodes. *Electroanalysis* **2003**, *15*, 557.

(63)    Schreiber, F.; Eberhardt, A.; Leung, T. Y. B.; Schwartz, P.; Wetterer, S. M.; Lavrich, D. J.; Berman, L.; Fenter, P.; Eisenberger, P.; Scoles, G. Adsorption Mechanisms, Structures, and Growth Regimes of an Archetypal Self-Assembling System: Decanethiol on Au(111). *Phys. Rev. B* **1998**, *57*, 12476.

(64)    Schwartz, P.; Schreiber, F.; Eisenberger, P.; Scoles, G. Growth Kinetics of Decanethiol Monolayers Self-Assembled on Au(111) by Molecular Beam Deposition: An Atomic Beam Diffraction Study. *Surf. Sci.* **1999**, *423*, 208.

(65)    Dubois, L. H.; Zegarski, B. R.; Nuzzo, R. G. Molecular Ordering of Organosulfur Compounds on Au(111) and Au(100) - Adsorption from Solution and in Ultrahigh-Vacuum. *J. Chem. Phys.* **1993**, *98*, 678.

(66)    Balzer, F.; Gerlach, R.; Polanski, G.; Rubahn, H. G. Chain Length Dependence of the Structure of Alkane Thiol Films on Au(111). *Chem. Phys. Lett.* **1997**, *274*, 145.

(67)    Roper, M. G.; Skegg, M. P.; Fisher, C. J.; Lee, J. J.; Dhanak, V. R.; Woodruff, D. P.; Jones, R. G. Atop Adsorption Site of Sulphur Head Groups in Gold-Thiolate Self-Assembled Monolayers. *Chem. Phys. Lett.* **2004**, *389*, 87.

(68)    Shimada, T.; Kondoh, H.; Nakai, I.; Nagasaka, M.; Yokota, R.; Amemiya, K.; Ohta, T. Structural Study of Hexanethiolate on Au(111) in the 'Striped' Phase. *Chem. Phys. Lett.* **2005**, *406*, 232.

(69)    Kondoh, H.; Iwasaki, M.; Shimada, T.; Amemiya, K.; Yokoyama, T.; Ohta, T.; Shimomura, M.; Kono, S. Adsorption of Thiolates to Singly Coordinated Sites on Au(111) Evidenced by Photoelectron Diffraction. *Phys. Rev. Lett.* **2003**, *90*, 066102.

(70)    Yourdshahyan, Y.; Rappe, A. M. Structure and Energetics of Alkanethiol Adsorption on the Au(111) Surface. *J. Chem. Phys.* **2002**, *117*, 825.

(71)    Molina, L. M.; Hammer, B. Theoretical Study of Thiol-Induced Reconstructions on the Au(111) Surface. *Chem. Phys. Lett.* **2002**, *360*, 264.

(72)    Maksymovych, P.; Sorescu, D. C.; Yates, J. J. T. Gold-Adatom-Mediated Bonding in Self-Assembled Short-Chain Alkanethiolate Species on the Au(111) Surface. *Phys. Rev. Lett.* **2006**, *97*, 146103.

(73)    Yu, M.; Bovet, N.; Satterley, C. J.; Bengio, S.; Lovelock, K. R. J.; Milligan, P. K.; Jones, R. G.; Woodruff, D. P.; Dhanak, V. True Nature of an Archetypal Self-Assembly System: Mobile Au-Thiolate Species on Au(111). *Phys. Rev. Lett.* **2006**, *97*, 166102.

(74)    Nagoya, A.; Morikawa, Y. Adsorption states of methylthiolate on the Au(111) surface. *J. Phys.-Condes. Matter* **2007**, *19*, 7.

(75)    Woodruff, D. P. The Role of Reconstruction in Self-Assembly of Alkylthiolate Monolayers on Coinage Metal Surfaces. *Appl. Surf. Sci.* **2007**, *254*, 76.

(76)    Gronbeck, H.; Hakkinen, H. Polymerization at the Alkylthiolate-Au(111) Interface. *J. Phys. Chem. B* **2007**, *111*, 3325.

(77)    Nagoya, A.; Morikawa, Y. Adsorption States of Methylthiolate on the Au(111) Surface. *J. Phys.-Condes. Matter* **2007**, *19*.

(78)    Wang, J. G.; Selloni, A. The c(4 × 2) Structure of Short-and Intermediate-Chain Length Alkanethiolate Monolayers on Au(111): A DFT Study. *J. Phys. Chem C* **2007**, *111*, 12149.

(79)    Chidsey, C. E. D.; Loiacono, D. N.; Sleator, T.; Nakahara, S. STM Study of the Surface Morphology of Gold on Mica. *Surf. Sci.* **1988**, *200*, 45.

(80)    Agilent Technologies Application Note, Hydrogen Flame Annealing. http://www.home.agilent.com/ (accessed May 2010).

(81)    Yaws, C. L. *The Yaws handbook of vapor pressure : Antoine coefficients*; Gulf Publication: Houston, Texas, 2007.

(82)    Cavalleri, O.; Hirstein, A.; Bucher, J. P.; Kern, K. Ordering Processes at the Decanethiol/Au(111) Interface. *Thin Solid Films* **1996**, *284*, 392.

# Chapter 3

## Atomically-Flat, Optically-Resonant Flat Gold Nanoparticles as Substrates for Scanning Tunneling Microscopy (STM) and Self-Assembled Monolayers (SAMs)

### 3.1 Abstract

Supported flat gold nanoparticles (FGNPs) are optically resonant substrates for high-resolution scanning tunneling microscopy (STM). These are atomically-flat single-crystal plates with large Au(111) faces that expose only two to four atomic layers at the surface. The nanoparticles (lateral size from tens to thousands of nanometers) are prepared using a modified solution growth technique and then deposited on indium tin oxide (ITO) coated glass substrates. Nanoparticles were characterized using STM, TEM, and SEM techniques. We demonstrate that FGNPs are excellent substrates for molecularly-resolved STM imaging of alkanethiolate self-assembled monolayers (SAMs).

## 3.2   Introduction

Nanophotonics is a developing nanoscale optical science and technology where light is confined and controlled on dimensions much smaller than its wavelength.[1-2] At the molecular scale, it takes the form of excited state energy flow between molecules such as in nature's photosynthetic systems and in artificially engineered molecules.[3-4] On slightly larger length scales, optically resonant structures such as metal nanoparticles can be used as nanophotonic antenna. Incident light (far-field) excites the plasmon resonance modes in the nanoparticle which have highly localized near-field modes that concentrate the incident optical energy near their surfaces. When molecules are located in the near-field region, this effect is responsible for surface enhanced fluorescence[4-8] and surface enhanced Raman scattering (SERS),[9-12] which are applications of the general concept of molecular plasmonics.[13] At even larger length scales, the coupled plasmon modes of nanoparticle arrays have been used to confine and to guide photonic energy to build plasmon optics.[14-17] The plasmon resonances of subwavelength metal apertures impart them with anomalous transmission characteristics,[18] and have been applied to create plasmonic lenses.[19]

Recently, shaped nanoparticles have attracted attention because of their application as photonic antennae.[20-22] Adjusting the nanoparticle shapes tunes the plasmon resonance frequency and controls the spatial structure of the near-field.[23] The very large SERS enhancements of $10^{14}$ observed in single molecule SERS experiments are thought to be due at least in part, to near-field hot spots around the particles.[24] Utilizing the local hot spots of shaped nanoparticles for nanophotonics will require precise placement of the molecular components at these positions as well as verification

70

of their location. The scanning tunneling microscope is ideally suited to image molecules in their local environment (Figure 3.1a), but typical nanoparticles have high curvature, therefore not flat enough for the STM to achieve molecular resolution where atomically flat terraces are required. Hence, the production and characterization of optically resonant atomically flat metallic nanoparticles that can be used as platforms for ordered self-assembled monolayers are important.

We establish methodology for growing atomically flat gold nanoparticles (FGNPs), depositing them onto indium tin oxide (ITO) coated glass supporting substrates, and coating the FGNPs with self-assembled monolayers (Figure 3.1b). The flat substrates will also be used for STM-based imaging of molecules and can be used for spatially precise excitation of molecules. These substrates offer the unique advantage that simultaneous structural and optical measurements can be made due to the FGNP's behavior as a photonic antenna. While the structural measurement can be performed with a variety of scanning probe techniques, STM provides the highest resolution, but also imposes the most stringent criteria on the substrate. The nanoparticle should be as thin as possible so that the STM feedback control can maintain the probe tip-sample distance while moving the probe tip from the supporting substrate to the particle. Stated another way, we need to be able to scan from the supporting substrate to the surface of the FGNP without crashing the tip of the STM into the edge of the particle. This is a practical consideration when scanning the ITO surface to find the particle. The greater the height difference, the slower the required scan rate. Even so, very abrupt changes in height, such as vertical edges can still be problematic.

The supporting substrate for the FGNPs must provide electrical contact for the STM tunneling current circuit but not quench the FGNP plasmon resonances. Thus the supporting substrate must be a both DC conductor and an optical insulator (optically transparent). The most commonly available material with this combination of properties is ITO coated glass. Although sputtered ITO coatings are not atomically flat, its function is only to make electrical contact to the FGNPs. As long as the grain structure is not so course or rough that the FGNPs cannot lie flat, it can be a satisfactory supporting substrate. Because we only require the nanoparticle to be atomically flat, the requirements for flatness of the conducting substrate are considerably relaxed. Molecules on the FGNP surface can be imaged by STM with molecular resolution so that the local nanometer-scale environment of the molecules can be known simultaneously with optical measurements. It should be noted that molecularly resolved STM images cannot be performed directly on the ITO surface because it is a polycrystalline sputtered thin film and does not exhibit atomically flat terraces. However it is flat enough to support the FGNPs which will play the role of an atomically flat gold raft on the rough ITO "sea." Thus this strategy can be applied generally to other polycrystalline or amorphous supporting substrates.
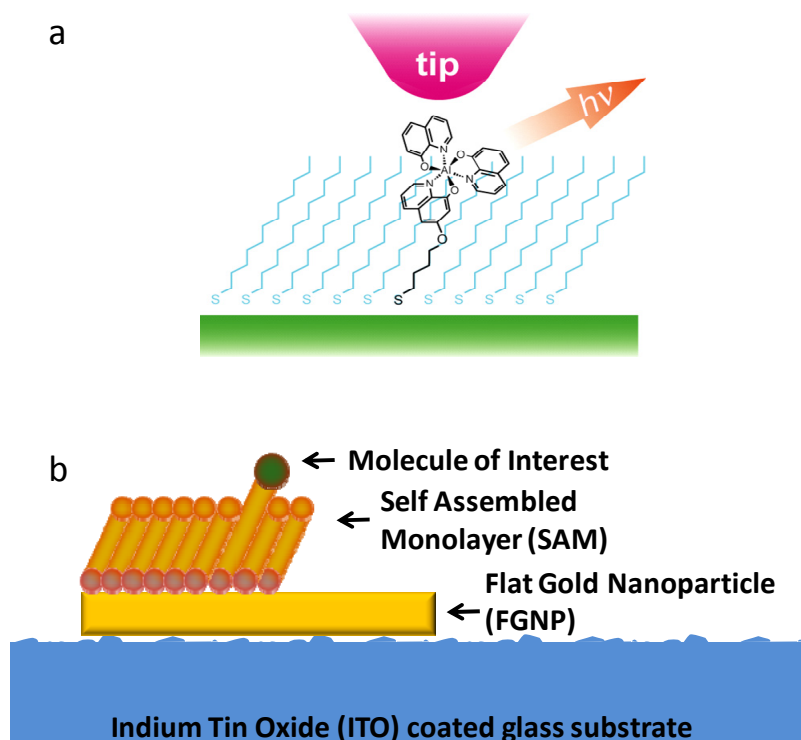
**Figure 3.1 A schematic of the FGNP/ITO substrate with SAMs**: a) a schematic of a molecule in the thiol matrix emitting light while it is being imaged with the STM, b) a cartoon of a cross section of a self assembled monolayer of molecules on a flat gold nanoparticle on an indium tin oxide coated glass substrate.

## 3.3   Materials and Methods

### 3.3.1   FGNP Preparation

FGNPs are prepared by adding 1.2 mL of 48 mM citric acid solution to 95 mL of 0.24 mM HAuCl$_4$ solution at 4 °C (refrigerator). The particles grow over a period of 3–4 days and produce large flat triangles, hexagons, and intermediate shapes such as truncated triangles along with spheroids. Particles with irregular shapes can be produced by adding 5 mL of 5 mg/mL polyvinylpyrrolidine (PVP) (MW 55000) to the initial mixture of solutions at the beginning.

### 3.3.2 FGNP Deposition on ITO Coated Glass

ITO coated glass substrates were obtained from Delta technologies and were cut to $6 \times 4$ mm pieces with a scribe before use. All ITO substrates were ultrasonically cleaned in detergent (Micro-90 catalog # 9032) and then in deionized water prior to use. The ITO substrates were placed ITO side up at the bottom of a test tube filled with the Au sol containing the FGNPs, and centrifuged in a swinging-bucket rotor for 10 min at 600–1500 g (min/max gs at the inner/outer radius, 2900 rpm) which is an IEC clinical centrifuge. Centrifugation deposits most of the particles in the column of solution onto the ITO surface. The resulting reddish brown layer of nanoparticles is visible by eye. Ultrasonication the sample in deionized water for at least 1 min removes the spheres and aggregates leaving a sparse coating where isolated FGNPs dominate (Figure 3.4).

### 3.3.3 TEM and SEM

TEM imaging were performed using a JEOL 2000-FX with 200 kV accelerating voltage. The copper TEM grids which were coated with carbon on one side and formvar on the other side were purchased from Ted Pella Inc (prod. # 01822 F). One drop of gold sol was put on the carbon coated side and let dry. The SEM is a JOEL JSM 880 with 15 kV accelerating voltage. No sample preparation is necessary as the substrate itself is conducting. Electrical connection between the surface of the ITO and the copper boat is established with Ag paint.

### 3.3.4 Scanning Tunneling Microscope

The STM is a custom designed beetle-style scan head using RHK Technology SPM100 control electronics and XPM Pro control software. The current amplifier is an Axon CV4 head stage with custom interface electronics. Probe tips are clipped Pt-Ir (80:20) wire.

They were cut using precision wire cutters. When the tip wire is in place in the tip holder, the edge of the tip should be between $0.108 - 0.140$ inches from the edge of the tip holder. Tips that are too short will never reach the tunneling range while those too long will be crash onto the sample. Figure 3.2 is a schematic of the positions of the tip and the tip holder tube with respect to the scale in the eyepiece of the tip changing station at the magnification of 10×. STM images are typically recorded at $-1.0$ V sample bias and a 1.0 pA tunneling current.
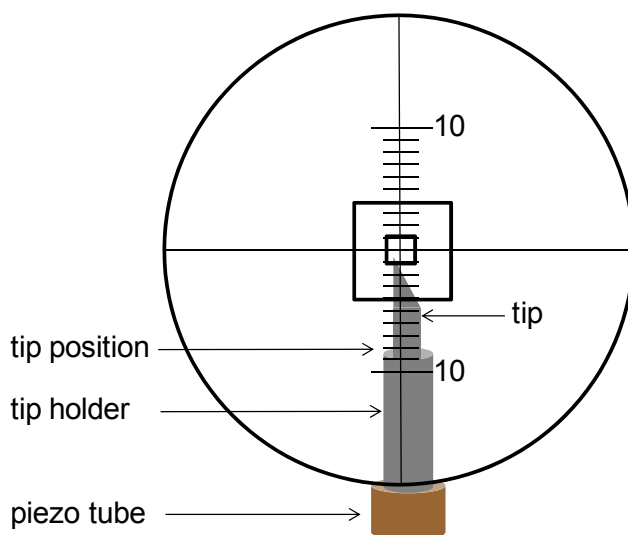


**Figure 3.2 A schematic of the position of the edge of the tip and the edge of the tip-holder with respect to the scale of the eyepiece of the tip-changing station at magnification of 10×.**

### 3.3.5 Single-Particle Dark-Field Spectroscopy

Single-particle dark-field spectroscopy was accomplished using a simple single-particle dark-field light-scattering spectrophotometer constructed by combining an epi-illuminated dark-field microscope (Nikon Eclipse ME600, 100X BD Plan ELWD NA 0.8) with a fiber coupled spectrometer (Ocean Optics HR2000) with the slits set for 23 nm bandwidth.

### 3.3.6 Zeta Meter Measurements

Zeta meter measurements were performed using a ZM3-83 zeta meter from Zeta-Meter Inc. The two solutions tested are 95 mL of 0.24 mM HAuCl4 + 5 ml of 48 mM citric acid (particles negatively charged) and 95 mL of 0.24 mM HAuCl4 + 0.2 ml of 48 mM citric acid (particles positively charged).

### 3.4 Results and Discussion

### 3.4.1 Growth of Flat Gold Nanoparticles

A wide variety of methods for growing shaped nanoparticles have been reported. Small single crystal cubo-octahedral nanoparticles can be grown in organic phase.[25] Nanorods can be grown in micelles.[26] Cubes, boxes, rings, and other shapes have been also demonstrated.[22,27-28] Large flat single-crystal FGNPs have been used in TEM studies since the early 1950s.[29-31] These FGNPs were prepared using a variety of methods most notably the reduction of $HAuCl_4$ by salicylic acid. Brüche performed a systematic study of FGNP growth via the reduction of $HAuCl_4$ by salicylic acid as a function of pH.[32] It was found that the largest FGNPs formed when the $HAuCl_4$ and salicylic acid were present in stoichiometric ratio and the pH was adjusted to ~2.5. These methods produced single crystal FGNPs in excess of 15 μm across. A later study by Turkevich investigated FGNP growth using a variety of reducing agents.[33] Recently FGNPs have been prepared using a stepwise growth process using gold nanoparticle seeds.[34-35] For reference, the standard Turkevich sol grown by reducing $HAuCl_4$ with sodium citrate at 100 °C produces only multiply-twinned spheroids.[36] Our own preparation is a variant of the standard sol, also described by Turkevich,[36] reducing $HAuCl_4$ with citric acid.[37] But the

ratio of flat particles to the spheroids is much higher in our method than the previously reported methods.

### 3.4.1.1 Proposed Models for Growth of Platelets

It has been shown in several studies that the large flat surface of platelets is Au(111) oriented.[38] Our TEM investigations also confirm those findings. In addition our studies of multiple dark-field TEM images show that the edges of large faces are parallel to the <110> and normal to the <211> directions (Figure 3.11, Figure 3.12, Figure 3.13). There are several explanations/models as to why platelets grow, from otherwise high symmetry fcc metal. The widely accepted hypothesis is given in Kirkland et al.[38] They model and hypothesize the existence of multiple twins parallel to the directions of planes.[39] Therefore the initial precursor nucleus has a unique axis. If a regular fcc tetrahedron is truncated on the <111> direction and twined by reflection on {111} surface, then it produces a suitable precursor for the growth of triangular platelet as seen in the Figure 3.3a. The reflection followed by a 30° rotation along the three fold axis will give rise to a precursor nucleus with six fold axis normal to the twin plane (Figure 3.3b). But in doing so, it eliminates the twin. Kirkland et al. suggests that such a precursor nucleus produces hexagonal shape platelet.

a                                                b
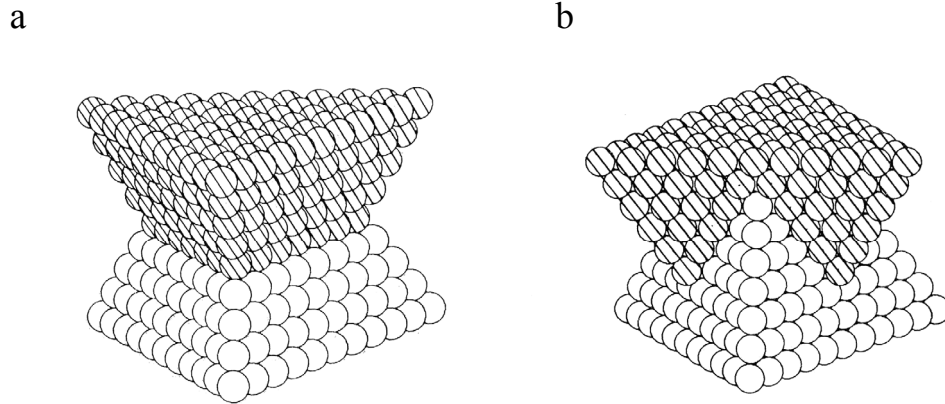


**Figure 3.3 A schematic representation of two proposed precursor nuclei**: a) the bi-tetrahedral precursor nucleus formed by reflection twinning of two fcc tetrahedra, b) an alternative precursor with a six-fold symmetry formed by reflection twinning and rotation by 30° of two fcc tetrahedra (Reprinted from Kirkland et al.[38]).

The presence of 1/3 422 spots (Figure 3.12) which are forbidden for perfect fcc structures in a {111} electron diffraction pattern is observed as an evidence to the presence of multiple twins in lamellar platelets. These patterns have been observed for both gold and silver platelets by many authors and numbers of explanations and models have been proposed. In these models the fcc structure is viewed as stacks of trigonal close-packed (111) layers along the [111] direction, which follows the stacking sequence of ABCABCABC..., where A, B, and C represent the three possible registrations of the close-packed planes. Those models can be summarized as follows.

Model 1: Forbidden 1/3 422 diffraction spots originates from truncation of the ABC stacking sequence along the [111] direction. When there are monatomic surface steps on the (111) surface, they result in a fractional unit cell along the [111] direction which in turn results in a fractional stacking period, e.g. ABCABC…AB.[40] This corresponds to perfect fcc stacking, but with the number of layers not an integer multiple of three. Model 2: This model hypothesizes the presence of a single twin parallel to the

78

(111) surface. Forbidden 1/3 422 reflection appears only if the number of atomic layers in (111) surface is not equal to 3n where n is an integer. The twin boundary in this case is not at the center of the crystal.[33,38]   Model 3: Regardless of number of (111) atomic layers, the presence of multiple twins on (111) planes causes the 1/3 422 reflections.[33,38] Model 4: When the twin boundary lies parallel to the surface and perpendicular to electron beam and if the twin boundary is in the center of the crystal (central twin), the 1/3 422 forbidden reflections and 3 422 fringes appear. The effect on the HRTEM image and the diffraction pattern caused by a twin in the fcc bicrystalline silicon nanowires has been reported.[41] Model 5: Insertion of an extra (111) layer, such as a B layer into the stacking sequence will produce a stacking fault of ABC(B)ABCABC---. Here the ABC(B)A is a twin-like thin slab. The forbidden 1/3 422 reflection appears due to the elongation of the reciprocal lattice points in the first order Laue zone.[42] Model 6: Surface reconstruction also may result in extra reflections.[43] Typically Au(111), surface reconstructions are only observed on clean surfaces. As we will discuss in the following sections, our particles are grown in solution and therefore the surfaces are covered by adsorbates, so we do not expect to observe any such reconstructions.

It is interesting that an fcc metal would grow in such a highly anisotropic manner if not constrained by micelles or other means. Extensive electron diffraction studies of Au and Ag particles have shown that they have stacking faults parallel to the large faces.[33,38] These defects are exposed at the edges of the growing nanoparticle and will be the fastest growth sites. A further clue to the growth mechanism is the remarkably uniform thickness of the FGNPs, which is uncorrelated with size (area) and shape which will be discussed later in this chapter. This supports the hypothesis that FGNPs grow from a narrow

population of seed particles with parallel stacking faults, where growth occurs preferentially at the edges. This hypothesis is further supported by Millstone, et al. who observed that the thickness of their FGNPs were approximately equal to the diameter of their seed particles.[34-35]

### 3.4.2 FGNPs on ITO Coated Glass
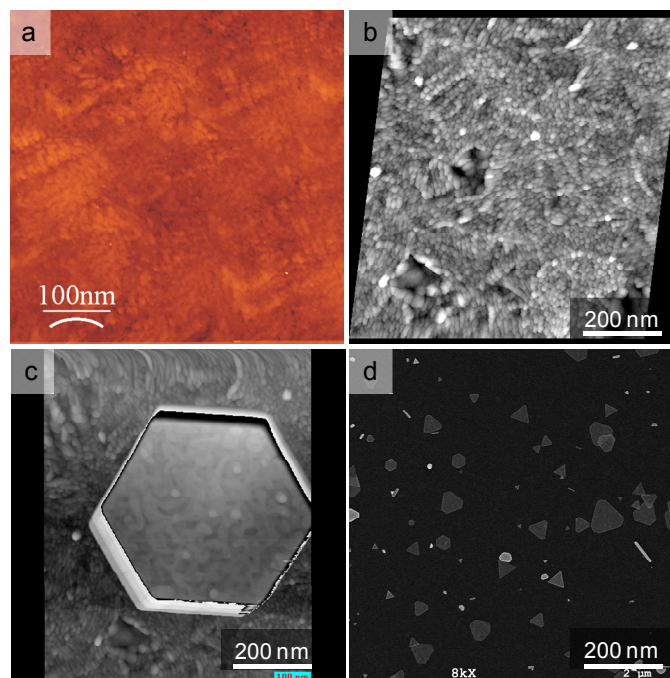


**Figure 3.4 Images of ITO, FGNP surfaces, and FGNP/ITO substrate:** a) AFM image of ITO surface, b) STM image of ITO surface, c) STM image of a hexagonal shaped particle on ITO surface, d) SEM image of FGNPs on ITO/Glass substrate which shows different shapes and sizes of FGNPs.
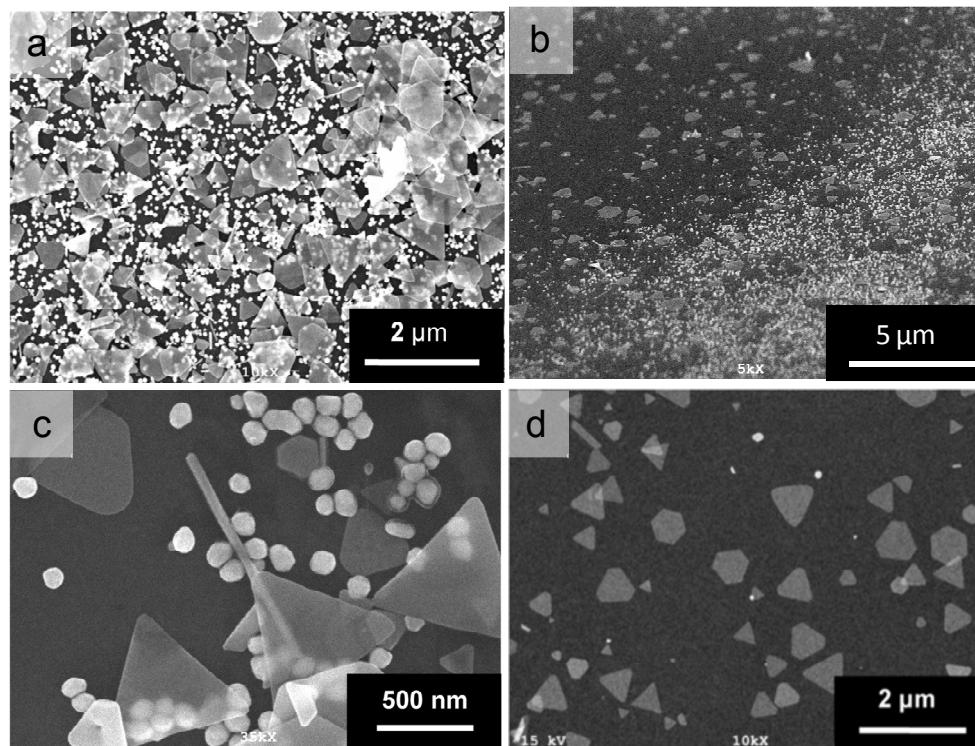
**Figure 3.5 SEM images of FGNPs ITO substrates**: a) the crude surface after deposition in the centrifuge, b) interrupted after 20 seconds of ultrasonication, c) close up showing FGNPs, spheres, and a rod. Note the thin single-crystal FGNPs are transparent to the electron beam, d) substrate free from spheres, aggregates, and poorly contacted FGNPs.

A previous study has shown that gold nanoparticles can be grown on ITO surfaces.[44] However the orientation of these crystals is not controlled. Because flat particles typically orient flat when deposited on a surface for simple mechanical reasons, our strategy was to simply deposit them on ITO coated glass.

The solution growth of the FGNPs produces a range of sizes and shapes. The usual 20–50 nm diameter multiple-twinned spheroids (spheres) outnumber the FGNPs. For our STM experiments we desire the FGNP fraction to dominate. Our initial work had focused on solution phase separation of the spheres from the FGNPs. This proved unnecessary because the spheres are easily removed after deposition on the ITO coated

glass. The resulting reddish brown layer of nanoparticles on the ITO surface is visible by eye. This is a very dense layer containing Au spheres, FGNPs, and aggregates (Figure3.4 a and b). Ultrasonication in deionized water for at least 1 min removes the spheres and aggregates leaving a sparse coating where isolated FGNPs dominate (Figure 3.4d). A few minutes of ultrasonication is generally enough to complete the process and longer ultra sonication times do not dramatically affect the results. We hypothesize that the FGNPs are more strongly bound to the ITO surface than the spheres due to their larger contact area. These substrates constitute our measurement ready samples. In addition to the ITO coated glass, we have also used the same procedure using other substrates such as glass and sapphire. However we will only focus on ITO coated glass substrates in this work.

The maximum size of the area that can be scanned by our STM is 4 μm × 4 μm. Only 2 μm × 2 μm area is survey scanned at a time. Therefore a good sample has at least one FGNP in each 2 μm × 2 μm area of the surface. The most rapid diagnostic screening procedure to determine the quality of the FGNP/ITO substrates proved to be dark-field microscopy (DFM) (Figure 3.6). Although only the largest FGNPs are optically resolved, all the FGNPs are visible, thus DFM is an excellent technique for confirming the density of FGNPs on ITO surface. The samples can be rapidly screened and do not require special sample mounting. If higher resolution was required SEM was employed.
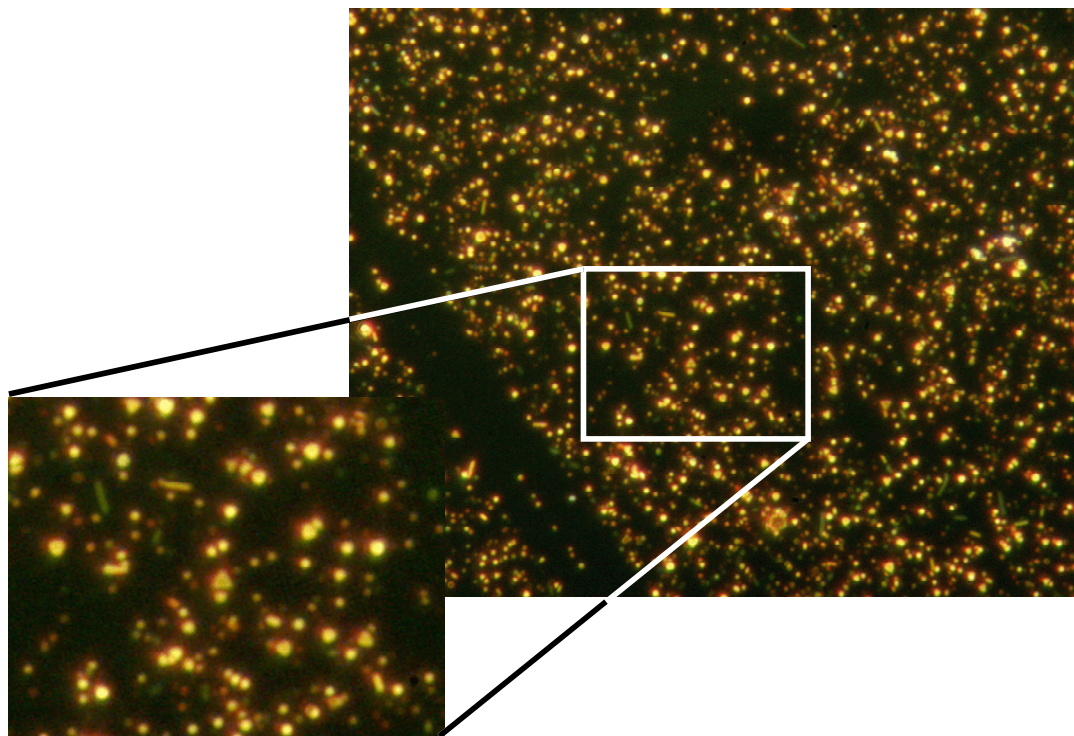
**Figure 3.6 Dark-Field micrograph of FGNPs on ITO** where different colors of particles according to their size and shapes are visible. (image size is 80 μm × 50 μm and inset is 24 μm × 14.5 μm).

For our work polydispersity of size and shape is an advantage, because we can easily choose the particles we want to study. We have varied the quantity of citric acid and found that the highest yield of well formed FGNPs occurs near the stoichiometric amount of citric acid described above (3:2, citric acid : HAuCl$_4$ , Figure 3.7). Less citric acid leads to particle defects (irregular shapes and particles with holes), while more produces a higher population of bipyramids and multiply-twinned spheroids. This agrees with the earlier work of Brüche using salicylic acid as the reducing agent.[32,45] From the Zeta meter measurements, we confirmed that the sign of the charge of the particles changes from negative to positive when the amount of citric acid added to the solution is changed from citric acid rich to citric acid deficient with respect to the stoichiometric amount. A solution with excess citrate produced particles that are negatively charged (adsorbed

citrate anions). A solution deficient in citrate (excess gold) should produced particles that are positively charged (adsorbed $Au^{+3}$), which we have confirmed by Zeta potential measurements.

$$AuCl_4 + 3e^- \rightarrow Au^0 + 4Cl^-$$

$$HOOCCH_2C(OH)(COOH)CH_2COOH \rightarrow HOOCCH_2C(O)CH_2COOH + 2H^+ + CO_2 + 2e^-$$

$$HOOCCH_2C(O)CH_2COOH \rightarrow CH_3C(O)CH_3 + 2CO_2$$
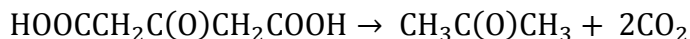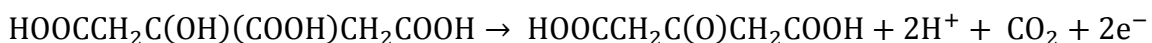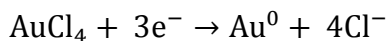
**Figure 3.7 The redox half reaction for the reduction of Au from HAuCl₄ by citric acid.**


### 3.4.3   STM Imaging
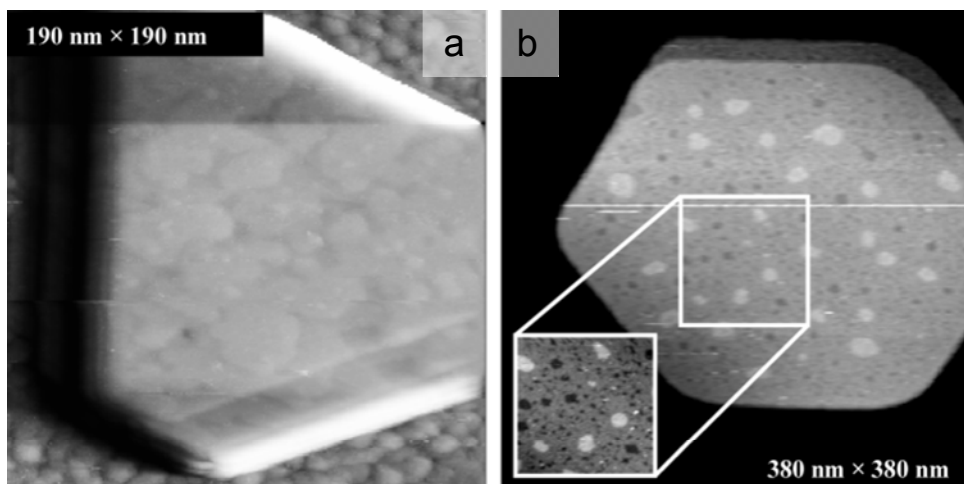


**Figure 3.8 STM images of atomic terraces on FGNPs:** a) a truncated triangular FGNP on ITO. The image has been processed to show simultaneously the topography on the FGNP and the ITO surfaces. b) a hexagonal FGNP on ITO. The image has been scaled to show the islands and vacancy islands on the surface of the FGNP. Both particles are covered with a decanethiol SAM. The steps visible at the FGNP edges are tip artifacts caused by the abrupt edge.

STM images of the FGNP/ITO substrates show that the terraces on the large {111} faces of the FGNPs are atomically flat (Figure 3.8 a and b). We observe that the FGNP {111} surfaces generally expose only 2–4 different atomic layers. The top most exposed layers are islands and the lowest exposed layers are vacancy islands. In all cases we have

observed, the island step edges are meandering steps. We only observe low index step edges at the FGNP edge. Furthermore the islands are distributed uniformly across the FGNP surface indicating that the thickness is uniform throughout the particle. Note that the ITO substrate is substantially rough at the nanometer scale (Figure 3.4 a and b). This is not surprising for a sputtered polycrystalline film. Despite the roughness of the ITO supporting substrate, the FGNPs remain flat for high quality STM imaging. The FGNPs shown in Figure 3.8 a, and b have decanethiol SAMs on their surfaces. High resolution images show that decanethiol forms well-ordered crystalline SAMs on FGNPs. Structural characterization of alkanethiol self assembled monolayers on FGNPs will be discussed later in this chapter and in chapter four.

We have also imaged FGNPs without the alkanethiolate SAMs. We presume the gold surfaces are covered by adsorbates such as citrate, because they are deposited from solution. The surface structure of the FGNP are similar in characteristic to the SAM covered FGNPs. However the quality of the images is lower. This is because citrate ions are disordered on the surface, in contrast to decanethiol SAMs. We attribute this difference to the displacement of adsorbed ions by the 1-decanthiol to create a more easily imaged, lower energy surface. This hypothesis is not necessarily true with adsobates such as polyvinylpyrolidine (PVP) a commonly used stabilizer for colloidal nanoparticles. Cleaning of such surfaces of FGNPs will be discussed in chapter four in more detail.

### 3.4.3.1 Tip Artifacts in STM Images

a

Tip moving direction

Tip 2

Tunneling current

Tip 1

Object being imaged

b

Same Surface reproduced by tip 2

Surface produced by tip 1

Image produced

c

400 nm

d

200 nm
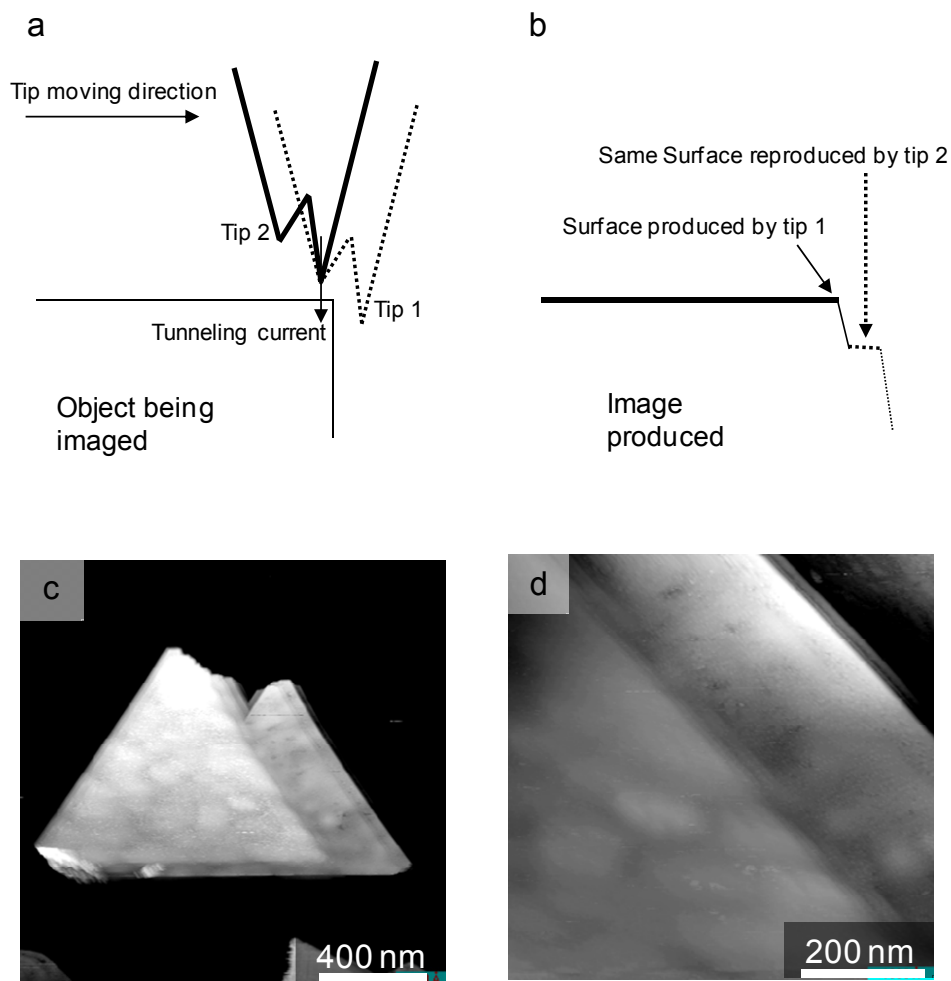
**Figure 3.9 Schematic diagram and STM images showing how multiple tips produce artifacts in STM images**: a) a sharp edge being imaged by a double tip, b) the topography produced by the two tips, c) an STM image of a triangular shaped particle produced by a double tip, d) high resolution image of the edge area.

The edges of the FGNPs are extremely sharp and steep. Because the FGNP surface falls away more steeply than the side of the STM probe tip, step like artifacts at the FGNP edges are produced (Figure 3.8). These are not steps in the surface of the FGNP, but rather the same edge imaged with different satellite tips of the master STM probe tip. Although the master tunneling tip is atomically sharp, it typically does not protrude more than a few atomic layers beyond the end of the gross probe tip structure. Very-steep

large-amplitude features like the FGNP edges are essentially a topographic step function. Indeed the sharpest edge transition we have measured in our imaging experiments dropped 15 nm from the FGNP surface to the ITO supporting substrate in about 1 nm. Thus, when the tip scans over the edge of the FGNP, the gross structure of the tip is revealed. In principle these FGNPs could be used to deconvolve the last 15 nm of the STM probe tip, we have not focused on this application. This is analogous to what is observed when the STM probe tip images an isolated molecule that protrudes above the surface; in this case the molecule is a topography delta function. That this is truly a tip artifact which can be verified by observing that identical surface features occur on each of the artifactural steps. An interesting application is that the same area can be imaged using different satellite-tips of the master probe tip. Thus if the master tip is bad, good images can often be obtained from one of the satellite-tips.

### 3.4.4 Effect of the Roughness of the ITO Substrate on the Large Scale Flatness of FGNP Surface
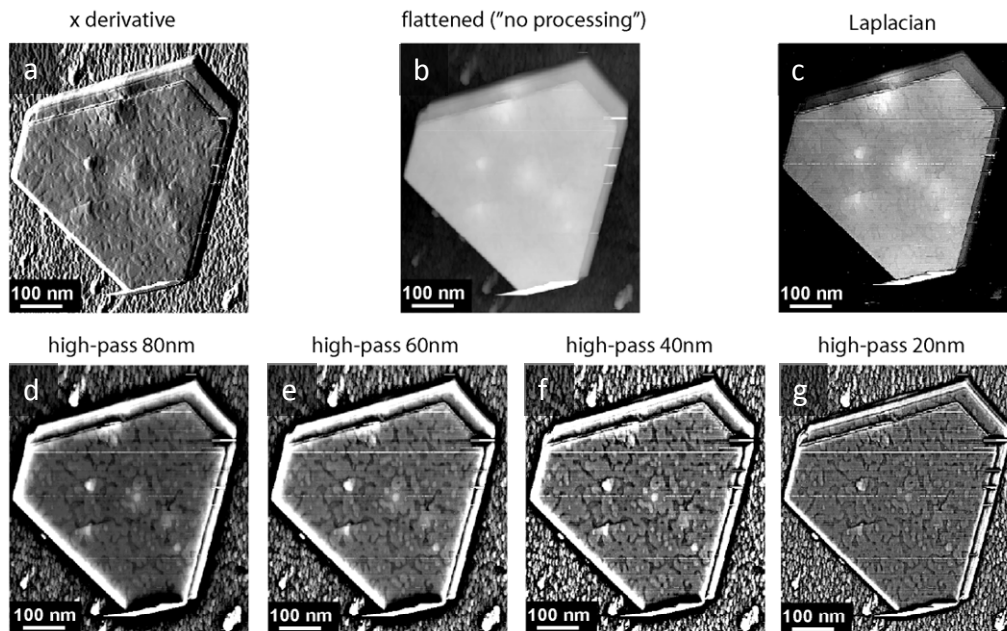


**Figure 3.10 Effect of the roughness of the ITO substrate on the large scale flatness of the FGNP surface revealed by different processing methods.** The bumps visible in the figures a–c are caused by the rough ITO surface as revealed in the high pass filtered images with different filters. Bumps are 2–3 nm in height with 2°–3° local slopes on 15 nm thick particle.

The ITO surface is rough on the nanometer scale, FGNPs are essentially atomically flat crystals. Figure 3.10 shows an FGNP on an ITO surface. The ITO surface can be seen to have asperities greater than 5 nm in the region surrounding the FGNP. The FGNP is also resting on similar asperities which cause it to bend. These create the high regions on the FGNP visible in the top row of imaging. We have determined that these are due to bending of the FGNP by the ITO rather than bumps inherent to the FGNP. The high spots are 2–3 nm high which will correspond to more than 10 atomic gold layers. If the particle was thicker in these areas, a series of atomic steps would be seen encircling these areas in the high-pass filtered images.

### 3.4.5 TEM and Crystallography
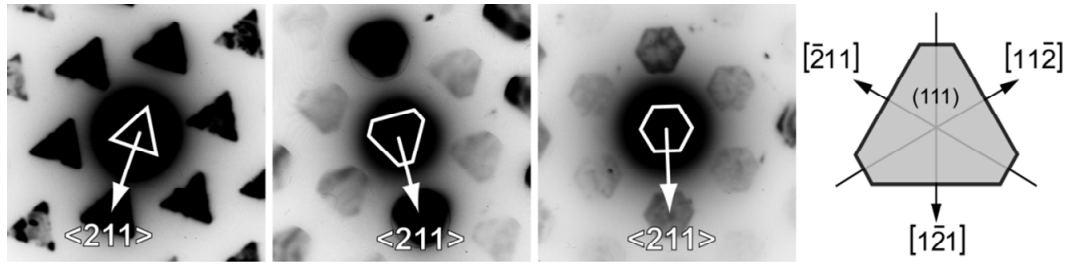


**Figure 3.11 In-focus multiple dark-field TEM images of the three dominant FGNP shapes, equilateral triangle, truncated triangle, and regular hexagon**. In each case the large face is {111} and the edges are normal to <211> directions. The schematic at the right show the crystallographic directions.
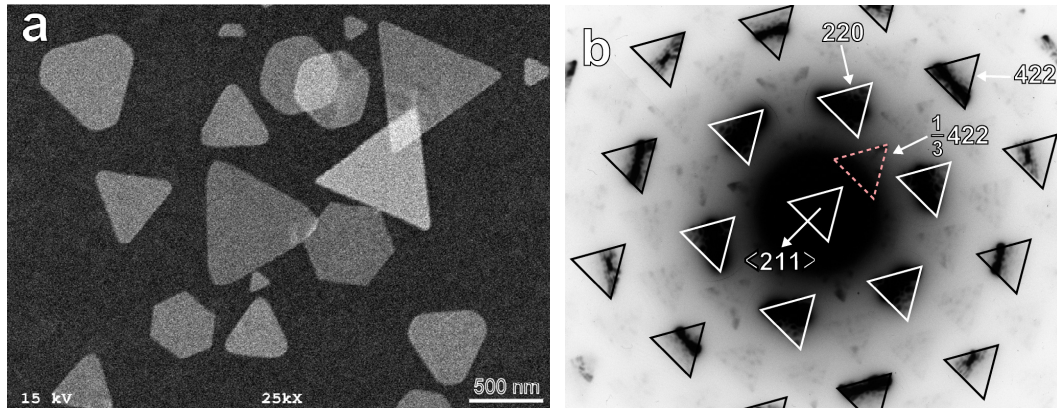


**Figure 3.12 SEM and multiple dark-field TEM image of FGNPs on ITO**: a) SEM image of flat gold nanoparticles deposited on an ITO coated glass substrate, b) in-focus multiple dark-field TEM image of a triangular shaped flat gold nanoparticle which shows the crystallographic orientation. The first ring of images, barely visible in the figure, are due to the normally forbidden 1/3 422 diffraction spots which appears in thin crystals.[33,38,40,46]
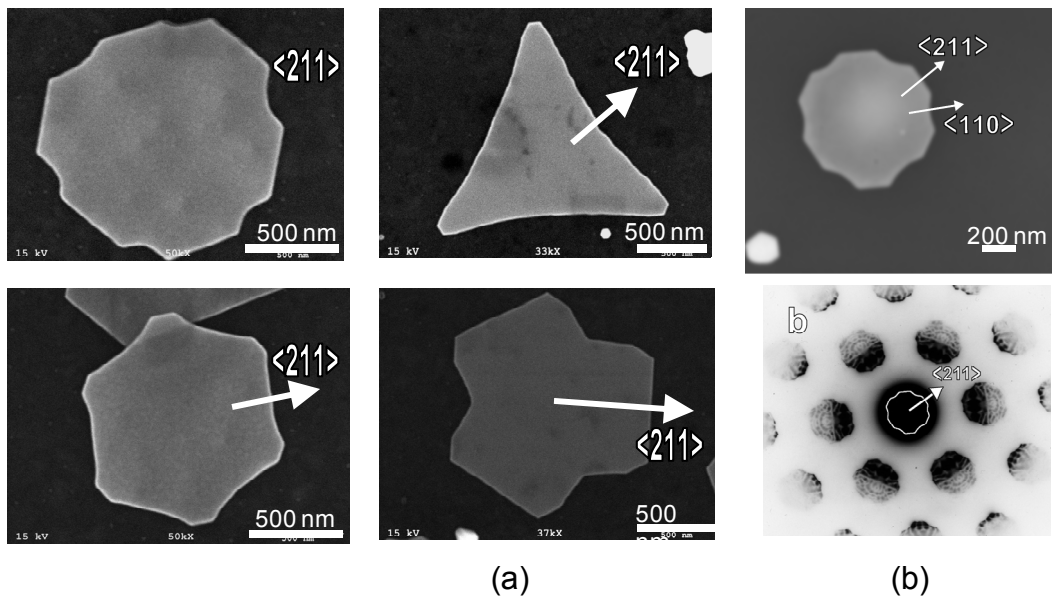
**Figure 3.13 SEM and multiple dark-field TEM images of PVP grown FGNPs:** a) SEM images of a PVP grown flat gold nanoparticles. b) TEM image and an in-focus multiple dark-field TEM image of a PVP grown particle which shows the crystallographic orientations of the faces.

Electron diffraction shows that the FGNPs are single crystals (Figure 3.11, Figure 3.12, Figure 3.13). The large faces are {111} and the edges are normal to <211> directions, which is consistent with prior work.[33,38] The first ring of images shown in the diffraction images are from the 1/3 422 reflections. We used in-focus multiple dark-field TEM imaging because each diffraction spot is a real space image of the particle and the orientation of each crystallographic direction with respect to the FGNP shape is clear. The contrast visible within the diffraction images of the particles is due to strain. Strain is commonly observed in these particles if they are not lying perfectly flat on the TEM grid. It is especially evident for FGNPs because they are quite thin and transparent to the electron beam.

### 3.4.6    FGNP Shape, Size, and Thickness

FGNP shape, size, and thickness were measured from the STM images. Our study was not intended to produce a statistical distribution, but to learn if there is a correlation between these parameters. Most of the particles measured have highly symmetrical shapes ranging from regular hexagons to equilateral triangles. The most frequently occurring shape was the symmetrically truncated equilateral triangle (Figure 3.14, Figure 3.15). The particles measured in this study ranged in size from 50 nm to 800 nm on a side. No correlation between size and shape was observed. Measurements of the particle thickness fell in a narrow range of 15–20 nm (60–80 atomic layers) and remarkably showed no correlation to size or shape of particles. Because we are interested in electronic measurements it is also interesting to note that the FGNP thickness is roughly one half the room temperature electron mean-free path (37 nm).[33,47] STM results of thickness agree with those obtained from TEM of shadowed samples. The thickness can also be gauged by the FGNP/ITO contrast in SEM images, where large number of FGNPs can be rapidly observed. We do observe some particles that are clearly thicker than the main population. No obvious difference in size and shape distinguishes them from the main population of thin particles. We emphasize that polydispersity is an asset for our experiments because we select individual particles to use for our measurements. The range of particle sizes and shapes facilitates size and shape dependence experiments. Fortuitously the most important parameter, thickness, is controlled within a narrow range.
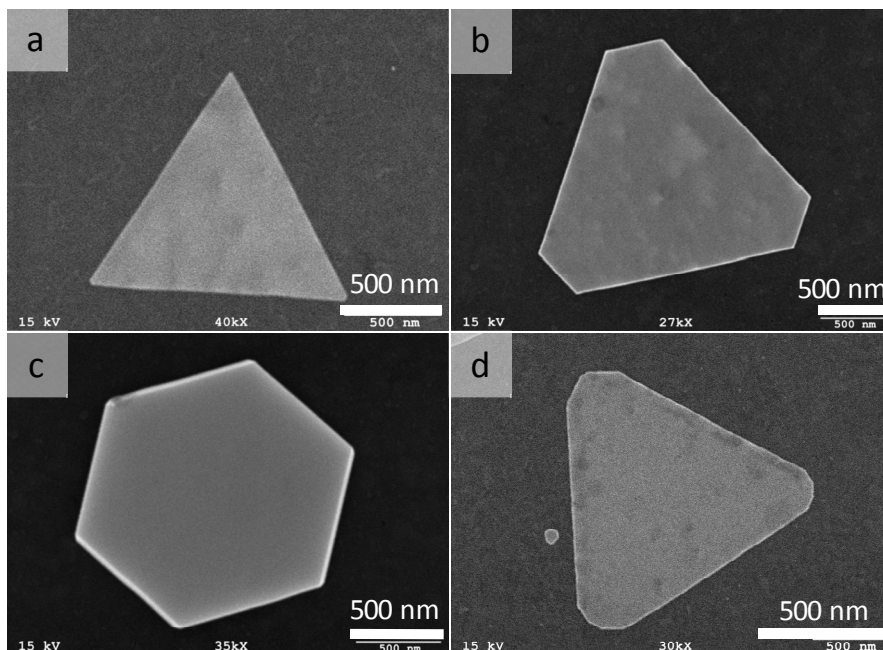
**Figure 3.14 SEM images of different shapes of flat nanoparticles found in the gold sol:** a) a triangle, b) a truncated triangle, c) a hexagon and, d) a triangle with rounded corners.
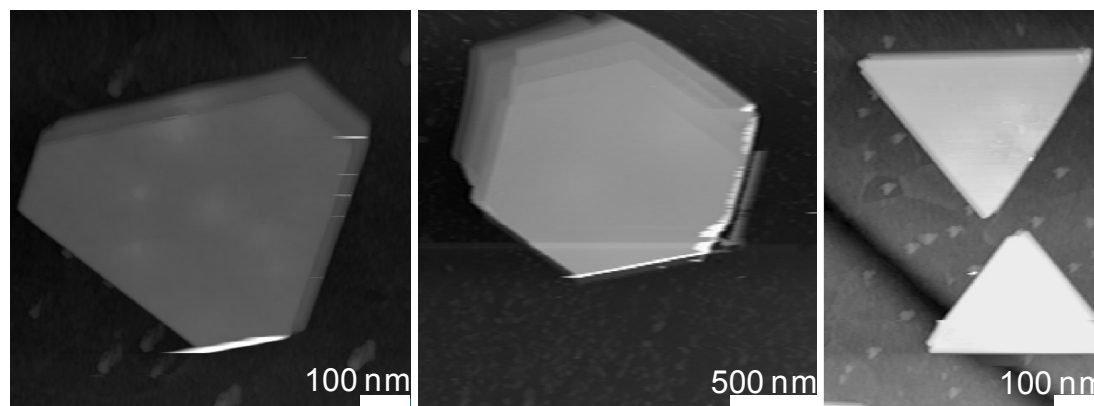


**Figure 3.15 STM images of different shapes of nanoparticles found in the gold sol:** a) truncated triangle, b) hexagon, and c) two perfect triangles.

Because the shapes range from equilateral triangles to regular hexagons through the intermediate truncated triangle shapes, we need to define our measurements carefully. For this study we made two measurements, the length of the longest side $L$, and the width

across the particle perpendicular to this edge *H* (geometric height). This is satisfactory for most of the particles, because they have very high symmetry. For the purpose of our measurement we defined the truncated triangle as an equilateral triangle with symmetrically snipped corners. Occasionally lower symmetry particles were observed and will be discussed separately. In addition to the variation in shape, there is also variation in the sharpness of the corners. For simplicity the rounding was not measured explicitly. Triangles with well rounded corners are counted as truncated triangles.

Figure 3.16 is a graph of geometric height versus length of particles. The symbols show the rough classification of the shape of each particle. We show for comparison the lines that constrain *L* and *H* for the high symmetry shapes hexagons (yellow), and equilateral triangles (green). The most frequently occurring shape is the truncated triangle. No correlation between size and shape is evident. The outlier FGNPs falling to the right of the equilateral triangle line are asymmetrically truncated triangles and elongated hexagons, which would require additional measurements for complete shape characterization. Thus shapes classified as hexagons, but appearing to the right of the regular hexagon line are elongated. Truncated triangles with one snip larger than the other two (trapezoids), will similarly appear to the right of the triangle line. The most highly asymmetric particles (not included in this study) have the appearance of rods but are elongated hexagons or trapezoids, distinguished on close inspection of the end facets. Note that even in these asymmetric particles, the angles between adjacent edges remain 120°, as expected from the crystallography.

The thicknesses of the FGNPs have also been measured from our STM images of the FGNP/ITO substrates. In Figure 3.17 we graph the thickness versus particle area. The

symbols designate the different particle shapes measured. The thickness of the particles is in the range of 15–20 nm, which corresponds to approximately 60–80 atomic layers. It is remarkable that there is no evident of correlation with the particle shape or area. Our STM results agree with those also obtained from TEM of shadowed samples.
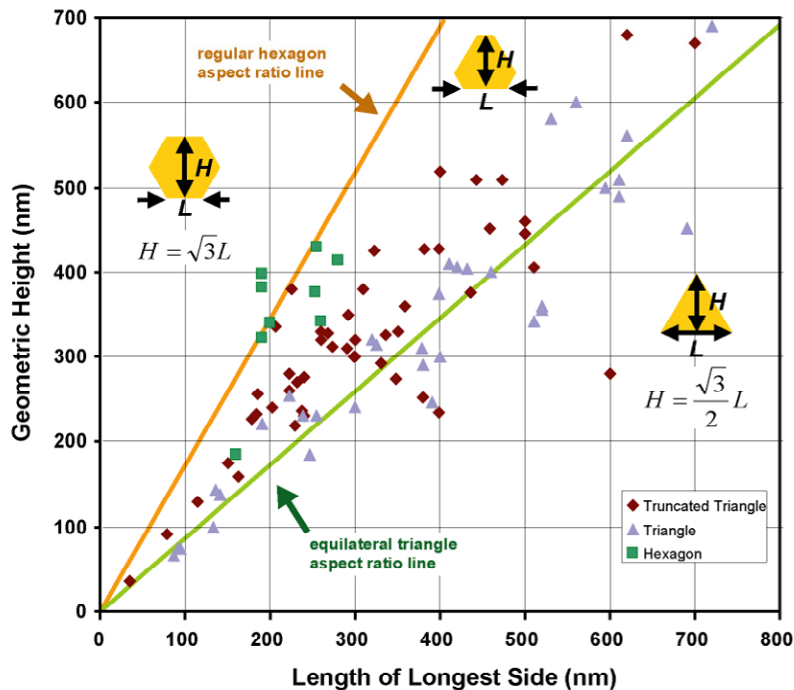


**Figure 3.16 Analysis of FGNP size and shape. A graph of the geometric height, _H_, versus the length of the longest side, _L_**, shows the distribution of FGNP shapes. The lines denote the _H/L_ aspect ratios for regular hexagons (yellow) and equilateral triangles (green). The symbols denote the particle shape, hexagon, truncated triangle, and triangle assigned by inspection. Asymmetric truncation causes the measured _H/L_ to deviate from the ideal position on the graph (see text).
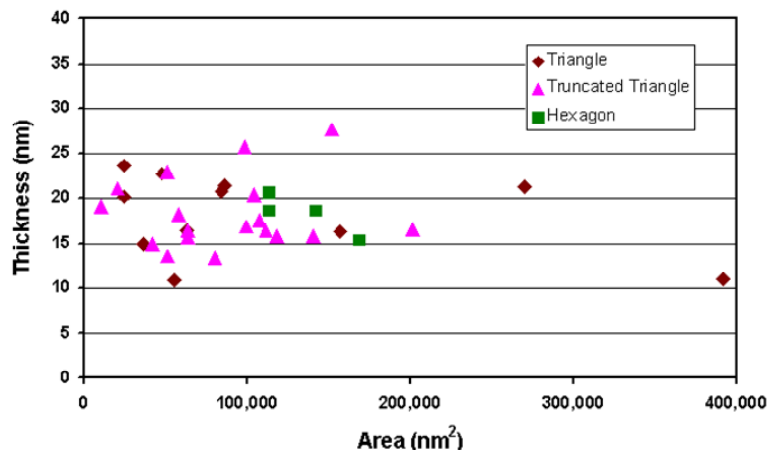
**Figure 3.17 Analysis of FGNP thickness. A graph of thickness versus area** shows that the FGNP thickness is controlled within a narrow range and that it is uncorrelated to the particle area. The symbols denote the particle shape, hexagon, truncated triangle, and triangle assigned by inspection. Note that there is also no apparent correlation of FGNP thickness with shape.

### 3.4.7   SAMs of Alkanethiol Molecules on FGNP/ITO Substrates

There has been considerable effort to study SAMs of alkanethiol and their derivatives on Au/mica(111) surface with STM. But very little attention has been drawn to study the SAMs of molecules on FGNP surfaces. Therefore it is important to study structural characteristics of SAMs of alkanethiols on FGNP surfaces and compare them to SAMs on Au/mica surfaces if FGNPs are to be used as atomically flat substrates for STM studies.

Characteristics of the SAM structure depend on the deposition conditions, growth temperature, and the concentration of alkanethiol. SAMs grown at room temperature from 1 mM solutions in ethanol form well ordered ($\sqrt{3} \times \sqrt{3}$)R30° structures with many structural domain boundaries, vacancy islands, and disordered regions with missing molecules. SAMs grown on FGNPs under similar conditions show the features (Figure 3.18). The deposition temperature reduces the number of vacancy islands and increases

95

the molecular domain size. Growth of alkanethiol SAMs also increases the size of the Au terraces on FGNPs. Compare Figure 3.10 of the as grown FGNP (no SAMs) and FGNPs after SAM growth. Just as we have observed for Au/mica substrates, increasing the growth temperature produces further smoothing of the FGNP. We will discuss this phenomenon in more detail in chapter four. At elevated temperatures the $(\sqrt{3} \times 4\sqrt{3})R30°$ striped-phase is also observed on FGNPs (see chapter two). FGNPs are nanometer-scale single crystal substrates suitable for alkanethiol. SAMs behave in the same way as they do on Au/mica surfaces.
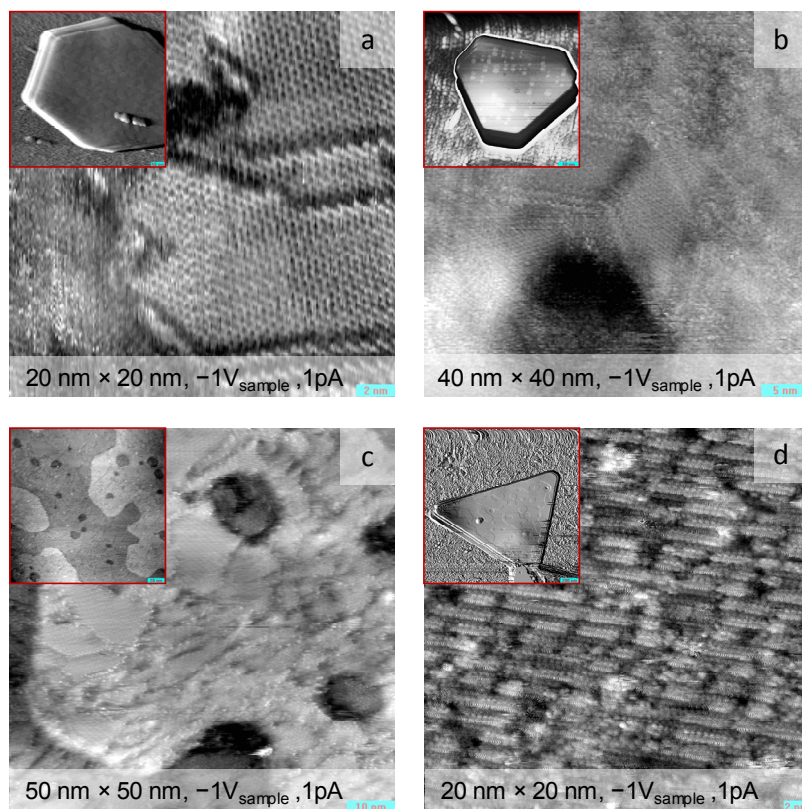


**Figure 3.18 1-decanethiol SAMs on FGNPs with different growth temperatures:** 1-decanethiol deposited from 1 mM solution at a) room temperature, b) 60 °C, c) 90 °C, d) 110 °C.

It is reasonable to assume that the as-grown FGNP surfaces are covered by citrate ions because they are negatively charged. Therefore the quality of the images of room

temperature deposited SAM is lower than the high temperature SAMs or SAMs on treated FGNPs which will be discussed in chapter four. The quality of the SAM layer depends on the ability of the alkanethiol molecules to replace the citrate ions.

As we showed in the chapter two, high temperature stripes of the striped-phase on Au(111)/mica surface are in <211> directions. They force the Au steps to rearrange such that they form low index step edges. The stripes on FGNPs also are in <211> directions as evidenced in the Figure 3.19c and d. We did not observed any low index step edges of terraces on FGNPs. The question of whether striped-phase alkanethiol does not promote the steps on FGNPs to convert to low index steps is open for further study.
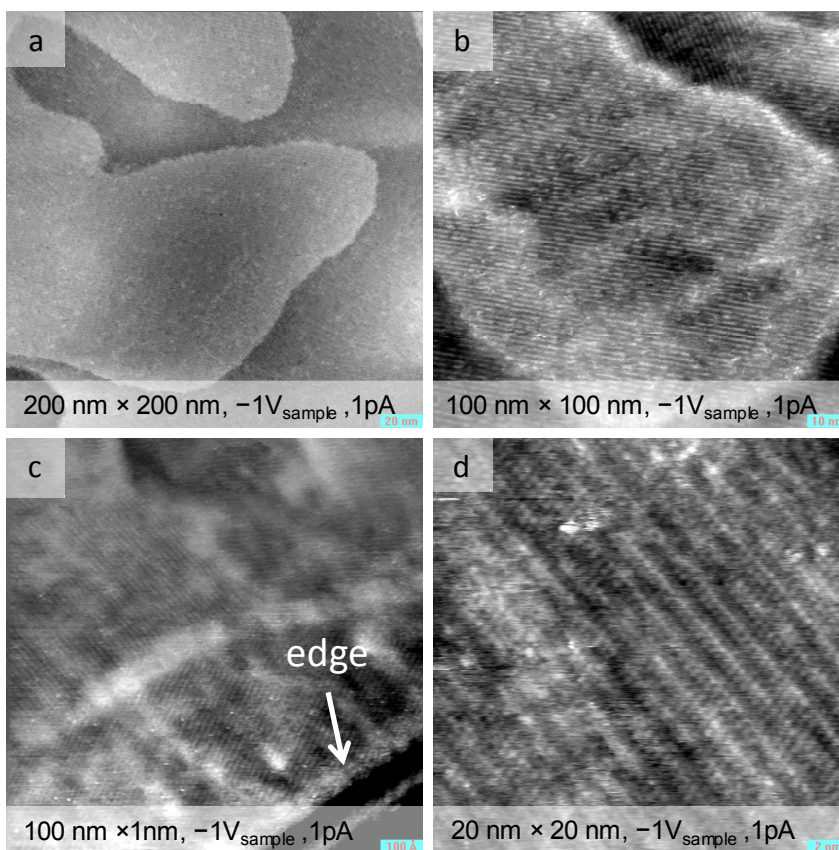


**Figure 3.19 STM images of terraces and high temperature stripe structure on FGNP:** a) terraces on an FGNP, b) stripes of decanethiol on the FGNP surface of a, c) stripes of decanethiol molecules with respect to the edge of the FGNP, b) molecularly resolved image of the stripes in c. (We did not see any evidence for presence of low index step edges with striped-phase on FGNPs we studied).

### 3.4.8 Guest Molecules in Thiol Matrix

The alkanethiol SAM is used as a matrix to support and isolate the single molecules to be studied. Therefore it is important to optimize the conditions of deposition of guest molecules in the thiol matrix on the FGNPs. We found that these guest molecules can be co-deposited on the FGNPs. The Figure 3.21a shows tethered anthracene molecules co-adsorbed with octanethiol (C8) on the FGNP. The measured height deference between the top of the octanethiol layer and the tethered anthracene molecules is $67 \pm 10$ pm. It has been reported that the measured height deference of organic molecules with STM is only a half of the physical height difference.[48-49] We estimate the maximum physical height of the anthracene moiety above the C8 SAM to be 240 pm (Figure 3.21), which would correspond to 120 pm in STM. Thus we hypothesize that these anthracene molecules are rotated or bent with respect to the rest of the C8 molecules.
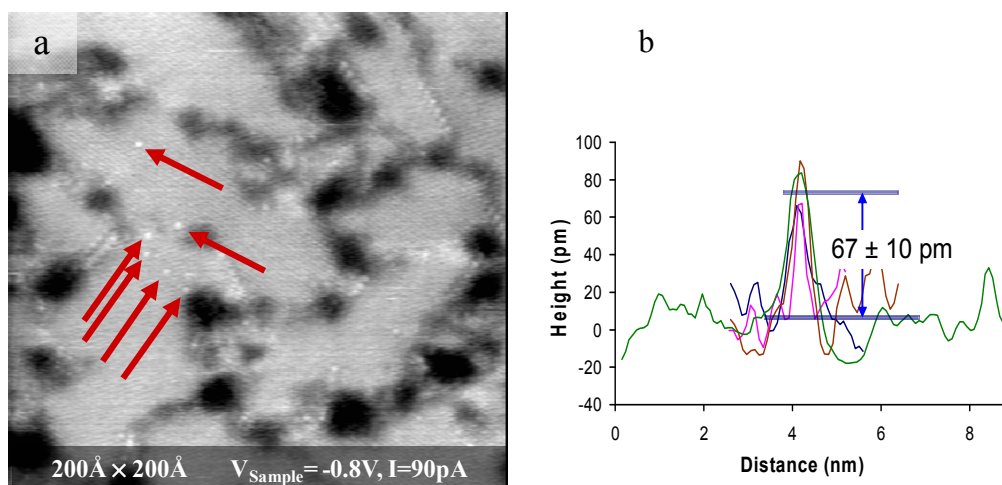


**Figure 3.20 STM image of tethered anthracene molecules co-adsorbed with the octanethiol on an FGNP (a)**, shown with red arrows (1 mM total octanethiol in EtOH, 90% octanethiol 10% tethered anthracene) and average height difference between the anthracene molecules and octanethiol layer (b).
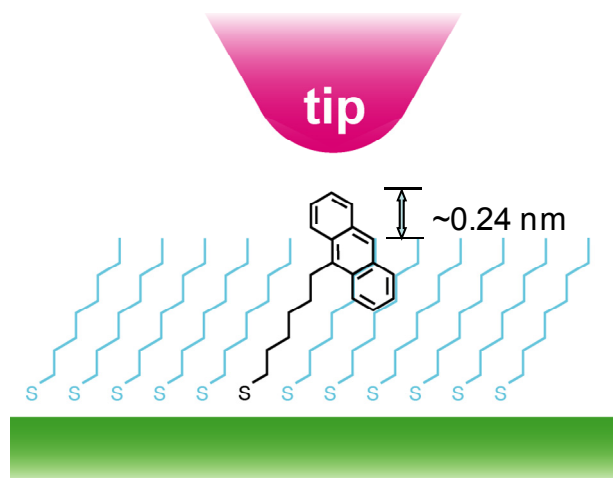
**Figure 3.21 A schematic diagram showing a tethered Anthracene molecule in the octanethiol matrix.**

### 3.4.9   Dark-Field Light-Scattering Spectroscopy
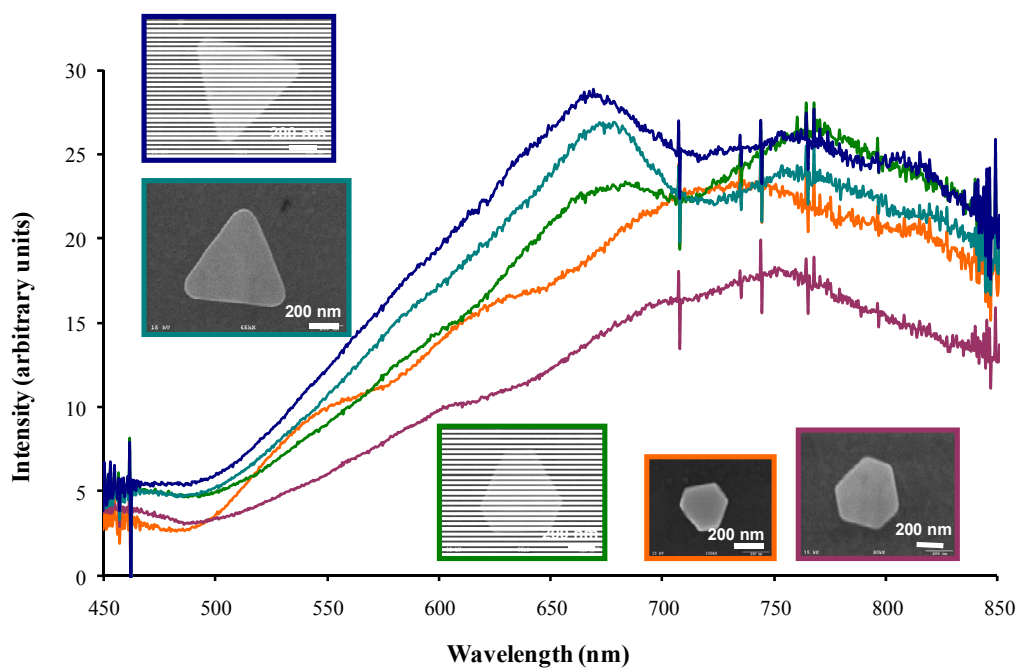


**Figure 3.22 Dark-field light scattering spectra of single FGNPs on ITO coated glass.** The color of the spectra matches the color of the frame of the SEM images of corresponding particles which they were measured.

Using FGNP/ITO substrates prepared such that the individual FGNPs can be resolved (a few microns apart), we can record spectra of the individual particles, Figure 3.22. Each of the spectra in Figure 3.22 are corresponds to the FGNP with the matching color of the frame. Our spectra show that there are two prominent peaks at about 675 nm and 775 nm for triangular shaped particles. When the particle is more hexagonal shape, the first peak at 675 nm disappears. We assign these peaks to the in-plane quadrupole mode observed by Millstone, et al.[34] Note that the peak is more red shifted for larger particles (orange and red color spectra). This is in agreement with the theoretical calculations of Shuford et at.[50] Furthermore, the scattering spectra of spherical FGNPs (Turkevich standard citrate sol) deposited on ITO coated glass exhibit resonances that are distinctly further into the green (550-600 nm range).[36,51]

## 3.5 Conclusion

In summary, FGNP/ITO substrates are optically-resonant atomically-flat Au(111) substrates suitable for STM studies. They offer the unique advantage that simultaneous structural and optical measurements can be made with the aid of FGNP plasmon resonances. The atomically-flat single-crystal FGNPs allow high resolution STM imaging of molecular monolayers so that the local nanometer-scale environment and the exact position of the molecules can be known. Furthermore, the preparation we describe produces a highly disperse distribution of sizes and shapes, which have the very narrow range of particle thicknesses desired for STM imaging. This size/shape polydispersity makes it possible to perform a wide range of experiments on a single substrate by characterizing individually each particle of interest.

An added benefit is low cost, simple preparation, and broad applicability. These substrates are low cost compared to Au single crystals and commercial Au(111)/mica substrates.[4848,49] The preparation of the FGNP/ITO substrates employs basic wet chemical techniques and does not require costly specialized equipment as do Au(111)/mica substrates. These substrates can be applied broadly as inexpensive, "easy-to-prepare" Au(111) STM substrates. Although our emphasis has been to develop substrates that satisfy the very stringent requirements of high-resolution STM (electrically conductive, single crystalline, and atomically flat), these substrates can also be used for other SPM techniques (AFM, NSOM, etc.). If electrical conductivity is not required, other substrates such as glass or mica can be substituted. These substrates should prove valuable for a wide variety of SPM and optical experiments.

## 3.6   References for Chapter 3

(1)     Hutter, E.; Fendler, J. H. Exploitation of Localized Surface Plasmon Resonance. *Adv. Mater.* **2004**, *16*, 1685.

(2)     Lieber, C. M. Nanoscale Science and Technology: Building a Big Furture from Small Things. *MRS Bull.* **2003**, *28*, 486.

(3)     Swallen, S. F.; Kopelman, R.; Moore, J. S.; Devadoss, C. Dendrimer Photoantenna Supermolecules: Energetic Funnels, Exciton Hopping and Correlated Excimer Formation. *J. Mol. Struct.* **1999**, *486*, 585.

(4)     Lakowicz, J. R.; Shen, Y.; D'Aurita, S.; Malicka, J.; Fang, J.; Gryczynski, Z.; Gryczynski, I. Radiative Decay Engineering 2. Effects of Silver Island Films on Fluorescence Intensity, Lifetimes, and Resonance Energy Transfer. *Anal. Biochem.* **2002**, *301*, 261.

(5)     Lakowicz, J. R. Radiative Decay Engineering 3: Surface Plasmon-Coupled Directional Emission. *Anal. Biochem.* **2004**, *324*, 153.

(6)     Lakowicz, J. R. Radiative Decay Engineering 5: Metal-Enhanced Fluorescence and Plasmon Emission. *Anal. Biochem.* **2005**, *337*, 171.

(7)     Lakowicz, J. R. Radiative Decay Engineering: Biophysical and Biomedical Applications. *Anal. Biochem.* **2001**, *298*, 1.

(8)     Gryczynski, I.; Malicka, J.; Gryczynski, Z.; Lakowicz, J. R. Radiative Decay Engineering 4: Experimental Studies of Surface Plasmon-Coupled Directional Emission. *Anal. Biochem.* **2004**, *324*, 170.

(9)     Kelly, K. L.; Coronado, E.; Zhao, L. L.; Schatz, G. C. The Optical Properties of Metal Nanoparticles: The Influence of Size, Shape, and Dielectric Environment. *J. Phys. Chem. B* **2003**, *107*, 668.

(10)    Mock, J. J.; Barbic, M.; Smith, D. R.; Schultz, D. A.; Schultz, S. Shape Effects in Plasmon Resonance of Individual Colloidal Silver Nanoparticles. *J. Chem. Phys.* **2002**, *116*, 6755.

(11)    Kneipp, K.; Kneipp, H.; Itzkan, I.; Dasari, R. R.; Feld, M. S. Ultra Sensitive Chemical Analysis by Raman Spectroscopy. *Chem. Rev.* **1999**, *99*, 2957.

(12)    Campion, A.; Kambhampati, P. Surface-Enhanced Raman Scattering. *Chem. Soc. Rev.* **1998**, *27*, 241.

(13)    Van Duyne, R. P. Molecular Plasmonics. *Science* **2004**, *306*, 985.

(14)    Maier, S. A.; Kik, P. G.; Atwater, H. A.; Meltzer, S.; Harel, E.; Koel, B. E.; Requicha, A. A. G. Local Detection of Electromagnetic Energy Transport Below the Diffraction Limit in Metal Nanoparticle Plasmon Waveguides. *Nat. Mater.* **2003**, *2*, 229.

(15)    Yin, L.; Vlasko-Vlasov, V. K.; Pearson, J.; Hiller, J. M.; Hua, J.; Welp, U.; Brown, D. E.; Kimball, C. W. Subwavelength Focusing and Guiding of Surface Plasmons. *Nano Lett.* **2005**, *5*, 1399.

(16)    Liu, Z.; Steele, J. M.; Srituravanich, W.; Pikus, Y.; Sun, C.; Zhang, X. Focusing Surface Plasmons with a Plasmonic Lens. *Nano Lett.* **2005**, *5*, 1726.

(17)    Ditlbacher, H.; Krenn, J. R.; Schider, G.; Leitner, A.; Aussenegg, F. R. Two-Dimensional Optics with Surface Plasmon Polaritons. *Appl. Phys. Lett.* **2002**, *81*, 1762.

(18)    Ebbesen, T. W.; Lezec, H. J.; Ghaemi, H. F.; Thio, T.; Wolff, P. A. Extraordinary Optical Transmission Through Sub-Wavelength Hole Arrays. *Nature* **1998**, *391*, 667.

(19)    Lezec, H. J.; Degiron, A.; Devaux, E.; Linke, R. A.; Martin-Moreno, L.; Garcia-Vidal, F. J.; Ebbesen, T. W. Beaming Light from a Subwavelength Aperture. *Science* **2002**, *297*, 820.

(20)    Fromm, D. P.; Sundaramurthy, A.; Schuck, P. J.; Kino, G.; Moerner, W. E. Gap-Dependent Optical Coupling of Single "Bowtie" Nanoantennas Resonant in the Visible. *Nano Lett.* **2004**, *4*, 957.

(21)    Grober, R. D.; Schoelkopf, R. J.; Prober, D. E. Optical Antenna: Towards a Unity Efficiency Near-Field Optical Probe. *Appl. Phys. Lett.* **1997**, *70*, 1354.

(22)    Xia, Y.; Halas, N. J. Shape-Controlled Synthesis and Surface Plasmonic Properties of Metallic Nanostructures. *MRS Bull.* **2005**, *30*, 338.

(23)    Hao, E.; Schatz, G. C. Electromagnetic Fields Around Silver Nanoparticles and Dimers. *J. Chem. Phys.* **2004**, *120*, 357.

(24)    Nie, S.; Emory, S. R. Probing Single Molecules and Single Nanoparticles by Surface-Enhanced Raman Scattering. *Science* **1997**, *275*, 1102.

(25)    Brust, M.; Walker, M.; Bethell, D.; Schiffrin, D. J.; Whyman, R. Synthesis of Thiol-derivatized Gold Nanoparticles in a Two-phase Liquid-Liquid System. *J. Chem. Soc., Chem. Commun.* **1994**, 801.

(26)    Murphy, C. J.; Sau, T. K.; Gole, A.; Orendorff, C. J. Surfactant Directed Synthesis and Optical Properties of One-Dimesional Plasmonic Metallic Nanostructures. *MRS Bull.* **2005**, *30*, 349.

(27)    Sun, Y.; Xia, Y. Shape-Controlled Synthesis of Gold and Silver Nanoparticles. *Science* **2002**, *298*, 2176.

(28)    Kim, F.; Connor, S.; Song, H.; Kuykendall, T.; Yang, P. Platonic Gold Nanocrystals. *Angew. Chem., Int. Ed. Engl.* **2004**, *43*, 3673.

(29)    Suito, E.; Uyeda, N. Spiral Growth of Lamellar Single Crystal of Colloidal Gold. *J. Electron Microsc.* **1960**, *8*, 25.

(30)    Suito, E.; Uyeda, N. Study of Single Micro-Crystals of Gold by a Three-Stage Electron Microscope. *Proc. Japan Acad.* **1953**, *29*, 324.

(31)    Suito, E.; Uyeda, N. Study of the Thickness of Single Micro-Crystals of Gold by Electron Diffraction Method. *Proc. Japan Acad.* **1953**, *29*, 331.

(32)    Brüche, B. Über sehr dünne Goldeinkristall-Plättchen. *Kolloid-Z.* **1960**, *170*, 97.

(33)    Wales, D. J.; Kirkland, A. I.; Jefferson, D. A. Structure and Growth of Colloidal Metal Particles. *J. Chem. Phys.* **1989**, *91*, 603.

(34)    Millstone, J. E.; Park, S.; Shuford, K. L.; Qin, L.; Schatz, G. C.; Mirkin, C. A. Observation of a Quadrupole Plasmon Mode for a Colloidal Solution of Gold Nanoprisms. *J. Am. Chem. Soc.* **2005**, *127*, 5312.

(35)    Shankar, S. S.; Rai, A.; Ankamwar, B.; Singh, A.; Ahmad, A.; Sastry, M. Biological Synthesis of Triangular Gold Nanoprisms. *Nat. Mater.* **2004**, *3*, 482.

(36)    Frens, G. Controlled Nucleation for the Regulation of the Particle Size in Monodisperse Gold Suspensions. *Nat. Phys. Sci.* **1973**, *241*, 20.

(37)    Turkevich, J.; Stevenson, P. C.; Hillier, J. Study of the Nucleation and Growth Processes in the Synthesis of Colloidal Gold. *Discuss. Faraday Soc.* **1951**, *11*, 55.

(38)    Kirkland, A. I.; Jefferson, D. A.; Duff, D. G.; Edwards, P. P.; Gameson, I.; Johnson, B. F. G.; Smith, D. J. Structural Studies of Triangular Lamellar Particles of Gold and Silver. *Proc. R. Soc. London, Ser. A* **1993**, *440*, 589.

(39)    Aflatooni, K.; Gallup, G. A.; Burrow, P. D. Temporary Anion States of closo-Carboranes and Diethyl Carborane. *J. Phys. Chem. A* **2002**, *106*, 4703.

(40)    Cherns, D. Direct Resolution of Surface Atomic Steps by Transmission Electron Microscopy. *Philos. Mag.* **1974**, *30*, 549

(41)    Carim, A. H.; Lew, K.-K.; Redwing, J. M. Bicrystalline Silicon Nanowires. *Adv. Mater.* **2001**, *13*, 1489.

(42)    Pileni, M.-P. The Role of Soft Colloidal Templates in Controlling the Size and Shape of Inorganic Nanocrystals. *Nat. Mater.* **2003**, *2*, 145.

(43)    Heyraud, J. C.; Métois, J. J. Anomalous 422 Diffraction Spots from {111} Flat Gold Crystallites: (111) Surface Reconstruction and Moiré Fringes Between the Surface and the Bulk. *Surf. Sci.* **1980**, *100*, 519.

(44)    Zhang, J.; Kambayashi, M.; Oyama, M. Seed Mediated Growth of Gold Nanopartcles on Indium Tin Oxide Electrodes: Electrochemical Characterization and Evaluation. *Electroanalysis* **2005**, *17*, 408.

(45)    Chiang, Y. S.; Turkevich, J. Formation of Platelike Colloidal Gold. *J. Colloid Sci.* **1963**, *18*, 772.

(46)    Germain, V.; Li, J.; Ingert, D.; Wang, Z. L.; Pileni, M. P. Stacking Faults in Formation of Silver Nanodisks. *J. Phys. Chem. B* **2003**, *107*, 8717.

(47)    Erts, D.; Olin, H.; Ryen, L.; Olsson, E.; Thölén, A. Maxwell and Sharvin Conductance in Gold Point Contacts Investigated Using TEM-STM. *Phys. Rev. B* **2000**, *61*, 12725.

(48)    Chidsey, C. E. D.; Loiacono, D. N.; Sleator, T.; Nakahara, S. STM Study of the Surface Morphology of Gold on Mica. *Surf. Sci.* **1988**, *200*, 45.

(49)    Bumm, L. A.; Arnold, J. J.; Dunbar, T. D.; Allara, D. L.; Weiss, P. S. Electron Transfer Through Organic Molecules. *J. Phys. Chem. B* **1999**, *103*, 8122.

(50)    Shuford, K. L.; Ratner, M. A.; Schatz, G. C. Multipolar Excitation in Triangular Nanoprisms. *J. Chem. Phys.* **2005**, *123*, 114713.

(51)    Ohtsu, M.; Kobayashi, K.; Kawazoe, T.; Sangu, S.; Yatsui, T. Nanophotonics: Design, Fabrication, and Operation of Nanometric Devices Using Optical Near Fields. *IEEE J. Quantum Electron.* **2002**, *8*, 839.

# Chapter 4

## Surface Treatment of Supported Flat Gold Nanoparticles and Gold/Mica Substrates for Ordered Molecular Self Assembly: A Scanning Tunneling Microscopy Study

### 4.1 Abstract

Surface treatment techniques were used to prepare the surfaces of flat gold nanoparticles (FGNPs) supported on indium tin oxide coated glass substrates (ITO) and Au/mica substrates for high-resolution scanning tunneling microscopy (STM) of 1-decanethiol (C10) self assembled monolayers (SAMs). These techniques include $Ar/O_2$ and $H_2$ plasma treatments, dry thermal annealing, and exposures to $UV/O_3$ of the surfaces of supported FGNPs and standard Au/mica substrates prior to the formation of SAMs. Molecularly resolved images of high-quality SAMs with the characteristic $(\sqrt{3} \times \sqrt{3})R30°$ structure and related superstructures of C10 grown on the pretreated Au/mica and FGNP/ITO surfaces are presented. The rough surfaces induced by plasma treatment can be repaired either by dry thermal annealing the substrates or alkanethiol deposition on the Au surface at elevated temperatures. An STM analysis of the terrace sizes reveals a range of 6–28 nm on the $Ar/O_2$ plasma treated FGNP surfaces. About 6–7 atomic layers exposed to the surface are observed after plasma treatment compared to about 3–4 atomic layers of as prepared FGNPs. In contrast, $UV/O_3$ treated FGNPs show relatively larger terraces of about 16–48 nm compared to the $Ar/O_2$ treated surfaces. We find that all plasma treatments roughen the surface considerably more than $UV/O_3$. Further, a change in the surface morphology is observed for those FGNPs which alkanethiolate deposited at 110 °C in solution. The edges of particles became thicker than the middle of the particle.

The sizes of terraces are bigger and a particle consists of only 2–3 terraces. However, overall shape of the FGNPs remains unchanged till 180 °C where gross changes in the FGNP morphology begin. The results suggest the viability of surface treatment procedures to prepare the surface of FGNPs for molecular self assembly without changing appreciably the surface morphology.

## 4.2    Introduction

In the last 25 years, Au substrates have been widely used for studies related to engineering the self-assembly and functional characteristics of adsorbed alkanethiol molecules.[1-6] SAMs of alkanethiols and their derivatives on Au are not only useful as model systems from the viewpoint of basic surface science but also important for advanced technology applications in molecular electronics, nanophotonics, and optoelectronics.[1,7] Au substrates which are used in STM studies are typically Au{111} oriented thin films on mica or Au{111} surfaces of bulk single crystals.[8-14] The surface of Au needs to be atomically flat, or be composed of atomically flat terraces large enough (at least few nano meters across) for high resolution STM of SAMs.

Characteristics of the SAM layer depend on the substrate on which the molecules are deposited. Some applications of SAMs require highly ordered SAMs while others do not. Surface conditioning or treatment of the Au substrates to remove contamination is a key to achieve highly ordered SAMs. SAMs with poor structural order have ubiquitous carbonaceous and ionic contaminants adsorbed on Au.[15] Roughness on the nanometer scale can also lead to disordered SAMs.

Common procedures for treating Au surfaces include electrochemical oxidation,[16] immersion into a strongly oxidizing solutions such as piranha solution,[17] exposure to UV/O$_3$,[18] or plasma (O$_2$, H$_2$, Ar),[19] H$_2$ flame annealing and thermal annealing.[20] Sputtering also is typically employed to treat single crystal Au surfaces in UHV. The surface-conditioning induced morphological changes in the Au surface and their effect on SAMs has been studied by X-ray photoelectron spectroscopy (XPS), ellipsometry, and contact angle measurements.[12,15] Some of the procedures oxidize the Au surface and have

a detrimental effect on the packing quality of SAM.[12,15,21-24] STM has been used to examine the surface morphology.[15,23,25-27] However there are no reports using molecularly resolved STM imaging of the alkanethiol SAMs grown on treated or conditioned Au surfaces.

In chapter three we introduced ITO supported FGNPs as single crystal Au(111) substrates which offer the benefits of relatively simple preparation, inexpensive compared to Au single crystals or commercial Au/mica substrates, and broad applicability.[28] These nanoparticles have edge lengths much larger than their thickness and possess multipolar plasmon resonances.[29-33] We showed that FGNP/ITO substrates can be applied as single crystal atomically flat Au{111} substrates for SAM growth and subsequent STM imaging, as well as optically-resonant atomically-flat Au{111} substrates.[28] However, surface treatment or conditioning of FGNP/ITO substrates is required if the solution grown surface with adsorbents interfere with the subsequent experiments. For instance, solution grown FGNPs synthesized by the reduction of Au from $HAuCl_4$ with citric acid usually result in adsorbed citrate ions and/or surfactants to the particle surface.[34] While we have demonstrated that molecularly resolved STM images of alkanethiol SAMs on FGNP surfaces can be obtained when no surfactants are used during FGNP growth, no molecular resolution of SAMs could be obtained if the FGNPs were grown with polyvinylpyrolidine (PVP) or stabilized with PVP after their growth. We hypothesize that the small alkanethiol molecules cannot displace the larger polyelectrolyte molecules from the surface, as they do to other small molecules such as citrate. This is not to suggest that alkanethiol does not adsorb in the presence of PVP, only that the PVP is not displaced, thus interferes with STM imaging. We do not expect

molecularly resolved STM imaging of adsorbed PVP molecules because they should be highly disordered and fluxional, in contrast to the sterically locked alkanethiol molecules in a well-ordered SAM. Surface treatment of PVP-stabilized FGNPs with plasma of UV/$O_3$ is expected to decompose PVP molecules into much smaller components such as CO, $CO_2$ and $H_2O$ that are easily removed from the surface.

The knowledge of FGNP surface morphology or shape upon treatment is not available. Therefore a detailed investigation is required to understand the surface morphology, the terrace size and structure of these nanoparticles, and how they influence the formation of alkanethiol SAMs. FGNPs are ideal probes to study how vigorous the destructive/reconstructive process of atomic redistribution occurs on sub-micron size Au surfaces upon treatment. In the event of larger scale redistribution of Au atoms, the particle morphology is expected to change dramatically along with the formation of small Au islands in their vicinity. Dry techniques are more suitable for treatment of FGNP/ITO substrates compared to wet chemical processes due to the fact that the later bear the potential danger of contamination as well as possible degradation of ITO substrate induced by the reagents used.

The purpose of this chapter is to describe the systematic investigation of dry surface treatments of FGNP/ITO substrates on the using thermal annealing, Ar/$O_2$ plasma, $H_2$ plasma, and UV/$O_3$ exposure, and study of the surface morphology/terrace structure along and subsequent alkanethiol SAM growth. While the primary aim is to investigate viability of surface treatment techniques on FGNP/ITO substrates, a parallel investigation of the effects of treatment on the surface morphology, SAM growth and chemical state of the standard Au/mica substrates was also carried out. In this chapter, a

STM-based analysis of the surface atomic layers/terrace morphology of treated FGNPs that suggests the applicability of treatment techniques without changing appreciably the surface morphology of the nanoparticles is presented. Molecularly resolved STM imaging of well-ordered alkanethiol SAMs grown on treated PVP stabilized FGNPs and Au/mica substrates is also discussed.

## 4.3 Materials and Methods

### 4.3.1 Au/mica Substrates

Au/mica substrates (1.0 cm × 1.1 cm Au film on 1.4 cm × 1.1 cm mica sheet) were cut into four approximately equal pieces used in the present study were purchased from Agilent Technologies.

### 4.3.2 FGNP/ITO Substrates

FGNP/ITO substrates were prepared using the method described in chapter three.[28] Briefly, 95 mL of 0.27 mM HAuCl4 was mixed with 1.2 mL of 48 mM citric acid solution and kept at 4 °C for 4 days in a refrigerator. The growth process of FGNPs was complete in 4 days. FGNPs were then deposited onto ITO coated glass by centrifuging the FGNP solution in a test tube with the ITO/glass substrate at the bottom for ten minutes. In a second step, spherical Au particles and small aggregates of FGNPs were removed by ultra-sonication of the FGNP/ITO glass sample in DI water for 30–60 s depending on the sample. Dark-field microscopy is a relatively simple and fast method to check the readiness of the sample. If it still contains spherical particles after the first sonication, then the process of sonication can be continued until the surface is free of spherical particles. Normally the gold sol is good for two weeks after the growth is

complete. If one needs to use it after two weeks then 5 ml of (5 mg/mL, MW 55000) PVP should be added to the sol to prevent aggregation of particles.

### 4.3.3   Alkanethiol SAM Growth

SAMs of C10 were grown on Au(111) surfaces by immersing the substrate in 1mM C10/ethanol and 1 mM C10/1-butanol solution in PFA vials at room temperature and at elevated temperatures. The selection of the solvent depends on the deposition temperature. The boiling points of ethanol and 1-butanol are 78.4 °C and 117.2 °C respectively. Deposition time was 16 hours.

### 4.3.4   Scanning Tunneling Microscope

The STM used is a home-built beetle-style STM with RHK SPM 1000 control electronics. All the imaging was performed in dry $N_2$ at room temperature. A detailed description of the STM can be found in chapter two.

### 4.3.5   X-ray Photoelectron Spectroscopy

XPS spectra were obtained using the PHI 5800 Physical Electronics Photoelectron Spectrometer with monochromatised Al $K_{\alpha}$ X-ray radiation (1486.6 eV). The background pressure of the analysis chamber was $2 \times 10^{-8}$ Torr. Energy of electrons was measured using hemispherical analyzer. Pass energy of the analyzer was set at 187.85 eV. The carbon peak at 284.8 eV was used as a reference.

### 4.3.6   UV/O$_3$ Treatment

UV ozone treatment was carried out using Novascan PST-UVT temperature controlled UV surface decontamination system in ambient air. The UV light was switched on for 5 minutes and the sample was kept in the chamber for another 25 minutes for the reaction

to complete. The temperature during the treatment was kept at room temperature (substrate heater off) or at 50 °C depending on the experiment.

### 4.3.7 Plasma Treatment

Plasma treatment was carried out using a March Plasmod (capacitively coupled plasma cleaner). Ar/O$_2$ and H$_2$ plasma were used. The recipe followed for Ar/O$_2$ plasma is, Ar 5 min, 0.6 Torr at 50 W followed by O$_2$ 5 min, 0.6 Torr at 50 W.[35] The recipe followed for H$_2$ plasma is, H$_2$ 5 min, 0.6 Torr at 50 W.

### 4.3.8 Thermal Annealing of Substrates

FGNP/ITO samples were resting on a watch glass inside a temperature controlled oven for one hour at temperatures ranging from 120 °C to 250 °C during dry thermal annealing.

### 4.3.9 Terrace Size Analysis

Terrace size analysis of STM images was performed using the following procedure. Equally spaced horizontal and vertical reference lines were drawn on the STM image (Figure 4.1) and distances between each step edge were measured alone each line. These results were binned by terrace with to produce histogram. The bin frequencies were then normalized for image size to give a linear fractional coverage. This is the probability of finding flat regions (terraces) within the bin range travelling along a straight line in any direction.

$$linear\ fractional\ coverage = \frac{frequency \times bin\ value}{image\ width} \qquad (4.1)$$

114

200 nm × 200 nm, -1V, 0.85 pA
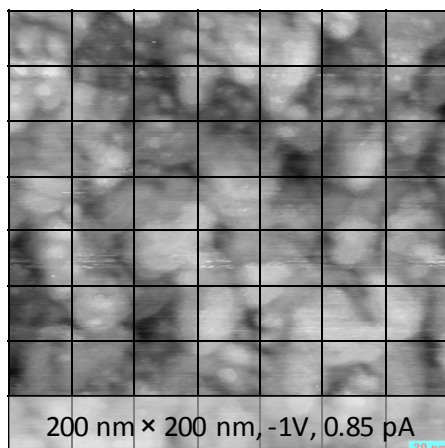
**Figure 4.1 Linear fractional coverage analysis; example with the analysis grid placed on an STM image.**

## 4.4   Results and Discussion

### 4.4.1   Plasma Treatment

#### 4.4.1.1   Ar/O$_2$ and H$_2$ Plasma Treatment of Au/mica Substrates

Ar/O$_2$ and H$_2$ plasma were employed to treat Au/mica substrates. X-ray photoelectron spectroscopy (XPS) was performed to study the chemical composition of treated substrates. STM images show that plasma treated Au surfaces are usually rough at the nanometer scale (Figure 4.2a). Thermal annealing after plasma treatment anneals the substrate forming well defined atomic terraces that are suitable for STM studies. Molecularly resolved STM images of the ($\sqrt{3}$ × $\sqrt{3}$)R30° structure and related superstructures of alkanethiols on Au(111)[36-39] could be obtained on Ar/O$_2$ plasma treated and thermally annealed Au/mica surface (Figure 4.2c). Similar STM images were obtained on H$_2$ plasma pretreated Au/Mica surface (Figure 4.2d) as well.
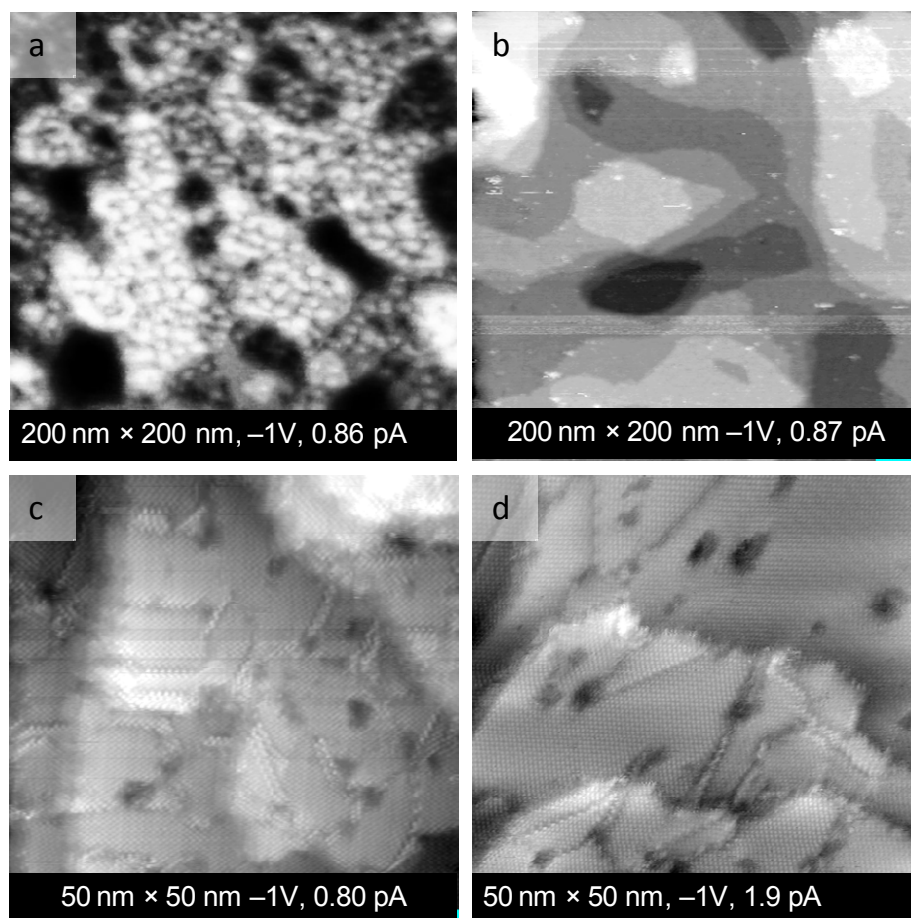
**Figure 4.2 STM images of Ar/O₂ and H₂ plasma treated Au/mica surfaces and SAMs deposited after the treatment:** a) after Ar/O$_2$ plasma treatment, b) after thermal annealing in air of Ar/O$_2$ treated sample at 150 °C, c) a higher resolution STM image after deposition of C10/EtOH SAM at room temperature on Ar/O$_2$ plasma and thermally treated Au/mica substrate showing a ($\sqrt{3} \times \sqrt{3}$)R30° structure, d) a high resolution STM image of C10 SAM on H$_2$ treated Au surface showing the ($\sqrt{3} \times \sqrt{3}$)R30° structure.

## 4.4.1.2 XPS Analysis of the Plasma Treated Au/mica Substrates

STM images of UV/O$_3$ treated samples shows some indication of formation of gold oxide on the surface. XPS elemental analysis was carried out on Ar/O$_2$, H$_2$, and UV/O$_3$ plasma treated Au/mica surfaces in order to examine the chemical composition of the treated Au surface. Figure 4.3 is XPS spectra of H$_2$, Ar/O$_2$, UV/O$_3$ plasma treated and untreated Au surfaces. Inconsistent with the earlier observation of gold oxide (Au$_x$O$_y$) formation during O$_2$ plasma treatment of gold,[12,23,27] we did not find any direct evidence of the presence of

gold oxide. According to the earlier reports,[22-23] presence of $Au_2O_3$ should give an additional peak at 85.7 eV in addition to the 84.03 eV and 87.7 eV regular Au 4f 7/2 peaks in the XPS spectrum. Our XPS results show absence of any additional gold peak (s) at 85.7 eV of the plasma treated samples ((Figure 4.3). We also did not find clear oxygen peaks at higher binding energies in the O 1s region of the corresponding XPS spectra (not shown here) that are normally found at around 531 eV and 529 eV. The peaks at 531 eV and 529 eV have been attributed to gold oxide and chemisorbed oxygen respectively.[12,21-23] Nevertheless, we do not exclude the possibility of the formation of gold oxide on the plasma treated Au/mica surface. Due to our experimental limitations, the XPS spectra could not be acquired immediately after the plasma treatment of Au/mica substrates. The time duration between the plasma treatment and the XPS scan was about 4 hours and there is a possibility that the gold oxide might have decomposed during this time.
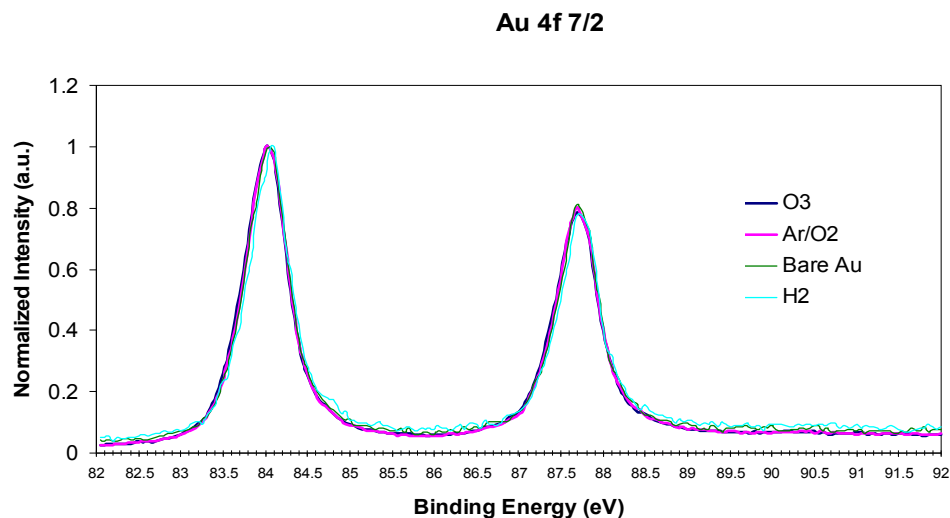


**Figure 4.3 XPS spectra of the Au 4f 7/2 peaks of four differently treated samples**: Dark blue line: UV/$O_3$ treated Au/mica, pink line: $Ar/O_2$ plasma treated Au/mica, green line: untreated Au/mica, light blue line: $H_2$ plasma treated Au/mica. Only peaks corresponding to metallic $Au^0$ were observed. No peaks corresponding to other oxidation states of Au were observed.

### 4.4.1.3 Ar/O₂ Plasma Treatment of FGNP/ITO Substrates and Terrace Width Analysis

Ar/$O_2$ plasma treatment of PVP-stabilized FGNP surface is expected to decompose the PVP molecules which are attached to the surface. The energetic species in the plasma react with the PVP to create small gaseous molecular compounds that are removed in the flowing gas. A terrace width analysis of Ar/$O_2$ plasma pretreated FGNP/ITO substrates was carried out. Figure 4.4 is STM images of the terrace structure on a typical FGNP before and after plasma treatment. Plasma treatment of FGNP substrates has created many small terraces on the surface.



100 nm × 100 nm, −0.36V, 0.86 pA     10 nm

200 nm × 200 nm, −1V, 0.85 pA     20 nm
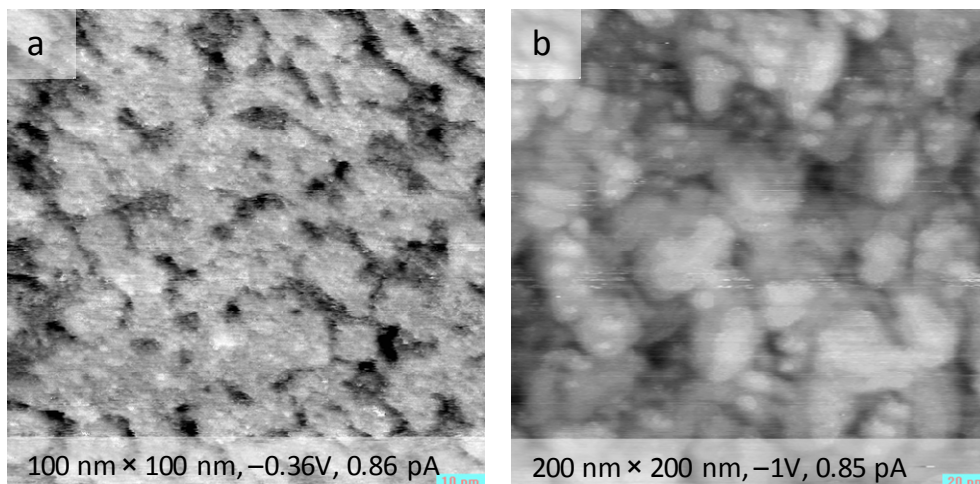
**Figure 4.4 STM images of the terrace structure on a FGNP:** a) before Ar/$O_2$ plasma treatment, b) after Ar/$O_2$ plasma treatment.

Significant changes in the surface morphology are observed after plasma treatment (Figure 4.4b). A detailed analysis of the terrace widths showed a range of 6–28 nm on the Ar/$O_2$ plasma treated FGNP surfaces (Figure 4.5). Due to the roughness, these surfaces were relatively difficult to image with STM at high resolution. They often display

artifacts due to multiple tips (Figure 4.4b). We observed 6–7 Au(111) atomic layers exposed at the surface after plasma treatment, compared to 3–4 atomic layers on the as prepared FGNPs. Further, the overall shape of the FGNPs remained unchanged after plasma treatment as verified by the scanning electron micrographs (Figure 4.6). Changes of the terrace morphology with temperature will be discussed in the next section.
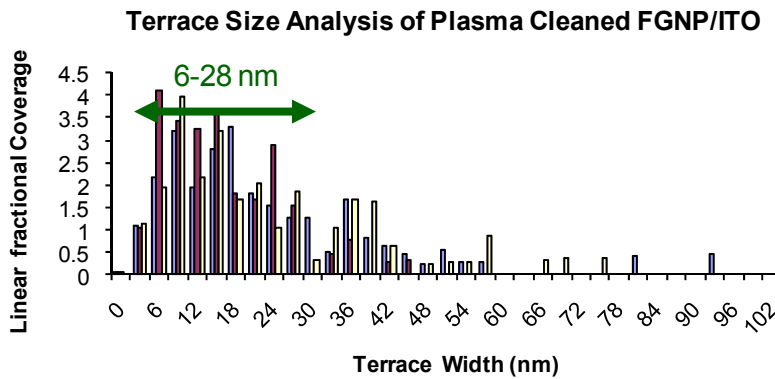


**Figure 4.5 A graph of linear fractional coverage vs. terrace width of plasma treated FGNPs.** The terraces widths range 6–28 nm. Three colors represent the three images analyzed.
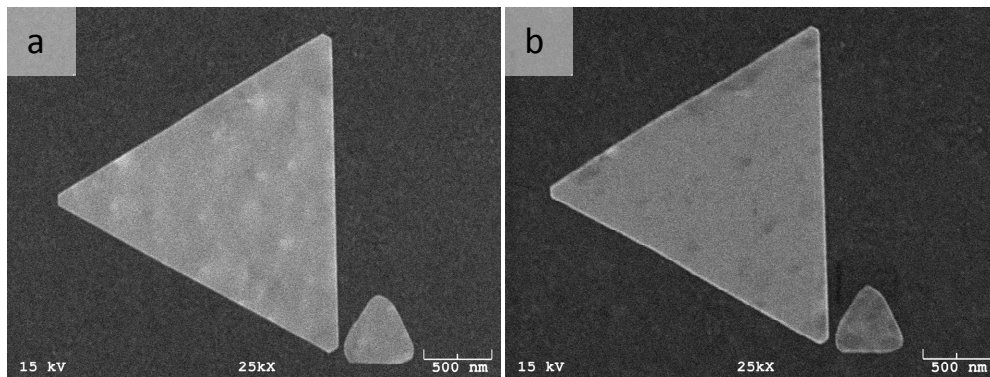


**Figure 4.6 SEM images of an FGNP a) before and b) after plasma treatment.**

### 4.4.1.4 Growth of Alkanethiol SAMs on Ar/O$_2$ Plasma Treated and Annealed FGNP Surfaces

Plasma treated FGNP substrates are rough at the nanometer scale. In this section we show that SAM growth at elevated temperatures smoothes the Au surface, by reducing the number of exposed Au layers and increasing the terrace width. This is attributed to the surface diffusion of gold atoms reported in earlier studies of gold films and bulk gold surfaces.[26,40-47] Porath et al.[41,48] states that surface diffusion is the main process for rearrangement of surface of annealed gold films below 300 °C. Lin et al. [43] studied the surface roughness with different annealing times. They reported a reduction of surface roughness with increased annealing time and temperature. This surface diffusion of atoms results in smoothing of the treated FGNP surface creating much larger terraces. Alkanethiol SAMs were grown on the plasma treated PVP-stabilized FGNP/ITO substrates in 1mM C10 solution in absolute ethanol at different temperatures. Figure 4.7 are STM images of the structure and sizes of terraces on plasma treated FGNP surfaces for various growth temperatures in C10 solution. The FGNP surface consists of small terraces just after plasma treatment (Figure 4.7a). Room temperature alkanethiol deposited FGNPs have larger terraces (Figure 4.7b) compared to the as treated FGNPs. The size of the terraces also increases with alkanethiol deposition temperature. These results are consistence with our results of high temperature alkanethiol deposition which we discussed in the chapter two. We see a thickening of edges of FGNP edges as the Au atoms diffuse from the edges onto the terraces at 110 °C. We attribute this to the early stages of the gross shape changes observed at much higher temperature, where the FGNP takes on a more compact shape (see section 0).
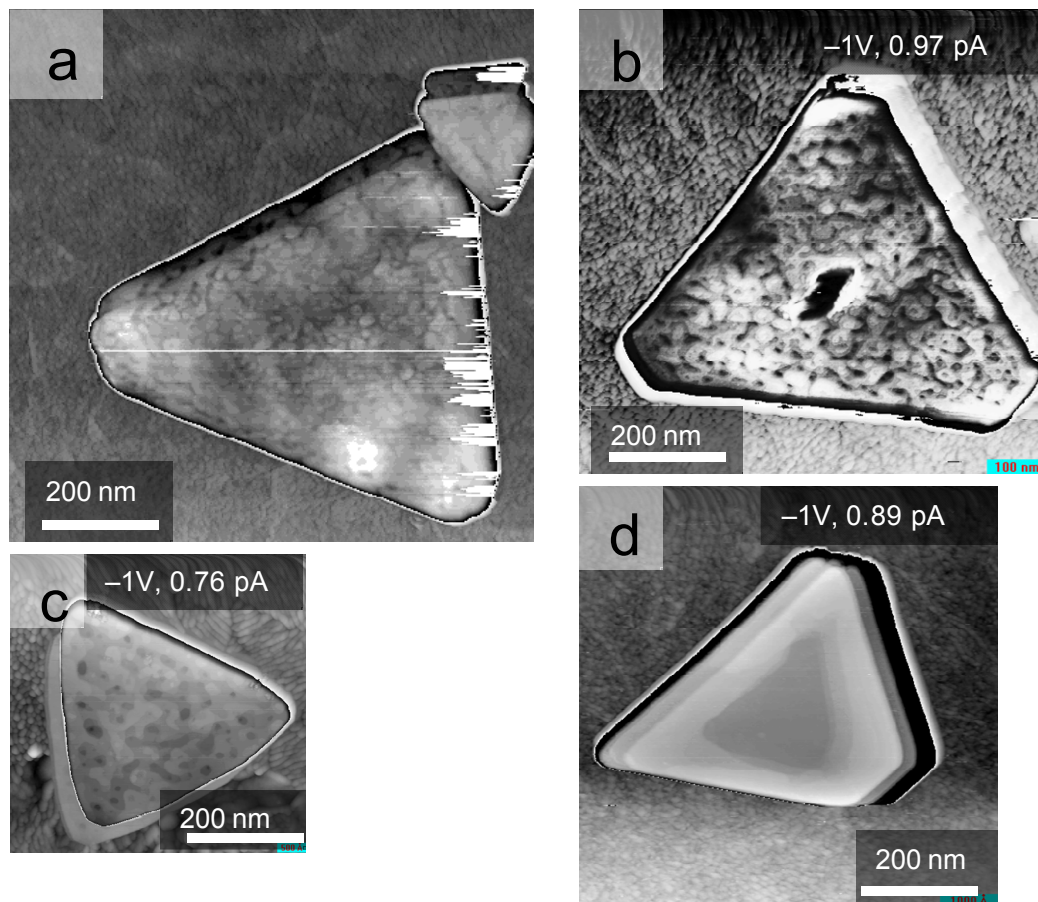
**Figure 4.7 STM images of a typical PVP-stabilized FGNP after Ar/O₂ plasma treatment and annealing in C10 solution** at various temperatures showing gradual increase in the terrace size with temperature: a) after the treatment, C10 deposition at b) at room temperature, c) at 60 °C, d) at 110 °C (The images are scaled to better represent the sizes of terraces).

The FGNP shown in Figure 4.8a is a plasma treated PVP-stabilized particle. Molecularly-resolved STM images of SAMs grown at 60 °C could be obtained on the FGNP (Figure 4.8 b, c, and d). The structural domain boundaries (blue arrow in Figure 4.8b) that are missing zig-zag rows of molecules oriented in Au<110> crystallographic directions—which are the same directions as the FGNP edges. The transition from the nano-roughness of the fresh plasma treated FGNP surfaces to the large terraces is dramatic and results in excellent quality SAMs for STM imaging. In this example no molecular resolved imaging was possible before removal of the PVP by Ar/O₂ plasma treatment.
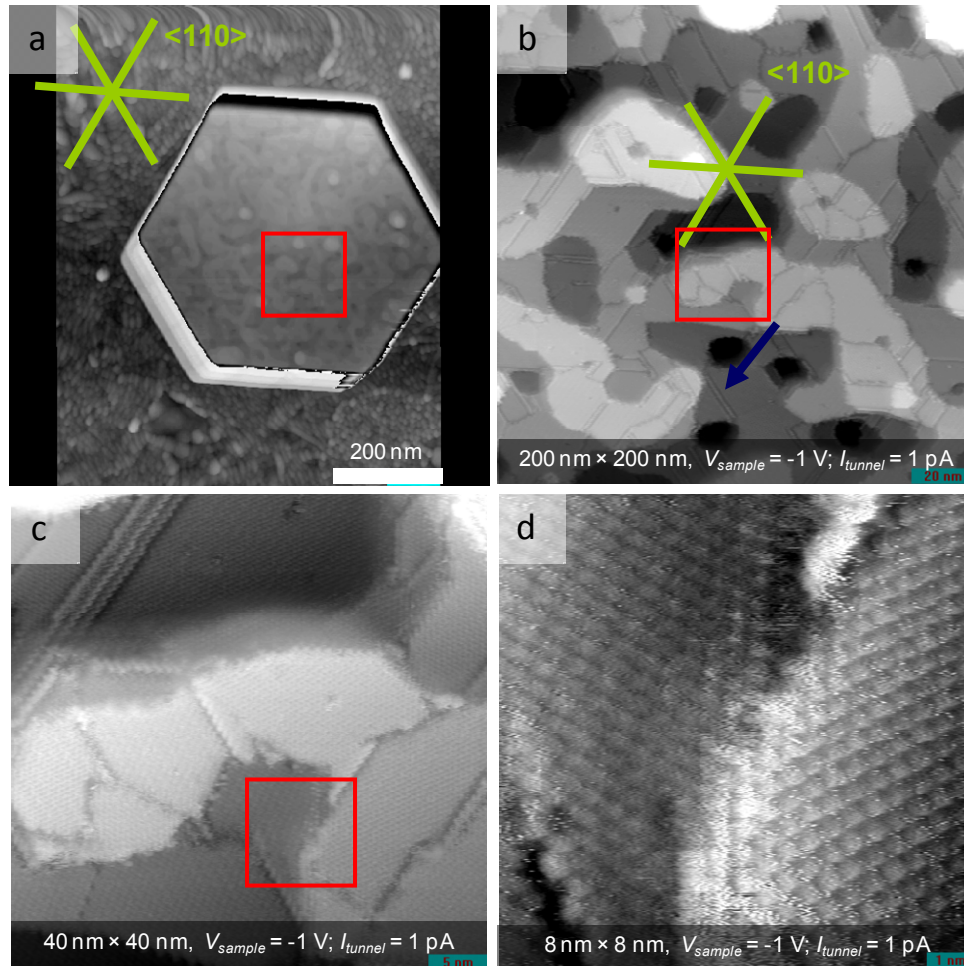
**Figure 4.8 STM images of a hexagonal shape FGNP after Ar/O₂ plasma treatment and C10 SAM growth at 60 °C:** a) Overview showing the FGNP on the ITO substrate. The rosette shows the Au<110> directions which are parallel to the FGNP edges, b, c, and d) series of successively higher magnification images on the FGNP.

### 4.4.2   UV/ O₃ Treatment

### 4.4.2.1   UV/O₃ Treatment of Au/mica Substrates

UV/O₃ is commonly employed as a surface treatment to remove organic contaminant. We decided to employ UV/O₃ as a treatment for FGNP surfaces and compare it to plasma treatment. Large terrace structures were seen on UV/O₃ treated Au/mica surfaces (Figure 4.9) compared to the Ar/O₂ or H₂ plasma treated surfaces that showed small terraces.

Also, the UV/O$_3$ treated Au/mica surfaces are not rough. However, STM images revealed 10–15 nm size islands which are 3 nm thick (bright regions in Figure 4.9 a and c). These islands were not present after about 20 hours but reappeared after UV/O$_3$ treating the sample again. The islands were pushed away by the STM tip which indicates that they have low conductance. Therefore, it is likely that these are gold oxides formed during the treatment. However, molecularly-resolved STM image showed a regular ($\sqrt{3} \times \sqrt{3}$)R30° SAM structure (Figure 4.9d) indicating that the gold oxide formation did not have significant impact on the SAM quality, possibly because it has been decomposed during the self assembly process.
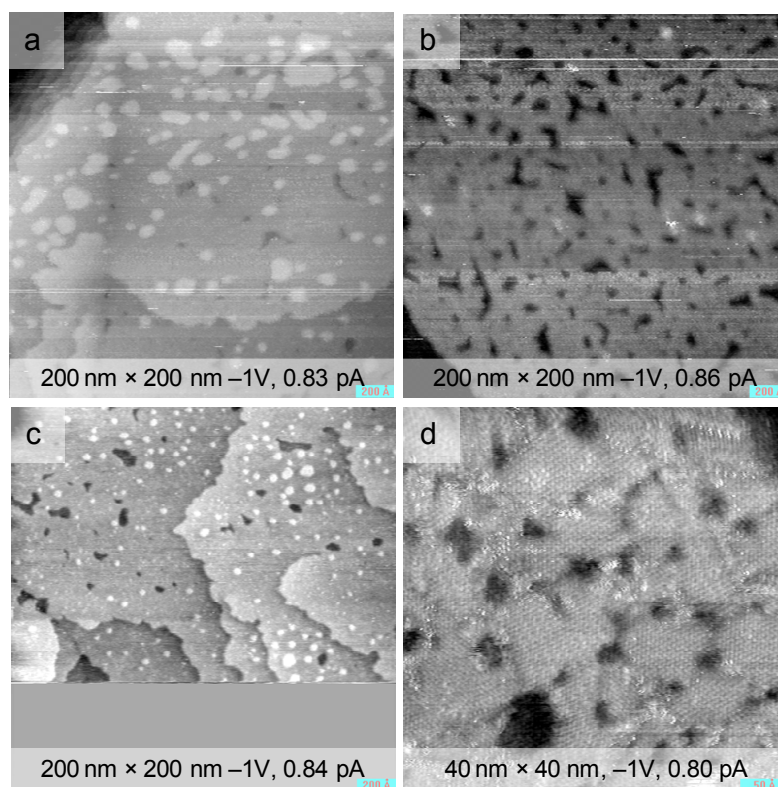


**Figure 4.9 STM images of UV/O$_3$ treated Au/mica substrate and SAMs:** a) STM image of a Au/mica surface after UV/O$_3$ treatment at 50 °C, b) STM image of the same sample after 20 hours, c) STM image of the same sample after ozone treatment at room temperature again, d) High-resolution STM image of C10 SAM deposited on the substrate shown in "c".

### 4.4.2.2   UV/O₃ Treated FGNP/ITO Substrates and Terrace Width Analysis

UV/O$_3$ was also applied to treat PVP-stabilized FGNP/ITO substrates. Relatively large terrace structures were observed compared to the Ar/O$_2$ pretreated FGNP surfaces (Figure 4.10). Terrace width analysis of UV/O$_3$ pretreated FGNP surfaces was performed. The terrace width ranged 16–48 nm. However, the distribution also includes some very large terraces as can be seen in the histogram (Figure 4.11), compared to the surface morphology resulting from Ar/O$_2$ plasma treatment. Nevertheless, the overall terrace morphology does not change appreciably after UV/O$_3$ treatment of FGNPs. This is likely due to the much lower energy of the UV/O$_3$ compared to Ar/O$_2$ plasma. UV/O$_3$ does not have enough energy to alter the gross morphology of the surface while Ar/O$_2$ plasma does.
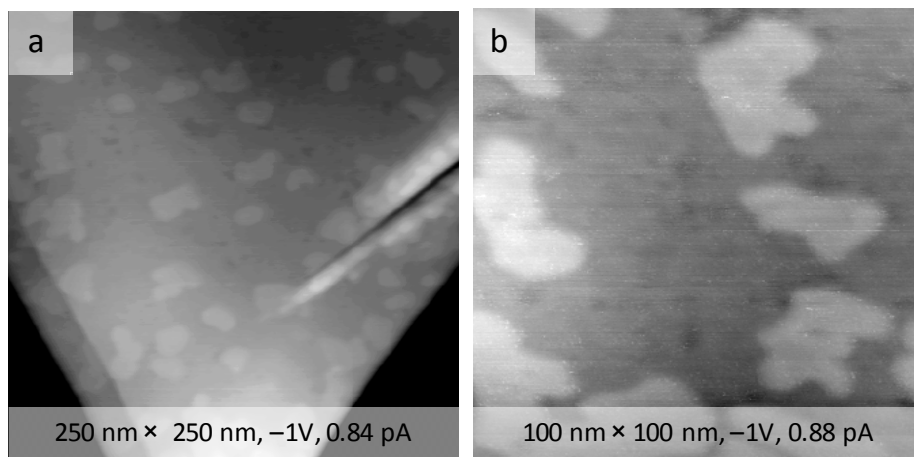


**Figure 4.10 STM images of a** UV/O$_3$ **treated PVP-stabilized FGNP surface** with different scan sizes showing the terrace morphology after surface conditioning.
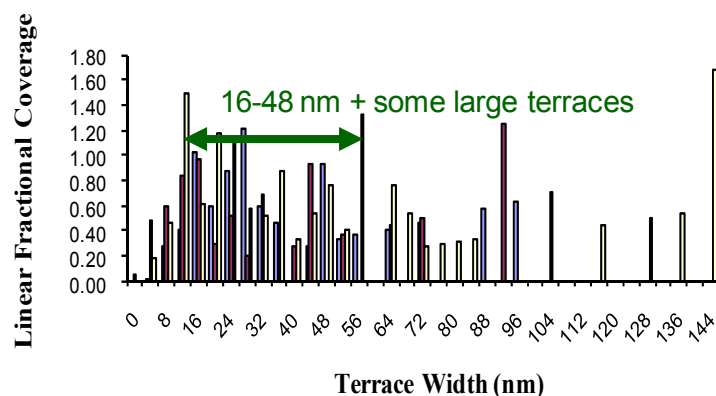
**Figure 4.11 Histogram showing linear fractional coverage vs. terrace width of UV/O$_3$ treated FGNPs.** The average size of terraces ranges from 16 nm to 48 nm. The different colors represent different images measured.
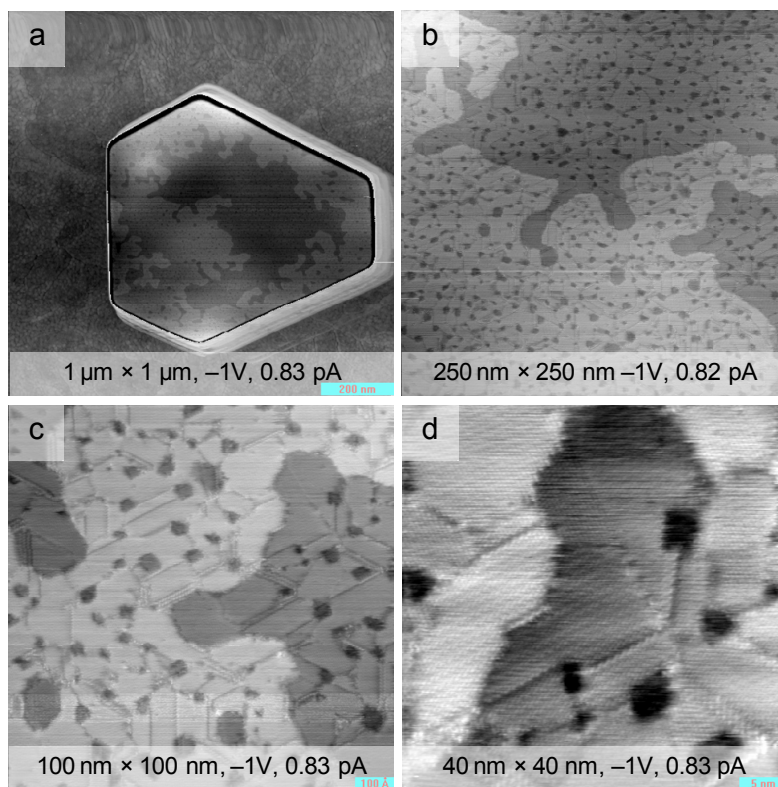


**Figure 4.12 STM images of 1-decanethiol SAM deposited (at 60 °C) after UV/O$_3$ treatment of FGNPs:** a) An overview image of SAM grown on a FGNP surface, b) SAM on the same particle, c) SAM structure showing the domain boundaries in the same directions as the FGNP edges, d) Molecularly resolved image showing a characteristic ($\sqrt{3} \times \sqrt{3}$)R30° structure.

STM imaging shows the characteristic ($\sqrt{3} \times \sqrt{3}$)R30° SAM structure on UV/O$_3$ treated FGNP (Figure 4.12). The characteristics of SAMs on Au/mica and FGNPs are similar. Therefore we can argue that the nano-size dimension of the substrate does not have any effect on the SAMs formation and produce similar results.

### 4.4.3 Thermal Stability of FGNPs
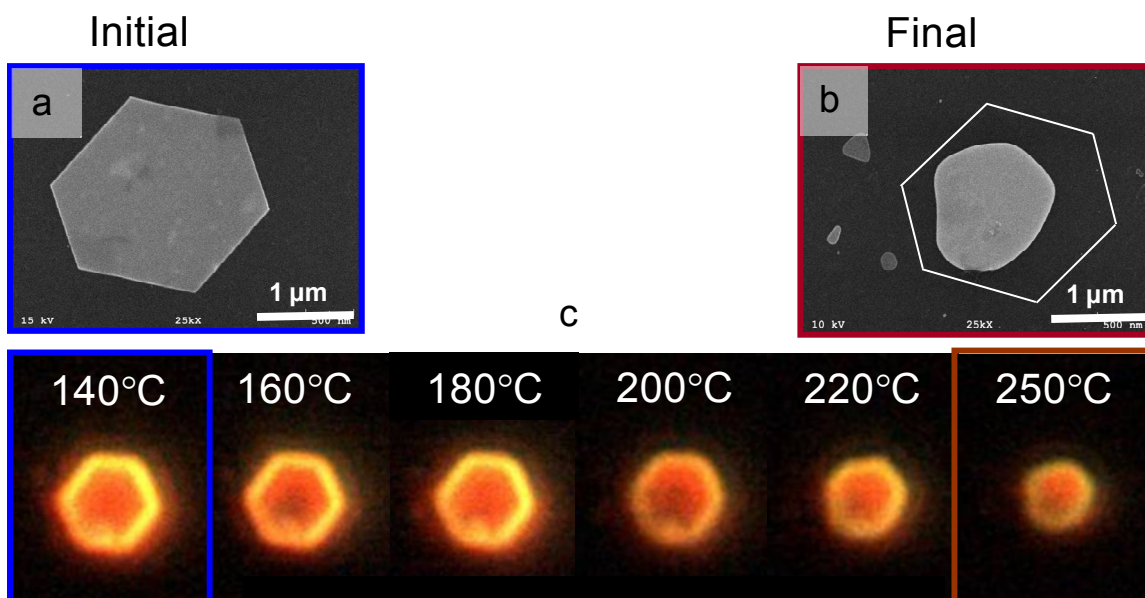


**Figure 4.13 SEM and DFM images of gradual change of the shape of an FGNP with increasing temperature:** a) SEM image of an FGNP before thermal annealing, b) SEM image of the same FGNP after thermal annealing at 250 °C for one hour, c) Series of consecutive Dark-field images of the same FGNP after thermal annealing at each temperature.

Alkanethiols can be deposited at different temperatures. Properties and quality of the SAM layer greatly depends on that particular temperature which it is grown. The FGNP substrate should be stable over the range of useful SAM growth temperatures. Although there are studies of melting temperatures of spherical Au nanoparticles,[49] the stability of FGNPs at elevated temperatures has not been investigated. In our study, we heated particles at successively higher temperatures, holding them at each temperature for one

hour. A dark-field microscopy image (Figure 4.14c) was taken after heating at each temperature. SEM images of the particle before the first heating and after the final heating (at 250 °C) were taken (Figure 4.14 a and b). Most of the particles measured started to deform at or around 180 °C a beginning of transition to more compact shapes. We expect the temperature at which FGNPs start to deform would depend on their thickness. The onset of melting for FGNPs begins around 180 °C, significantly lower than 1064.18 °C for bulk Au. The change of the shape of these thin platelets (FGNPs) is driven by their transition to a more stable compact structure, e.g. spherical shape has a lower surface energy than a thin platelet.

Peppiatt et al.[50-51] observed a change of shape from polyhedral to spherical of Bi and Pb crystals whose diameter is about 20 nm due to an effect associated with the melting. The chemical potential of the particle is different from the bulk material and depends on the size of the particle. Therefore the chemical and physical properties also change with the changes of chemical potential. Consequently a dependence of the melting point on the size of the particle is also expected. They show that particles with diameter of 20 Å melts at 600 K. Same is true for larger size particles. The thicknesses of our FGNPs are in the range of 15–25 nm. Therefore a similar behavior of the melting point of FGNPs is expected.

The bright contrast at the edge of the particle in Figure 4.14c is the first stage of this melting process which is similar to the thickening of edges of the FGNP we observed for particles annealed in C10 at 110 °C. The Au atoms diffuse from the corners and edges of the particles towards the middle transforming the platelet to a more spherical shape. We did not explore temperatures above 250 °C. We anticipate that higher temperatures

127

would lead to more compact shapes. However the temperature-thickness dependence is beyond the scope of this study. The deformation of FGNP particles can be attributed to the surface diffusion of gold atoms similar to what has been seen in gold films.[40-42,44-47,52]

## 4.5    Conclusions

A systematic study of treatment of standard Au/mica and ITO supported FGNP substrates with plasmas of Ar/O$_2$, H$_2$ and UV/O$_3$ was carried out to remove contaminants adsorbed on those surfaces. STM analysis showed that molecularly resolved images of high-quality SAMs of C10 can be grown on Au/mica and FGNP/ITO surfaces after these pretreatments. XPS analysis of the plasma treated Au/mica substrates showed no evidence of gold oxide formation. Highly ordered ($\sqrt{3} \times \sqrt{3}$)R30° SAMs of C10 were grown and could be imaged with molecular resolution on previously PVP stabilized FGNPs after pretreatment. Rough surfaces induced by plasma treatment can be repaired by dry thermal annealing the substrates or alkanethiol deposition on the Au surface at higher temperatures. SAMs grown at 110 °C show surface diffusion in the very early stages of gross morphological changes to the FGNP shape. This is evidence by the thickening of edges of the FGNP. Gross changes to the FGNP shape by thermal annealing begin at 180 °C. Therefore the FGNP/ITO substrates may not be suitable as atomically flat substrates at temperatures higher than 180 °C. However that the context of alkanethiol SAMs, the stability of alkanethiols is the limiting factor because they begin to decompose at lower temperatures.

## 4.6 References for Chapter 4

(1)    Vericat, C.; Vela, M. E.; Benitez, G. A.; Martin Gago, J. A.; Torrelles, X.; Salvarezza, R. C. Surface Characterization of Sulfur and Alkanethiol Self-Assembled Monolayers on Au(111). *J. Phys.: Condens. Matter* **2006**, *18*, R867.

(2)     Dunbar, T. D.; Cygan, M. T.; Bumm, L. A.; McCarty, G. S.; Burgin, T. P.; Reinerth, W. A.; Jones, L.; Jackiw, J. J.; Tour, J. M.; Weiss, P. S.; Allara, D. L. Combined Scanning Tunneling Microscopy and Infrared Spectroscopic Characterization of Mixed Surface Assemblies of Linear Conjugated Guest Molecules in Host Alkanethiolate Monolayers on Gold. *J. Phys. Chem. B* **2000**, *104*, 4880.

(3)     Poirier, G. E. Characterization of Organosulfur Molecular Monolayers on Au(111) using Scanning Tunneling Microscopy. *Chem. Rev.* **1997**, *97*, 1117.

(4)     Vericat, C.; Vela, M. E.; Salvarezza, R. C. Self-Assembled Monolayers of Alkanethiols on Au(111): Surface Structures, Defects and Dynamics. *Phys. Chem. Chem. Phys.* **2005**, *7*, 3258.

(5)     Love, J. C.; Estroff, L. A.; Kriebel, J. K.; Nuzzo, R. G.; Whitesides, G. M. Self-Assembled Monolayers of Thiolates on Metals as a Form of Nanotechnology. *Chem. Rev.* **2005**, *105*, 1103.

(6)     Schreiber, F.; Eberhardt, A.; Leung, T. Y. B.; Schwartz, P.; Wetterer, S. M.; Lavrich, D. J.; Berman, L.; Fenter, P.; Eisenberger, P.; Scoles, G. Adsorption Mechanisms, Structures, and Growth Regimes of an Archetypal Self-Assembling System: Decanethiol on Au(111). *Phys. Rev. B* **1998**, *57*, 12476.

(7)     Love, J. C.; Wolfe, D. B.; Chabinyc, M. L.; Paul, K. E.; Whitesides, G. M. Self-Assembled Monolayers of Alkanethiolates on Palladium Are Good Etch Resists. *J. Am. Chem. Soc.* **2002**, *124*, 1576.

(8)     Barrena, E.; Palacios-Lidon, E.; Munuera, C.; Torrelles, X.; Ferrer, S.; Jonas, U.; Salmeron, M.; Ocal, C. The Role of Intermolecular and Molecule-Substrate Interactions in the Stability of Alkanethiol Nonsaturated Phases on Au(111). *J. Am. Chem. Soc.* **2004**, *126*, 385.

(9)     Camillone III, N.; Eisenberger, P.; Leung, T. Y. B.; Schwartz, P.; Scoles, G.; Poirier, G. E.; Tarlov, M. J. New Monolayer Phases of *n*-Alkane Thiols Self-Assembled on Au(111): Preparation, Surface Characterization, and Imaging. *J. Chem. Phys.* **1994**, *101*, 11031.

(10)    Kautz, N. A.; Kandel, S. A. Alkanethiol/Au(111) Self-Assembled Monolayers Contain Gold Adatoms: Scanning Tunneling Microscopy before and after Reaction with Atomic Hydrogen. *J. Am. Chem. Soc.* **2008**, *130*, 6908.

(11)     Monnell, J. D.; Stapleton, J. J.; Jackiw, J. J.; Dunbar, T.; Reinerth, W. A.; Dirk, S. M.; Tour, J. M.; Allara, D. L.; Weiss, P. S. Ordered Local Domain Structures of Decaneselenolate and Dodecaneselenolate Monolayers on Au{111}. *J. Phys. Chem. B* **2004**, *108*, 9834.


(12)     Ron, H.; Rubinstein, I. Alkanethiol Monolayers on Preoxidized Gold. Encapsulation of Gold Oxide under an Organic Monolayer. *Langmuir* **1994**, *10*, 4566.


(13)     Subramanian, S.; Sampath, S. Enhanced Thermal Stability and Structural Ordering in Short Chain *n*-Alkanethiol Monolayers on Gold Probed by Vibrational Spectroscopy and EQCM *Anal. Bioanal. Chem.* **2007**, *388*, 135.


(14)     Woodward, J. T.; Walker, M. L.; Meuse, C. W.; Vanderah, D. J.; Poirier, G. E.; Plant, A. L. Effect of an Oxidized Gold Substrate on Alkanethiol Self-Assembly. *Langmuir* **2000**, *16*, 5347.


(15)     Ron, H.; Matlis, S.; Rubinstein, I. Self-Assembled Monolayers on Oxidized Metals. 2. Gold Surface Oxidative Pretreatment, Monolayer Properties, and Depression Formation. *Langmuir* **1998**, *14*, 1116.


(16)     Feng, C. L.; Li, Y.; Tong, Y. C. Cleaning and Elecrochemical Characterization of Gold Surface. *Liaoning Shifan Dax.Xue.Zir.Kex.* **2004**, *27*, 440.


(17)     Evans, S. D.; Sharma, R.; Ulman, A. Contact Angle Stability: Reorganization of Monolayer Surfaces? *Langmuir* **1991**, *7*, 156.


(18)     Sondaghuethorst, J. A. M.; Fokkink, L. G. J. Potential-Dependent Wetting Of Octadecanethiol-Modified Polycrystalline Gold Electrodes. *Langmuir* **1992**, *8*, 2560.


(19)     Sabatani, E.; Rubinstein, I.; Maoz, R.; Sagiv, J. Organized Self-Assembling Monolayers on Electrodes : Part I. Octadecyl Derivatives on Gold. *J. Electroanal. Chem.* **1987**, *219*, 365.


(20)     Sakata Tomomi; Okabe Yuichi; Kuwabara Kei; Sato Norio; Ono Kazuyoshi; Shimoyama Nobuhiro; Machida1 Katsuyuki; Hiromu, I. Surface Cleaning of Gold Structure by Annealing during Fabrication of Microelectromechanical System Devices. *Japanese Journal of Applied Physics* **2009**, *48*, 26501.

(21)    King, D. E. Oxidation of Gold by Ultraviolet-Light and Ozone at 25 °C. *J. Vac. Sci. Technol., A* **1995**, *13*, 1247.

(22)    Krozer, A.; Rodahl, M. X-ray Photoemission Spectroscopy Study of UV/Ozone Oxidation of Au under Ultrahigh Vacuum Conditions. *J. Vac. Sci. Technol., A* **1997**, *15*, 1704.

(23)    Raiber, K.; Terfort, A.; Benndorf, C.; Krings, N.; Strehblow, H.-H. Removal of Self-Assembled Monolayers of Alkanethiolates on Gold by Plasma Cleaning. *Surf. Sci.* **2005**, *595*, 56.

(24)    Schonenberger, C.; Jorritsma, J.; Sondag-Huethorst, J. A. M.; Fokkink, L. G. J. Domain Structure of Self-Assembled Alkanethiol Monolayers on Gold. *J. Phys. Chem.* **1995**, *99*, 3259.

(25)    Emch, R.; Nogami, J.; Dovek, M. M.; Lang, C. A.; Quate, C. F. Characterization of Gold Surfaces for Use as Substrates in Scanning Tunneling Microscopy Studies. *J. Appl. Phys.* **1989**, *65*, 79.

(26)    Nichols, R. J.; Magnussen, O. M.; Hotlos, J.; Twomey, T.; Behm, R. J.; Kolb, D. M. An in-situ STM Study of Potential-Induced Changes in the Surface Topography of Au(100) Electrodes *J. Electroanal. Chem.* **1990**, *290*, 21.

(27)    Schneeweiss, M. A.; Kolb, D. M.; Liu, D.; Mandler, D. Anodic oxidation of Au(111). *Can. J. Chem.* **1997**, *75*, 1703.

(28)    Dahanayaka, D. H.; Wang, J. X.; Hossain, S.; Bumm, L. A. Optically Transparent Au{111} Substrates: Flat Gold Nanoparticle Platforms for High-Resolution Scanning Tunneling Microsocopy. *J. Am. Chem. Soc.* **2006**, *128*, 6052.

(29)    Achermann, M.; Shuford, K. L.; Schatz, G. C.; Dahanayaka, D. H.; Bumm, L. A.; Klimov, V. I. Near-Field Spectroscopy of Surface Plasmons in Flat gold Nanoparticles. *Opt. Lett.* **2007**, *32*, 2254.

(30)    Millstone, J. E.; Park, S.; Shuford, K. L.; Qin, L.; Schatz, G. C.; Mirkin, C. A. Observation of a Quadrupole Plasmon Mode for a Colloidal Solution of Gold Nanoprisms. *J. Am. Chem. Soc.* **2005**, *127*, 5312.

(31)     Kelly, K. L.; Coronado, E.; Zhao, L. L.; Schatz, G. C. The Optical Properties of Metal Nanoparticles: The Influence of Size, Shape, and Dielectric Environment. *J. Phys. Chem. B* **2003**, *107*, 668.

(32)     Sherry, L. J.; Jin, R.; Mirkin, C. A.; Schatz, G. C.; Van Duyne, R. P. Localized Surface Plasmon Resonance Spectroscopy of Single Silver Triangular Nanoprisms. *Nano Lett.* **2006**, *6*, 2060.

(33)     Shuford, K. L.; Ratner, M. A.; Schatz, G. C. Multipolar Excitation in Triangular Nanoprisms. *J. Chem. Phys.* **2005**, *123*, 114713.

(34)     Turkevich, J.; Stevenson, P. C.; Hillier, J. Study of the Nucleation and Growth Processes in the Synthesis of Colloidal Gold. *Discuss. Faraday Soc.* **1951**, *11*, 55.

(35)     Zaluzec, N. J. In *USPTO*; US, Ed.; The University of Chicago: USA, 1996.

(36)     Zhang, L.; Goddard III, W. A.; Jiang, S. Molecular Simulation Study of the c(4 × 2) Superlattice Structure of Alkanethiol Self-Assembled Monolayers on Au(111). *J. Chem. Phys.* **2002**, *117*, 7342.

(37)     Delamarche, E.; Michel, B.; Gerber, C.; Anselmetti, D.; Guentherodt, H. J.; Wolf, H.; Ringsdorf, H. Real-Space Observation of Nanoscale Molecular Domains in Self-Assembled Monolayers. *Langmuir* **1994**, *10*, 2869.

(38)     Poirier, G. E.; Tarlov, M. J. The c(4 × 2) Superlattice of *n*-Alkanethiol Monolayers Self-Assembled on Au(111). *Langmuir* **1994**, *10*, 2853.

(39)     Camillone III, N.; Chidsey, C. E. D.; Liu, G. Y.; Scoles, G. Substrate Dependence of the Surface Structure and Chain Packing of Docosyl Mercaptan Self-Assembled on the (111), (110), and (100) Faces of Single Crystal Gold. *J. Chem. Phys.* **1993**, *98*, 4234.

(40)     Porath, D.; Bar-Sadeh, E.; Wolovelsky, M.; Grayevsky, A.; Goldstein, Y.; Millo, O. Annealing Study of Gold Films Using Scanning Tunneling Microscopy. *J. Vac. Sci. Technol., A* **1995**, *13*, 1165.

(41)     Porath, D.; Goldstein, Y.; Grayevsky, A.; Millo, O. Scanning Tunneling Microscopy Studies of Annealing of Gold Films. *Surf. Sci.* **1994**, *321*, 81.

(42)    Porath, D.; Millo, O.; Gersten, J. I. Scanning Tunneling Microscopy Studies and Computer Simulations of Annealing of Gold Films. *J. Vac. Sci. Technol., B* **1996**, *14*, 30.

(43)    Lin, T.-S.; Chung, Y.-W. Measurement of the Activation Energy for Surface Diffusion in Gold by Scanning Tunneling Microscopy *Surf. Sci. Rep.* **1989**, *207*, 539.

(44)    Alonso, C.; Salvarezza, R. C.; Vara, J. M.; Arvia, A. J.; Vazquez, L.; Bartolome, A.; Baro, A. M. The Evaluation of Surface Diffusion Coefficients of Gold and Platinum Atoms at Electrochemical Interfaces from Combined STM-SEM Imaging and Electrochemical Techniques. *J. Electrochem. Soc.* **1990**, *137*, 2161.

(45)    Beszeda, I.; Szabó, I. A.; Gontier-Moya, E. G. Morphological Evolution of Thin Gold Films Studied by Auger Electron Spectroscopy in Beading Conditions. *Appl. Phys. A* **2004**, *78*, 1079.

(46)    Dalton, A. S.; Seebauer, E. G. An improved theory for temperature-dependent Arrhenius parameters in mesoscale surface diffusion. *Surface Science* **2007**, *601*, 728.

(47)    Watanabe, M. O.; Kuroda, T.; Tanaka, K.; Sakai, A. Scanning Tunneling Microscopy Observation Of Crystal-Growth Of Deposited Gold-Films During Annealing. *J. Vac. Sci. Technol., B* **1991**, *9*, 924.

(48)    Porath, D.; Millo, O.; Gersten, J. I. Scanning Tunneling Microscopy Studies and Computer Simulations of Annealing of Gold Films. *J. Vac. Sci. Technol., B* **1996**, *14*, 30.

(49)    Buffat, P.; Borel, J. P. Size Effect on the Melting Temperature of Gold Particles. *Phys. Rev. A* **1976**, *13*, 2287.

(50)    Peppiatt, S. J. Melting of Small Particles 2. Bismuth. *Proc. R. Soc. London, Ser. A* **1975**, *345*, 401.

(51)    Peppiatt, S. J.; Sambles, J. R. Melting of Small Particles 1. Lead. *Proc. R. Soc. London, Ser. A* **1975**, *345*, 387.

(52)    Semin, D. J.; Lo, A.; Roark, S. E.; Skodje, R. T.; Rowlen, K. L. Time-Dependent Morphology Changes in Thin Silver Films on Mica: A Scaling Analysis of Atomic Force Microscopy Results. *J. Chem. Phys.* **1996**, *105*, 5542.

# Chapter 5

## Scanning Tunneling Microscopy Characterization of Functionalization of Reactive Self Assembled Monolayers and Observation of Surface Structure Directed Chemistry

### 5.1 Abstract

Self-assembled monolayers can be used as platforms for molecular electronics, molecular photonics, and for biology. In order to incorporate the functional molecular components in the monolayer, a SAM tethering moiety is typically attached to the functional component requiring a new synthesis for each component and tether length. We developed a convergent approach in which ordered mixed monolayers comprised of alkanethiols and azidoalkanethiols are initially formed and characterized on Au(111) surfaces. A subsequent IMesCu$^I$Br catalyzed [3+2] "click" cycloaddition reaction with substituted alkyne, introduced dilute substituent onto the ordered surface. We produced islands of 10-azido 1-decanethiol surrounded by 1-decanethiol and obtained STM images with molecular resolution in both regions. The tethered azide moeities were reacted with *p*-tolylacelylene at the presence of IMesCu$^I$Br catalyst. Analysis of the special distribution of reacted azide sites showed that, the first two rows of molecules at the boundary react most rapidly, the rate decreasing with distance toward the interior of the island. The reaction rate of the molecules near the edge of the island is 4–10 times faster than the molecules at the interior of the islands.

**5.2 Introduction**

The importance of self assembled monolayers (SAMs) in surface science and surface modification was discussed in chapter one in detail. We showed that they have drawn considerable attention as model systems for fundamental studies in nanoscale surface science[1-4] as well as for their potential in molecular functional applications.[5-6] Also we discussed the structure of alkanethiol-Au{111} system  and showed that it forms a well ordered SAM due to the chemisorption of the sulfur head groups on the Au surface and the van der Waals interactions between alkyl chains. There have been extensive investigations carried out to understand fundamental features of alkanethiolate SAMs such as molecular structure, growth process, stability, and interface properties using surface sensitive spectroscopy and microscopy.[3,7-19] Among those, scanning tunneling microscopy (STM) has allowed study of the structure of SAMs with molecular resolution.[7-8,10-11,13-15,20] Developing methodologies for the control of structural and chemical properties of these surfaces is the key to extend their utility. Research to tune SAM surfaces includes control of the spatial arrangement (physical structure) of the SAM and the chemical properties of the exposed functional group.

SAMs are used as model systems and are used as a support matrix to immobilize other molecules (redox-molecules, oligonucleotides or any other molecule with a functional group of interest) or nanomaterials on surfaces such as gold, silver, silicon, silica.[2,4,21] Typically functional molecules are tethered to a thiol pendent group in one end and co-deposited with alkanethiol or backfilled into the already formed alkanethiol monolayer.[22-23] Unfortunately this process does not always produce good results. Some molecules do not form well ordered monolayers on their own while others reduce the

crystalline order of the existing alkanethiol monolayer when they are inserted. Thus it may not be practical or possible to grow a well-ordered SAM using a thiol with any arbitrary terminal functional group.[22]

A possible methodology that circumvents this problem is to first grow a monolayer of thiol with a reactive end group. Then in a subsequent step, a second molecule which has the desired chemical functional group couples to the functional SAM surface. This in-situ coupling reduces a significant amount of time involved in process development and synthesizing individual functional molecules and enables use of large number of functional groups. Wide use of this method is hindered by difficulties in introducing reactive groups, requirements of harsh conditions, side reactions, difficulties of removing by products and low yield.[24-26] Unlike the conventional solution chemistry, performing chemical reactions on surfaces is very challenging due to difficulties of removing the molecules that are not reacted or byproducts of the reaction.[23]

Therefore for this purpose, two reactive chemical functional groups must be selected, their reaction must be specific so they only react with each other. Elimination of side reactions reduces the difficulties of removing any by-products.[27] Their reaction should also occur readily and with mild conditions. This is important because harsh conditions will affect the order of the SAM. Click chemistry has been widely used to couple between two groups and has been demonstrated as versatile and highly selective.[28] Although all Click reactions may not be suitable for every situation, Sharpless "click" chemistry, specifically which uses $Cu^I$-catalyzed 1,3-dipolar cycloaddition of azide and alkyne has been proved to be very effective way to make connections between broad variety of functional groups.[29-30] Not only does this produce a high yield but the

chemistry is relatively simple. The functional groups used in click chemistry are highly specific and do not react with each other and with solvents. Incorporation of azide and alkyne groups into other molecules is relatively easy. The reaction occurs under very mild conditions and the coupling occurs only between the two reactants. The $Cu^I$ catalyst not only increases the rate of Huisgen 1,3-dipolar cycloaddition but also promotes the regiospecificity of the 1-2-3-triazole.[31-32]

### 5.2.1 $Cu^I$ Catalyzed Alkyne-Azide "Click" Chemistry
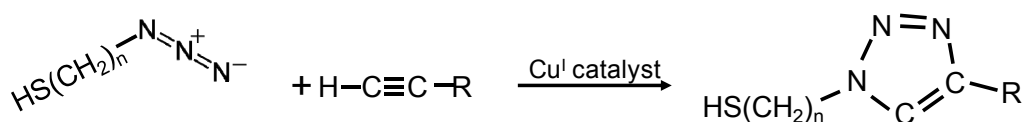


**Figure 5.1 Huisgen 1,3-dipolar cycloaddition of azide with alkyne to form 1,2,3-triazole**

$Cu^I$-catalyzed alkyne-azide coupling was introduced independently by Sharples and Meldal groups.[29,33] Both the alkyne and azide can be introduced and remain unaffected due to their kinetic stability until the catalyst is introduced. Without the catalyst this reaction requires elevated temperatures and long reaction times.[27] Introduction of $Cu^I$ catalyst significantly increases the reaction rate up to $10^7$ times.[34] Only the terminal acetylenes react with the azide to form 1,4 substituted 1-2-3-triazol.[33] In general, terminal end groups can be any functional group. In the experiments presented here, the azide molecules are immobilized on the Au(111) surface, but the acetylene group can also be tethered on the surface.[35-36]

Various surface characterization techniques such as polarized infrared external reflectance spectroscopy (PIERS),[37] X-ray photoelectron spectroscopy (XPS),[38] electrochemical measurements, grazing-angle infrared spectroscopy have been used to monitor and to characterize reactions on surfaces. There have been no reports of using high resolution scanning probe microscopy (STM, AFM) to image the surface of reactive SAMs and determine if the reaction is spatially homogeneous or occurs faster in some regions than others. We might expect that the reactivity of the azide group will depend on the local environment, specially the degree to which the solution reagent has access to each azide group. The molecules which are immobilized on a surface have limited spatial degree of freedom and therefore they are sterically locked (Figure 5.3). To answer some of the questions stated above, mixed SAMs of 1-decanethiol ($CH_3(CH_2)_9SH$, Figure 5.1-(1)) and 10-azido-1-decanethiol ($N_3(CH_2)_{10}SH$, Figure 5.1-(2)) on Au(111) substrates were formed first and then reacted with $p$-tolylacetylene ($C_9H_8$, Figure 5.1-(3)) in the presence of $Cu^I$ catalyst. The samples were imaged with STM before and after the reaction with molecular resolution.
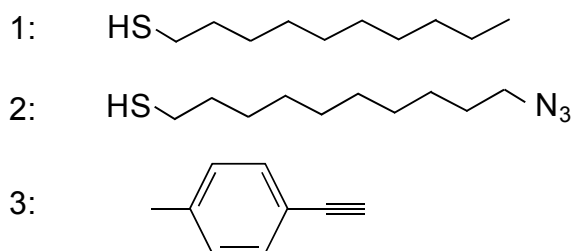


**Figure 5.2 Molecules used in the study**: 1) 1-decanethiol, 2) 10-azido-1-decanethiol, 3) $p$-tolylacetylene.
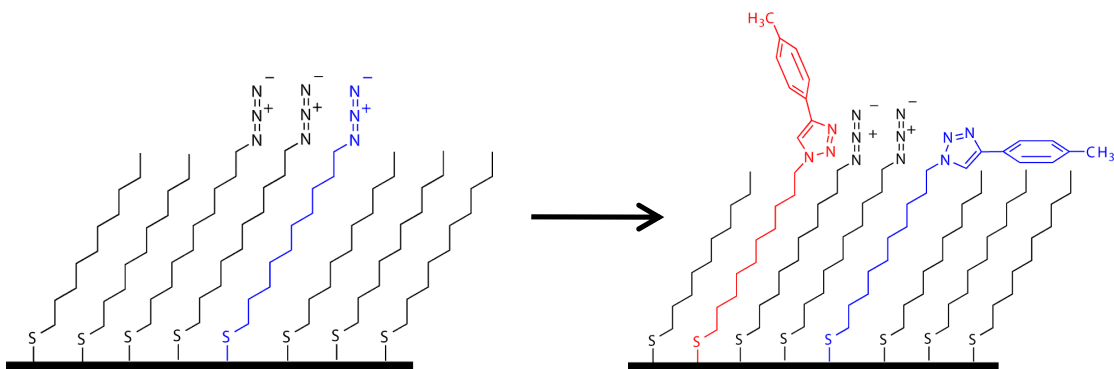
**Figure 5.3 Schematic of SAM of 1-decanethiol and 10-azido-1-decanethiol before and after the reaction with *p*-tolylacetylene**.

## 5.3 Materials and Methods

### 5.3.1 Preparation of (10-Azidodecyl) Disulfide

In this scheme the starting material is 1,10-decanediol, but any length carbon chain could be chosen simply by using a different alkanediol. First one alcohol group is converted to a bromide. The bromide is then subsequently replaced with azide to form 10-azido-1-decanol. The hydroxyl group is next activated with methane sulfonyl chloride to produce the methanesulfonate (mesylate). Thiourea displacement and hydrolysis gives 10-azido-1-decanethiol. The thiol converts to disulfide upon storage. In ethanol or chloroform conversion to disulfide is essentially complete within 24 hours, while the neat thiol liquid is stable for several days (Figure 5.4).
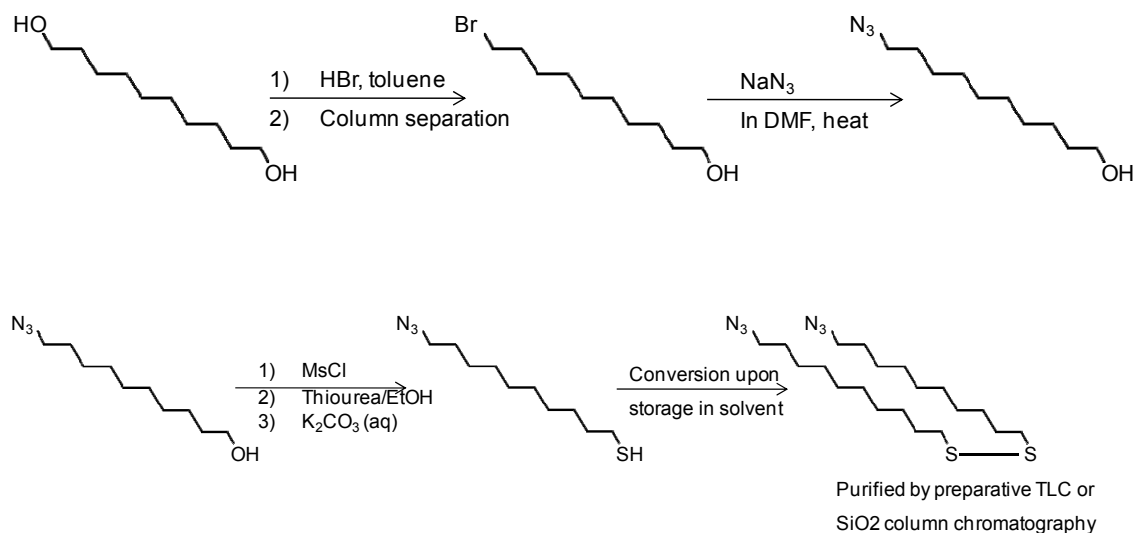
**Figure 5.4 The reaction path for converting 1,10-decanediol into 10-azido-1-decanethiol**.

## 5.3.2 Au/mica Substrate

Gold films grown on mica (1.0 cm × 1.1 cm Au film on 1.4 cm × 1.1 cm mica) were cut into four approximately equal pieces) used in the study were purchased from Agilent Technologies (formerly Molecular Imaging). They were $H_2$ flame annealed before use.[39]

## 5.3.3 SAM Preparation

5 ml PFA vials with conical bottom (purchased from Jenson Inert Products) were used to prepare SAMs. The vials were cleaned with ethanol rigorously and dried at 120 °C for several hours before using them. The cleaning procedure of PFA vials in $H_2SO_4$ which we discussed in the chapter one was not used here as it was not established at the time of this study.

### 5.3.3.1   Azide SAM

The initial deposition of azide on the Au/mica substrate was done with 1 mM solution of azide in absolute ethanol at room temperature for 16 hours. Following SAM growth, the substrate was washed in absolute ethanol and blown dried with nitrogen.

### 5.3.3.2   Azide Island SAMs

The azide SAM layer was back-filled with 1-decanethiol vapor at 60 °C for 6 hours. The sample was washed in absolute ethanol and blown dried with nitrogen.

### 5.3.3.3   Reaction of the SAMs

The 10-azido-1-decanethiol molecules which were immobilized on the surface were reacted with 50 mM $p$-tolylacelylene with the presence of 0.1 mM IMesCu$^I$Br catalyst at 45±0.25 °C for 2 hours. The solvent for both $p$-tolylacelylene and catalyst was a 1:3 mixture of $H_2O$ and $t$-BuOH. The samples were washed in $t$-BuOH and in absolute ethanol respectively and blown dried with nitrogen at the end.

### 5.3.3.4   Scanning Tunneling Microscope

The STM is a custom designed beetle-style scan head STM which uses RHK Technology SPM100 control electronics and XPM Pro control software. The current amplifier is an Axon CV4 head stage with custom interface electronics. Probe tips are clipped Pt-Ir (80:20) wire. STM images are typically recorded at −1.0 V sample bias and a 1.0 pA tunneling current. A detailed description of the STM can be found in chapter one.

### 5.4 Results and Discussions

10-azido-1-decanethiol SAMs on Au/mica were made using different conditions such as deposition time, solution concentration and deposition method (i.e. vapor or solution growth). Although the only structural difference between the 10-azido-1-decanethiol and

1-decanethiol is that the former has terminal azido group while the latter has a terminal methyl group at the tail positions, we observed that well ordered SAMs of 10-azido-1-decanethiol molecules could not be prepared. A sample STM image of 10-azido-1-decanethiol is shown in Figure 5.5. Although we can observe Au substrate steps and vacancy islands, we were not able to observe SAM structural domain boundaries on molecularly resolved images. Also the disorder in the 10-azido-1-decanethiol monolayer may be a result of other factors. Sulfur as well as azide can bind to the Au surface, which would contribute to disorder in the monolayer. The self assembly may have been hindered by impurities in the 10-azido-1-decanethiol as well, e.g. disulfides.



40 × 40 nm, −1 Vsample, 1 pA

5 nm
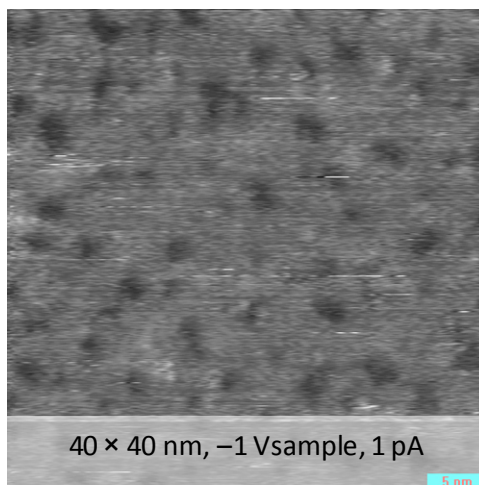
**Figure 5.5 An STM image of 10-azido-1-decanethiol SAM on Au/mica**.

The order in SAMs can sometimes be improved by a subsequent exposure to vapor of a second "matrix" alkanethiol at elevated temperature. This procedure adds additional molecules to the SAM to tighten it up, and provides additional thermal energy to allow the SAM to order. We term this method "back filling". We found that backfilling the

disordered 10-azido-1-decanethiol SAMs enforced an ordered structure. A surprise benefit was that some 10-azido-1-decanethiol desorbed leaving domains of well ordered 10-azido-1-decanethiol surrounded by 1-decanethiol. The coverage of 10-azido-1-decanethiol on the surface depends on the duration of the back-filling and the temperature. The islands could occur due to kinetics of SAM replacement or due to phase separation. Phase separation could be driven by the dipolar interaction between neighboring azido groups which is lacking with the C10 molecules. Determining the origin of island formation is beyond the scope of this work. Although there are several previous studies of similar type of reactive monolayers on Au(111),[23,37,40] ours is the first study to show structural arrangement of molecules on the surface with high resolution STM topographic images (Figure 5.6).
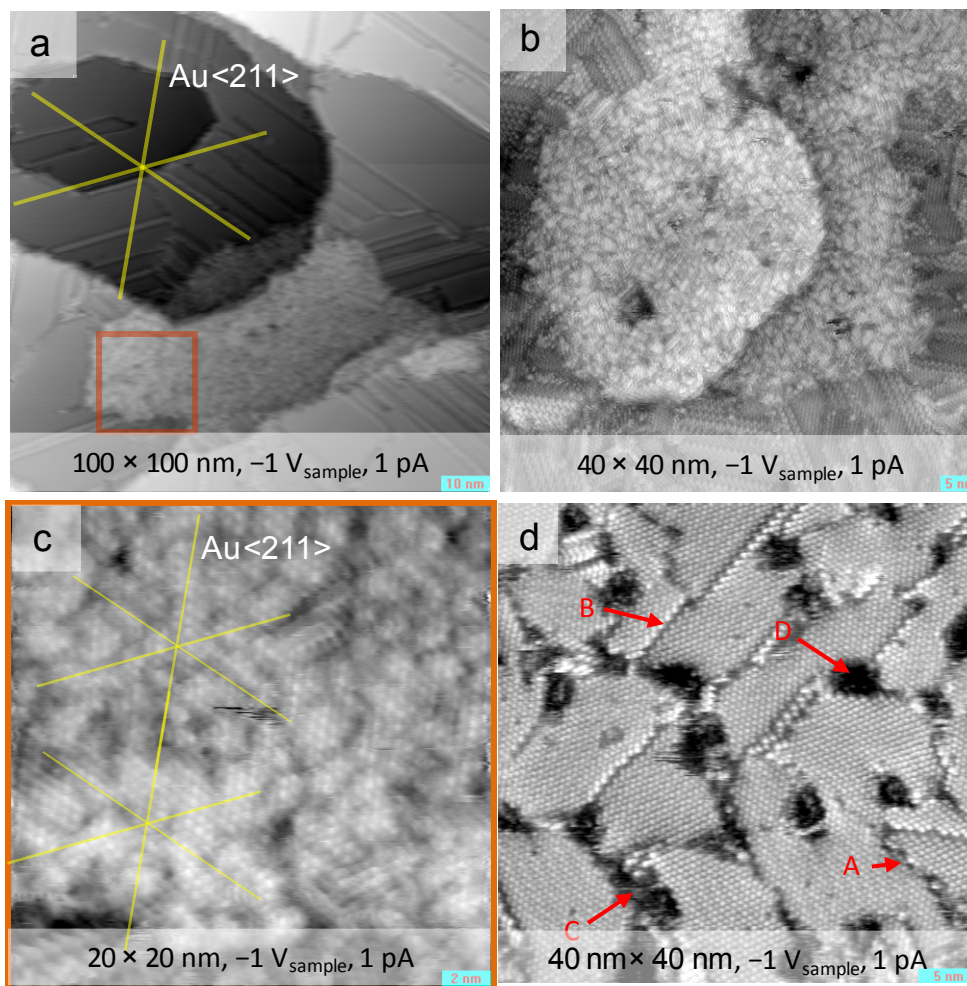
**Figure 5.6 STM images of 10-azido-1-decanethiol islands surrounded with C10 molecules**: a) large area STM image of a 10-azido-1-decanethiol island and the 1-decanethiol SAMs around it, b) an 10-azido-1-decanethiol island surrounded with C10, c) an image which shows the structure of 10-azido-1-decanethiol domains (yellow lines are in Au<211> directions), d) normal 1-decanethiol SAM with, A and B – domain boundaries, C – disordered areas, D – vacancy island.

Typical alkanethiol monolayers make $(\sqrt{3} \times \sqrt{3})R30°$ structure with respect to the Au(111) lattice. There are common characteristic features of a monolayer such as domain boundaries, vacancy islands, missing rows of molecules, and disordered areas (Figure 5.6d). Those features can be tuned with deposition conditions. The size of domains of 1-decanethiol increases with temperature and a single domain has large number of

molecules even at room temperature deposition. Molecular rows of 1-decanethiol follow Au next nearest neighbor directions, which are Au<211>. STM images of mixed monolayer of 10-azido-1-decanethiol and 1-decanethiol (Figure 5.6) reveal that the islands of 10-azido-1-decanethiol consist of much smaller ordered domains. Each domain has 10–15 molecules in it. The molecular rows do not exactly follow the commensurate of the gold under-layer and has a slight rotation. The nearest neighbor spacing for ($\sqrt{3} \times \sqrt{3}$)R30° structure of alkanethiol with methyl end group is 5.0 Å. The van der Waals diameter of azide 'tube' is 3.1 Å. Formation of small domains and rearranging the molecular orientation is a result of the azide group trying to bunch together yet constrained by the alkyl SAM roots.

### 5.4.1 Reaction of 10-azido-1-decanethiol Molecules on the Surface with *p*-Tolylacetylene

Surfaces present a different environment for reactions than in solution. In solution, the reactants are free to tumble and explore many possible configurations. At surfaces where one reactant is bound to the surface, the number of accessible configurations is greatly restricted. Figure 5.7 a and b are two STM images of 10-azido-1-decanethiol molecules on Au(111) substrate before and after reacting with *p*-tolylacetylene. In Figure 5.7 b, there are three different height levels. From lowest to the highest are C10 SAM, 10-azido-1-decanethiol, and reacted 10-azido-1-decanethiol. According to the Figure 5.7b only the 10-azido-1-decanethiol molecules which are close to the boundaries of islands has reacted most. In the control experiment without the *p*-tolylacetylene (Figure 5.7 d), we do not see any reaction sites and therefore it confirms the accuracy of the images in Figure 5.7 b.
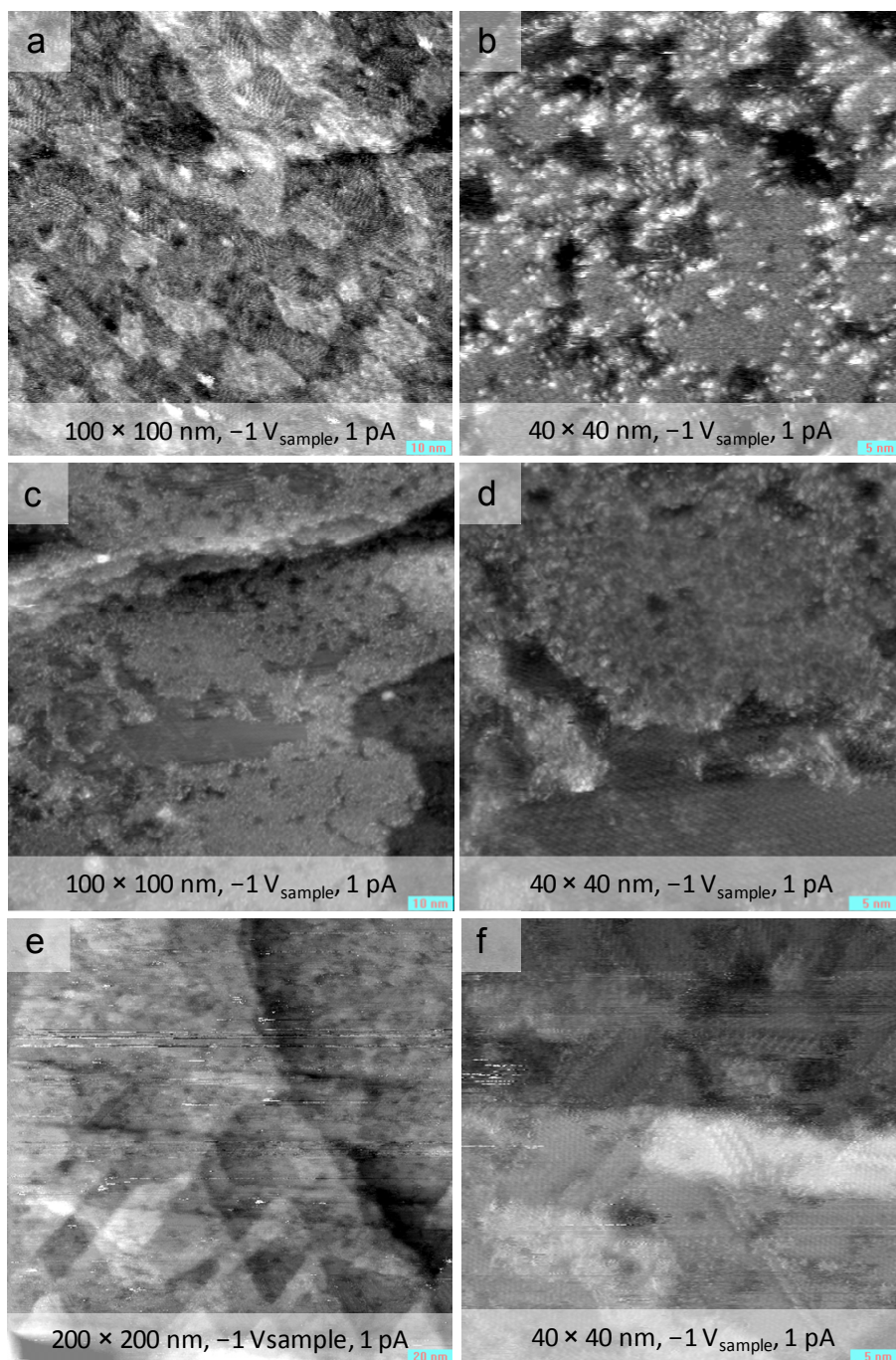
**Figure 5.7  STM images of 10-azido-1-decanethiol reacted with *p*-tolylacetylene and the control sample**: a and b) STM images of 10-azido-1-decanethiol (a) before and (b) after reacting with *p*-tolylacetylene, The bright spots are the reacted 10-azido-1-decanethiol molecules, c, d, e, f) STM images of the control samples, (c) before and (d) reacted without *p*-tolylacetylene, (e) and (f) reacted without Cu[I] catalyst. In control samples no such reaction is visible.

### 5.4.2 Reaction Sites

According to STM images, only a fraction of the 10-azido-1-decanethiol molecules which are located close to the edge of the islands have reacted. This can be explained by considering the molecule's ability to orient itself in the right configuration to react with another molecule. The 10-azido-1-decanethiol molecules bound on surface have fewer degrees of freedom compared to molecules in solutions. The surface bound 10-azido-1-decanethiols at the edge of the islands have more degrees of freedom than of those within the islands. This effect is essentially the steric hindrance of the surface, which is a surface blocking effect. The steric hindrance inhibits transition state from forming in interior of close packed 10-azido-1-decanethiol SAM region. This transition state with Cu$^I$Mes still connected, span over the surface through several 10-azido-1-decanethiol molecules blocking their interaction with the *p*-tolylacetylene making the transition state of the reaction in the interior of the islands less likely. Some of the azide-alkyne cycloadditon reactions which are prohibited by the steric hindrance effect has been reported in Tornøe et al.[33]
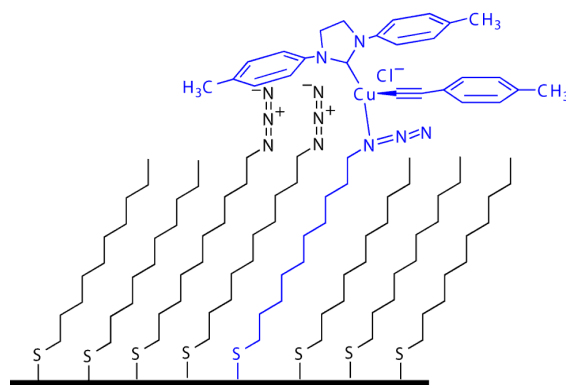


**Figure 5.8 Transition state of the 10-azido-1-decanethiol and *p*-tolylacetylene reaction.**

### 5.4.3 Quantitative Analysis of Reaction Site Distribution

To test the hypothesis that the reaction occurs fastest at the perimeter of the azide islands, we performed a quantitative analysis using the STM images of reacted monolayers. Reacted area versus total area as a function distance from the boundary was measured using a Matlab code specially developed for the analysis. STM images which were in RHK SPMPro ".SM3 or .SM4" formats were imported into Matlab using another Matlab code developed by our laboratory. Height thresholds were applied to pick out the C10 matrix, 10-azido-1-decanethiol which have not reacted, and reacted 10-azido-1-decanethiol. Then the 10-azido-1-decanethiol area was divided into bands (Figure 5.9 a) offset from the boundary and the number of pixels for the reacted sites and the total area were counted.
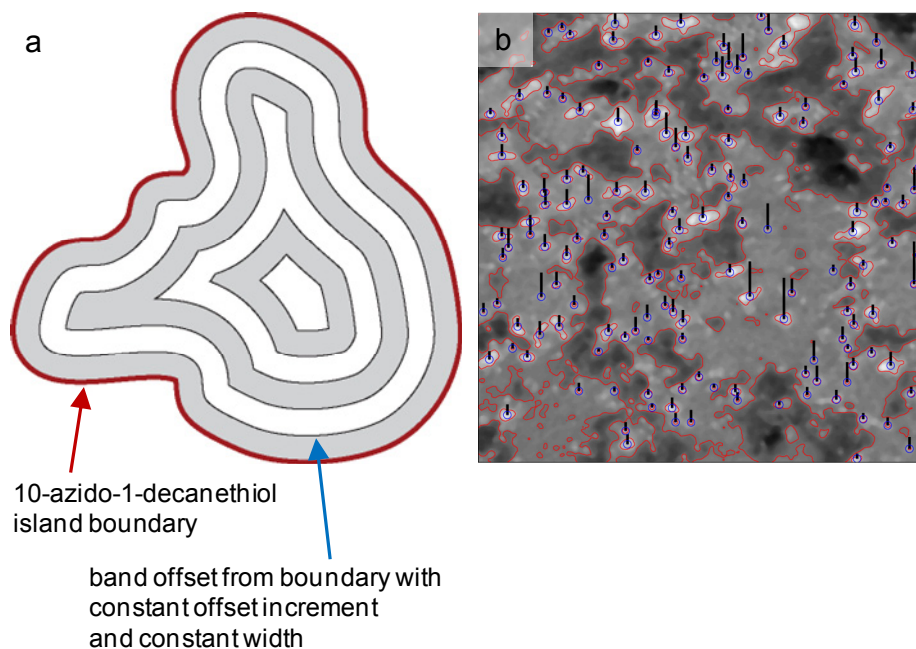


**Figure 5.9 A Diagram and an STM image which marks the bands for analyzing reaction sites**: a) a schematic of the way of selecting bands within an island of 10-azido-1-decanethiol, b) a STM image recreated in Matlab with the 10-azido-1-decanethiol islands marked in red and reacted sites selected. The length of the blue line is the distance to the nearest boundary from the reaction site.
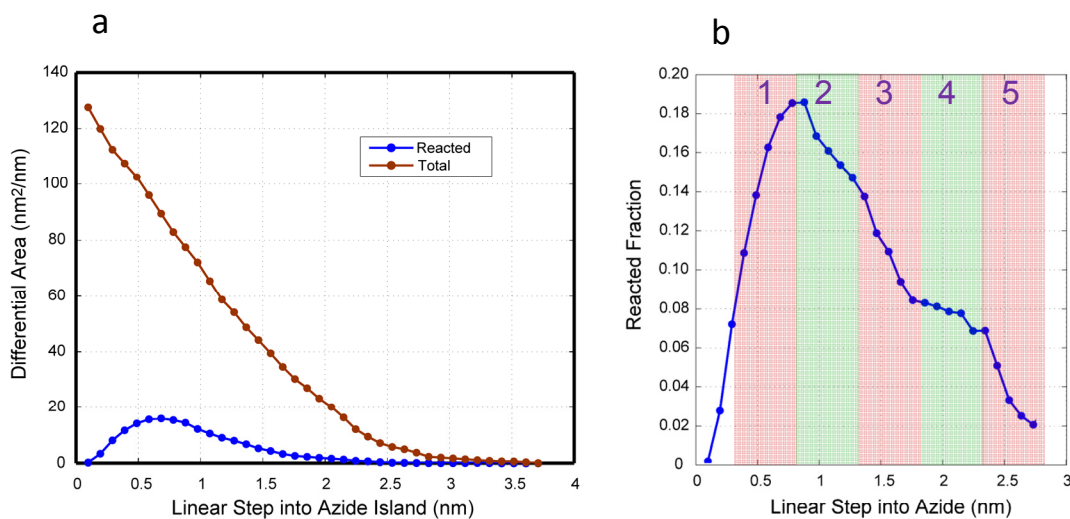
**Figure 5.10 Azide reaction sites analysis:** a) a graph of differential total and reacted area of selected steps, b) a graph of the molecular fraction reacted in different steps compared to the total molecules available.

The analysis showed that, the first two rows of molecules at the boundary react most rapidly, the rate decreases with distance toward the interior of the island (Figure 5.10). The reaction rate of the molecules near the island edge is 4–10 times faster than the molecules at the interior of the islands.

### 5.4.4 Height Differences of Molecules in the SAM

The chain length of 1-decanethiol, 10-azido-1-decanethiol and 10-azido-1-decanethiol reacted with *p*-tolylacetylene are 12.85 Å, 16.13 Å and 21.26 Å respectively. Therefore in an ideal situation i.e. all the molecules are stretched to their maximum length, expected height differences between 1-decanethiol or 10-azido-1-decanethiol and reacted molecule are 2.8 Å and 4.4 Å (Figure 5.11). But in our studies always the measured height differences were different than the calculated values. We measured a 2.4 Å height difference between the C10 and 10-azido-1-decanethiol SAM and 3 Å height difference between 10-azido-1-decanethiol SAM and reacted molecules (Figure 5.12). These

differences of measured and calculated heights can be explained by assuming the reacted and non-reacted 10-azido-1-decanethiol molecules having different orientational configurations than the orientations in figure 5.11. Figure 5.3 has such two extreme possible orientations for a reacted 10-azido-1-decanethiol molecule. Part of the molecule which is above the rest of the monolayer cannot support itself and therefore may bend over on the surface with varying degrees.
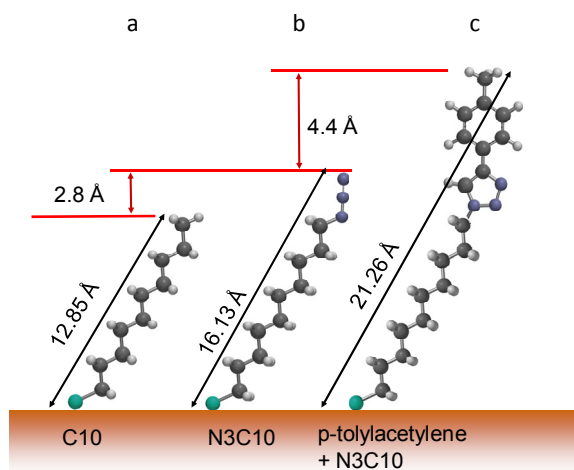


**Figure 5.11 A schematic which shows the height differences of 1-decanethiol, 10-azido-1-decanethiol and 10-azido-1-decanethiol reacted with *p*-tolylacetylene.**
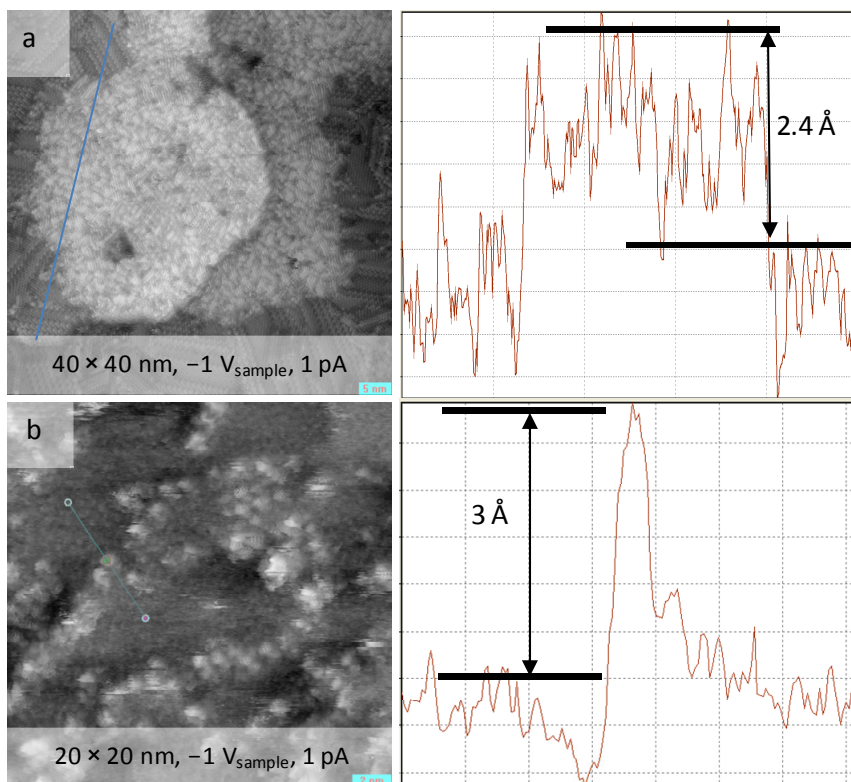
**Figure 5.12 Cross sections of STM images which show the height differences between a) 10-azido-1-decanethiol and C10, b) 10-azido-1-decanethiol and 10-azido-1-decanethiol reacted with *p*-tolylacetylene.**

## 5.5   Conclusions

We were able to obtain molecularly resolved STM images of reactive 10-azido-1-decanethiol islands on Au(111) surface. The domain size of the 10-azido-1-decanethiol is small compared to the regular 1-decanethiol domains and the 10-azido-1-decanethiol molecular rows are slightly rotated with respect to the underlying Au <211> directions. Also we conclude that 10-azido-1-decanethiol molecules which are inside the islands are less likely to react and their rate is 4–10 times slower than the molecules at the periphery of the island. We obtained molecularly resolved images of 10-azido-1-decanethiol SAMs reacted with *p*-tolylacetylene.

151

## 5.6 References for Chapter 5

(1)     Schonenberger, C.; Jorritsma, J.; Sondag-Huethorst, J. A. M.; Fokkink, L. G. J. Domain Structure of Self-Assembled Alkanethiol Monolayers on Gold. *J. Phys. Chem.* **1995**, *99*, 3259.

(2)     Love, J. C.; Estroff, L. A.; Kriebel, J. K.; Nuzzo, R. G.; Whitesides, G. M. Self-Assembled Monolayers of Thiolates on Metals as a Form of Nanotechnology. *Chem. Rev.* **2005**, *105*, 1103.

(3)     Vericat, C.; Vela, M. E.; Benitez, G. A.; Martin Gago, J. A.; Torrelles, X.; Salvarezza, R. C. Surface Characterization of Sulfur and Alkanethiol Self-Assembled Monolayers on Au(111). *J. Phys.: Condens. Matter* **2006**, *18*, R867.

(4)     Schreiber, F. Structure and Growth of Self-Assembling Monolayers. *Prog. Surf. Sci.* **2000**, *65*, 151.

(5)     Bumm, L. A.; Arnold, J. J.; Cygan, M. T.; Dunbar, T. D.; Burgin, T. P.; Jones, L., II; Allara, D. L.; Tour, J. M.; Weiss, P. S. Are Single Molecular Wires Conducting? *Science* **1996**, *271*, 1705.

(6)     Tour, J. M. Molecular Electronics. Synthesis and Testing of Components. *Acc. Chem. Res.* **2000**, *33*, 791.

(7)     Poirier, G. E.; Fitts, W. P.; White, J. M. Two-Dimensional Phase Diagram of Decanethiol on Au(111). *Langmuir* **2001**, *17*, 1176.

(8)     Camillone III, N.; Eisenberger, P.; Leung, T. Y. B.; Schwartz, P.; Scoles, G.; Poirier, G. E.; Tarlov, M. J. New Monolayer Phases of *n*-Alkane Thiols Self-Assembled on Au(111): Preparation, Surface Characterization, and Imaging. *J. Chem. Phys.* **1994**, *101*, 11031.

(9)     Camillone, N.; Leung, T. Y. B.; Schwartz, P.; Eisenberger, P.; Scoles, G. Chain Length Dependence of the Striped Phases of Alkanethiol Monolayers Self-Assembled on Au(111): An Atomic Beam Diffraction Study. *Langmuir* **1996**, *12*, 2737.

(10)    Fitts, W. P.; White, J. M.; Poirier, G. E. Low-Coverage Decanethiolate Structure on Au(111): Substrate Effects. *Langmuir* **2002**, *18*, 1561.

(11)    Fitts, W. P.; White, J. M.; Poirier, G. E. Thermodynamics of Decanethiol Adsorption on Au(111): Extension to 0 °C. *Langmuir* **2002**, *18*, 2096.

(12)    Poirier, G. E. Mechanism of Formation of Au Vacancy Islands in Alkanethiol Monolayers on Au(111). *Langmuir* **1997**, *13*, 2019.

(13)    Poirier, G. E. Characterization of Organosulfur Molecular Monolayers on Au(111) using Scanning Tunneling Microscopy. *Chem. Rev.* **1997**, *97*, 1117.

(14)    Poirier, G. E.; Pylant, E. D. The Self-Assembly Mechanism of Alkanethiols on Au(111). *Science* **1996**, *272*, 1145.

(15)    Poirier, G. E.; Tarlov, M. J. The c(4 × 2) Superlattice of *n*-Alkanethiol Monolayers Self-Assembled on Au(111). *Langmuir* **1994**, *10*, 2853.

(16)    Poirier, G. E.; Tarlov, M. J. Molecular Ordering and Gold Migration Observed in Butanethiol Self-Assembled Monolayers Using Scanning-Tunneling-Microscopy. *J. Phys. Chem.* **1995**, *99*, 10966.

(17)    Qian, Y. L.; Yang, G. H.; Yu, J. J.; Jung, T. A.; Liu, G. Y. Structures of Annealed Decanethiol Self-Assembled Monolayers on Au(111): an Ultrahigh Vacuum Scanning Tunneling Microscopy Study. *Langmuir* **2003**, *19*, 6056.

(18)    Woodward, J. T.; Walker, M. L.; Meuse, C. W.; Vanderah, D. J.; Poirier, G. E.; Plant, A. L. Effect of an Oxidized Gold Substrate on Alkanethiol Self-Assembly. *Langmuir* **2000**, *16*, 5347.

(19)    Poirier, G. E.; Tarlov, M. J.; Rushmeier, H. E. 2-Dimensional Liquid-Phase and The p × √3 Phase of Alkanethiol Self-Assembled Monolayers On Au(111). *Langmuir* **1994**, *10*, 3383.

(20)    Yang, G.; Liu, G.-y. New Insights for Self-Assembled Monolayers of Organothiols on Au(111) Revealed by Scanning Tunneling Microscopy. *J. Phys. Chem. B* **2003**, *107*, 8746.

(21)    Schreiber, F. Self-Assembled Monolayers: from 'Simple' Model Systems to Biofunctionalized Interfaces. *J. Phys.-Condes. Matter* **2004**, *16*, R881.

(22)    Chidsey, C. E. D.; Bertozzi, C. R.; Putvinski, T. M.; Mujsce, A. M. Coadsorption of Ferrocene-Terminated and Unsubstituted Alkanethiols on Gold: Electroactive Self-Assembled Monolayers. *J. Am. Chem. Soc.* **1990**, *112*, 4301.

(23)    Collman, J. P.; Devaraj, N. K.; Eberspacher, T. P. A.; Chidsey, C. E. D. Mixed Azide-Terminated Monolayers: A Platform for Modifying Electrode Surfaces. *Langmuir* **2006**, *22*, 2457.

(24)    Yousaf, M. N.; Mrksich, M. Diels−Alder Reaction for the Selective Immobilization of Protein to Electroactive Self-Assembled Monolayers. *J. Am. Chem. Soc.* **1999**, *121*, 4286.

(25)    Wollman, E. W.; Kang, D.; Frisbie, C. D.; Lorkovic, I. M.; Wrighton, M. S. Photosensitive Self-Assembled Monolayers on Gold: Photochemistry of Surface-Confined Aryl Azide and Cyclopentadienylmanganese Tricarbonyl. *J. Am. Chem. Soc.* **1994**, *116*, 4395.

(26)    Frey, B. L.; Corn, R. M. Covalent Attachment and Derivatization of Poly(l-lysine) Monolayers on Gold Surfaces As Characterized by Polarization-Modulation FT-IR Spectroscopy. *Anal. Chem.* **1996**, *68*, 3187.

(27)    Bock, V. D.; Hiemstra, H.; van Maarseveen, J. H. Cu[I]-Catalyzed Alkyne–Azide "Click" Cycloadditions from a Mechanistic and Synthetic Perspective. *Eur. J. Org. Chem.* **2006**, 51.

(28)    Rodionov, V. O.; Fokin, V. V.; Finn, M. G. Mechanism of the Ligand-Free Cu[I]-Catalyzed Azide-Alkyne Cycloaddition Reaction. *Angew. Chem. Int. Ed.* **2005**, *44*, 2210.

(29)    Rostovtsev, V. V.; Green, L. G.; Fokin, V. V.; Sharpless, K. B. A Stepwise Huisgen Cycloaddition Process: Copper(I)-Catalyzed Regioselective "Ligation" of Azides and Terminal Alkynes. *Angew. Chem. Int. Ed.* **2002**, *41*, 2596.

(30)    Kolb, H. C.; Finn, M. G.; Sharpless, K. B. Click Chemistry: Diverse Chemical Function from a Few Good Reactions. *Angew. Chem. Int. Ed.* **2001**, *40*, 2004.

(31)    Huisgen, R. Kinetik und Mechanismus 1.3-Dipolarer Cycloadditionen. *Angew. Chem. Int. Ed.* **1963**, *75*, 742.

(32)    Huisgen, R. 1.3-Dipolare Cycloadditionen - Ruckschau and Ausblick. *Angew. Chem. Int. Ed.* **1963**, *75*, 604.

(33)    Tornoe, C. W.; Christensen, C.; Meldal, M. Peptidotriazoles on Solid Phase: [1,2,3]-Triazoles by Regiospecific Copper(I)-Catalyzed 1,3-Dipolar Cycloadditions of Terminal Alkynes to Azides. *J. Org. Chem.* **2002**, *67*, 3057.

(34)    Appukkuttan, P.; Dehaen, W.; Fokin, V. V.; Van der Eycken, E. A Microwave-Assisted Click Chemistry Synthesis of 1,4-Disubstituted 1,2,3-Triazoles via a Copper(I)-Catalyzed Three-Component Reaction. *Org. Lett.* **2004**, *6*, 4223.

(35)    Lummerstorfer, T.; Hoffmann, H. Click Chemistry on Surfaces: 1,3-Dipolar Cycloaddition Reactions of Azide-Terminated Monolayers on Silica. *J. Phys. Chem. B* **2004**, *108*, 3963.

(36)    Lee, J. K.; Chi, Y. S.; Choi, I. S. Reactivity of Acetylenyl-Terminated Self-Assembled Monolayers on Gold: Triazole Formation. *Langmuir* **2004**, *20*, 3844.

(37)    Collman, J. P.; Devaraj, N. K.; Chidsey, C. E. D. "Clicking" Functionality onto Electrode Surfaces. *Langmuir* **2004**, *20*, 1051.

(38)    Daugaard, A. E.; Hvilsted, S.; Hansen, T. S.; Larsen, N. B. Conductive Polymer Functionalization by Click Chemistry. *Macromolecules* **2008**, *41*, 4321.

(39)    Agilent Technologies Application Note, Hydrogen Flame Annealing. http://www.home.agilent.com/ (accessed May 2010).

(40)    Devaraj, N. K.; Collman, J. P. Copper Catalyzed Azide-Alkyne Cycloadditions on Solid Surfaces: Applications and Future Directions. *QSAR Comb. Sci.* **2007**, *26*, 1253.

# Chapter 6

# Scanning Surface Photovoltage Microscopy (SSPVM) for Stress Characterization in CMOS Devices

## 6.1 Abstract

Mechanical stress is one of the major factors in current design and manufacture of very large scale integrated (VLSI) devices. Mechanical stress in deep sub-micron silicon technologies can drastically alter carrier mobility (approximately 25% dependent on device geometry). This affects the device performance. Current in-line production stress metrology is conducted only at a wafer monitor level. For design purposes, the stress state in active device regions has been inferred from electrical data. The available stress measurement techniques such as micro-Raman spectroscopy, nano-beam diffraction (NBD), and converging electron beam diffraction (CEBD) either do not have adequate resolution or they require complex data interpretation. Therefore when devices are scaled down, these methods cannot be used for measuring local stress levels present in devices. In this chapter we present the proof of concept of instrument development and method for measuring mechanical stress in deep sub-micron silicon devices with high spatial resolution using scanning surface photovoltage microscopy.

## 6.2 Introduction

Process-induced mechanical stress is an important parameter in engineering of performance of sub-micron size microelectronic devices such as complementary metal oxide field effect transistors (CMOS FETs) and bipolar junction transistors (BJTs). While uncontrolled stress can be parasitic and degrade device performance, it can act to enhance performance of some devices. For example, stress is currently used to enhance the performance of devices in strained Si/SiGe technologies.[1-6] Thus it is vital to accurately monitor and control stress in these structures for correct engineering, so it can be used to advantage. The available methods for measuring stress either do not have adequate resolution, need complex data interpretation, or are not suitable for current in-line production stress metrology. Therefore the demand for a method of measuring and manipulating mechanical stress quantitatively with high spatial resolution exists in the semiconductor industry.

Many of the processes involved in the silicon IC fabrication technology contribute to development of stress in the active area of silicon. The effect of mechanical stress in the active area of the devices become more prominent with the scaling down of size of devices.[7] Stress may cause formation of dislocations and cracks inside devices.[7] It can influence dopant diffusion, carrier degradation, and oxide reliability.[7]

### 6.2.1 Sources of Mechanical Stress

Mechanical stress is caused by certain processing steps in the device fabrication. Local oxidation of silicon (LOCOS) to isolate the active areas of silicon introduces a significant amount of local mechanical stress in the silicon substrate and within the active areas of silicon (Figure 6.1 a and b).[7] After deposition of pad oxide, silicon nitride is deposited

and patterned to mask the silicon active areas. Further oxidation of the rest of the silicon creates high stress fields at and around the devices, because silicon dioxide is 2.2 times larger in volume than silicon itself.[8] The area directly underneath the edge of the nitride mask, called the bird's beak due to its shape (Figure 6.1 c), is a high stress region because of the mechanical restriction for expansion.[7]
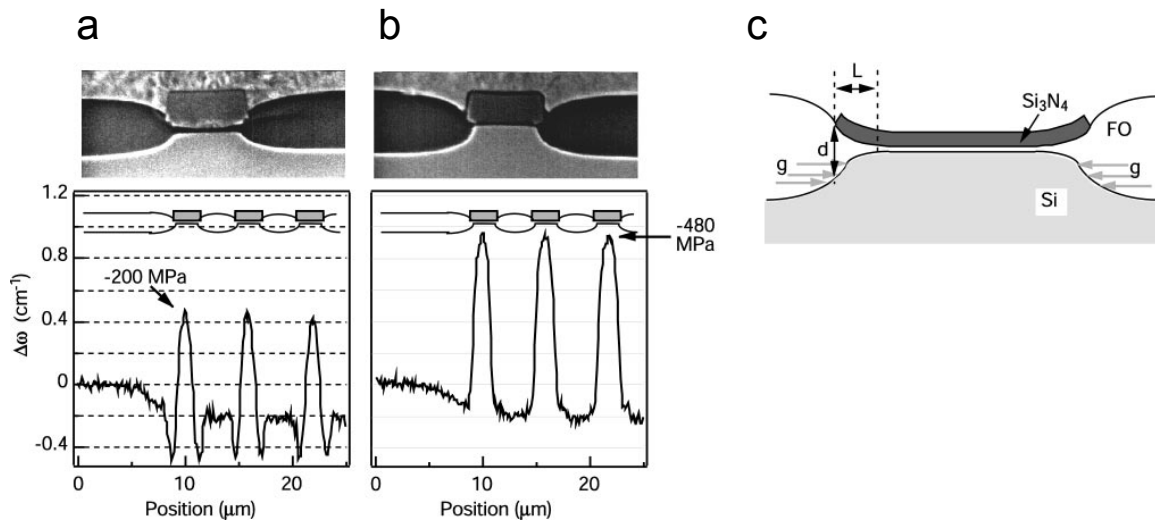


**Figure 6.1 LOCOS isolation:** Shift of the phonon frequency, $\Delta\omega$ measured on three lines of an array of 3 µm wide a) PBLOCOS (poly buffered local oxidation of silicon), b) PELOX (polysilicon encapsulated local oxidation of silicon) isolation structures. A typical SEM picture of the corresponding structure is shown at the top, c) schematic of a LOCOS structure (Reprinted from Wolf et al).[9]
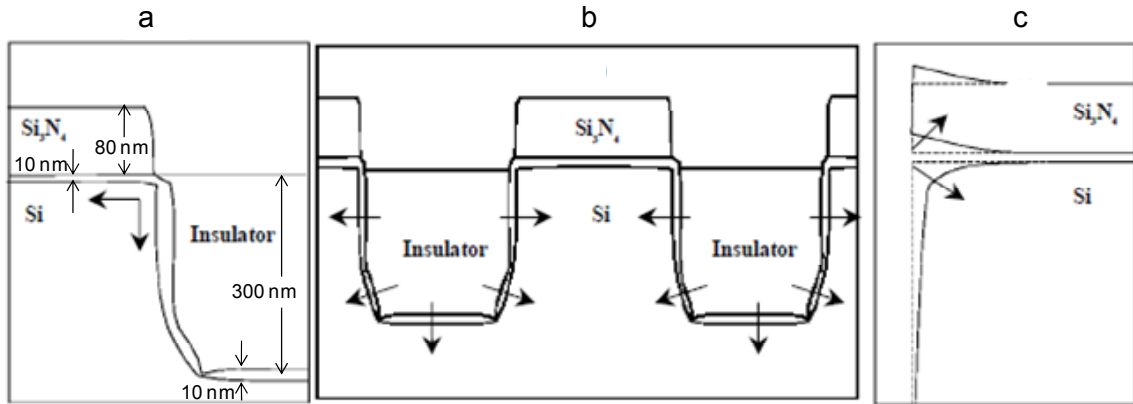
**Figure 6.2 Diagram of STI isolation and sources of stress in it**: Major sources of stress in STI fabrication include the following: (a) nitride film edge-induced, (b) insulator thermal expansion mismatch induced, and (c) sidewall oxidation volume expansion-induced stress. (Figure c shows the uplift at the corner of STI where the $Si_3N_4$ puts backpressure on the liner oxide as it grows giving rise to high compressive stress at the upper corner of the adjacent silicon. The oxide fill in the STI is deposited. The distance between STI trenches is the silicon RX width (WRX), where RX is active silicon region bounded by STI isolation. Arrows indicate force vectors (Reprinted from Rueda et al.).[8]

Shallow Trench Isolation (STI) (Figure 6.2) is another isolation technique which is widely used today in CMOS process technology. In this method the nitride patterning follows by creating a trench surrounding the active area of silicon by reactive ion etching. This follows sacrificial side wall oxidation, oxide deposition in the STI, and chemical mechanical polishing. Although the stress field produced in this process may not be large compared to that of LOCOS oxidation, it can significantly affect the device performance (Figure 6.3).[10] Apart from those two causes of stress generation, other process steps such as thin film deposition and ion implantation can also contribute via differential thermal expansion and generation of dislocations.
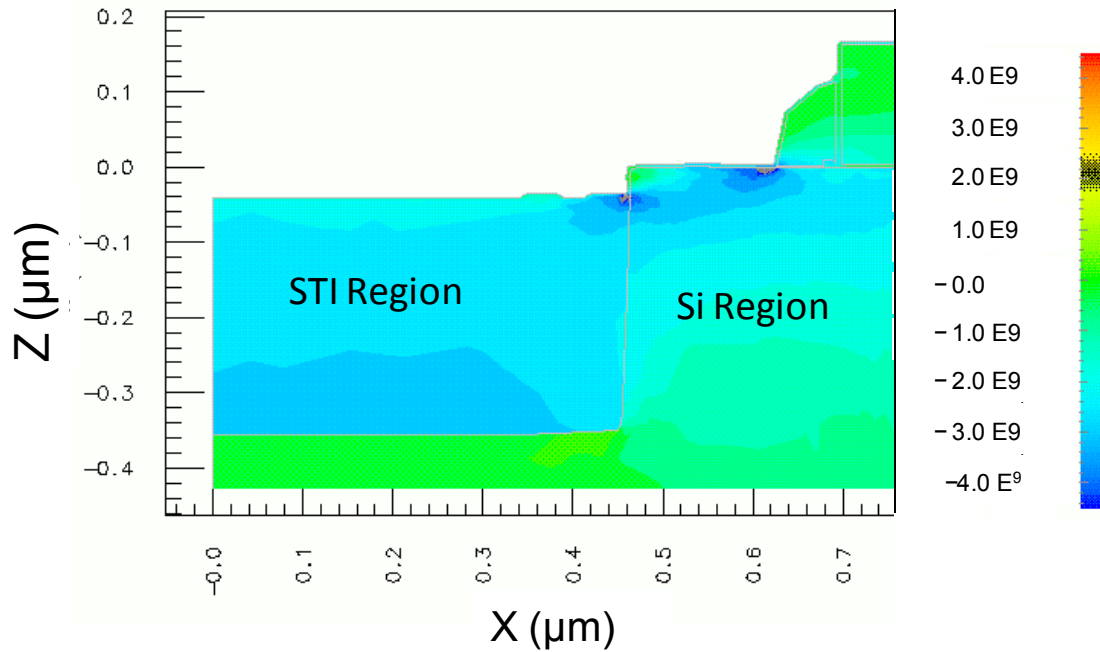
**Figure 6.3 Cross sectional TCAD simulation showing stress distribution in half of a device with STI, silicon active area, and with the gate region**, where negative/positive values are compressive/tensile stress respectively. Dark blue regions have highest tensile stress. (Figure courtesy Dr. James Slinkman, IBM).

### 6.2.2  Influence of Stress on Energy Bands and Band Gap

Understanding how mechanical stress influences the mobility of carriers and energy bands of silicon requires a discussion of the piezoresistive effect of silicon. The relationship between the electric field vector ($\varepsilon$) and the current vector ($i$) can be expressed along with a resistivity tensor ($\rho$) as follows (Equation 6.1).

$$
\begin{bmatrix} \varepsilon_1 \\ \varepsilon_2 \\ \varepsilon_3 \end{bmatrix} = \begin{bmatrix} \rho_1 & \rho_4 & \rho_6 \\ \rho_4 & \rho_2 & \rho_5 \\ \rho_6 & \rho_5 & \rho_3 \end{bmatrix} \begin{bmatrix} i_1 \\ i_2 \\ i_3 \end{bmatrix} \tag{6.1}
$$

If the three major system axes are aligned with the <100> crystallographic directions of silicon, then the diagonal terms represent the electric fields and currents along the same

160

axes and the off diagonal elements represent that of perpendicular directions. In an

isotropic condition all the diagonal terms reduces to a single component and the off

diagonal elements are zero, which we can write as

$$\varepsilon = \rho i \tag{6.2}$$

If the system is subjected to mechanical stress, then we can express the change of the

resistivity components by adding a small perturbation to it (Equation 6.3).

$$\begin{bmatrix} \varepsilon_1 \\ \varepsilon_2 \\ \varepsilon_3 \\ \varepsilon_4 \\ \varepsilon_5 \\ \varepsilon_6 \end{bmatrix} = \begin{bmatrix} \rho \\ \rho \\ \rho \\ 0 \\ 0 \\ 0 \end{bmatrix} + \begin{bmatrix} \Delta\rho_1 \\ \Delta\rho_2 \\ \Delta\rho_3 \\ \Delta\rho_4 \\ \Delta\rho_5 \\ \Delta\rho_6 \end{bmatrix} \tag{6.3}$$

The change in the resistivity can be related to the stress by which the change was initiated

with piezoresistance coefficients $\pi_{ij}$. The 36 components of piezo coefficients reduce to

three independent components due to the cubic crystal symmetries of silicon (Equation

6.4).

$$\frac{1}{\rho}\begin{bmatrix} \Delta\rho_1 \\ \Delta\rho_2 \\ \Delta\rho_3 \\ \Delta\rho_4 \\ \Delta\rho_5 \\ \Delta\rho_6 \end{bmatrix} = \begin{bmatrix} \pi_{11} & \pi_{12} & \pi_{12} & 0 & 0 & 0 \\ \pi_{12} & \pi_{11} & \pi_{12} & 0 & 0 & 0 \\ \pi_{12} & \pi_{12} & \pi_{11} & 0 & 0 & 0 \\ 0 & 0 & 0 & \pi_{44} & 0 & 0 \\ 0 & 0 & 0 & 0 & \pi_{44} & 0 \\ 0 & 0 & 0 & 0 & 0 & \pi_{44} \end{bmatrix} \begin{bmatrix} \sigma_1 \\ \sigma_2 \\ \sigma_3 \\ \sigma_4 \\ \sigma_5 \\ \sigma_6 \end{bmatrix} \tag{6.4}$$
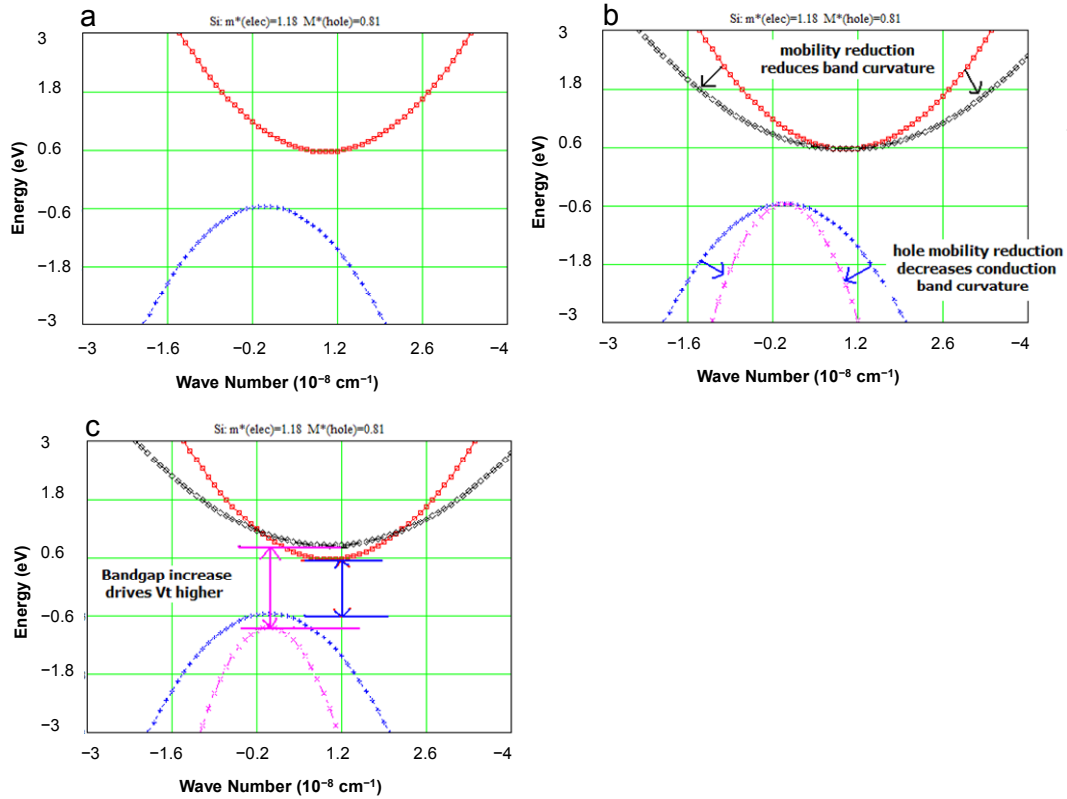
**Figure 6.4 Energy band distortion and change of band gap of silicon**: a) conduction and valence bands for unstressed silicon, b) change of the curvature of bands, c) change of band gap and reduction of mobility which in return drive the threshold voltage higher. (Diagrams courtesy of Dr. James Slinkman, IBM)

In the simple case of uniaxial stress, similar to the mechanical stress created by the STI process, magnitude of the distortion of the conduction bands are different for directions parallel and perpendicular to the axis of stress (Figure 6.4). The effective masses of the carriers are proportional to the curvature of bands and the mobility of carriers is a function of the effective masses. Therefore distortion of energy bands results in carrier mobilities and resistivities which are dependent on crystallographic directions of the semiconductor. This phenomenon affects devices such as *p-n* junctions and bipolar transistors where the operation is governed by the flow of minority carries. The reader is referred to Rueda et al. for a complete discussion.[8] Typically devices are fabricated on

Si(100) wafers and are aligned parallel to Si <110> crystallographic directions. The perpendicular direction is also <110> due to 4-fold cubic symmetry of the Si(100) face. The differential surface photovoltage (DSPV) method makes use of this difference of the band distortion and the surface photovoltage in the parallel and perpendicular directions of the devices to measure stress. The method will be discussed in detail later in this chapter.

### 6.2.3 Methods for Mechanical Stress Analysis

There are several techniques used to measure mechanical stress. These include micro-Raman spectroscopy, X-ray diffraction (XRD), nano-beam diffraction (NBD), and converging beam electron diffraction (CEBD) which will be discussed in the following sections in detail. Attempts have been made to measure stress in devices and in strained membranes by mapping surface potential with scanning Kelvin probe force microscopy (SKPFM).[8,11] As VLSI device feature sizes shrinks, the importance of stress to the function of device increases. This trend severely challenges spatial resolution of available stress measurement techniques.

### 6.2.3.1 Confocal Micro-Raman Spectroscopy

Confocal micro-Raman spectroscopy has been extensively used to study stress in silicon devices and in silicon structures.[9,12-16] This is a chemically and structurally sensitive analytical technique which combines Raman spectral imaging with high resolution confocal microscopy. It enables identification of chemical composition of the sample as well as imaging of spatial variations of those compositions. Mechanical stress in silicon changes lattice parameters of silicon and as a result changes the phonon frequency. By

comparing the Raman shift of the phonon frequency, quantitative measurement of stress and its spatial distribution (imaging) can be obtained.

In confocal microscopy, light from a laser is focused to a spot on the sample surface and scattered light from the sample is brought to a focus at the image plane. A pinhole placed at the image plane and aligned with the laser spot image, only allows scattered light from the laser spot to pass through to the detector and rejects all other stray light. The sample is then scanned in x, y, and z and an image is built up from the resulting pixels. This provides a 3D resolved image and significantly reduces background signals. A complete Raman spectrum is recorded at every imaging point. In our study, only a 2D image was recorded. The Raman scattering is the inelastic scattering of light (photons) from the lattice vibrations (phonons). The frequency shift of the scattered light is the frequency of lattice vibrations, 520 cm$^{-1}$ for unstressed silicon. Stress changes the lattice constant and thus the phonon frequency. Compressive stress causes an increase in the phonon frequency (positive shift) while tensile stress causes the phonon frequency to decrease (negative shift). By recording this shift in the phonon frequency, a stress image of the sample can be obtained. Spatial resolution of this technique is ultimately limited by diffraction, but typically to 400–1000 nm (0.61$\lambda$/2N.A.). By using shorter wavelength light sources resolutions down to 200 nm could be achieved.[17] Spatial resolution limits the applicability of Raman spectroscopy for measuring the local stress present in devices of silicon CMOS technologies with size of device or the width of the RX region (WRX) less than 150 nm.

### 6.2.3.2 Nano-Beam Electron Diffraction (NBD)

Nano-beam electron diffraction often referred to as simply nano-beam diffraction (NBD) is a TEM based method which can be used to measure stress with submicron spatial resolution (~10 nm) limited by the electron beam size.[18-19] This method has been used extensively to characterize stress present in CMOS devices made with strained Si/SiGe technology.[18-20] The method is most suitable for measuring stress in individual regions in the device. Because the diffraction pattern must be measured and calculated at each position, it is technologically challenging to map the stress profile of a sample. Other TEM based techniques such as high resolution transmission microscopy (HRTEM)[21] and electron diffraction contrast imaging (EDCI)[22] also have been used for stress profiling. Detrimental to accurate stress measurements is the issue that the energy of the electron beam can impart enough energy to heat the sample a few nanometers deep, relaxing the stress. Hence these methods are potentially destructive and limit the use in routine stress measurements.

### 6.2.3.3 Converging Beam Electron Diffraction (CEBD)

Other TEM based techniques such as converging beam electron diffraction (CBED) need complex data deconvolution and interpretation.[23-25] Quantitative values for stress can be calculated by comparing the experimental data with simulated data.[26] Higher-order Laue zone (HOLZ) lines are sensitive to lattice parameters. Lattice parameters are a function of stress present in the sample. Any shift of the shapes of the HOLZ lines from that of unstressed sample is a representation of the stress/strain condition of the sample.

### 6.2.4 Major Processing Steps Involved in Fabricating a CMOS Transistor

Present CMOS technology requires fabrication of complimentary $n$MOS and $p$MOS transistor pairs on the same substrate. This requires creation of special regions (wells) on the substrate which are opposite to the substrate semiconductor type. For $n$-well fabrication technology, the $n$MOS transistor is fabricated on $p$-type substrate and a $p$MOS transistor is fabricated in the $n$-well, which is built into the $p$-type substrate. The industrial CMOS manufacturing process is complicated, but a description of the essential basic steps involved in the fabrication process follows.

The starting substrate for CMOS fabrication process is a lightly doped $p$-type silicon substrate. The impurity concentration is typically less than $10^{15}$ cm$^{-3}$. After growing the initial oxide layer on the surface which is about 1 μm thick, the processes of defining well regions starts. The various steps involved in the process are as follows (Figure 6.5).

1. RX pattern definition

2. Planarization

3. $n$-well implant

4. $p$-well implant

5. Removal of PW mask (block mask) and sacrificial oxide

6. Gate oxide deposition

7. Gate poly silicon deposition

8. Gate mask and poly silicon gate RIE etching

9. Side wall oxidation

10. NFET $n$ "extension" and $p$-type (halo) implants

11. PFET $p$ "extension" and $n$-type (halo) implants

12. Final spacer nitride deposition

13. Final spacer nitride RIE etch

14. $n^+$ source/drain mask and implant

15. $p^+$ source/drain mask and implant

16. Silicide (ohmic refractory metal) deposition

17. Ohmic contacts (silicide) formation anneal

18. Metal contacts and wiring
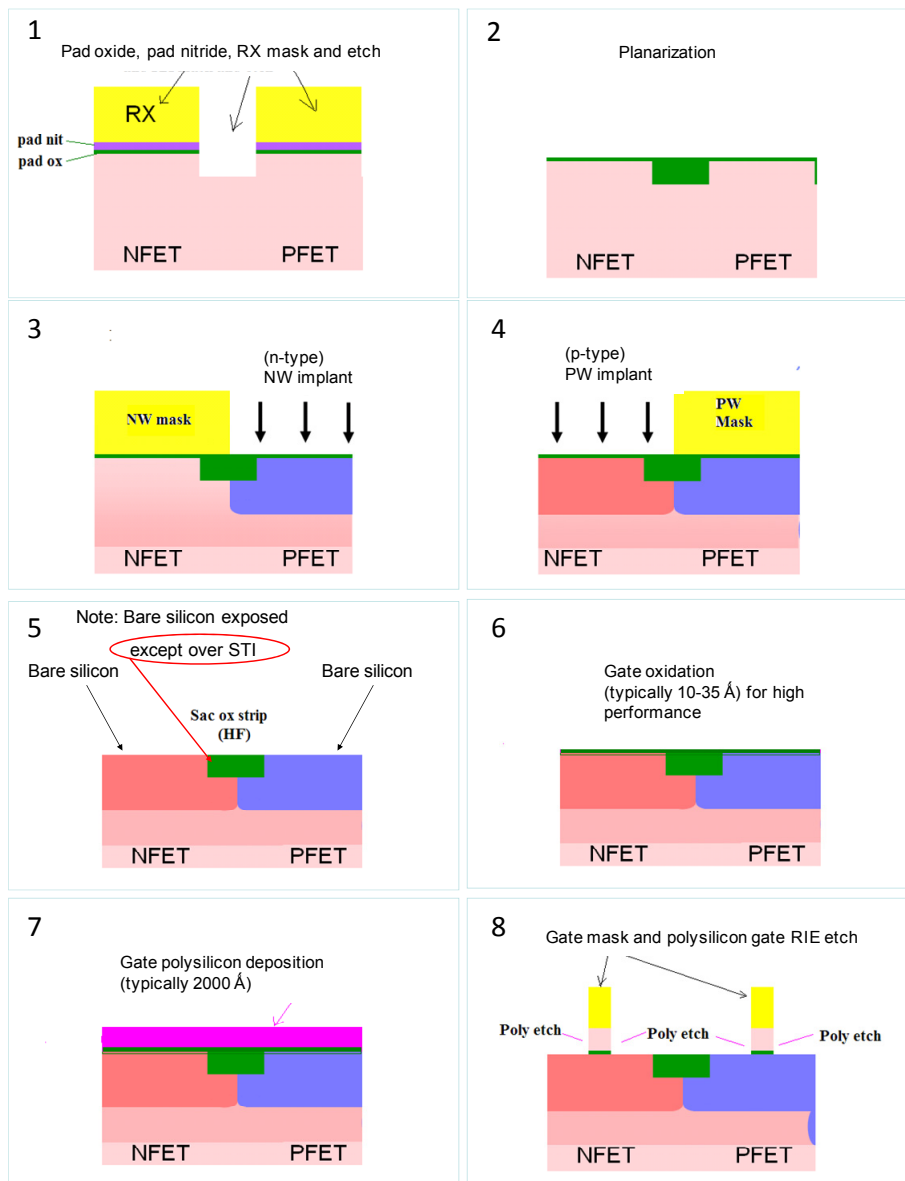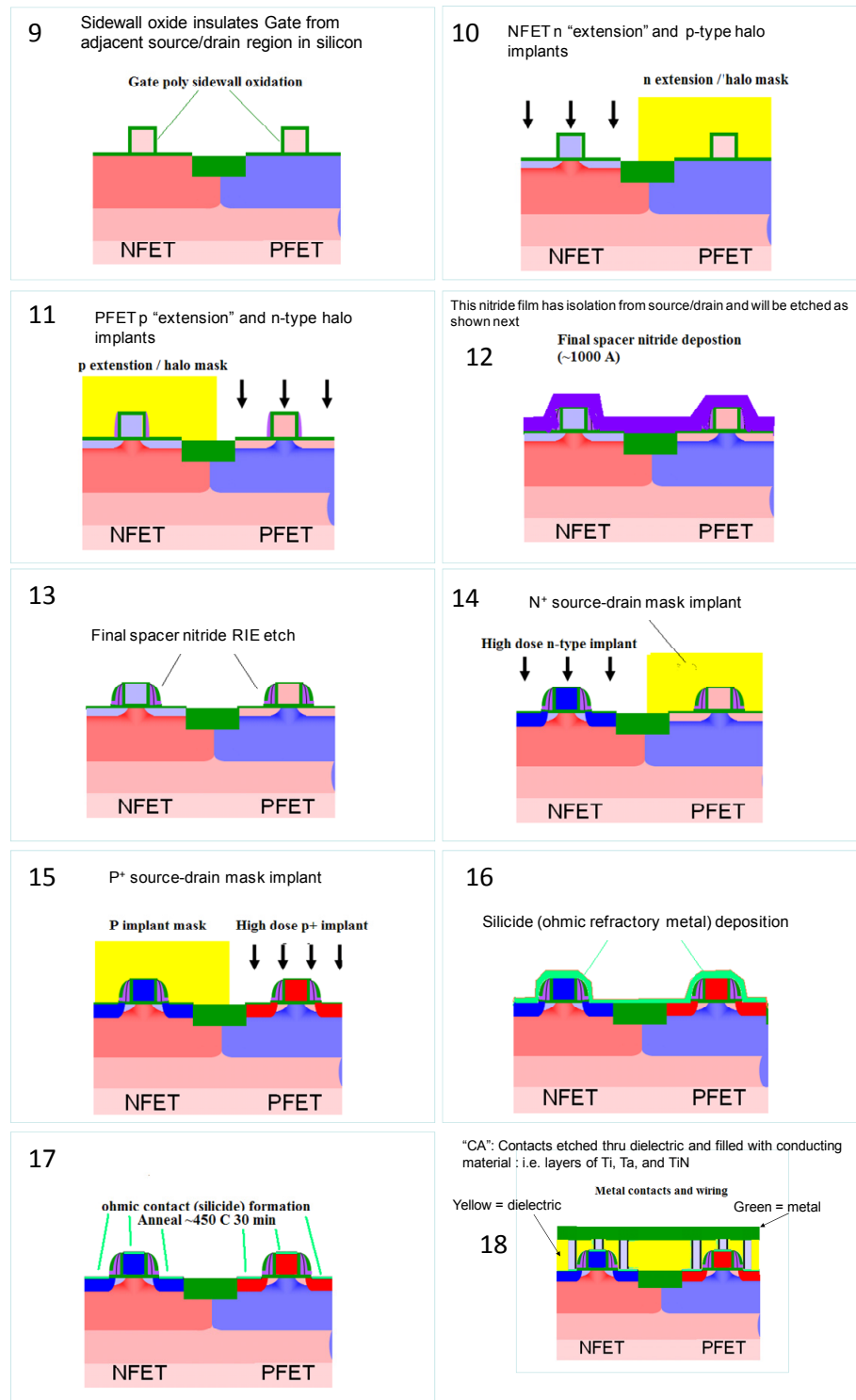
**Figure 6.5 Main steps of the process flow for fabrication of CMOS *n*FETs and *p*FETs** (diagram courtesy Dr. James Slinkman, IBM).

### 6.2.5 Photolithography

Patterning of the silicon dioxide surface is achieved by a photolithographic process. The silicon dioxide surface is covered with a photoresist, which is a light sensitive organic polymer and a material insensitive to acids. If the photoresist is exposed to light, it becomes soluble in a developer solution (positive photoresist). The patterns are defined by shielding the areas of photoresist we want to keep with a mask and exposing the rest of the surface to UV light. The exposed areas then become soluble to the developer solution and are thus removed. Silicon dioxide in the exposed areas can be removed by using hydrofluoric acid or dry plasma etching. After the treatment of the exposed surface is finished, the photoresist is stripped off from the entire surface.

There are two types of photoresists which are called positive and negative photoresist, used in silicon semiconductor technology. Positive photoresist is initially insoluble but becomes soluble after exposing to UV radiation. Negative photoresist has the opposite behavior. It is initially soluble but becomes insoluble after UV exposure. Therefore defining of the mask depends on the type of photoresist to use. Positive photoresists are the most widely used in manufacture of high density integrated circuits. Although the solubility of positive photoresists is lower than that of their negative counterparts; positive resists have better photolithographic resolution.

### 6.2.6 Surface Photovoltage (SPV)

The periodic structure of an ideal crystalline semiconductor results in the appearance of energy bands separated by forbidden energy gaps. Symmetry breaking lattice termination at the surface, dangling bonds, reconstructions, steps, kinks, and impurity atoms at the surface result in formation of surface localized energy states at the surface.[27-28] This

results in charge redistribution between the surface and the bulk of the semiconductor in order to maintain a thermal equilibrium and formation of a surface space-charge region. This region is not electrically neutral so there is an electric field between the surface and the bulk. Therefore the surface is at a different potential than the bulk of the semiconductor.

The photovoltaic effect of a semiconductor is the illumination induced change of the equilibrium potential distribution of the semiconductor. The surface photovoltage is a specific variant of the more general photovoltaic effect and only occurs if the carrier generation due to the illumination followed by net charge distribution. The driving force for the redistribution of carriers is localized in the space charge region (SCR), while the rest of the bulk remains neutral. The charge neutrality condition $Q_{ss} + Q_{sc} = 0$ ($Q_{ss}$ − charge in the surface states, $Q_{sc}$ − charge in the space charge region) must hold in the absence of an external electric field even under illumination. The absorbed photons induce the formation of free carriers by creating electron-hole pairs via trap-to-band transitions and/or releasing captured carriers via trap-to-band transitions. Thus a considerable amount of charge is transferred from the surface to the bulk or bulk to the surface and redistributed in two regions. The charge distribution and the electric potential are interdependent. Therefore the potential drops across the SCR and also the surface potential.

SPV strongly depends on the incident photon energy i.e. whether it is a super-band gap, where the photon has sufficient energy to initiate a band to band transition, or sub-band gap energy photon, where the photon can only initiate sub-band to band or band to sub-band transitions. Figure 6.6 illustrates various types of excitation mechanisms

which lead to the SPV for an *n*-type semiconductor. The electrons created by the photons are swept away from the surface by the electric field at the SCR and holes are attracted to the surface, thus reducing the charge at the surface (Figure 6.6a). This results in reducing the band bending at the surface. Figure 6.6b shows the situation where electrons or holes are preferentially trapped in defect states thus modifying the surface potential. In the case of sub-band gap illumination, the trapped carriers in surface states are excited and results in modification of surface charge. If the photon energy $hv > E_c–E_t$ where $E_t$ is the energy of the surface state, then those electrons get excited into the conduction band and are swept away by the electric field reducing the band bending as shown in Figure 6.6c(i). If the photon energy $hv > E_t–E_c$ then valence band electrons get excited into the surface states or similarly holes in the surface states get excited to the valence band, hence increasing the density of charge in surface states which results in increasing the band bending. In photon assisted tunneling (Franz-Keldysh effect), sub-bandgap photons whose energy is close to $E_g$ excites band-to-band transitions in the presence of an external electric field. All the experiments we describe here fall into the category of super-bandgap illumination.
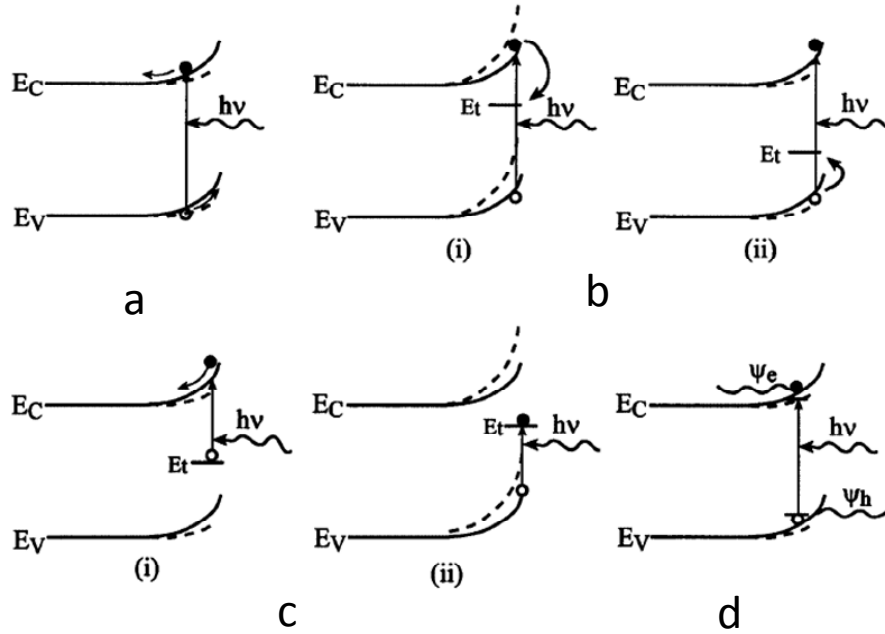
**Figure 6.6 Band diagrams of the surface space charge-region at a depleted *n*-type semiconductor surface under different conditions** showing the energy levels as a functions of distance from the surface: (a) super-bandgap illumination with carrier separation under an electric field; (b) super-bandgap illumination with preferential trapping of electrons (i) and holes (ii); (c) sub-bandgap illumination with excitation of trapped electrons (i) and holes (ii); (d) sub-bandgap illumination with Franz-Keldysh absorption, where e and h denote electron and hole wave functions, respectively. In all diagrams, solid and dashed lines indicate band positions in the dark and under illumination, respectively. Straight arrows denote carrier generation and curved arrows denote carrier trapping. (Reprinted from Kronik et al.).[27]

### 6.2.7   Kelvin Probe Method

The Kelvin probe is a non-contact method to measure the contact potential difference between a reference material and a sample and is sensitive to changes in the work function. Its function can be understood by considering a parallel plate capacitor. The schematic band diagram of two metals in such arrangement is shown in Figure 6.7. The metals are electrically neutral and share a common vacuum level, Figure 6.7a. Now if the two plates are electrically connected, charge must flow from the metal with smaller work function to the other until equilibrium of the Fermi levels is achieved. The charge transfer

results in an electric field between the two plates shown by the slope of the local vacuum level within the gap (Figure 6.7b). This potential difference is equal to the difference of work functions also known as the contact potential difference (Equation 6.5).

$$eV_{CPD} = W_1 - W_2$$

<div align="right">(6.5)</div>
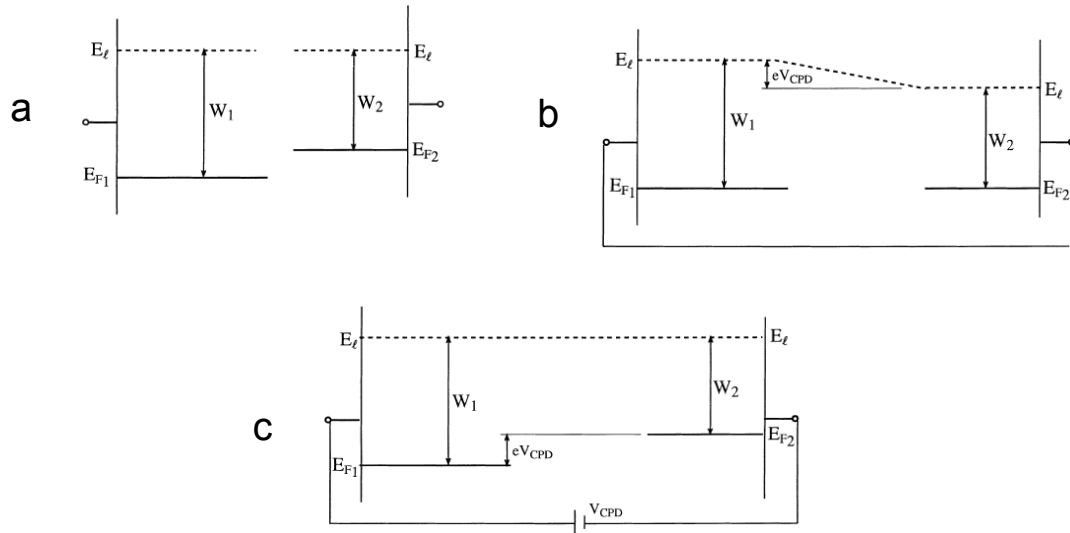


**Figure 6.7 Schematic band diagram of a parallel plate capacitor formed from two different metals**, with the two plates: (a) isolated, (b) short-circuited, (c) connected through a DC bias equal and opposite to the contact potential difference (Reprinted from Kronik et al.).[29]

Contact potential difference cannot be measured by conventional contact methods (e.g. voltmeter). This difficulty was overcome by using a noncontact technique to measure the CPD by a current null method. If an external voltage is applied between the plates of the capacitor (in this case, between the probe and the sample) until the electric field between the plates is zero, the applied voltage is then equal and opposite in sign to the CPD (Figure 6.7c). The null point is detected by changing the separation between the capacitor plates. If the electric field between the plates is not zero, charge still resides on

the plates. Changing the separation between the plates changes the capacitance and causes a current to flow in the external circuit which can be easily detected. This current is zero if and only if the applied voltage exactly cancels the CPD. Thus the CPD can be easily found by determining the external bias for which no external currents are observed upon changing the spacing between the plates. This type of arrangement is known as a Kelvin probe. The Kelvin probe is commonly used to measure the changes of the work function and can also be used to measure SPV. Kelvin used an electrometer to manually check the capacitor discharge which took several minutes for each measurement. In 1932 Zisman introduced a more convenient vibrating capacitor Kelvin probe technique which is used today.[30] In this method, the capacitor plate separation is varied using a vibrating reference plate. The resulting ac voltage is nulled by an applied dc bias.

### 6.2.7.1 Scanning Kelvin Probe Force Microscopy

Invention of the scanning tunneling microscope by Gerd Binnig and Heinrich Rohrer in 1981 followed by development of many other scanning probe techniques (SPM) enlightened the scientific community who study surfaces/interfaces of materials in atomic scale.[31] SPM techniques are used to obtain high resolution images of surfaces and gives information on spatial structure and surface homogeneity. SPM is a family of imaging methods which create images using a contrast mechanism dependent on the "probe" technique. One such SPM technique is the atomic force microscope (AFM) which detects the short range van der Waals force between the tip and the sample. When combined with Kelvin probe technique this instrument is capable of probing the contact potential differences with higher spatial resolution than the normal scanning Kelvin probe. Wickramasinghe and co-workers pioneered the scanning Kelvin probe force microscope

(SKPFM) in 1988.[32] After the initial report, there were many studies which used SKPFM to characterize semiconductors and devices.[33-40] Figure 6.8 is a generic diagram of the scanning Kelvin probe force microscope (SKPFM) which operates in a non-contact mode.

The AFM measures the deflection of the cantilever due to local forces exerted on the tip by the surface of the sample. The tip is vibrated at a frequency $\omega_1$. The amplitude of oscillation is altered by the tip sample interaction. This deflection is typically monitored by the optical deflection of a laser by the cantilever using a position sensitive detector or a laser interferometer. A feedback loop modifies the tip sample distance so as to keep the vibration amplitude constant while the tip scans across the sample. Therefore the tip follows the topography of the sample. This method which keeps the vibration amplitude constant is the amplitude modulation method. A force gradient between the tip and the sample shifts the resonance frequency of the cantilever as well. It is possible to measure this change of the resonance frequency and use a feedback loop to bring it to the original value. This type of feedback control is frequency modulation. For a conducting tip which is electrically connected to the sample, the electrical potential difference and the field between them are well defined. The Coulomb force $F$ between them is defined as in equation 6.6.

$$F_e = -\frac{\mathrm{d}}{\mathrm{d}z}\left(\frac{1}{2}CV^2\right) = -\frac{V^2}{2}\frac{\mathrm{d}C}{\mathrm{d}z} \tag{6.6}$$

where $V$ and $C$ are voltage and capacitance between the tip and the sample, and the $z$ is tip-sample distance. The applied voltage between the tip and the sample is sinusoidal $V_{ac}\sin(\omega_2 t)$. The gradient of $C$ or $\mathrm{d}C/\mathrm{d}z$ is poorly known and is not a well controlled

experimental parameter. Therefore mapping of $V$ as a measure of $F$ is difficult and not very reliable. Instead of using only an ac voltage, if a combination of an ac and a dc voltage $V_{dc}$ (equation 6.7) is used, a more accurate measurement of surface potential mapping can be achieved.[36]
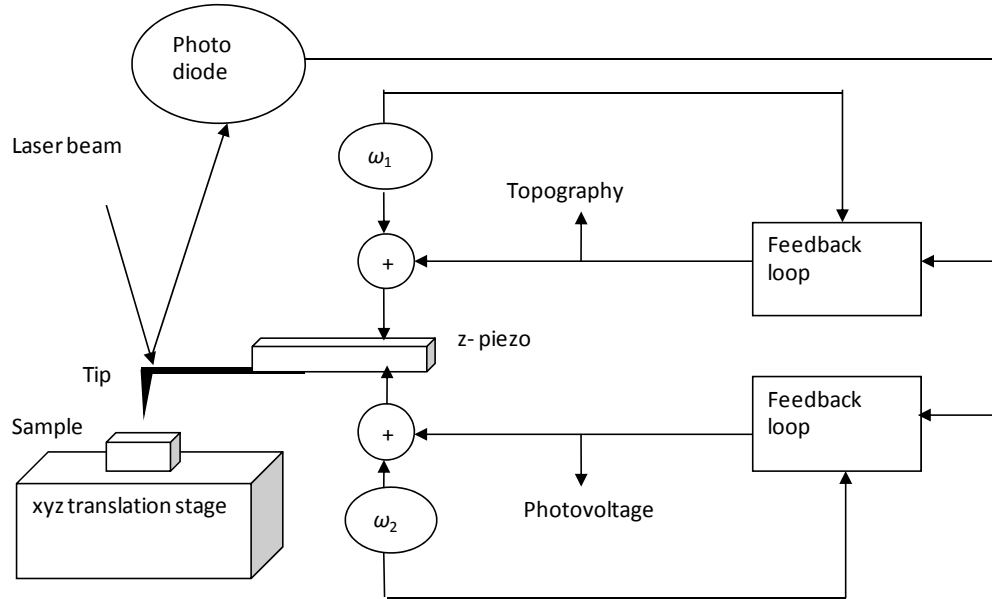


**Figure 6.8 Block diagram of the scanning Kelvin probe force microscope**

$$V = V_{dc} + V_{ac} \sin(\omega_2 t) \tag{6.7}$$

Here the dc part consists of the applied bias voltage and the surface potential. Hence,

$$V_{dc} = V_b - \frac{\Delta \Phi}{q}$$

Therefore, the electrostatic force can be written as

$$F_e = -\frac{1}{2} \frac{dC}{dz} \left[ V_{dc}^2 + 2V_{dc}V_{ac}\sin(\omega_2 t) - \frac{1}{2}V_{ac}^2\cos(2\omega_2 t) \right] \tag{6.8}$$

The force consists of three parts, *dc* component, an *ac* component at frequency $\omega_2$, and an *ac* component at frequency $2\omega_2$.

Substituting for $V_{dc}$ we can write the force as

$$F_e = \frac{dC}{dz}\left[\left(\left(V_b - \frac{\Delta\Phi}{q}\right)^2 + \frac{1}{2}V_{ac}^2\right) + \left(V_b - \frac{\Delta\Phi}{q}\right)V_{ac}\sin(\omega_2 t) + \frac{1}{4}V_{ac}^2\cos(2\omega_2 t)\right](6.9)$$

The full force acting on the tip is,

$$F = V_1\sin(\omega_1 t) - \frac{H}{Z^6}$$

$$-\frac{dC}{dz}\left[\left(\left(V_b - \frac{\Delta\Phi}{q}\right)^2 + \frac{1}{2}V_{ac}^2\right) + \left(V_b - \frac{\Delta\Phi}{q}\right)V_{ac}\sin(\omega_2 t) + \frac{1}{4}V_{ac}^2\cos(2\omega_2 t)\right]^{(6.10)}$$

In equation 6.10, the first term is the driving force applied to the cantilever. The second term is the attractive van der Waals force between the tip and the sample. The third term is the electrostatic force and has three different components: DC, $\omega_2$, and $2\omega_2$. A mixed DC and AC bias is applied to measure the surface potential.[29] If the DC bias is adjusted such that the force at the frequency $\omega_2$ is nulled through a feedback control system, then the potentials of the tip and the sample are equal and the electric field will be zero. Therefore the knowledge of the d$C$/d$z$ is avoided and the measurement is insensitive to the variation of capacitance at different points.

In the diagram shown in Figure 6.8, there are two feedback loops each operating at different frequencies. The topography feedback loop maintains constant amplitude of oscillation of the tip at the frequency $\omega_1$ by changing the tip sample separation. A second feedback loop maintains a null oscillation at the $ac$ voltage frequency $\omega_2$ by changing the dc bias on the tip. In practical situation, the voltage feedback loop can be performed

simultaneously with the topography feedback loop. The SKPFM has been used to measure SPV of semiconductors and devices.[41-42]

## 6.3    Materials and Methods

### 6.3.1    CMOS Devices Used in the Study

The structure consists of a silicon stripe which is used for the construction of active areas of the device surrounded by a shallow trench isolation which is again surrounded by a thin silicon stripe. A schematic of the cross section and plan views of the device is shown in Figure 6.9 a and b. Figure 6.9c is a SEM image of cross section of the array of devices while Figure 6.9d is an optical image of the plan view of the structure. We investigated similar type devices in five silicon wafers which were pulled at different stages of processing. The full details of the process parameters for wafers pulled at different processing stages of processing can be found in Appendix 2.
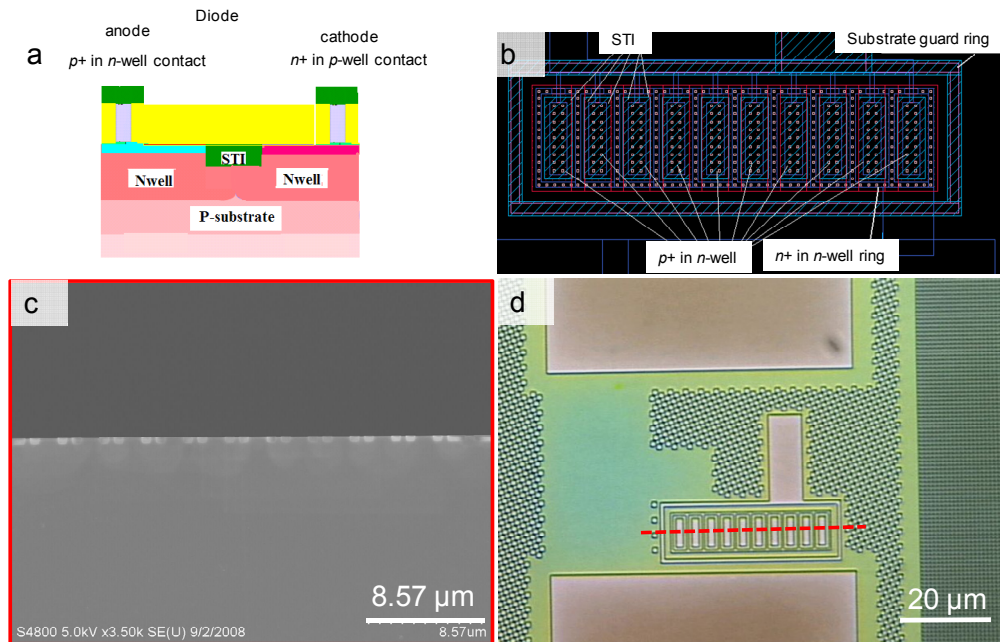


**Figure 6.9 Device structures (diode) used in the study:** a) diagram of the cross section of one of the diode, b) plan view of the array of diode structures, c) SEM image of the cross section of the entire array, d) optical micrograph of the array of devices.

### 6.3.2    Calibration Structures

We used arrays of indents on a silicon substrate as calibration structures to compare the data obtained from SSPVM to that from micro-Raman spectroscopy. One array consists of nine indents in a 3 × 3 matrix. The forces which were used to make the arrays are 7.5 mN and 10 mN and the separations of indents in row and column directions were 2 μm and 5 μm. We only discuss results for the 7.5 mN, 2 μm array of indents in this chapter. The indenter was a Hysitron Ubi1 nano-indenter with Berkovich tip.
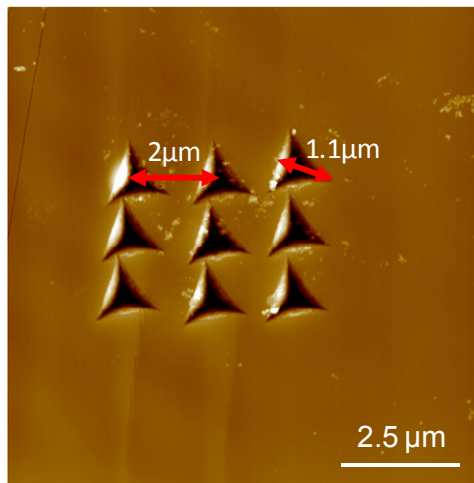


**Figure 6.10 AFM image of an array of indents** (7.5 mN force, 2 μm separations)

### 6.3.3    Confocal Raman Imaging

A WITec Confocal Raman microscope CRM 200 was used to obtain Raman spectroscopic data. The system combines a triple grating Raman spectrometer with a high resolution confocal optical microscope. Combination of these two systems provides sub-micrometer lateral resolution Raman imaging. Using green excitation light, a resolution down to 220 nm is possible. The laser which is fitted with the microscope is 514.725 nm and the spectral center was at 499.21 nm. The integration time was 0.02 seconds. The grating is 1800 g/mm and the objective used is 100× with 0.9 numerical aperture.

### 6.3.4  Differential Surface Photovoltage (DSPV) and Instrumentation

### 6.3.4.1  Modification to the Scan Head of the Digital Instrument's Multimode AFM

The scan head assembly of the Digital Instruments Nanoscope III multimode AFM was modified to accommodate the two lasers. The lasers are aligned such that they are perpendicular to each other and make 45° with the axis of the cantilever. Both of the laser beams are *p*-polarized and incident on the surface of the sample at a Brewster's angle to optimize the interaction of the silicon substrate.
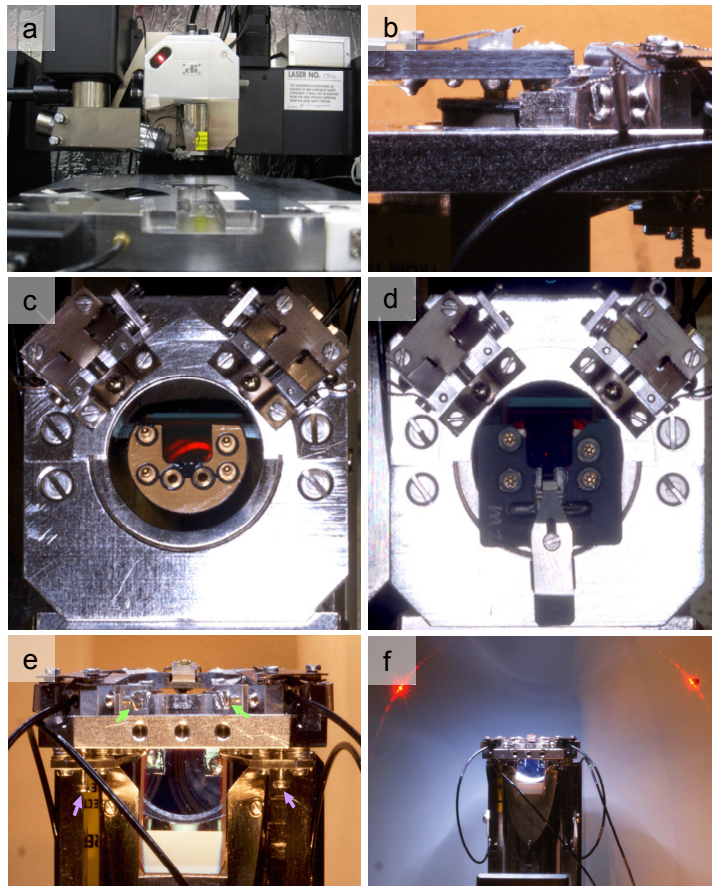


**Figure 6.11 Photographs of mechanical modifications to the scanning head assembly of the Digital Instrument's Nanoscope III AFM**: a) scanning head in position above the stage in the instrument with optical fibers attached, top-down view of the scanning head and the mechanical guide of the optical fibers b) without the tip assembly c) with the tip assembly, d) side view of the same system, and e) laser light scattered from the AFM tip.
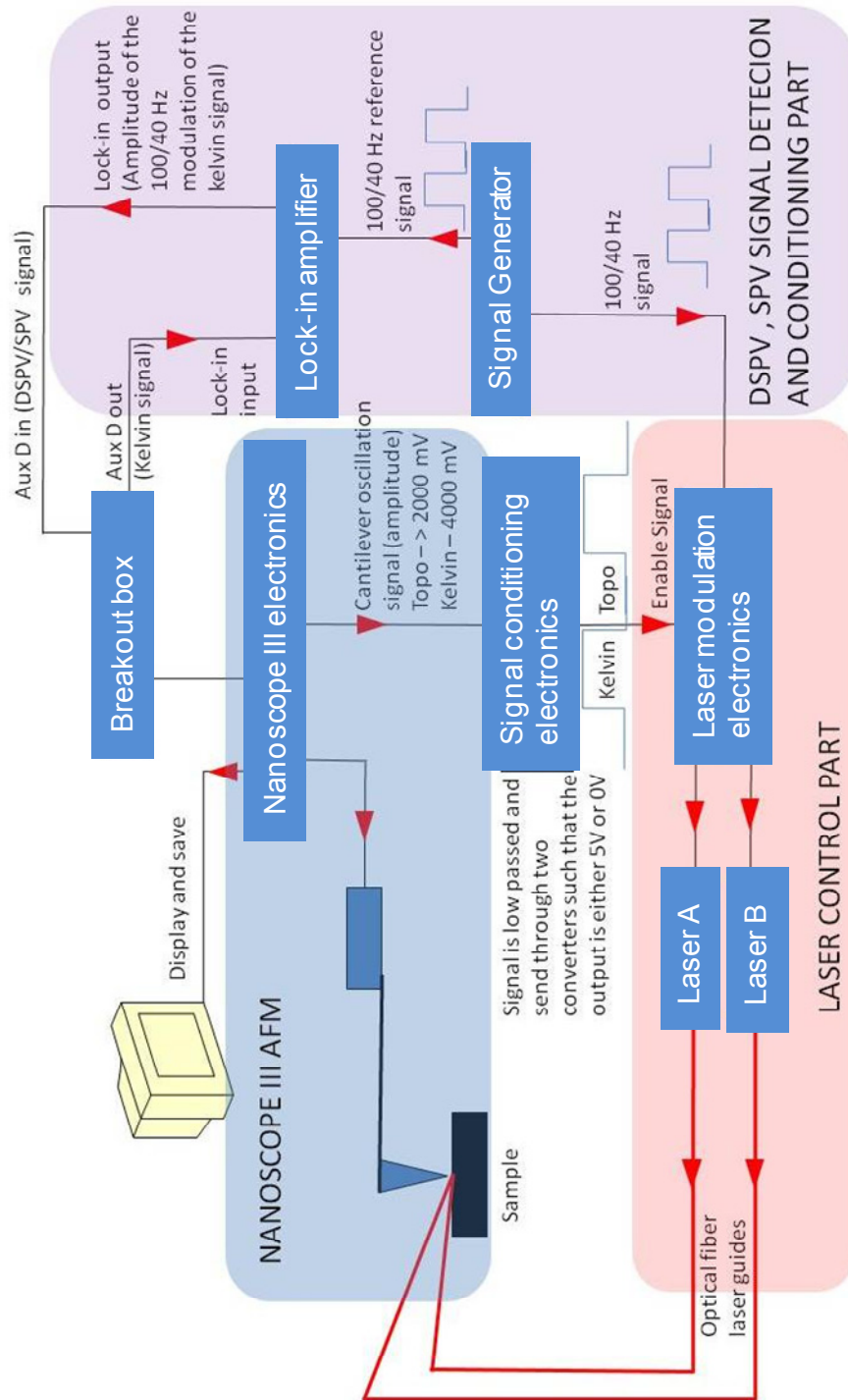
**Figure 6.12 Block diagram of the instrument setup and the method.**

### 6.3.4.2 Measurement of SPV and DSPV by Single Lock-in Method

The Nanoscope III AFM is set to operate in Kelvin mode. It first obtains topographic data for a line scan. Then it disables the topography feedback loop and enables the Kelvin feedback loop for measuring the potential difference between the tip and the sample. The tip rescans the sample line using the topographic data just recorded allowing the tip to maintain a constant height from the surface during Kelvin data acquisition. For these SPV/DSPV measurements, we only wanted the lasers to be active during the Kelvin part of the scan. To achieve this we built interface electronics to provide a TTL signal that was +5 V during the Kelvin portion of the scan and 0V otherwise.

This signal was extracted from the amplitude of the cantilever oscillation for the topography image which is normally less than 2 V, and the amplitude of the ac signal applied to the tip during the Kelvin image which is set to 4 V. This signal was extracted from the instrument and conditioned using a low pass filter to remove high frequency oscillations and passed through two voltage inverters to provide the TTL laser control (enable) signal. The two lasers are switched on only during the Kelvin measurement using the enable signal 5 V. The lasers are modulated either in unison (SPV) or differentially (DSPV) depending on the type of the measurement required.

Modulation of the two lasers in unison makes the surface potential of the semiconductor change between the dark and illuminated potential values. If the two lasers have different intensities and they are modulated differentially then the surface potential will modulate between two values corresponding to the laser powers. Two lasers with perfectly balanced intensities will produce exactly the same SPV values unless the SPV depends on the direction of the laser with respect to the crystallographic

182

directions of silicon and the local properties of the semiconductor of those contribute to SPV. In fact it is this same principal as described in an earlier paragraph that we use to measure stress, i.e. DSPV. The presence of anisotropic mechanical stress on the surface leads to a slightly different measured SPV each of the two lasers if the lasers are incident on the surface in correct directions (in our experiment both of them are in silicon <110> direction, one is parallel to the device and the other is perpendicular to it).

Modulation of the two lasers means modulation of surface potential and it will cause to modulate the Kelvin signal at a similar frequency as the laser modulation if the two SPV values are not the same. The Kelvin signal is coupled out from the breakout box which is connected between the scan electronic module (SEM) and the control electronic module and input to the lock-in amplifier. The amplitude of the low frequency modulation is detected with the lock-in amplifier, fed back into the system, and recorded as an image while the tip is rastered over the surface.

### 6.3.4.3 Double Lock-in Method

Although this method is more accurate and can overcome the problem of having beat frequencies, due to some other technical difficulties we could not do our experiments in this method. But it is open for further improvements. In this method the first lock-in amplifier is locked in to the cantilever driving frequency which is higher than the laser modulation frequency. This signal is input to the second lock-in amplifier and the second lockin amplifier detects the amplitude of modulation of the cantilever driving frequency due to the SPV and laser modulation. Any variation of the amplitude of this signal is a function of the difference of surface photovoltage for the two lasers.

## 6.4    Results and Discussion

### 6.4.1    Testing of the Instrument and the Method

To test the instrument and the concept, we used an SRAM which has both *n* and *p* type regions. Measured surface photovoltage should have opposite polarity for the different dopings and be propotional to the doping level because the direction of the band bending depends on the type of doping hence the sign of the measured surface photovoltage. As explained in the previous section, lasers modulating in unison produce a SPV measurement while the differentially modulating lasers produce a DSPV measurement which is the difference between SPVs from the two lasers. Figure 6.13 is such a set of images where Figure 6.13a is AFM topographic image of the two *n* and *p* FET devices, Figure 6.13b is an SPV image, Figure 6.13c is a surface potential image without light, and Figure 6.13d is a DSPV image. The two types of doping regions (*n* and *p*) have opposite polarity for SPV with respect to the charge neutral region (Figure 6.13b). This is a clear evidence for the proof of concept. The *n* and *p* regions of the two types of devices have different doping concentrations. The *n* region in the *n*FET is the source and the drain and is highly doped ($10^{19}$/cm$^3$). The *n* region in *p*FET is the channel and is lightly doped ($10^{15}$/cm$^3$). Therefore the contrast difference of *n* regions in the SPV image for the two types of devices is due to the differences of doping levels. There is a feature in the left side of the Kelvin image (Figure 6.13 c) which is not present in the topography. This can be attributed to a dislocation[36] or contamination within the silicon substrate.[43] SPV measurements are sensitive to potential variations few tens of nano meters deep within the silicon substrate depending on the penetration depth. The DSPV image (Figure 6.13d) has a contrast difference for the two regions. This may be due to stress or to slightly

imbalanced laser intensities. Therefore balancing the two laser intensities such that the surface receives a same amount of light from both lasers is critical for accurate DSPV measurements. We will discuss the issues relating to the DSPV measurements in detail at the end of this chapter.
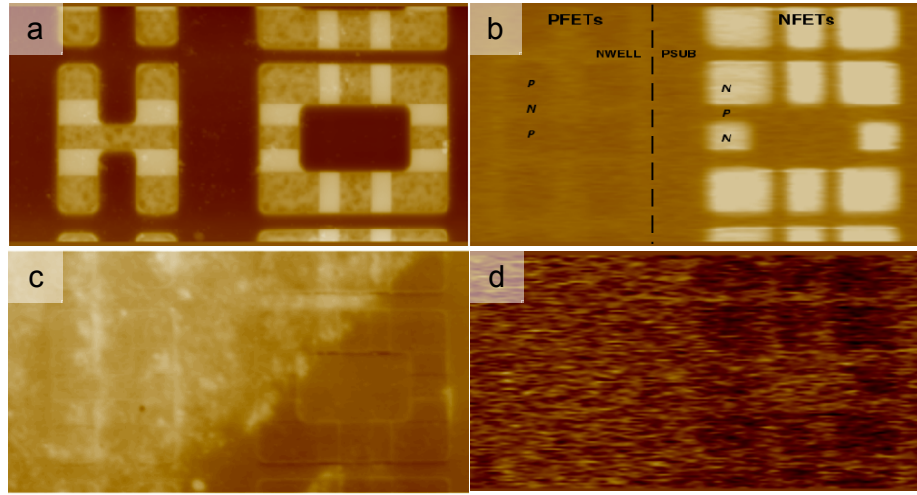


**Figure 6.13 Kelvin, SPV, and DSPV images of an SRAM:** a) AFM image of the topography of the *n* and *p*-type FETs, b) SPV signal extracted from the lockin amplifier when the two lasers are modulating in unison between dark and illumination, c) a Kelvin image acquired without any light, d) a DSPV images with lasers modulating differentially.

### 6.4.2    Analysis of Calibration Structures

We used Raman spectral imaging as a second method for testing the SPV and the DSPV (stress) data obtained from our method. The test structures were 3 × 3 arrays of indents described earlier. A similar type of study has been conducted by Schmidt et al.[44] on Vickers indents (creates square shape indents) produced at various load forces on a Si(111) surface. They have been able to obtain a stress resolution of 9 MPa for 70 ms integration period with standard deviation of the silicon peak position at unstressed regions of 0.02 cm. The type of stress present at the corners of the indents is tensile while

it is compressive at the edges and strongly depends on the geometry of the indents. Cracks in the silicon surface have been observed for higher loads such as 100 mN.

It is reported in many theoretical as well as experimental studies that the stress has a linear relationship with the silicon phonon frequency shift although the constant coefficient between stress and Raman peak shift is different in magnitudes from group to group. Experimental values reported are Schmidt et al.[44] −435 MPa cm and Wu et al.[16] −462 MPa cm. The theoretical value reported in Horsfall et al. is −434 MPa cm.[45] The disadvantage of using micro-Raman spectroscopy for measuring stress is that, the shift of the Raman peak position depends on all components of the stress tensor. Therefore data interpretation is difficult for complex stress patterns.

$$Stress = -434 \text{ MPa cm} \times \Delta\omega \tag{6.11}$$

### 6.4.3   Raman Spectroscopic Analysis of Stress in Indented Silicon Substrates

A change of the frequency of the silicon phonon is used to calculate the stress using the equation 6.11. When the unit of the wave number is $cm^{-1}$, the stress is in MPa. Raman signal intensity decreased with time as the sample was scanned from the top to bottom in Figure 6.15 a and b. This was attributed to either a decrease in laser power at the sample and/or a change in detector alignment. Because the scattered laser light is proportional to the laser power, we used these data as a pixel by pixel internal channel to correct the Raman images. A simple ratio of the Raman intensities to the scattered light intensity at the corresponding pixel corrects for this effect in Figure 6.15 c. Image c in the Figure 6.15 is a intensity sums for silicon after correction for the incident intensity gradient.
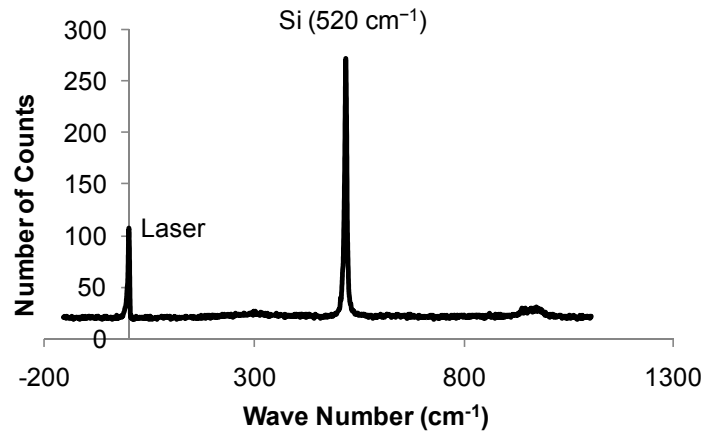
**Figure 6.14 Raman spectrum of silicon** which shows the silicon phonon peak for unstressed silicon at 520 cm$^{-1}$. The peak near the zero is caused by the scattering of laser light from the surface.
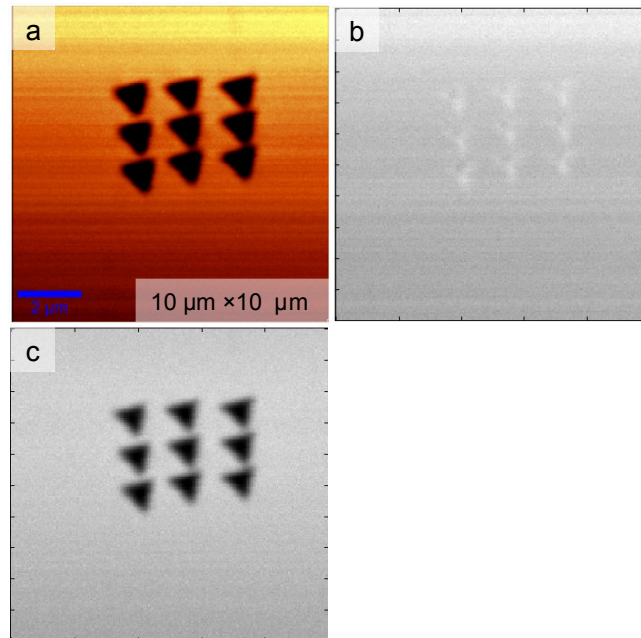


**Figure 6.15 Micro-Raman images of an array of indents on silicon:** a) micro-Raman intensity sum image, b) scattered light image ($-13 - 187$ cm$^{-1}$), c) silicon phonon intensity ($505 - 527$ cm$^{-1}$) corrected for intensity gradient.

## 6.4.3.1 Calculation of Stress from the Raman Image
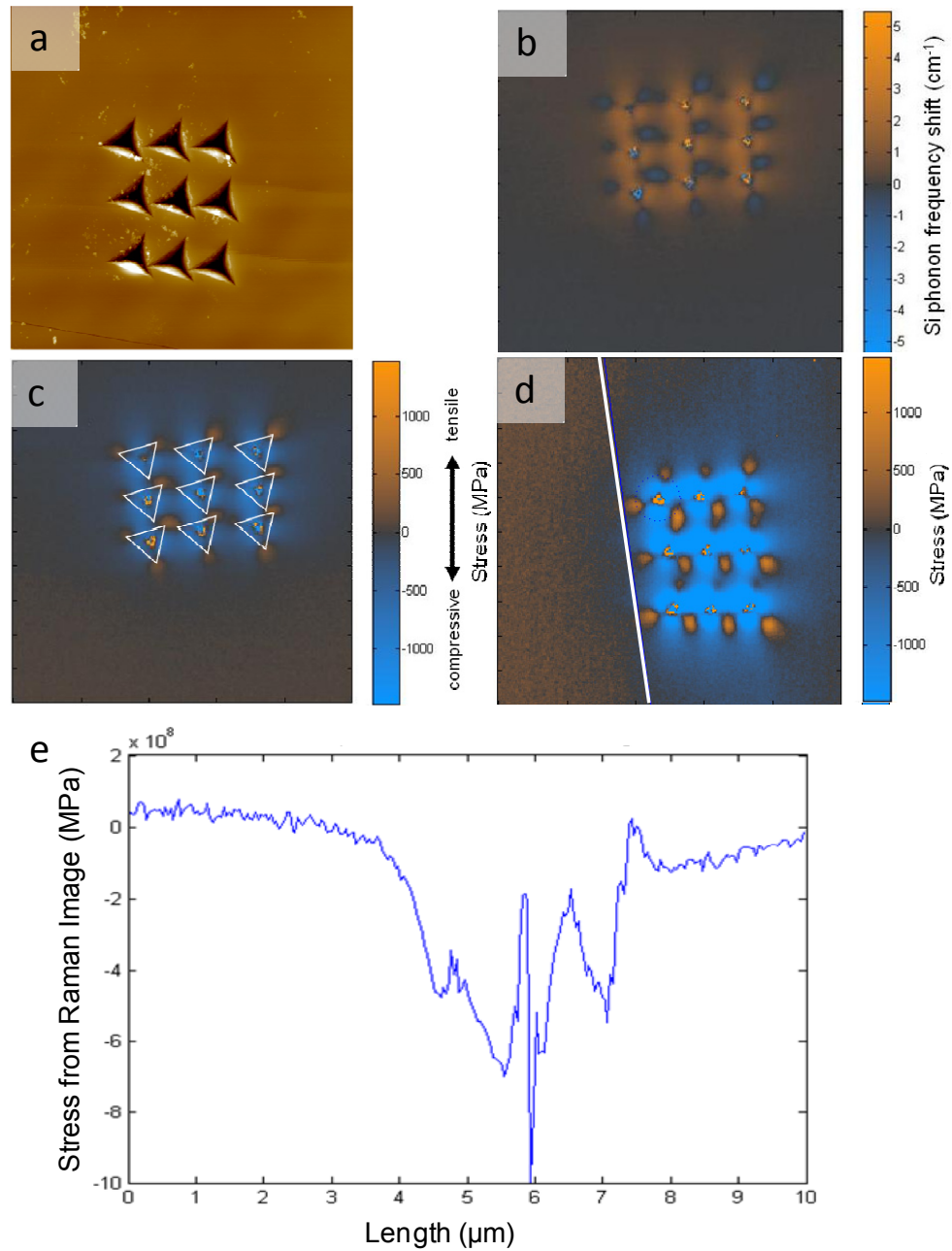


**Figure 6.16 Stress image calculated from the silicon phonon frequency shift:** a) topography image of the array of indents (7.5 mN, 2 μm separation), b) phonon frequency shift for silicon, c) calculated tensile and compressive stress map for the same indented array, d) image showing the position of the line cut of the stress image closer to the array of indents (note that the image was rotated 90° counter-clockwise to match the SPV images in Figure 6.17 from the instrument), e) stress along the line shown in "d".

Calculation of stress from the Raman signal is performed in the following way. First, the shift of the frequency of the Raman signal for silicon was extracted from the Raman data (Figure 6.16b). Then stress is calculated using the Equation 6.11 (Figure 6.16c). Note that the stress is tensile at the corners of the indents and compressive at the insides. The stress profile along a line cut 1 μm away from a row of indents shows the regions of neutral, tensile, and compressive stress (Figure 6.16e).

### 6.4.4  Measured Surface Photovoltage from the SSPVM
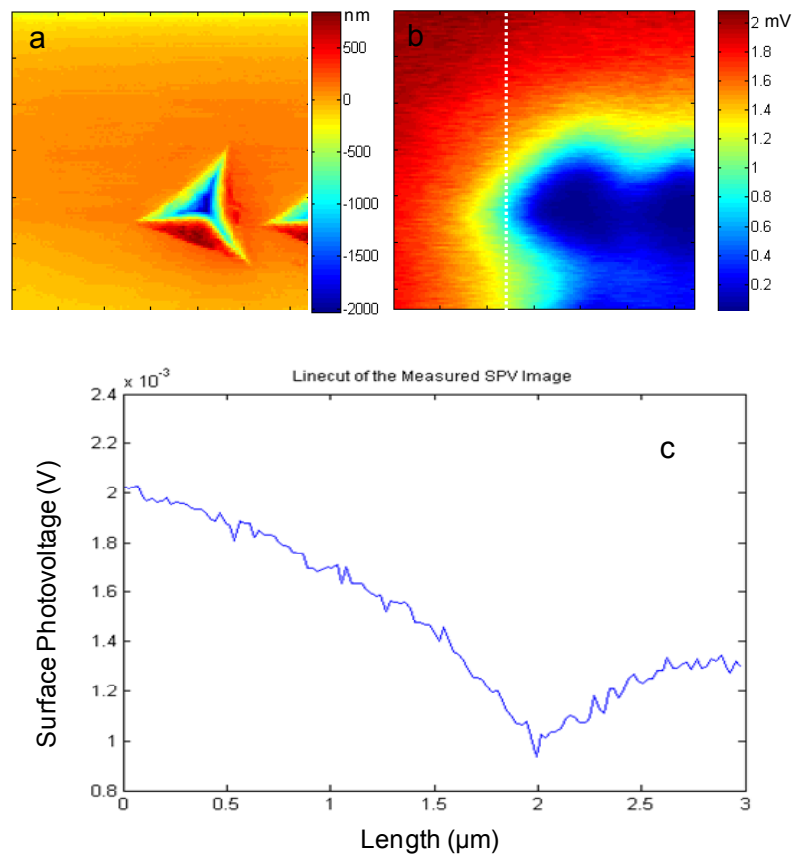


**Figure 6.17 Direct SPV measurements on an indent on silicon substrate:** a) AFM topography image of the upper left corner indent of the array of indent in Figure 6.16, b) SPV image of the same indent, c) SPV along the dotted line in "b".

One of the main advantages of the SSPVM method is the ability to measure SPV of samples directly. Normally it is a two step processes which requires measuring surface

potentials during dark and illumination and then subtracting the two to calculate SPV. The measured SPV of the indented samples are in millivolts (Figure 6.17b and c). According to the graph shown in the Figure 6.17c, the regions closer to the indented area have lower SPV values than that of the other regions. This is due to two reasons. The damaged area of the indent acts as an excellent source for carrier generation and recombination which in turn alters the magnitude of band bending. This is the largest contribution to the SPV. Differences in SPV produced by the stress fields present in and around the indent are expected to be considerably smaller. In addition, there are other contributions such as meta stable phases silicon formed by the high mechanical pressure exerted on the surface during indentation. Therefore modeling of SPV of indents is rather complicated, but a more simplified analytical model will be presented in the next section.

### 6.4.5   An Analytical Model which Relates SPV and Mechanical Stress

As discussed in the previous sections, stress levels can be calculated from Raman data easily. SSPVM can be used to obtain direct surface photovoltage measurements and a signal related to the stress in the sample depending on its mode of operation. As the SPV is itself a function of mechanical stress, the SPV measurements can be used to calculate the mechanical stress as well. Therefore it is important to develop a model which relates SPV and stress terms. The analytical model shown in equation 6.12 was developed by comparing the direct SPV measurements from the SSPVM to SPV calculated from the stress values from the Raman measurements using the model.

The first term in Equation 6.12 calculates the SPV which depends on the local stress while the second term calculates the SPV due to indents acting as source points for carrier generation and recombination. For each source point (each indent), terms similar

to the second term should be added to the equation ($i=1,2,\ldots$). For actual devices, the STI can be considered as the source. All nine indents on the calibration structure act as sources for minority carrier generation/recombination.

$$SPV_{r,g} = C \frac{(1-R)\,\Phi\,L_n}{\left(s_{r,g} + \dfrac{D_n}{L_n}\right)\left(L_n + \dfrac{1}{\alpha}\right)} \quad - \quad |G| \sum_i \frac{\left[\exp\left(\dfrac{-3\,(r-r_{0i})}{L}\right)\right]}{(r-r_{0i})^{3/2}} \quad (6.12)$$

$$\alpha = -10696.4 + \frac{33498.2}{\lambda} + \frac{36164.9}{\lambda^2} + \frac{13483.1}{\lambda^3} \quad (6.13)$$

$$1 - R = 0.6786 + \frac{0.03565}{\lambda} - \frac{0.03149}{\lambda^2} \quad (6.14)$$

$$D_n = \frac{kT}{q}\,\mu_n^0\,e^{\Omega\sigma/kT} \quad (6.15)$$

$$L_n = \sqrt{D_n \tau_n} \quad (6.16)$$

Where;

| | | |
|---|---|---|
| $i$ | – | number of source points (indents) |
| $r_{0i}$ | – | positions of indents |
| $r - r_{0i}$ | – | distance from the indent |
| $s_{r,g}$ | – | surface recombination, generation velocity ($\pm 10 - 1000$ cm sec$^{-1}$). High numeric value means more recombination or generation respectively. High positive (recombination) value is due to surface states suppressing the effective lifetime and therefore suppressing SPV. |
| $C$ | – | arbitrary constant |
| $D_n$ | – | local (position and stress dependent) minority carrier diffusion coefficient |
| $G$ | – | arbitrary constant |
| $K$ | – | Boltzmann Constant |
| $L_n$ | – | diffusion length which depends on local stress |
| $L$ | – | diffusion length for silicon ($\sim 200$nm) |
| $R$ | – | reflectivity |
| $T$ | – | temperature |
| $\alpha$ | – | absorption coefficient |
| $\lambda$ | – | wave length of the incident light |

$\mu_n^0$ – carrier mobility which is related to the carrier diffusion coefficient by the Einstein relation

$\sigma$ – local position dependent stress ($\sim 10^9$ dynes cm$^{-2}$)

$\tau_n$ – carrier lifetime ($\sim 10^{-3} - 10^{-4}$ sec)

$\Phi$ – light intensity

$\Omega$ – activation volume for stress ($\sim 10^{-11}$ cm$^{-3}$)

### 6.4.6 Calculation of SPV from Stress using the Model and Fitting it to Experimental Data
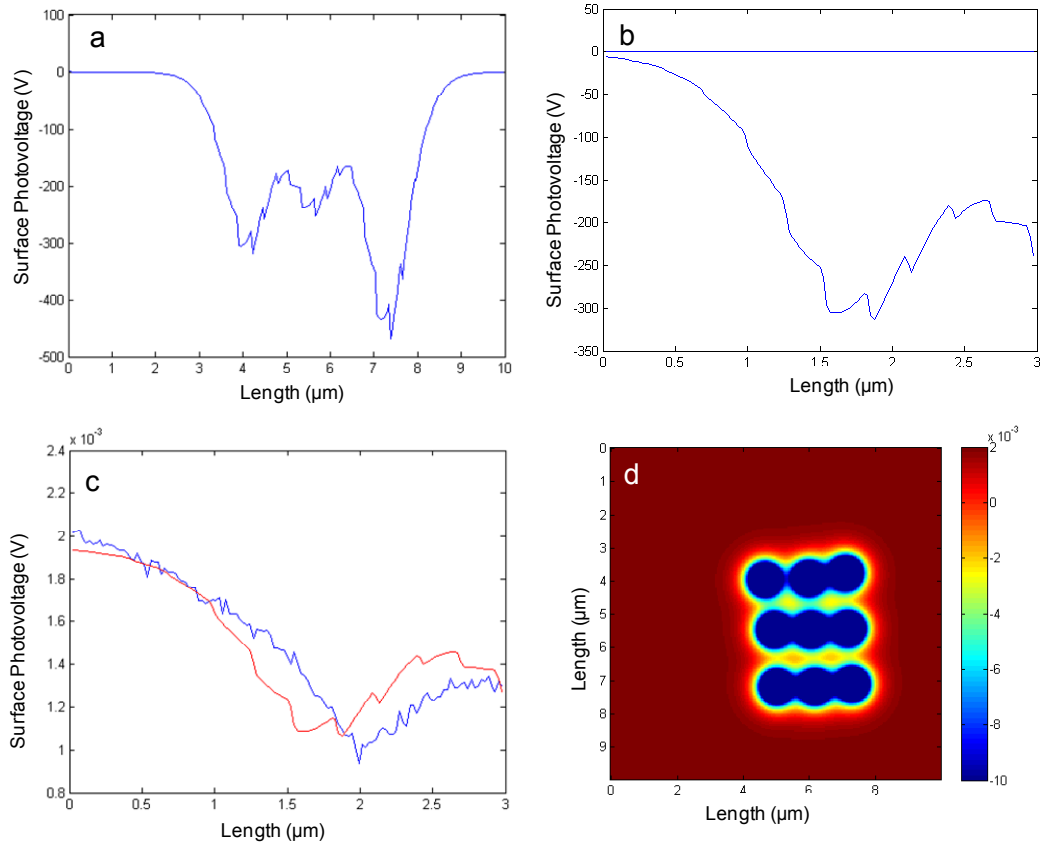


**Figure 6.18 Calculated and fitted SPV for the cross section from the Raman stress and the calculated SPV for the entire image**: a) calculated SPV from stress data, b) parts of the lines extracted from the calculated and the measured SPV, c) calculated and measured SPV after linear fit, d) calculated SPV for the entire array of indents using the fitted parameters.

$$(SPV\,measured) = P \times (SPV\,calculated) + Q \qquad (6.17)$$

All of the calculations were performed using the MatLab program. The data used to calculate SPV from stress is from the same Raman image in section 6.4.3.1. It was a 10 μm × 10 μm image with 256 × 256 data points. The experimental SPV image was obtained on the same array of indents for the upper left corner indent in Figure 6.16d and is a 3 μm × 3 μm image. The line cuts were obtained after careful overlaying of the two images with the topography image. The data points were interpolated so the SPV and the Raman data could be compared. The calculation was a two step process. First SPV was calculated for the line cut of the Raman stress image disregarding the second source terms. The calculated SPV values were fitted linearly to the experimental data to get a correct offset range for the two data sets. Then in the second calculation, all the source terms were included and the offset obtained from the first calculation was used as the value for "G". Then again the same linear fit was performed to get more accurate results. As we mentioned in an earlier section, the contribution from the generation/recombination centers (source terms) is very large and dominates over the contribution from the stress (Figure 6.18a and b). After the second round of fitting, the two signals were matched very closely and the fitting constants $P$ and $Q$ have values of $2.83 \times 10^{-6}$ and $1.95 \times 10^{-3}$ respectively. The calculated SPV for the entire image using the model and the fitting parameters is shown in Figure 6.18d. It should be noted here that the phenomenon inside the indent is complex and our model is not valid there. Our model is valid in the regions outside including the immediate surrounding area. From a practical standpoint, the indents are similar to STI in the diode structures and the region outside the indent is comparable to the active device region.

### 6.4.7 Diode Characteristic of Nano-Indents on Silicon

Figure 6.19a is a graph of variation of SPV over an array of three indents of 7.5 mN with 2 μm separation. Laser power increases from zero to the maximum when the potentiometer control setting varies from zero to 1000. Until the value on the potentiometer control reaches 350, the laser intensity is zero and therefore the measured SPV remains zero. Then, SPV on and closer to the indents increases while SPV for the rest of the silicon area decreases up to some laser power and then the SPV starts to decrease everywhere. This is similar to the electrical characteristics of a semiconductor *p-n* junction. This can be explained by assuming a change of material characteristics at the indents during indentation. There are many studies which suggest that silicon undergoes many phase transformations when it is subjected to high pressure and we suggest that a similar phenomenon is responsible for the observed diode behavior of indents.[46-49] High pressure indentation experimental studies have shown that the diamond cubic Si-I phase transforms to a metallic Si-II phase (β-Sn phase) at a pressure of ~11 GPa. Under slow decompression, Si-II retransforms to crystalline high pressure phase Si-XII, which then partly transforms to Si-III upon further pressure release, resulting in a mixture of crystalline high pressure phases Si-XII and Si-III following full pressure release.[46-55] Our intention of using indented silicon is to calibrate the stress measured from DSPV method with the stress calculated from Raman spectroscopy. The phase change of silicon at the indents complicated this task and therefore it is open to further investigations.
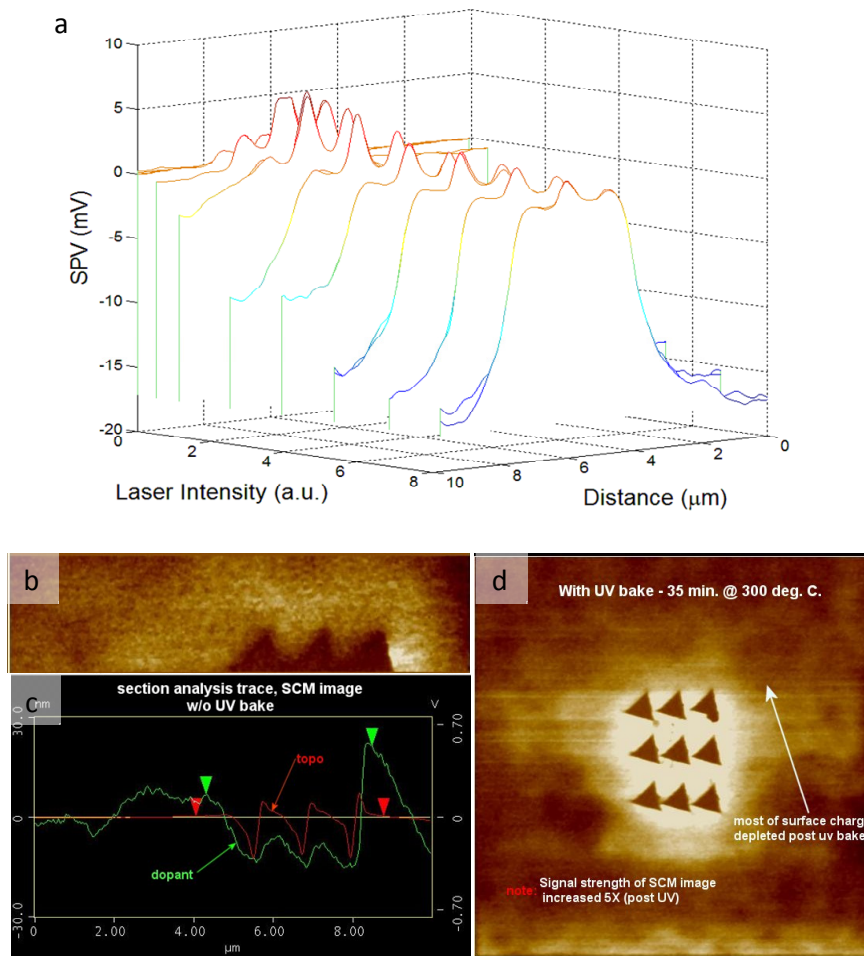
**Figure 6.19 SPV versus laser power graph for an area over three indents and scanning capacitance images of indents:** a) SPV over a row of three indents with varying laser power, b) scanning capacitance microscopy (SCM) image of a section of a row of three indents, c) cross sections of topographic and SCM images, d) SCM image of the entire array of indents.

### 6.4.8 SPV and DSPV Measurements of Devices (Diode Structures)

As we showed in section 6.4.4, the SSPVM method is capable of measuring surface photovoltage of devices directly. We used SSPVM method to investigate device structures in different wafers which were removed at different processing steps. Although we present results from only one such device in Figure 6.20, the SPV and DSPV measurements obtained for other devices are consistent. Figure 6.20a is an AFM

topography image while the Figure 6.20b is the corresponding SPV image. The red and

yellow regions are silicon and silicon dioxide respectively. The DSPV signal is weak and

the contrast variation in the DSPV image is not conclusive evidence that we measure

stress in the device. It can be due to stress and/or imbalanced laser intensities. The

SSPVM method and the instrument setup require further improvements for accurate

stress measurements.
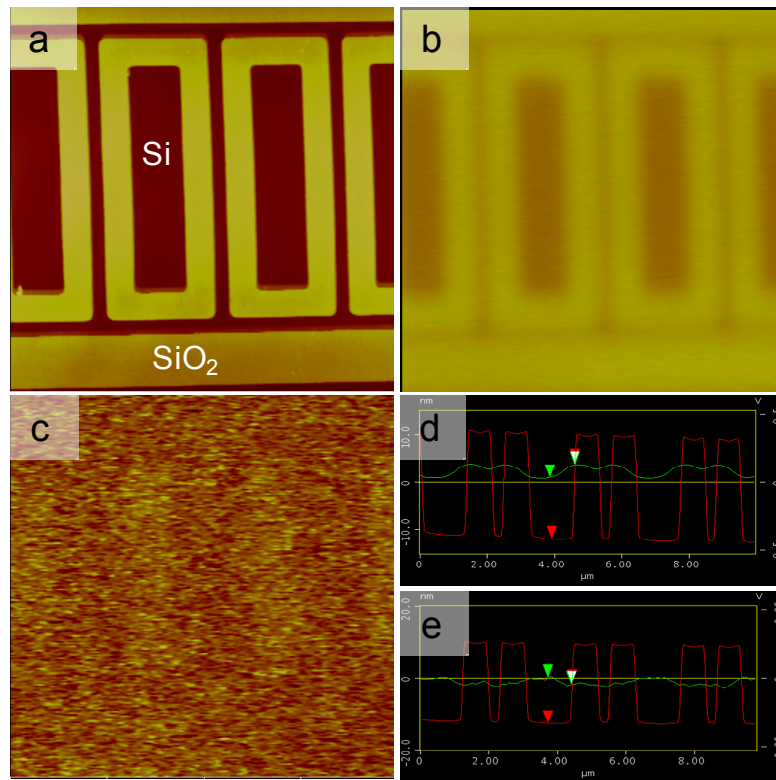


**Figure 6.20 Topography, SPV, and DSPV images and cross sections of an array of devices** (Note that the structures have only silicon and STI)**:** a) topography image, b) SPV image, c) DSPV image, d) cross section of the SPV image (red line is topography and the green line is SPV), e) cross section of the DSPV image (red line is topography and the green line is DSPV), Note: the vertical scale is not calibrated to the sensitivity of the lockin amplifier.

### 6.4.9 Suggestions for improvements of the DSPV method

The current SSPVM setup is capable of directly measuring SPV while results for DSPV stress measurements were not conclusive. The difference of the surface photovoltages due to the difference of the stress distribution in the two laser directions is very small and therefore the sensitivity of the instrument should be further improved. This can be achieved by modulating the two lasers at the cantilever resonance frequency (may be at a higher-order resonance). This idea was tried first but abandoned due to its interference with the scanning. But it will be worthwhile to reinvestigate and find a way to overcome the interference. The image contrast produced in the DSPV image due to imbalanced lasers is a major barrier for correct interpretation of stress. Therefore it would be advantageous to develop methodology to guarantee a similar laser intensity level at the surface directly underneath the tip for the two lasers. We have a large amount of Raman and SPV data collected on device structures. Therefore it will be advantageous to analyze those further.

### 6.5 Conclusion

The proof of concept for measuring mechanical stress present in CMOS devices was established. The instrument and the DSPV setup requires further improvements to increase the sensitivity for correct stress measurements. In addition, the instrument is capable of measuring surface photovoltage directly. A simple analytical model which relates the SPV and stress was developed.

### 6.6 References for Chapter 6

(1)     Haugerud, B. M.; Bosworth, L. A.; Belford, R. E. Mechanically Induced Strain Enhancement of Metal-Oxide-Semiconductor Field Effect Transistors. *J. Appl. Phys.* **2003**, *94*, 4102.

(2)     Andrieu, F.; Ernst, T.; Ravit, C.; Jurczak, M.; Ghibaudo, G.; Deleonibus, S. In-Depth Characterization of the Hole Mobility in 50-nm Process-Induced Strained MOSFETs. *IEEE Electron Device Lett.* **2005**, *26*, 755.

(3)     Roldan, J. B.; Gamiz, F.; Cartujo-Cassinello, R.; Cartujo, P.; Carceller, J. E.; Roldan, A. Strained-Si on $Si_{1-x}Ge_x$ MOSFET Mobility Model. *IEEE Trans. Electron Devices* **2003**, *50*, 1408.

(4)     Maikap, S.; Yu, C. Y.; Jan, S. R.; Lee, M. H.; Liu, C. W. Mechanically Strained Strained-Si NMOSFETs. *IEEE Electron Device Lett.* **2004**, *25*, 40.

(5)     Keyes, R. W. High-Mobility FET in Strained Silicon. *IEEE Trans. Electron Devices* **1986**, *33*, 863.

(6)     Zhang, Y.; Fischetti, M. V.; Soree, B.; Magnus, W.; Heyns, M.; Meuris, M. Physical Modeling of Strain-Dependent Hole Mobility in Ge *p*-Channel Inversion Layers. *J. Appl. Phys.* **2009**, *106*, 083704.

(7)     Fahey, P. M.; Mader, S. R.; Stiffler, S. R.; Mohler, R. L.; Mis, J. D.; Slinkman, J. A. Stress-Induced Dislocations in Silicon Integrated-Circuits. *IBM J. Res. Dev.* **1992**, *36*, 158.

(8)     Rueda, H. A. Modeling of Mechanical Stress in Silicon Isolation Technology and its Influence on Device Characteristics. PhD Thesis, University of Florida, 1999.

(9)     De Wolf, I.; Maes, H. E. Mechanical Stress Measurements using Micro-Raman Spectroscopy. *Microsyst Technol* **1998**, *5*, 13.

(10)    Gallon, C.; Reimbold, G.; Ghibaudo, G.; Bianchi, R. A.; Gwoziecki, R.; Orain, S.; Robilliart, E.; Raynaud, C.; Dansas, H. Electrical Analysis of Mechanical Stress Induced by STI in Short MOSFETs Using Externally Applied Stress. *IEEE Trans. Electron Devices* **2004**, *51*, 1254.

(11)    Unal, K.; Wickramasinghe, H. K. Nanoscale Quantitative Stress Mapping with Atomic Force Microscopy. *Appl. Phys. Lett.* **2007**, *90*, 113111.

(12)    McCarthy, J.; Bhattacharya, S.; Perova, T. S.; Moore, R. A.; Gamble, H.; Armstrong, B. M. Composition and Stress Analysis in Si Sructures Using Micro-Raman Spectroscopy. *Scanning* **2004**, *26*, 235.

(13)     De Wolf, I. Micro-Raman Spectroscopy to Study Local Mechanical Stress in Silicon Integrated Circuits. *Semicond. Sci. Technol.* **1996**, *11*, 139.

(14)     De Wolf, I. Stress Measurements in Si Microelectronics Devices using Raman Spectroscopy. *J. Raman Spectrosc.* **1999**, *30*, 877.

(15)     Ajito, K.; Sukamto, J. P. H.; Nagahara, L. A.; Hashimoto, K.; Fujishima, A. Strain Imaging Analysis of Si using Raman Microscopy. *J. Vac. Sci. Technol., A* **1995**, *13*, 1234.

(16)     Wu, X.; Yu, J.; Ren, T.; Liu, L. Micro-Raman Spectroscopy Measurement of Stress in Silicon *Microelectron. J.* **2006**, *38*, 87.

(17)     Ibach, W.; Hollricher, O. *High Resolution Optical Microscopy*, WiTech, 2002.

(18)     Favia, P.; Klenov, P.; Eneman, G.; Verheyen, P.; Bauer, M.; Weeks, D.; Thomas, S. G.; Bender, H. Strain Study in Transistors with SiC and SiGe Source and Drain by STEM Nano Beam Diffraction,Proceedings of the EMC 2008 14th European Microscopy Congress 1–5 September 2008, Aachen, Germany, 2008

(19)     Vartuli, C. B.; Jarausch, K.; Inada, H.; Tsunet, R.; Dingley, D. J.; Marley, E. A. Strain Measurements Using Nano-Beam Diffraction on a FE-STEM. *Microsc. Microanal.* **2007**, *13*, 836.

(20)     Li, J.; Lamberti, A.; Domenicucci, A.; Gignac, L.; Utomo, H.; Luo, Z.; Rovedo, N.; Fang, S.; Ng, H.; Holt, J. R.; Madan, A.; Lai, C. W.; Ku, J.-H.; Schepis, D. J.; Han, J.-P.; Lagus, M. Channel Strain Characterization in Embedded SiGe by Nano-beam Diffraction. *ECS Trans.* **2008**, *16*, 545.

(21)     Ang, K.-W.; Chui, K.-J.; Bliznetsov, V.; Tung, C.-H.; Du, A.; Balasubramanian, N.; Samudra, G.; Li, M. F.; Yeo, Y.-C. Lattice Strain Analysis of Transistor Structures with Silicon-Germanium and Silicon-Carbon Source/Drain Stressors. *Appl. Phys. Lett.* **2005**, *86*, 093102.

(22)     Li, J.; Anjum, D.; Hull, R.; Xia, G.; Hoyt, J. L. Nanoscale Stress Analysis of Strained-Si Metal-Oxide-Semiconductor Field-Effect Transistors by Quantitative Electron Diffraction Contrast Imaging. *Appl. Phys. Lett.* **2005**, *87*, 222111.

(23)    Clement, L.; Cacho, F.; Pantel, R.; Rouviere, J. L. Quantitative Evaluation of Process Induced Strain in MOS Transistors by Convergent Beam Electron Diffraction. *Micron* **2009**, *40*, 886.

(24)    Toh, S. L.; Loh, K. P.; Boothroyd, C. B.; Li, K.; Ang, C. H.; Chan, L. Strain Analysis in Silicon Substrates under Uniaxial and Biaxial Stress by Convergent Beam Electron Diffraction. *J. Vac. Sci. Technol., B* **2005**, *23*, 940.

(25)    Clément, L.; Rouviere, J. L.; Cacho, F.; Pantel, R. *Measuring Strain in Semiconductor Nanostructures by Convergent Beam Electron Diffraction*: *Microscopy of Semiconducting Materials 2007*; Springer Netherlands: 2008; Vol. 120, p 423.

(26)    Zhang, P.; Istratov, A. A.; Weber, E. R.; Kisielowski, C.; He, H.; Nelson, C.; Spence, J. C. H. Direct Strain Measurement in a 65 nm Node Strained Silicon Transistor by Convergent-Beam Electron Diffraction. *Appl. Phys. Lett.* **2006**, *89*, 161907.

(27)    Kronik, L.; Shapira, Y. Surface Photovoltage Sectroscopy of Semiconductor Structures: At the Crossroads of Physics, Chemistry and Electrical Engineering. *Surf. Interface Anal.* **2001**, *31*, 954.

(28)    Schroder, D. K. Surface Voltage and Surface Photovoltage: History, Theory and Applications. *Meas. Sci. Technol.* **2001**, *12*, R16.

(29)    Kronik, L.; Shapira, Y. Surface Photovoltage Phenomena: Theory, Experiment, and Applications. *Surf. Sci. Rep.* **1999**, *37*, 5.

(30)    Zisman, W. A. A New Method of Measuring Contact Potential Differences in Metals. *Rev. Sci. Instrum.* **1932**, *3*, 367.

(31)    Binnig, G.; Rohrer, H.; Gerber, C.; Weibel, E. Surface Studies by Scanning Tunneling Microscopy. *Phys. Rev. Lett.* **1982**, *49*, 57.

(32)    Nonnenmacher, M.; Boyle, M. P. O.; Wickramasinghe, H. K. Kelvin Probe Force Microscopy. *Appl. Phys. Lett.* **1991**, *58*, 2921.

(33)    Henning, A. K.; Hochwitz, T.; Slinkman, J.; Never, J.; Hoffmann, S.; Kaszuba, P.; Daghlian, C. Two-Dimensional Surface Dopant Profiling in Silicon using Scanning Kelvin Probe Microscopy. *J. Appl. Phys.* **1995**, *77*, 1888.

(34)    Kikukawa, A.; Hosaka, S.; Imura, R. Silicon *p-n* Junction Imaging and Characterizations using Sensitivity Enhanced Kelvin Probe Force Microscopy. *Appl. Phys. Lett.* **1995**, *66*, 3510.

(35)    Weaver, J. M. R.; Abraham, D. W. High Resolution Atomic Force Microscopy Potentiometry. *J. Vac. Sci. Technol., B* **1991**, *9,* 1559.

(36)    Weaver, J. M. R.; Wickramasinghe, H. K. Semiconductor Characterization by Scanning Force Microscope Surface Photovoltage Microscopy. *J. Vac. Sci. Technol., B* **1991**, *9,* 1562.

(37)    Meoded, T.; Shikler, R.; Fried, N.; Rosenwaks, Y. Direct Measurement of Minority Carriers Diffusion Length using Kelvin Probe Force Microscopy. *Appl. Phys. Lett.* **1999**, *75*, 2435.

(38)    Vatel, O.; Tanimoto, M. Kelvin Probe Force Microscopy for Potential Distribution Measurement of Semiconductor Devices. *J. Appl. Phys.* **1995**, *77*, 2358.

(39)    Mizutani, T.; Arakawa, M.; Kishimoto, S. Two-Dimensional Potential Profile Measurement of GaAs HEMT's by Kelvin Probe Force Microscopy. *IEEE Electron Device Lett.* **1997**, *18*, 423.

(40)    Hochwitz, T.; Henning, A. K.; Levey, C.; Daghlian, C. Capacitive Effects on Quantitative Dopant Profiling with Scanned Electrostatic Force Microscopes. *J. Vac. Sci. Technol., B* **1996**, *14*, 457.

(41)    Loppacher, C.; Zerweck, U.; Teich, S.; Beyreuther, E.; Otto, T.; Grafstroem, S.; Eng, L. M. FM Demodulated Kelvin Probe Force Microscopy for Surface Photovoltage Tracking. *Nanotechnology* **2005**, *16*, S1.

(42)    Saraf, S.; Shikler, R.; Yang, J.; Rosenwaks, Y. Microscopic Surface Photovoltage Spectroscopy. *Appl. Phys. Lett.* **2002**, *80*, 2586.

(43)    Lagowski, J.; Edelman, P.; Erickson, R. High Speed, High Density SPV Mapping of Iron Contamination in Silicon Wafers,Proceedings of the Defect Recognition and Image Processing in Semiconductors, Boulder, CO, 1995; Vol. 149,91.

(44)     Schmidt, U.; Ibach, W.; Müller, J.; Weishaupt, K.; Hollricher, O. Raman Spectral Imaging - A Nondestructive, High Resolution Analysis Technique for Local Stress Measurements in Silicon. *Vib. Spectrosc.* **2006**, *42*, 93.


(45)     Horsfall, A. B.; Santos, J. M. M. D.; Soare, S. M.; Wright, N. G.; O'Neill, A. G.; Bull, S. J.; Walton, A. J.; Gundlach, A. M.; Stevenson, J. T. M. Direct Measurement of Residual Stress in Sub-Micron Interconnects. *Semicond. Sci. Technol.* **2003**, *18*, 992.


(46)     Ruffell, S.; Bradby, J. E.; Williams, J. S.; Munoz-Paniagua, D.; Tadayyon, S.; Coatsworth, L. L.; Norton, P. R. Nanoindentation-Induced Phase Transformations in Silicon at Elevated Temperatures. *Nanotechnology* **2009**, *20*.


(47)     Ruffell, S.; Bradby, J. E.; Fujisawa, N.; Williams, J. S. Identification of Nanoindentation-Induced Phase Changes in Silicon by In-Situ Electrical Characterization. *J. Appl. Phys.* **2007**, *101*, 083531.


(48)     Ruffell, S.; Bradby, J. E.; Williams, J. S.; Warren, O. L. An In Situ Electrical Measurement Technique via a Conducting Diamond Tip for Nanoindentation in Silicon. *J. Mater. Res.* **2007**, *22*, 578.


(49)     Bradby, J. E.; Williams, J. S.; Swain, M. V. In Situ Electrical Characterization of Phase Transformations in Si During Indentation. *Phys. Rev. B* **2003**, *67*, 085205.


(50)     Bradby, J. E.; Williams, J. S.; Wong-Leung, J.; Swain, M. V.; Munroe, P. Transmission Electron Microscopy Observation of Deformation Microstructure under Spherical Indentation in Silicon. *Appl. Phys. Lett.* **2000**, *77*, 3749.


(51)     Ruffell, S.; Bradby, J. E.; Williams, J. S. High Pressure Crystalline Phase Formation During Nanoindentation: Amorphous Versus Crystalline Silicon. *Appl. Phys. Lett.* **2006**, *89*, 091919.


(52)     Ruffell, S.; Bradby, J. E.; Williams, J. S. Annealing Kinetics of Nanoindentation-Induced Polycrystalline High Pressure Phases in Crystalline Silicon. *Appl. Phys. Lett.* **2007**, *90*, 131901.


(53)     Ruffell, S.; Bradby, J. E.; Williams, J. S.; Munroe, P. Formation and Growth of Nanoindentation-Induced High Pressure Phases in Crystalline and Amorphous Silicon. *J. Appl. Phys.* **2007**, *102*, 063521.

(54)    Fujisawa, N.; Keikotlhaile, R. T.; Bradby, J. E.; Williams, J. S. Indentation-Induced Phase Transformations in Silicon as a Function of History of Unloading. *J. Mater. Res.* **2008**, *23*, 2645.


(55)    Rao, R.; Bradby, J. E.; Ruffell, S.; Williams, J. S. Nanoindentation-Induced Phase Transformation in Crystalline Silicon and Relaxed Amorphous Silicon. *Microelectron. J.* **2007**, *38*, 722.

# Appendix 1

**Relationship between film thickness (*h*), molecular area (*A*), and molecular volume (*V*)**

The primary assumption is that the molecular volume is constant. Molecular area, i.e. the molecular foot print, depends on the surface coverage. Calculation for the known structure of the ($\sqrt{3} \times \sqrt{3}$)R30° with a molecular tilt angle of $\theta = 30°$ from the surface normal is as follows;

Molecular area $\qquad A = a^2 \sin\varphi$; a=0.499 nm, $A$=0.217 nm$^2$



unit cell of
($\sqrt{3} \times \sqrt{3}$)R30°
contains
one molecule
per unit cell
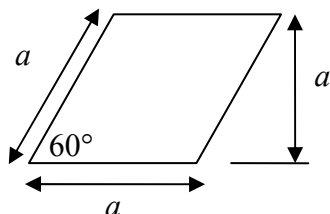
Length of alkanethiolate $HS(CH_2)_nCH_3$ on Au surface is calculated with

$$l = 0.4 \text{ nm} + (0.127 \text{ nm/methylene carbon}) \times n \qquad \text{(Bain et al)}[1]$$

and the thickness of ($\sqrt{3} \times \sqrt{3}$)R30° monolayer is

$$h = l \cos\theta.$$

Therefore for decanethiol, $l = 0.4 + 0.127 \times 9 = 1.543$ nm; $h = 1.543 \cos (30°) = 1.34$ nm

Molecular volume is

$$V = Ah = (0.217 \text{ nm}^2)(1.34 \text{ nm}) = 0.289 \text{ nm}^3$$

**Determining the surface coverage (*A'*) of an unknown monolayer from the height difference Δ*h***

$$V = Ah = A'h'$$

$$\Delta h = h - h'$$

$$h' = h - \Delta h$$

$$Ah = A'(h - \Delta h)$$

$$A' = \frac{Ah}{h - \Delta h} = A\left(\frac{1}{1 - \frac{\Delta h}{h}}\right)$$

Relative surface coverage (*A'/A*)

$$V = V', \qquad \frac{A}{A'} = \frac{h - \Delta h}{h} = \left(1 - \frac{\Delta h}{h}\right)$$

Where

| | | |
|---|---|---|
| *V* | – | volume |
| *A* | – | area of $(2\sqrt{3} \times 3)$rect. SAM |
| *A'* | – | area of $(\sqrt{3} \times 4\sqrt{3})$R30° striped-phase SAM |
| *h* | – | height of $(2\sqrt{3} \times 3)$rect. SAM |
| *h'* | – | height of $(\sqrt{3} \times 4\sqrt{3})$R30° striped-phase SAM |
| Δ*h* | – | difference of height of $(2\sqrt{3} \times 3)$rect. and $(\sqrt{3} \times 4\sqrt{3})$R30° striped-phase SAM |

**Procedure for calculating the coverage of the striped phase from STM images containing a reference structure**

The average $\Delta h_{\text{STM}}$ between the striped structures and the $(2\sqrt{3} \times 3)$rect. reference structure was measured as follows. A cross section from an STM image of a surface that displays well defined $(2\sqrt{3} \times 3)$rect. and $(\sqrt{3} \times 4\sqrt{3})$R30° striped structures was extracted. The cross section should run across a striped region and contain two well-defined and spatially separated $(2\sqrt{3} \times 3)$rect. regions. Then cross-sectional data was graphed. A line at the height defined by the $(2\sqrt{3} \times 3)$rect. regions was drawn. Next average height

difference of the stripe unit cell ($\Delta h_{STM}$) was calculated. To do this, the cross-sectional area between the reference line and striped region between an integer number of stripes was calculate. The $\Delta h_{STM}$ is then this area divided by the distance over which the cross sectional area is calculated. For purpose of calculating the striped coverage, $\Delta h$ equals $2\Delta h_{STM}$.[2]

Measured height difference ($\Delta h_{STM}$)= 1.16 Å

Therefore the physical height difference $\Delta h = 2\Delta h_{STM} = 2.33$ Å

Then the relative surface coverage,

$$\frac{A}{A'} = \left(1 - \frac{\Delta h}{h}\right) = \left(1 - \frac{2.33}{13.4}\right) = 0.8261$$

**References for Appendix 1**

(1)    Bain, C. D.; Troughton, E. B.; Tao, Y. T.; Evall, J.; Whitesides, G. M.; Nuzzo, R. G. Formation of Monolayer Films by the Spontaneous Assembly of Organic Thiols from Solution onto Gold. *J. Am. Chem. Soc.* **1989**, *111*, 321.


(2)    Bumm, L. A.; Arnold, J. J.; Dunbar, T. D.; Allara, D. L.; Weiss, P. S. Electron Transfer Through Organic Molecules. *J. Phys. Chem. B* **1999**, *103*, 8122.

# Appendix 2
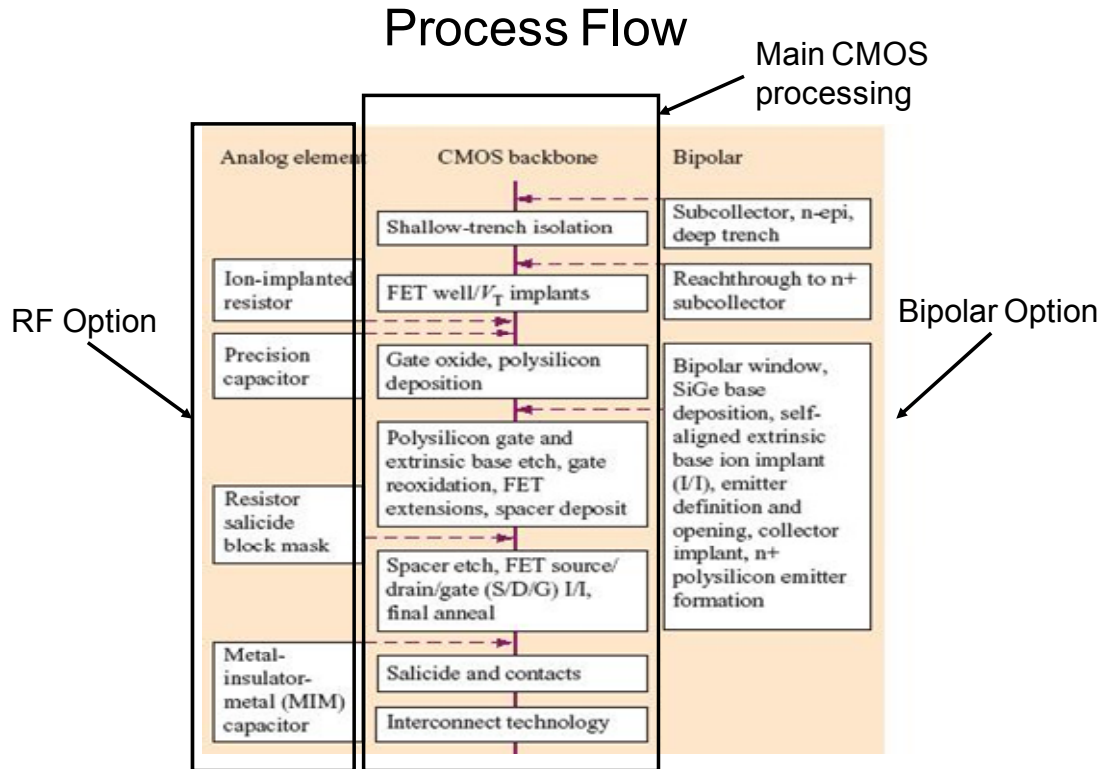
**CMOS Process Flow and the Stages of the Samples Pulled Out**



**Figure A2.1 CMOS and Bipolar process flow** (Diagram courtesy, Dr. James Slinkman, IBM)

| GATE | Operation | Key "stress" steps noted in RED<br>Comment | Process Exception | PULL |
|---|---|---|---|---|
| Wafer | [100] p- Si ( 1 ohm-cm = 1.0E15 cm-3 Boron) | Notch @ (110) | | |
| | | | | |
| SC | 20 nm pad oxide | | | |
| SC | 80 nm pad nitride | | | |
| | | | | |
| RX | CVD oxide hard mask deposit | Etch stop | | |
| RX | deposit photo resist | | | |
| RX | Mask & expose & develop | Defines where STI will be etched | | |
| RX | Hard Mask open | Remove HM to pad films | | |
| RX | remove resist | Plasma strip | | |
| RX | clean | Meg clean organics | | |
| RX | STI (Shallow Trench Isolation) Silicon Etch | Reactive Ion Etch (RIE) into Silicon by 280 nm | | |
| RX | HF EG | Round STI bottom corners (reduce high stress points) | | |
| RX | 1120 Dry STI Liner Oxidation | Stress source (Compessive) | | |
| RX | STI neutral implant | Proprietary | | |
| RX | End of Gate | | | |
| | | | | |
| RX CMP | HD Plasma STI oxide fill (deposition) | Stress source (Tensile?) | | |
| RX CMP | HDP oxide CMP (Chem-Mech Polish) | Leaves ~80 nm HDP (1/2 pad nitride removed when level) | | |
| RX CMP | 900 C STI Anneal (20 min N2 ambient) | Stress source (Comp) | | |
| RX CMP | BHF HDP Etch | Remove HDP close to level of adjacent Si (under pad films) | | |
| RX CMP | Hot phosphoric pad nitride etch | | | |
| RX CMP | Huang clean | remove organics | | |
| RX CMP | End of Gate | 5 -> 20 nm oxide on Silicon remaining | | PULL #1 |
| | | | | |
| BT | Blanket Deep boron implant | 1E13 cm-3 @ depth = 1.2 um | SKIPPED ion 2C | |
| | | | | |
| NW | Apply Nwell photoresist | | SKIPPED on 2C | |
| NW | Mask & expose & develop | Open up areas to receive N-type (phosphorus) well implants | SKIPPED on 2C | |
| NW | Implant Phos | Retrograde wells (1E17 cm-3 surface to 1E13  cm-3 @ 0.5 um) | SKIPPED on 2C | |
| NW | Remove resist | Plasma strip | SKIPPED on 2C | |
| NW | S/P Clean | remove organics | SKIPPED on 2C | |
| | | | | |
| BF | Apply Pwell photoresist | | | |
| BF | Mask & expose & develop | Open up areas to receive P-type (Boron) well implants | SKIPPED ON 2C | |
| BF | Implant boron | Retrograde wells (1E17 cm-3 surface to 1E13  cm-3 @ 0.5 um) | SKIPPED ON 2C | |
| BF | Remove resist | Plasma strip | SKIPPED ON 2C | |
| BF | Meg clean | remove organics | SKIPPED ON 2C | |
| BF | Pwell anneal | 1000 C 20 minutes 6% O2 | | |
| BF | Clean | remove oxide for FET gate ox growth | Grows ~5 nm oxide, diffuses dopants and relaxes stress (?) | PULL #2 |
| BF | FET gate oxide | 700 C dry-wet-dry ox process (proprietary) | | |

**Figure A2.2 Stages of pulling out the wafers for SSPVM**

208

**Appendix 3**

**Calibration of the Scale of the Potentiometer**

The output intensities of the two lasers are controlled by four potentiometers which have inputs of 0–5 V for a reading of 0–1000 in the scale. Laser was directly coupled through optical beam splitter fiber optic cables which have 0.01× and 0.1× attenuations to a Thorlabs DET36A Silicon based detector. The output voltage of the photo detector was measured by varying the dial reading of the potentiometer.

The purpose of calibration is to see how the laser power scales with the potentiometer control and how the intensities of both lasers are related. If we simply measure the current using the photo diode, we see a threshold (expected), linear rise, and then saturation.  Is the saturation a behavior of the laser or of the photodiode? To separate the two we repeat the measurement using progressively more attenuators.  The attenuators reduce the intensity at the photodiode.  If the intensity is always in the linear regime of the photodiode, we will see the true behavior of the lasers. We compare 50% duty cycle modulated at 1 kHz to see if the average laser power is roughly proportional to the duty cycle. We did not perform a dependence on duty cycle because 50% compared to 100% are the only duty cycles of interest to us. The graphs in the Figure 1 is  measured raw data and Figure 2 is photo diode current normalized for attenuation and duty cycle. The normalized graph shows that the laser power is in fact linear with the potentiometer control. The non linearity seen with less attenuation is due to saturation of the photodiode detector.  Correctly for duty cycle overlaps the lines to within experimental error.
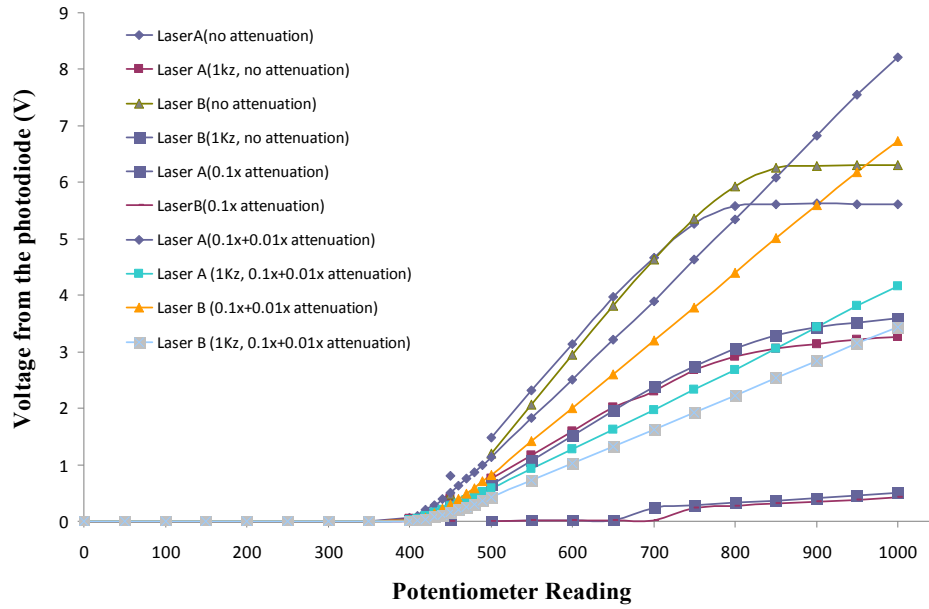
**Figure A3.1 Voltage from the photodiode for constant and 1Kz laser modulation versus potentiometer reading for lasers A and B with three different attenuations.**
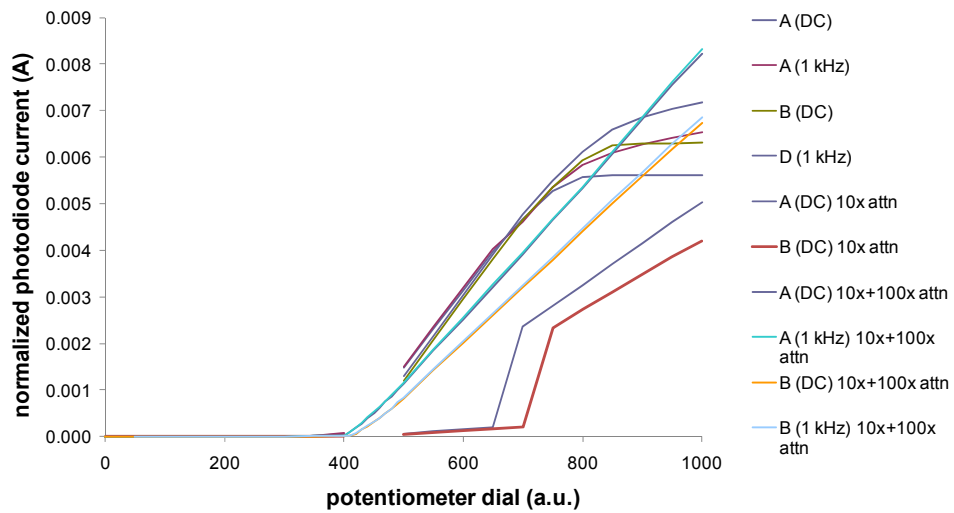


**Figure A3.2 Photo diode current normalized for attenuation and duty cycle.**

**Appendix 4**

**List of Abbreviations**

| | | |
|---|---|---|
| AFM | — | atomic force microscope |
| C10 | — | 1-decanethiol |
| C12 | — | 1-dodecanethiol |
| C8 . | — | octanethiol |
| CEBD | — | converging electron beam diffraction |
| CMOS | — | complimentary metal oxide semiconductor |
| DFM | — | dark field microscopy |
| DSPV | — | differential surface photovoltage |
| FET | — | field effect transistor |
| FGNP | — | flat gold nanoparticle |
| Imes | — | imidazoline(mesythyl) |
| ITO | — | indium tin oxide |
| KP | — | Kelvin probe |
| KPFM | — | Kelvin probe force microscopy |
| LOCOS | — | local oxidation of silicon |
| N3C10 | — | 10-azodo-1-decanethiol |
| NBD | — | nano-beam diffraction |
| PVP | — | polyvinylpyrrolidone |
| SAM | — | self assembled monolayers |
| SEM | — | scanning electron microscopy |
| SPV | — | surface photovoltage |
| SRAM | — | static random access memory |
| SSPVM | — | scanning surface photovoltage microscopy |
| STM | — | scanning tunneling microscopy |
| TEM | — | transmission electron microscopy |
| UHV | — | ultra high vacuum |
| UV | — | ultraviolet |
| VI | — | vacancy islands |
| VLSI | — | very-large-scale integration |
| XPS | — | X-ray photoelectron microscopy |